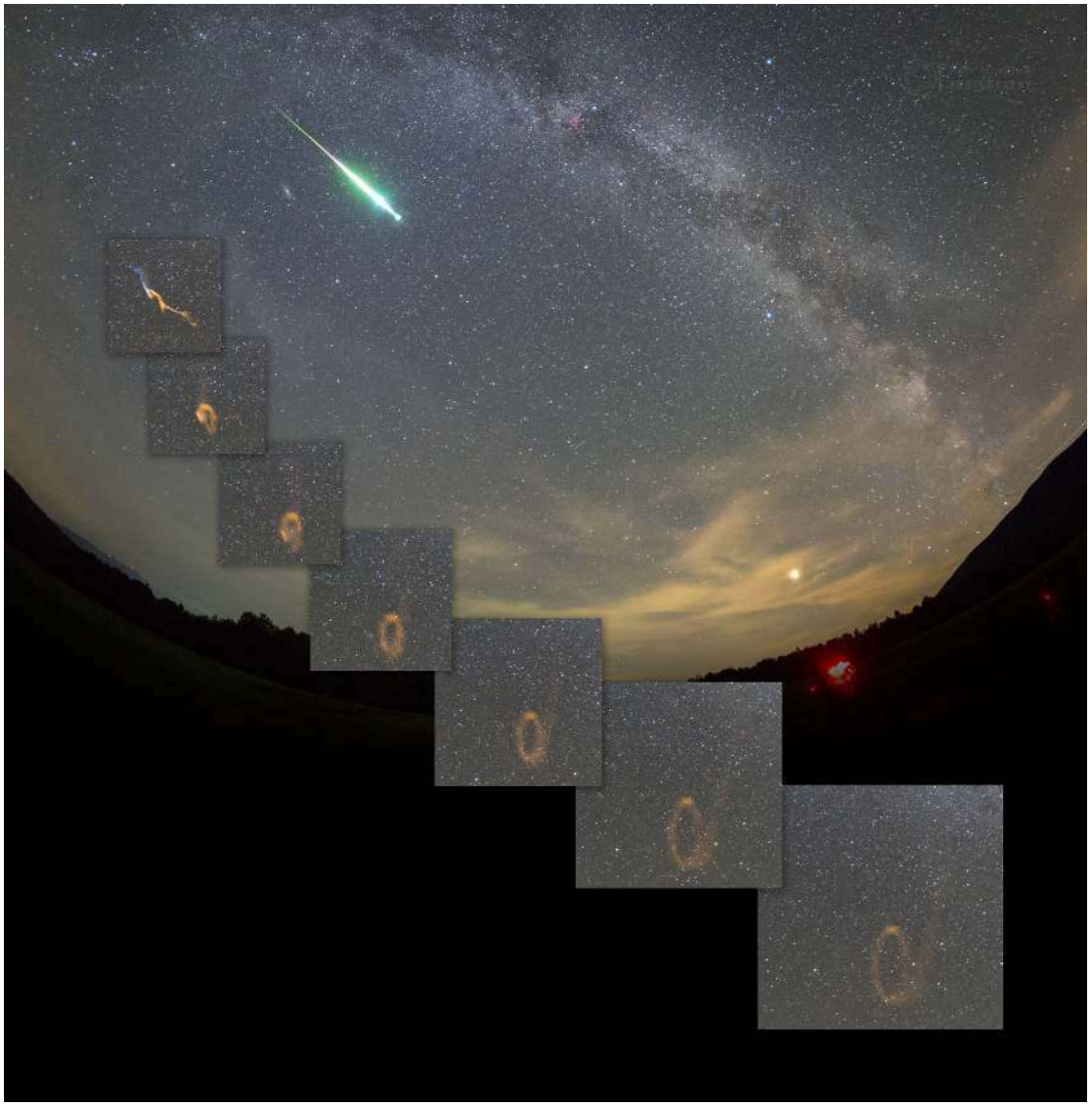
International Meteor Organization

HANDBOOK FOR METEOR OBSERVERS



Edited by
Jürgen Rendtel
2022

.

Cover images:
Perseid fireball 2018 August 12, 21:55:07.67 UTC over Kolonica Observatory, Czech Republic – Petr Holácek

Handbook for meteor observers
2022 edition

ISBN 978-2-87355-034-9

Printed in Germany

©2022 International Meteor Organization

HANDBOOK FOR METEOR OBSERVERS

Edited by
Jürgen Rendtel

With contributions from

Rainer Arlt, David J. Asher, Peter G. Brown, Pete Gural, Ralf Koschack, Sirko Molau, Jean-Louis Rault, Jürgen Rendtel, Janko Richter, Cis Verbeeck, and William Ward

International Meteor Organization
Potsdam, 2022

Table of contents

Preface 4
Foreword 5

Chapter 1: Meteor astronomy (Jürgen Rendtel) 7
Introduction 7
What are shooting stars? 7
Meteor showers and meteoroid streams 10
Sporadic meteors 14
Parent bodies 17
Meteoroid stream evolution 18
Fireballs 22
Meteorites 26
History of post-medieval meteor astronomy 30
Modern meteor science 33
Meteor observations 35

Chapter 2: Visual meteor observations (Jürgen Rendtel, Rainer Arlt and Ralf Koschack) 41
Aims 41
General advice 41
Observing location 42
Observing equipment 42
Preparing to observe 43
Visual counting observations 44
Reporting data of a visual observation 47
Meteor shower peaks 51
Observation at storm level 51
Fireball observations 54
Telescopic observations 56
VMDB – the Visual Meteor Database 56
The IMO meteor shower working list 57
Tables and charts 57

Chapter 3: Visual observations of minor showers (Rainer Arlt, Jürgen Rendtel and Ralf Koschack) 73
Plotting meteor trails 73
Background of the method 76
Example shower association 83
Summary of observing methods 85
Gnomonic Atlas Brno 2000.0 86

Chapter 4: Video observations (Sirko Molau and Pete Gural) 91
Introduction 91
Hardware 91
Analysis of video observations 94
Video meteor networks 97

Chapter 5: Photographic observations (Jürgen Rendtel and William Ward) 103
Scientific motivation 103
Faint meteors 104
Fireball patrols 105
Double-station photography 108
Meteor spectra 112
Meteor trains 113
Unusual meteor trails 115
Artistic meteor imaging 117

Chapter 6: Radio meteor observations (Cis Verbeeck and Jean-Louis Rault) 119
Introduction 119
The principle of forward scatter and radar observations 119
Forward scatter and radar setups 121
What do radio observations look like? 122
Underdense and overdense reflections 123
Which information can we deduce from forward scatter observations? 129
Estimating sporadic and shower activity from forward scatter observations 132
Further reading 137

Chapter 7: Analyses and calculations (Ralf Koschack, Jürgen Rendtel and Janko Richter) .. 139
Introduction 139
ZHR and population index 139
Analysis of visual observations 140
Determination of the population index 148
Accuracy of the ZHR 156
Flux density and spatial number density from visual observations 160

Appendix: 175

Glossary and Journal abbreviations 175

Authors 179

Preface

The *International Meteor Organization (IMO)* published its first *Handbook for Visual Meteor Observers* in 1995. It lasted until 2008 when a new edition of the handbook was published. The 1995 edition was written before the series of spectacular Leonid outbursts which greatly changed our knowledge about meteoroid streams and their evolution. At that time, a series of unusual Perseid peaks was still in progress, and other events like the return of the June-Bootids and the predicted and well-observed α-Monocerotid and Aurigid outbursts were still to come. Further events happened after the 2008 handbook edition was published, such as the outbursts of the September ε-Perseids in 2008 and 2013, or the different types of October Draconid peaks in 2011, 2012 and 2018, another α-Monocerotid outburst in 2019 and finally a brief Aurigid outburst in 2021. Descriptions of the various showers always reflect the current knowledge based on recent observations and their analyses. Comprehensive analyses of video data improved our knowledge about minor sources and "outer regions" of major showers. At the same time, the IAU established a meteor shower data base and shower designations became unambiguous. Since we will continuously find new results, the part of the Handbook describing the meteor showers will need updates on a regular basis.

The description of the observing techniques and analysing methods undergoes fewer changes. Therefore we decided already for the previous edition to publish two separate parts. The present 'first part' which is devoted to the observing techniques and analysing methods was more or less a 'constant part' since 2008. It was revised for the 2014 edition and received additional material for the 2021 edition. Changes of the observing techniques over the last decade allowed meteor workers to tackle open questions which were difficult to solve earlier when the amount of data or the available accuracy was not sufficient.

The evolution of observing techniques imply both additions to some sections while others become obsolete. For example, the former field of telescopic observations is completely covered by video cameras now.

Also the photographic work has changed a lot. When the previous edition was written, photographic meteor images were still a main source for precise calculations of atmospheric meteor/fireball trajectories and meteoroid orbits. Nowadays, still imaging is mostly known and used for aesthetic images, perhaps except the meteor spectra. Nevertheless, we decided to keep the information provided in the original chapter, amended by recent information mainly regarding technical parameters.

Visual work is an exception concerning the question of old and new. Here we have the 'connecting point' between the chance to combine historic shower data, recent shower data and to calibrate modern video data. This way we may establish information of the evolution of some meteor showers over more than a century which is important for theoretical modelling of meteoroid streams. The Chapters on radio and video meteor observations as well as the analysis and calculations Chapter have been essentially re-written and extended to be up to date.

As in the previous editions of the Handbook, we carefully checked all references. These have been placed into the sections rather than into a long list at the end of the book, even if a few citations appear more than once. We also updated the extended Glossary which may serve as a reference by itself.

We hope this publication – which is a joint effort of many people – will encourage meteor workers all over the world to further extend and improve their work, to learn more about the phenomena they are observing, and, above all, to participate in the continuously growing international efforts in meteor science.

Potsdam, Germany, December 2021

Jürgen Rendtel

Foreword

Peter G. Brown

The field of meteor science continues to change at a rapid pace. This evolution has been primarily driven by new instruments and techniques. These have provided increasingly precise and novel measurements of meteors and ultimately better probes of the nature of meteoroids. This in turn helps us understand the properties of the parent objects (comets and asteroids) which produce this debris. In this way, meteor science provides insight into the early formation and evolution of our solar system through deeper understanding of small solar system bodies.

Unlike other fields of astronomy, meteor science measurements are not entirely dominated by a few expensive facilities (though such facilities do exist in the field such as high power large aperture radars). Significant information about meteor shower activity, meteoroid composition and meteorite producing fireballs are gathered by a uniquely distributed network of global instruments. These are often operated by amateur astronomers and consist of visual observations (where the amateur is the instrument), video cameras, radio and even infrasonic microphones. Understanding what science questions these instruments can address and how to make measurements in a scientifically meaningful way is the purpose of this handbook.

There are several sources which exhaustively cover the broadly interdisciplinary aspects of meteor science. The best recent review of the entire field can be found in the book "Meteoroids: Sources of Meteors on Earth and Beyond" (Ryabova, Asher & Campbell-Brown, 2019). Here the interested reader will find reviews of the technical details of various observational approaches (Koten et al., 2019; Kero et al., 2019), the physics of meteor entry and ablation (Popova, Borovička & Campbell-Brown, 2019) as well as chapters filling in linkages between zodiacal dust and meteoroids (Koschny et al., 2019). An excellent comprehensive review of the relationship between meteoroids and their parent bodies is given in (Jenniskens, 2006). Earlier works such as Ceplecha et al. (1998) and Bronsthen (1983) and even McKinley (1961) remain useful references for comprehensive coverage of earlier literature and often hard to find details of the physics of meteor ablation.

These works provide a solid footing for researchers with focus on meteor science and related questions in astronomy and planetary science. What is lacking in the existing literature is a book which covers in detail how to make meteor observations using different instruments, in a scientifically useful manner, while also providing a basic theoretical foundation for each technique. In particular, how to make visual observations, which now represent the longest continuous source of reliable activity measurements for meteor showers, and the analyses underpinning these measurements is not described in detail in these works.

The value of scientifically useful meteor observations is demonstrated by one of the earliest examples produced from global, standardised visual meteor observations, namely identification of the early peak in the Perseids in 1988–1989. This new peak was a subtle feature found in some of the first global standardised analyses of visual meteor observations by the IMO (Roggemans, 1989). This feature, as it turned out, presaged the return of 109P/Swift-Tuttle by several years, thus establishing beyond doubt the veracity of standardised visual meteor observations. Observations of such outbursts in recent showers (most notably the Leonids) have proven critical to validation of newer numerical models of stream evolution proving yet again the worth of visual meteor data gathered in a standardised manner.

The present book is an updated version of an edition first published in 2008 and updated in 2014. Earlier versions in 1995 and 1989 concentrated solely on visual meteor observations and meteor shower descriptions. While there are several popular books which describe how to make meteor observations, none provide the background science motivation and theoretical underpinnings to the depth of this book.

Of special note in this edition is the significant update to the visual analysis section (Chapter 7). This represents the most comprehensive description of the nuances of transforming visual observations into solid measures of meteor shower characteristics (flux, ZHR, magnitude distribution) yet published. It should be essential reading for everyone (particularly professional meteor astronomers) who make use of these metrics and their associated uncertainties.

This edition, as was the case with the 2014 version, contains chapters which provide basic background on many techniques amateurs can use to record meteors. These encompass radio to video observations to visual measurements. Each chapter includes updated and useful background for hardware construction and setup and clearly communicates the results which an amateur may expect. The handbook does not water down the level

of the content (yes, there are many math equations in the handbook), but emphasizes physical understanding first while also providing in-depth discussion of techniques and helpful references for further reading.

Among all the techniques, none has evolved more since the 2014 edition than video meteor measurements. This has been driven by the rapid pace of development of new, ultra sensitive imaging sensors which are now extremely inexpensive. The video chapter has undergone extensive updates and expansion and includes information covering the major video meteor networks in operation, their software packages and hardware now in wide use within the amateur community, such as CAMS, FRIPON and the GMN. Of great interest to the professional meteor community are the tens of thousands of high quality video meteor orbits now being gathered by amateurs. Whereas amateur meteor observers in the 20th century primarily recorded meteors visually, permitting flux measurements and long shower activity profiles to be produced globally for the first time much of the data collected for meteor science in the 21st century will be driven by video observations.

All of these new developments, the associated instruments and the best way to make scientifically useful meteor observations are covered in this 2021 updated edition of the Handbook. This book will surely stand as the definitive manual for those wishing to make such observations and we can only hope that as the science of meteors continues to change in the coming years new editions of this classic work will also be forthcoming.

References:

Bronsthen V., 1983: Physics of Meteoric Phenomena, volume 22 of *Geophysics and Astrophysics Monographs*, Springer Netherlands, 358pp.

Ceplecha Z., Borovičká J., Elford W.G., ReVelle D.O., Hawkes R.L., Porubčan V., Šimek M., 1998: Meteor phenomena and bodies. *Space Science Reviews* **84,** 327–471.

Jenniskens P., 2006: Meteor showers and their parent comets, Cambridge Univ. Press, Cambridge, UK, 790pp.

Kero J., Campbell-Brown M., Stober G., Chau J.L., Mathews J.D., Pellinen-Wannberg A., 2019: Radar observations of meteors. In: *D.J. Asher, G.O. Ryabova, M.D. Campbell-Brown (eds.), Meteoroids: Sources of Meteors on Earth and Beyond,* Cambridge Univ. Press, 65–89

Koschny D., Soja R.H., Engrand C., Flynn G., Lasue J., Levasseur-Regourd A.-C., Malaspina D., Nakamura T., Poppe A.R., Sterken V.J., Trigo-Rodriguez J., 2019: Interplanetary dust, meteoroids, meteors and meteorites. *Space Science Reviews* **215,** 0038-6308.doi:10.1007/s11214-019-0597-7.

Koten P., Rendtel J., Shrbený L., Gural P.S., Borovička J., Kozak P., 2019: Meteors and meteor showers as observed by optical techniques. In: *D.J. Asher, G.O. Ryabova, M.D. Campbell-Brown (eds.), Meteoroids: Sources of Meteors on Earth and Beyond,* Cambridge Univ. Press, 90–116

McKinley D., 1961: Meteor Science and Engineering, McGraw-Hill, 309pp.

Popova D.O., Borovička J., Campbell-Brown M., 2019: Modelling the entry of meteoroids. In: *D.J. Asher, G.O. Ryabova, M.D. Campbell-Brown (eds.), Meteoroids: Sources of Meteors on Earth and Beyond,* Cambridge Univ. Press, 9–36

Roggemans P., 1989: The Perseid meteor stream in 1988: a double maximum!. *WGN* **17,** 127–137.

Ryabova G.O., Asher D.J., Campbell-Brown M.D., 2019: Meteoroids – Sources of Meteors on Earth and Beyond. Cambridge University Press, Cambridge, UK, 306pp.

1 | Meteor astronomy

Jürgen Rendtel

1.1 Introduction

A group of amateur astronomers hastily prepared for a November observing night somewhere in a thinly-populated area. Clouds in the evening had made them nervous, but they knew that the second half of the night would be much more important for recording what they hoped would be an abundance of shooting stars. Just before midnight, the clouds dissipated, and the first, spectacular, long-pathed, meteors were seen, all streaking up from the eastern horizon. The observers counted meteors in five-minute intervals, and noticed a gradual increase in their counts during the first hour. At the same time, the lengths of the meteor paths notably decreased.

The observers witnessed a storm of Leonid meteors on 2001 November 18. Their meteor tallies reached twenty, thirty, or more shooting stars per minute in the peak hour. Towards dawn, the meteor rate obviously decreased, and the astronomers were no longer very excited by the remaining two or three meteors a minute, although they would have been delighted by such activity at any other time of year. When they finished their observing in morning twilight, they knew there were other amateur astronomers west of them where midnight had just passed. They would be following the Leonid activity over the coming hours, until they too handed over monitoring meteors to people at still more westerly locations.

As the first group stopped watching, another meteor expert was sitting at his computer receiving e-mails from people who had also just finished their observations, sometimes even live counts reported by telephone from the observing site or through the IMO's web page. At this data centre, the observed numbers were calibrated to a standard activity measure. Averaged activity profiles were then sent back to all the contributing observers via e-mail, and theoretical computations of meteor peak timings were compared with the actual activity at the same time.

Campaigns like this were carried out between 1998 to 2002, when high Leonid activity was expected, and indeed observed. Such a very swift analysis and response was possible because an efficiently working system was set up, based on previous experience. For the observers, the task was simply to count visual meteor numbers in short, consecutive intervals, and report them along with an estimate of how their eyes had perceived the quality of the sky. By collecting large numbers of such reports at the data centre in a short time, modern computing power enabled the relevant correction factors to be rapidly and accurately applied to the raw counts of each individual. These numbers were then averaged with what others saw at the same time. As with all such statistical analyses, the larger the number of individual values available for averaging, the more reliable and meaningful the results, and the more scientifically useful they became.

The input of amateur astronomers—from observing experts to more casual star-gazers—who log and report meteor shower observations is of vital importance to the progress of meteor science. From occasional recordings of major shower maxima to elaborate all-year-round monitoring of meteor activity, the great collaboration of such unpaid but enthusiastic observers is an essential element to our understanding of meteors.

1.2 What are shooting stars?

Meteors occur when solid particles enter the Earth's atmosphere at high speed and ablate ('burn up') by friction, i.e. collisions with the air molecules at great height above the surface. The streak of light in the night sky so-produced is what we call a *meteor*, or, colloquially, a 'shooting star'. The word meteor is of Greek origin and means 'in the air'. The particles are known as *meteoroids*, sizes range from micrometers to meters. Any particle large and robust enough to survive its fiery passage through the atmosphere, to reach the surface still partly intact, is called a *meteorite* (Section 1.8). Dust particles below a certain size are so small that they lose their cosmic velocity before they can ablate. These gently rain down through the atmosphere constantly as *micrometeorites*. We will look at all of these in more detail in this Chapter.

Meteoroids enter the Earth's upper atmosphere with velocities between 11 and nearly 73 km/s. This speed range converts to 40 000 to 260 000 km/h. The main effect at such velocities is the collision of meteoroid atoms or molecules with molecules in the air. Electrons are stripped off atoms which are then called ions. When these electrons recombine with ions, they emit light which causes the phenomenon of a meteor. Meteor spectra show both atomic emission lines and molecular

bands. One of the essential questions is, how much of the kinetic energy is transferred into light – described by the luminous efficiency. The entry velocity has a strong effect on this parameter (Popova, Borovička & Campbell-Brown, 2019; Drolshagen et al., 2020) which may be below 1 percent or above 10 percent. Fragmentation and composition also affect the luminous efficiency.

The actual ionisation starts in the outermost fringes of the atmosphere, but the interactions here may be regarded as single, independent events because of the extremely low atmospheric density. Only when the number of collisions between the meteoroid and atoms and molecules in the atmosphere increases significantly, does the energy transformation become sufficient for easy recognition by a surface observer. Consequently, the luminous trajectory of a meteor normally begins at an altitude of 110 km. Radars can be used to detect meteoric ionisation at altitudes of up to 140 km. In most cases, the luminous trajectory ends at about 80 km above the Earth's surface (Figure 1.1). Thus, any meteor seen is normally more than 100 km away from the observer. A meteor which is comparable in brightness to the naked eye stars is caused by a meteoroid of millimeter or centimeter-size. (The relation between meteoroid mass and meteor brightness is discussed in Section 7.6.3 – see Table 7.17 on page 166.)

A meteor which exceeds the brightness of Jupiter at its best (magnitude −3) is called a *fireball*. You may find the term bolide sometimes used, primarily with exceptionally brilliant fireballs; often only meteors producing audible sounds are defined as bolides (Section 1.7). Events with magnitudes brighter than −17 are called *superbolides* (Section 1.7.2).

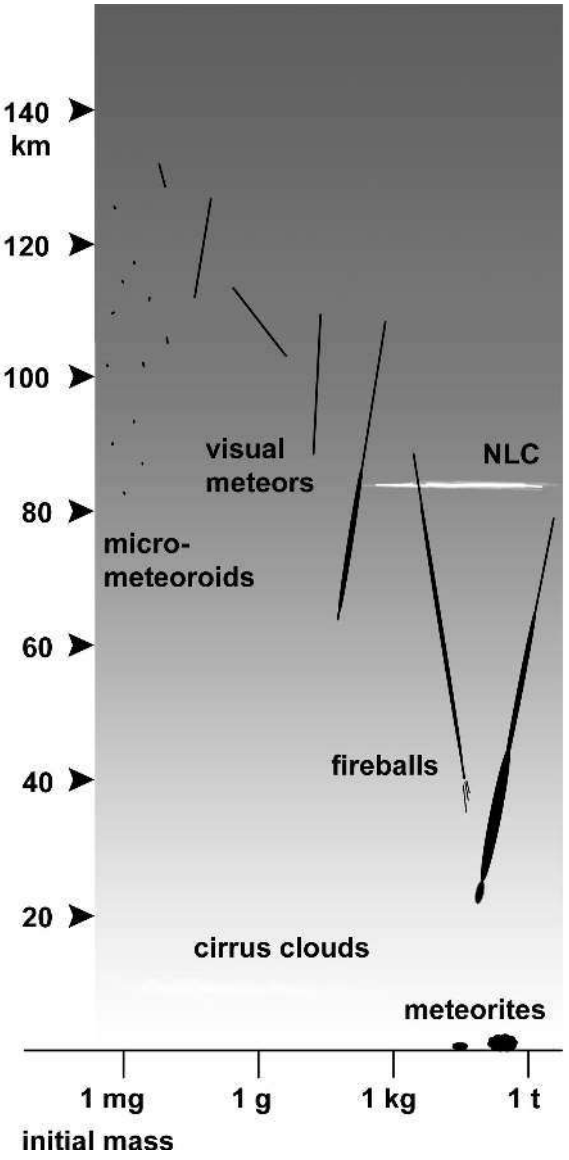


Figure 1.1: Meteoroids entering the Earth's atmosphere cause different meteor phenomena dependent on their pre-atmospheric mass. The smallest particles do not cause luminous trails (they settle to the Earth's surface extremely slowly as micrometeorites). All other meteoroids are visible during their luminous ablative phase, and, in the case of heavy, solid meteoroids, a meteorite may survive, providing several other conditions are met. Additionally, the height of noctilucent clouds (NLC) is indicated. The formation of the ice particles is assumed to happen around tiny dust particles provided by meteoroids.

The beginning height of the luminous trail increases from about 95 km for the slower-moving objects (25 km/s entry velocity) to about 130 km for the fastest meteoroids (70 km/s entry velocity). The very fast Leonid meteoroids occasionally light up above 140 km. The luminous terminal height is determined by several variable parameters, such as the particle's entry velocity, the material strength of the meteoroid and the angle of entry.

Very bright meteors are caused by very large meteoroids—occasionally by masses of several kilograms—and reach low heights of below 50 km. Coming back to the example of the Leonids, their meteoroids are of cometary constitution which is very fragile. They do not necessarily consist of a 'single rock' entering the atmosphere. They rather are a poorly glued chunk of dirt which quickly disintegrates upon penetrating the air layers. As the density of our atmosphere increases dramatically towards the ground, only the most solid, rocky bodies can reach the surface as a meteorite. There is no Leonid matter which is known to have fallen to the ground.

As will be clear to anyone who has seen even a few 'shooting stars' when casually sky-gazing, meteors are not all the same. They vary in their apparent speeds and brightnesses, and the effects seen along their trajectories: some may show sudden brightenings or *flares*; some may leave a glow after they have vanished, a *persistent train*; others may break up into fragments. Many meteors are too faint to be seen with the naked eye. These may be detected using wide-field telescopes or binoculars as *telescopic meteors*, by radio or radar equipment, or by modern video systems.

Having explained the basic nature of meteors, our next step is to find out where meteoroids come from.

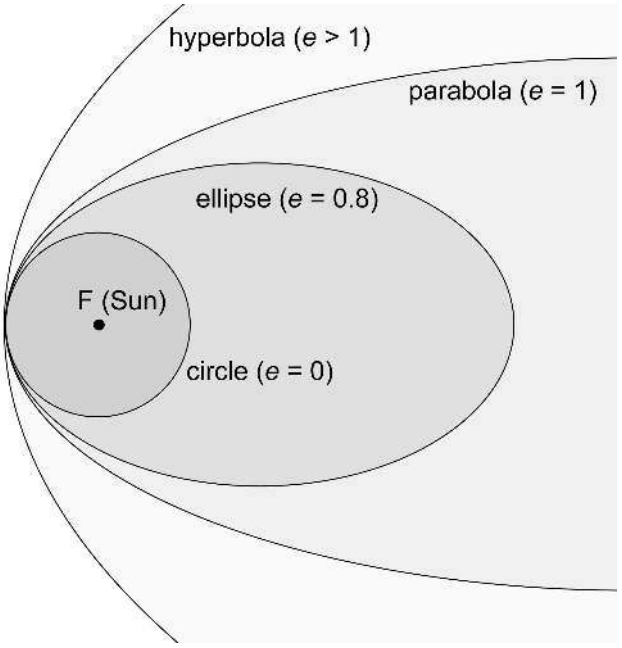


Figure 1.2: Types of orbits in the Solar System: circle, ellipse, parabola, and hyperbola. Ellipses have an eccentricity $e < 1$; the greater is e, the less like a circle is the orbit. The circle and the parabola are marginal cases which are actually never followed precisely by any celestial body. The parabola, where $e = 1$, is generally used as an approximation for initial orbit computations. Most of the orbits eventually turn out to be very eccentric ellipses.

According to Kepler's laws, every celestial body under the influence of the Sun's gravity moves in either an elliptical or hyperbolic orbit around the Sun (shown in Figure 1.2), the Sun being at one focus of the orbit. The parabolic approximation is often used for an initial computation of a comet's orbit. Elliptical orbits are closed, while parabolic and hyperbolic ones are open. Consequently, celestial bodies with open orbits can move unlimitedly far from the Sun, and so do not strictly belong to the Solar System at all. To move on such an open orbit, a body must have a sufficiently large velocity. Close to the Earth, which revolves around the Sun at about 30 km/s, this escape velocity amounts to about 42 km/s. As derived from orbital mechanics, it equals the 30 km/s circular orbital velocity at the Earth's mean distance from the Sun (1 astronomical unit, or 1 au), multiplied by $\sqrt{2}$.

Assessing whether meteoroids are part of the Solar System or not comes down to verifying whether their velocities relative to the Sun (called their *heliocentric velocities*) are lower or higher than 42 km/s at a distance of 1 au from the Sun. Now, thanks to precise photographic, video and radar observations, it has been established that this velocity is only exceeded in less than one percent of all cases. There was once much debate over this matter as will be discussed in Section 1.9.4.

Heliocentric velocities are not the same as the *geocentric velocities* we can measure for meteoroids in the Earth's atmosphere, which velocities are all relative to the Earth. For example, let us take a meteoroid with a heliocentric velocity at the upper limit for a Solar System body near the Earth, of 42 km/s. If it approaches the Earth head-on—that is, orbiting the Sun in the opposite direction to the Earth (see Figure 1.3)—its geocentric velocity is the sum of its own heliocentric velocity, plus that of the Earth's: $42 + 30 = 72$ km/s. At the other extreme, we may visualise a meteoroid moving in an orbit nearly identical to the Earth's. In this case the heliocentric velocities will differ by only a very small amount and the meteoroid will fall towards the Earth only under the influence of the Earth's gravity. This can be treated as a free fall from infinity, and it results in an entry velocity of 11.2 km/s. This is the same velocity a rocket must reach to take a spaceship away from the Earth's gravitational field. Lower entry velocities are impossible. Logically, it follows that this same gravitational attraction by the Earth must also accelerate even the fastest incoming meteoroids. Thus, from orbital mechanics, head-on meteoroids actually enter the Earth's atmosphere at $\sqrt{72^2 + 11.2^2} = 72.9$ km/s instead of 72 km/s.

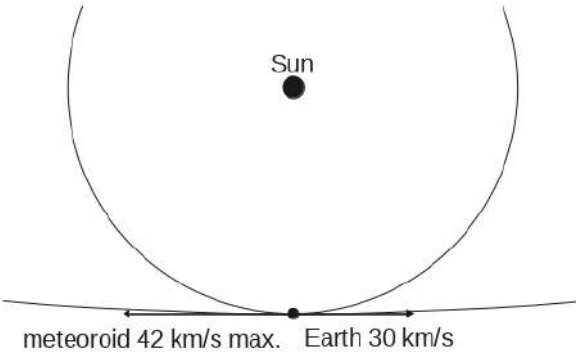


Figure 1.3: The maximum geocentric velocity of a meteoroid occurs if it moves in the opposite direction to the Earth along their respective orbits.

In different literature sources you will find different terms for the velocity data. While the meaning of the heliocentric velocity V_h is clear, the meaning of the geocentric velocity V_g is often not. At first, it may seem the same as the pre-atmospheric or entry velocity v_∞, but the effect of gravitation is not treated in all cases in the same manner. The values given above (72.9 and 11.2 km/s, respectively) include the Earth's gravitation. The corresponding geocentric velocities—without this gravitational effect—should then be 72 and 0 km/s. Because the processes which affect the meteoroids in the Earth's atmosphere depend on their entry velocities v_∞, these values should be preferred for a fuller understanding. The subscript in V_∞, intended to suggest 'at infinity', means beyond the atmosphere, not beyond the Earth's gravitational influence.

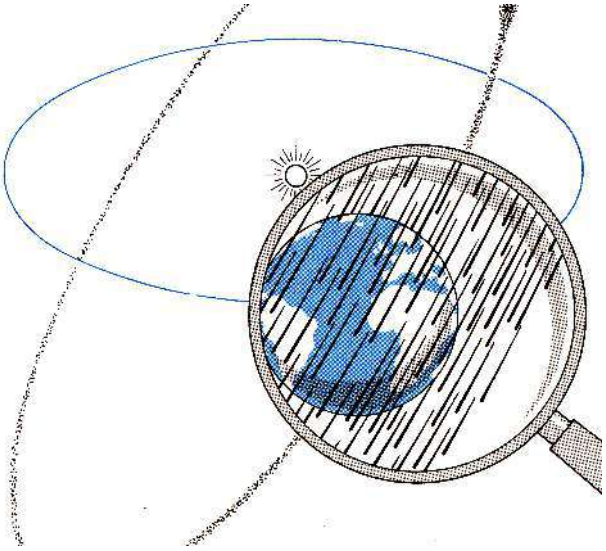


Figure 1.4: Meteoroids of one stream describe nearly parallel orbits in space.

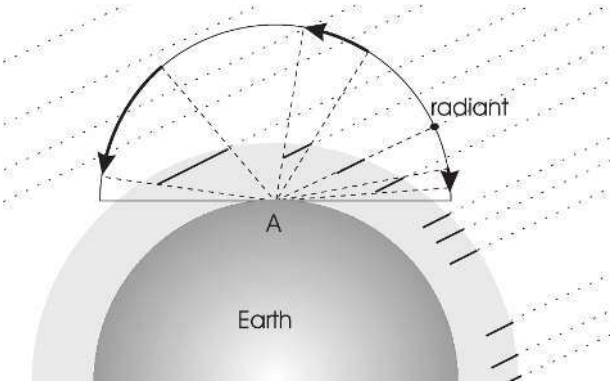


Figure 1.5: Particles moving along parallel paths are caught by the Earth's atmosphere. An observer will see meteors moving along great circles in the sky, coming from one point, the radiant.

1.3 Meteor showers and meteoroid streams

Near the maximum of major meteor showers, the observers know that most of the meteors they expect to record seem to emanate from one region in the sky. The streaks themselves may appear at any place in the sky, but the backward prolongation of the meteor paths must reach the radiant area. Meteors which do not fulfill this criterion are mostly sporadic intruders from weaker or unknown sources (Section 1.4).

Meteors which have the common property to emanate from one small region of typically 1° angular diameter form a *meteor shower*. The place where the backward prolongations meet is called the *radiant* of the meteor shower.

There is an official meteor shower nomenclature defined by the IAU. The general rule is that a meteor shower (and a meteoroid stream) should be named after the constellation that contains the radiant, specifically using the possessive Latin form with the final suffix being replaced by '-id', or plural '-ids'. The list of established meteor showers is posted at the IAU Meteor Orbit Data Center website: `http://www.astro.amu.edu.pl/~jopek/MDC2007/`. Additionally to the shower name a number is given in the IAU database. A shower is unambiguously designated by its IAU number, code, and the listed name. As an example, the list begins with the α-Capricorninds (001 CAP). In this Handbook, we add the IAU number and code only for the less known showers for better readability (except the working list on page 58). Details of the meteor shower nomenclature are given in the Meteor Shower Workbook.

This radiating effect is a consequence of perspective; actually the meteoroids all enter the atmosphere on parallel trajectories. But the prolongation of the trajectories to infinity in space appears as a meeting point of prolongations in the two-dimensional sky.

The meteoroids actually have nearly parallel orbits in interplanetary space (Figure 1.4). Such a set of many very similar orbits is called a *meteoroid stream*. A meteoroid stream can thus be linked to a comet or minor planet if orbital parameters resemble each other. The stream particles constitute material ejected from the parent.

While there are definitions for almost everything in astronomy, there is no quantitative definition of the terms 'meteor shower' and 'meteoroid stream'. About hundred years ago, meteor shower radiants were defined from visual observations. Backwards prolongations of a few apparent meteor trails crossing in a small area were sufficient (see e.g. the discussion in Denning, 1905). In 1961, the Sub-Commission 22 of the IAU considered 'meteor shower' as *a number of meteors with approximately parallel trajectories* and a 'meteor stream' as *a group of meteoric bodies with nearly identical orbits* (Millman, 1963) with no quantification. Also the current definitions give no numbers, ranges nor even parameters for these terms. A detailed discussion of this matter is found in Williams et al., 2019.

For most of the year, meteor rates are relatively low, but, on a few dates, meteor numbers rise significantly above this 'drizzle' level. Among these special times are dates around August 10–14 or December 12–14, when we can observe the maxima of major meteor showers. After the constellations Perseus and Gemini in which the radiants of these meteor showers are located, the showers are called the Perseids and the Geminids, respectively.

Shower meteoroids thus move along nearly parallel orbits in space. Technically, the direction of their radiant is given by the vectorial superposition of the direction and velocity of the meteoroids and the Earth at the

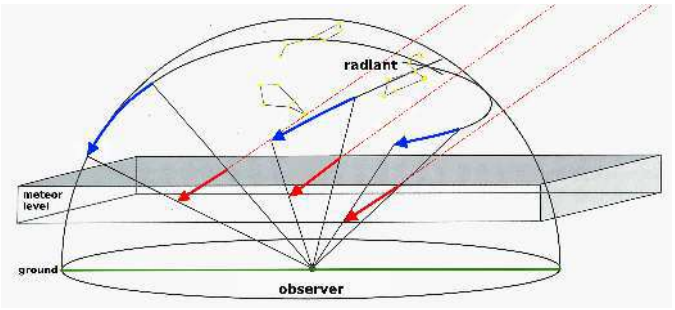


Figure 1.6: Meteoroids of a stream moving nearly parallel in space (thin dashed lines) enter the Earth's atmosphere. In the range around 100 km above the ground (indicated by the plane layer) they cause meteors which are basically straight (shown as red arrows). An observer on the ground sees the meteors against the background of stars where they appear as points moving along great circles (blue arrows) in the sky which cross each other in the radiant. The graph is not to scale and omits the curvature of the Earth.

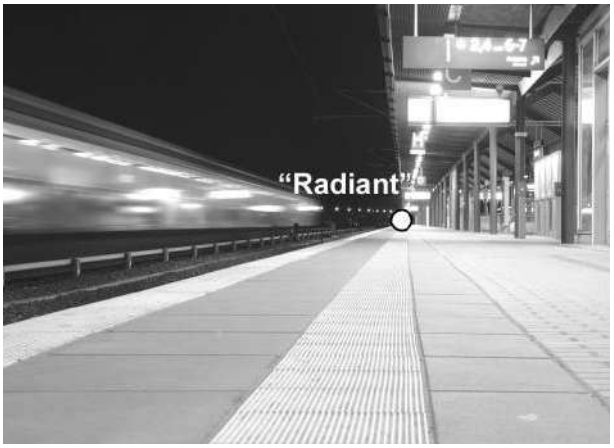


Figure 1.7: The effect of perspective and radiant demonstrated on a train station. Train, platform and roof are all parallel in space, but are diverging lines on the two-dimensional projection – here the photo.

point where they intersect the Earth's orbit (Figure 1.10 later). Less technically, and using a more familiar example, think about sitting in a car moving through falling snow. The snowflakes move on nearly parallel paths to each other, but from the car they seem to come (radiate) from a certain point and apparently flow away from this radiant in all directions. The car's velocity affects the direction that the snowflakes appear to come from.

Another terrestrial instance of parallel lines seeming to radiate from a point, is the view from a railway station as shown in Figure 1.7. Here, the train, the platform canopies and platform edges all seem to meet at a point on the horizon, the artist's 'vanishing point', though, in reality, we know they are really parallel to one another. Figure 1.5 shows how such parallel-moving meteoroids enter the Earth's atmosphere. Note that the thickness of the atmosphere and the meteor trail lengths in the figure have been considerably exaggerated for clarity. The parallel movement of the particles is not recognised as such because the trails will be projected against different parts of the star background for a visual observer. This can be best understood by imagining a hemisphere placed above the observer, like the dome of a planetarium. The meteor trails, as projected from this observer's viewpoint onto the imaginary hemisphere, are shown in Figure 1.6. When so-projected, the meteor trails become small sections of great circles, which can be extended to intersect at the radiant.

One can see another effect in Figure 1.7, too, which is often called foreshortening. The columns on the right side mark equal distances. Near the radiant, the same distance has a small extent on the two-dimensional picture, while the right-most columns have larger virtual distances in the photograph. Meteors appearing close to the radiant are short, while meteors far from the radiant have long paths.

Figure 1.8 shows how the direction of the meteoroid's orbit determines the radiant. An observer A at the

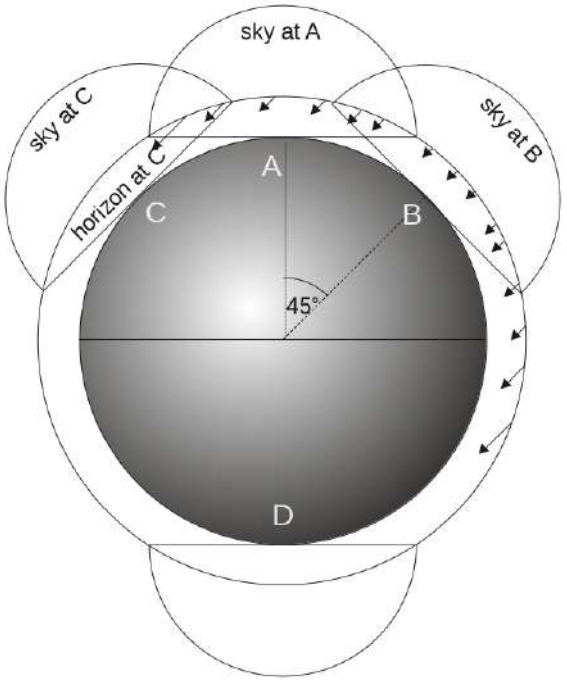


Figure 1.8: The radiant position as seen from different places on Earth at a particular time. The observer in C has the radiant at the horizon; meteor paths are long. The radiant for the observer in A is at 45° elevation, and it is in the zenith at B. The observer at the latter point sees very short meteors.

north pole will see this radiant at an elevation of 45°. Meteors of the same shower enter the atmosphere vertically at site B at latitude 45° north. To this observer, meteors descend perpendicularly towards the horizon. They seem to come from the zenith, which also coincides with the radiant. Observer C, at +45° latitude but 180° (or 12 hours in local time) away in longitude from observer B, sees considerably fewer meteors. The direction the meteoroids come from here coincides with the northern horizon, and only those meteors just graz-

ing the Earth's atmosphere will be visible at this site. Twelve hours later the situation is reversed because of the Earth's rotation. At that time observer C has the radiant in the zenith while it is on observer B's northern horizon. Observer D sees no meteors at all from this active radiant, since it is well below the horizon all the time, and meteors cannot reach the atmosphere above this site.

As a rule, major meteor showers are named after the Latin designation of the constellation in which their radiant lies. The August meteors emanating from Perseus are therefore called the Perseids. The December shower is called the Geminids, as their radiant is in Gemini, Leonids radiate from Leo as we learnt earlier, and so on. There is only one main exception to this: the Quadrantids. The constellation Quadrans Muralis was removed by the International Astronomical Union when the borders of the constellations were re-defined in 1925 and 1928. This area is now split between the constellations Hercules, Draco, and Bootes. As the shower's radiant ended up in the part allocated to northern Bootes, sometimes it is named the Bootids as a result. Information about the most important showers visible throughout the year as well as details for the naming of showers are given in the book *Meteor Shower Workbook.*

Most showers, like the Perseids, are active every year at a certain time, i.e. at the same position along the Earth's orbit. Some showers may be active only occasionally, perhaps in just one or a few years. In other years their activity remains low, or even undetectable. A famous example of such a periodic shower is the Leonids, which enjoys a popular reputation of producing strong meteor activity at 33-year intervals, including great meteor storms in 1799, 1833, 1866 and 1966. We use the term *meteor storm* where the observed meteor numbers cease to be fully recordable by a visual watcher. In the literature, this is sometimes taken to be where rates are at least 1000 meteors an hour – then the Leonids of 1999 and 2001 also belong to the list. In most years the Leonids show activity far below storm levels. Other well-known periodic showers are the June-Bootids (170 JBO), the October Draconids (009 DRA) and the α-Monocerotids (246 AMO).

While the meteoroids of a meteoroid stream may be spread more or less uniformly along their entire orbit, the intersection of the Earth's orbit through the stream is different in each case. The most famous examples for periodic intense appearances are the Leonids of comet 55P/Tempel-Tuttle (roughly 33 year orbital period) and the October Draconids of comet 21P/Giacobini-Zinner (approximately 6.5 years). In these cases we observe particles of both comets in relative proximity to their parent bodies. For the October Draconids we may expect the chance of this type of activity on roughly every second orbit, or once in every 13 years or so. We collectively call the meteoroids moving on similar, nearly parallel orbits like these a meteoroid stream. High activity can only occur if the Earth crosses a dense part of a meteoroid stream. In reality, the situation is more complex, because a parent (comet) releases new dust particles mainly around each perihelion passage. All these particles are subsequently subject to perturbations as shown for the Leonids in Figure 1.9. Effects come from the gravitation of planets and solar radiation. While gravitational perturbances may either increase or decrease the aphelion, the radiation forces particles mainly to spiral towards the Sun (Poynting-Robertson effect; see page 21). Consequently, a stream becomes wide and meteoroids do not necessarily follow the parent object's orbit or may concentrate at different locations. This also explains why we can encounter dust trails in years well before and after the actual perihelion of the parent.

The length of a shower's visible period depends on the size of the stream, and is very different from one shower to the next. The distribution of the particles along the orbit and the stream's width are affected by various influences (such as dust ejection from the parent body, gravitational perturbations, solar radiation, etc., as we shall discuss later). The angle at which the Earth crosses the orbit of the meteoroid stream also helps to determine the duration of shower activity.

The **Perseid** stream is quite broad, and thus we can observe Perseids on July 17 as well as on August 24, or at any point in between, as well as occasionally on dates before and after, with the maximum occurring around August 12 or 13. The **Quadrantids** have a much narrower stream width, and consequently produce visually observable activity for just two weeks (December 28 to January 12). The Quadrantid-maximum lasts for only a few hours. By contrast, the **Taurids** are visible for over two months with a rather diffuse double radiant and no sharp maximum, although somewhat enhanced activity occurs in October (southern branch, 002 STA) or during early November (northern branch, 017 NTA). They are therefore of far greater stream width than even the Perseids.

A radiant is not a mathematical point, since it is determined by the individual orbits of particles, each emitted from their parent object under slightly different conditions and varying perturbations affecting each section of a stream in a different way. As a consequence, the directions from which individual meteoroids enter the atmosphere vary slightly. The shorter the time interval between this emission and the observation, the less the orbits have dispersed and the sharper the radiant. Orbital dispersion is due to variations of direction and velocity at which the particles are thrown out of the parent comet, and to the gravitational pull of the planets. All observable meteoroid streams are naturally influenced by the gravity of the Earth. The giant planets, however, are the major perturbers.

A meteor shower thus has a physical radiant size. However, the accuracy of our observing method determines how well we can define a radiant in this way. While photographs or video records allow fairly precise measurements, visual observations include larger uncertainties. When associating the meteors seen with a radiant, we should not assume too small a radiant size, because we will lose actual shower members to the inaccuracy of recording. On the other hand, if we take into account too many meteors not belonging to the shower

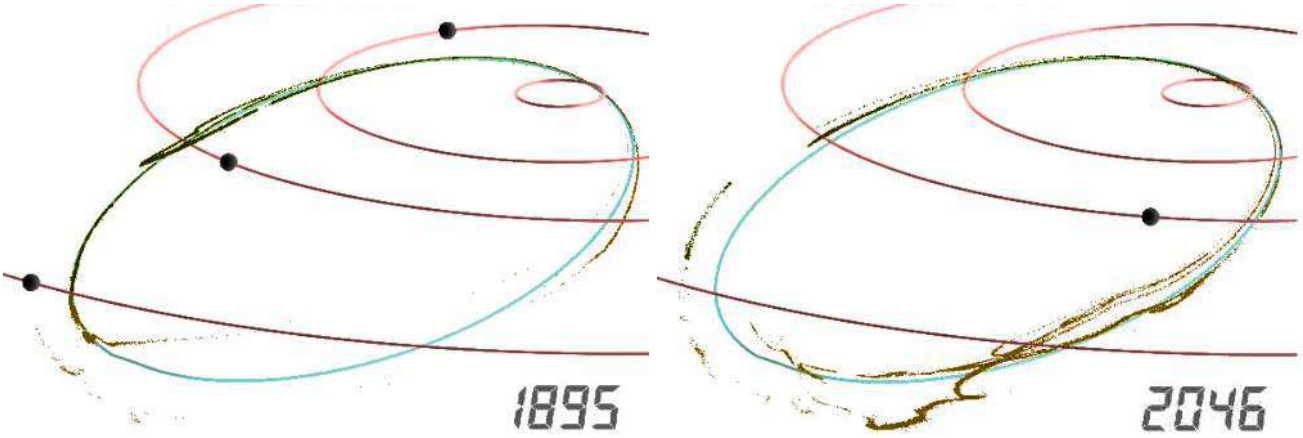


Figure 1.9: Meteoroids of the Leonids ejected from the parent comet 55/Tempel-Tuttle around its 1499 perihelion undergo gravitational perturbations mainly due to Jupiter and Saturn encounters. Here we show the shape of the stream in different years (given at lower right). The outer orbit represents Saturn, the inner shown orbit is the Earth. Note that this is the evolution of only one trail; the comet releases a new one around each subsequent perihelion passage. (Images from a simulation of Jeremie Vaubaillon, 2006.)

under study we also introduce errors. How the right balance is achieved is explained in Chapter 3.

During the active period of most showers, the radiant moves nearly one degree eastwards, parallel to the ecliptic, against the stellar background each day (Figure 1.10). This is called the radiant's *diurnal drift*, and is largely due to the Earth's own orbital motion around the Sun, which also proceeds at nearly one degree a day. As the radiant is determined by the superposition of the motions of Earth and meteoroid, the changing orbital direction of the Earth towards the east causes the radiant to move to the east as well. This is shown for the Perseid radiant in Figure 1.11. As the Earth's orbit projected onto the sky is the ecliptic, it follows that this radiant drift will be virtually parallel to the ecliptic, and because of this, it is not linear in right ascension and declination (cf. the values given for the individual showers in the book *Meteor Shower Workbook.*

Although the Earth's orbital motion accounts for this daily apparent movement of shower radiants in the sky, the orbits of the meteoroids met by the Earth differ slightly from one day to the next, too. We have to bear in mind that each individual particle was originally released from its parent body as a separate object. Depending on these and other processes operating on the surface of such a body (which themselves depend on factors including its distance from the Sun, its material structure, its prior history, and so on), the meteoroids will all have slightly different escape velocities and therefore slightly different orbits. This means that the intersection point of the Earth's orbit with that of the stream will also be displaced somewhat during the shower's duration. Consequently, the above idea that the tangent to the stream orbit moves about one degree of ecliptic longitude eastwards per day, creating the radiant motion we see from Earth, is a simplification. For instance, the particles in some streams are extremely well spread out, so that meteoroids towards the stream's inner edge may have significantly different orbits from those in the more outward regions. As these particles reach the Earth, the directions of the tangents to their orbits differ, resulting in the impression of diffuse radiants, such as those of the Taurids. If groupings appear

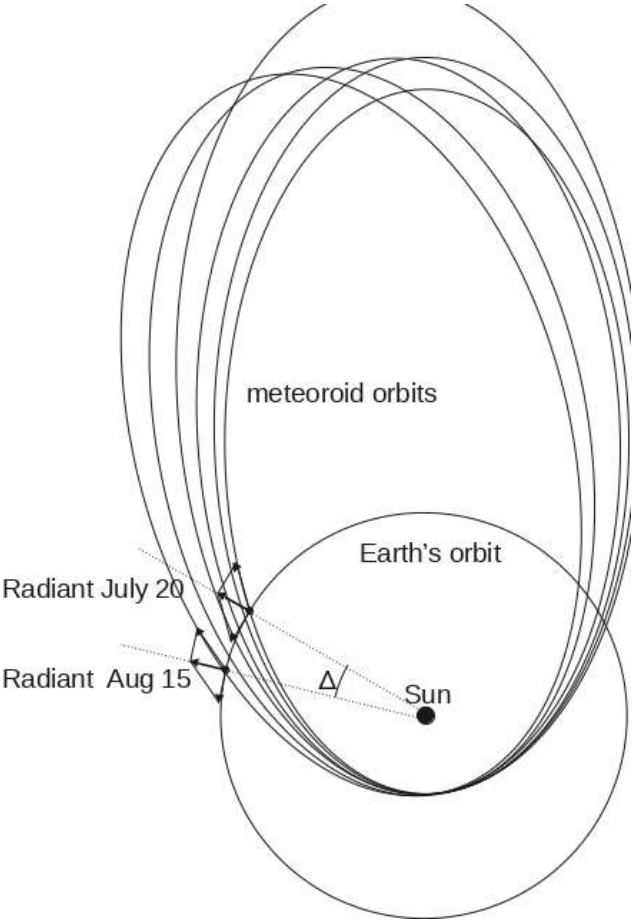


Figure 1.10: The drift of a radiant. The Earth moves along its orbit at a velocity of 30 km/s. If it crosses a stream of meteoroids moving (at a usually higher velocity) on similar orbits as shown, the direction of the shower radiant shifts by an angle Δ with time.

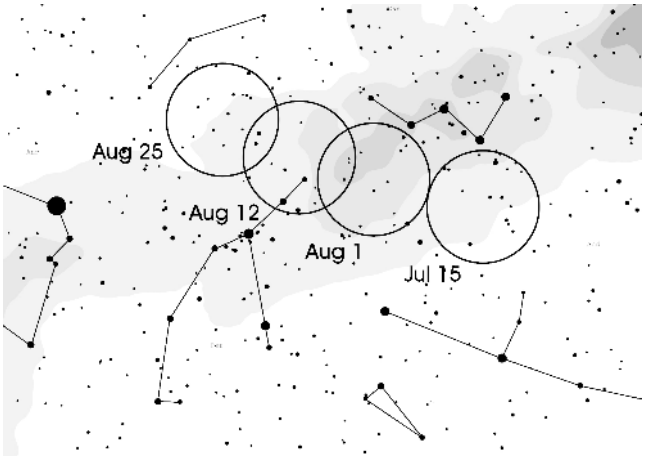


Figure 1.11: Example of the radiant drift in the case of the Perseids. At the beginning of their activity in July the radiant is south of Cassiopeia. Only around their peak, the radiant is actually in Perseus while the radiant ends in Camelopardalis after mid-August.

in these orbits, and hence also in the radiant positions, it may be possible to distinguish radiant sub-centres, or relatively short activity fluctuations. Such small-scale concentrations are caused by filaments in the particle stream.

Filaments are thought to usually result from an accumulation of meteoroids in a mean-motion resonance. Such an orbital resonance occurs when two bodies – a planet and meteoroids – have periods of revolution that are a simple integer ratio of each other. If the objects move in a synchronised way that they never closely approach, this stabilise the meteoroids' orbits. Evidence from several showers demonstrates that such filaments can cause short-lived activity outbursts. The duration of such events (i.e. the time needed for the Earth to pass through such a particle concentration) is typically less than an hour. Such events have been observed on several occasions in recent times. Apart from filament passages in major showers (Leonids, Perseids) outbursts have been recorded in minor showers as well:

- (246 AMO) α-Monocerotids 1995 (Rendtel et al., 1996) and 2019 (Rendtel, 2020a),
- (206 AUR) Aurigids 2007 (Rendtel, 2007) and 2021 (Rendtel & Koschack, 2021),
- (208 SPE) September ε-Perseids 2008 and 2013 (Rendtel & Molau, 2010; Rendtel et al., 2014)
- (009 DRA) October Draconids 2011 (Jenniskens et al., 2011) and 2018 (Rendtel, 2020b)
- (451 CAM) Camelopardalids 2014 caused by comet 209P/LINEAR (Jenniskens, 2014)
- (281 OCT) October Camelopardalids 2018 (Rendtel & Molau, 2018).

In addition to the widely-known major showers, many minor showers exist. Nobody can give their exact number, because their detectability depends strongly on the criteria defining what constitutes a reliable radiant and on the method of observation. Jenniskens et al. (2016) conclude from statistics that about 700 meteor showers exist, of which 71% are on Jupiter-family-type orbits. The more than 900 entries in the IAU meteor shower database may indicate that we are close to identifying nearly all showers but also hints at problems of confirmation and subsequent update of the working list (also meaning that some entries may be excluded). Problems with the IAU data base are discussed by Koseki (2016). Currently, parent objects are known and confirmed for about 10–15% of the showers (summarised by Williams et al., 2019).

Since the meteors of a shower under study are always only part of the overall activity, we have to keep in mind that other meteors occur as a background from which we have to distinguish our chosen shower's meteors. The limit for visual observations to reliably identify a specific shower from the background is around three meteors an hour from that shower. This aspect of observing is discussed further in Chapter 2. Other criteria apply for video data (discussed in Molau & Rendtel, 2009) and for radar or radio data. Neslušan and Hajduková (2017) analysed data from several sources to identify meteor showers. More than hundred showers were found in at least one data set when candidate showers with a poor statistical significance were discarded. It is also important to keep in mind that major showers have to be treated like minor showers outside their central region.

1.4 Sporadic meteors

If meteors are observed which cannot be associated with any active radiant from a given list of meteor showers, they are usually classified as sporadic meteors. Meteoroid streams disperse in space, and individual particles may end up on orbits totally unrelated to their original stream. In this way, all the meteoroid streams contribute to a background activity of meteors apparently appearing at random. Apart from stream dispersion, collisions of minor bodies of the Solar System provide meteoroid-sized particles moving on nearly random orbits.

Sporadic meteors appear throughout every night of the year. It is obvious that the definition of what constitutes a shower will also determine the level of the sporadic activity. It therefore becomes necessary for all observers to refer to the same list of active meteor showers in order to standardise the definition of the sporadic flux.

The sporadic meteor activity is much less striking than that of the meteor showers because of its generally low hourly rates. Dependent on the time of day and the season, we may expect to see roughly 5 to 15 sporadic meteors per hour, under excellent skies.

The sporadic meteors do not have totally random orbits. Some are members of meteor showers whose activity is below our threshold of detectability. From visual results it has been estimated that perhaps up to 20% of

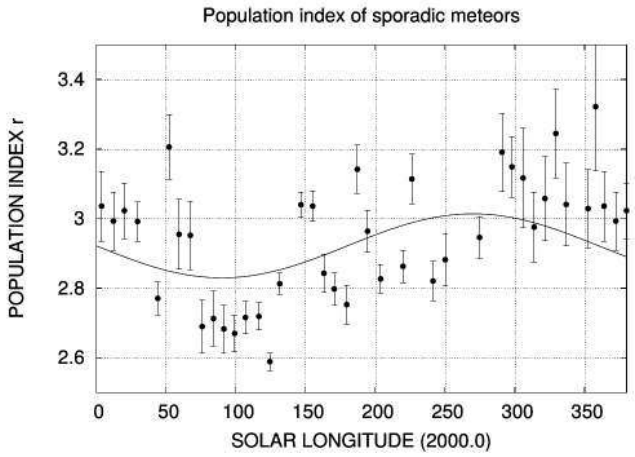


Figure 1.12: Annual variation of the population index r determined from visual observations (Rendtel, 2004). For the solar longitude definition refer to the Glossary.

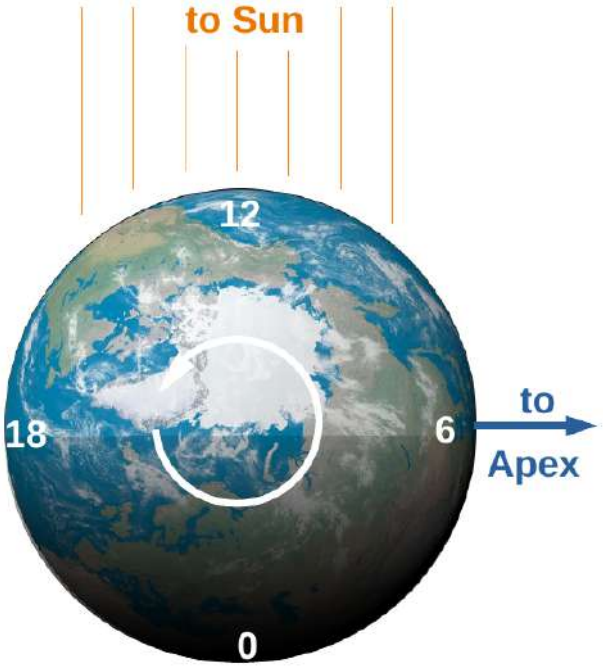


Figure 1.13: The diurnal variation is basically caused by the position of the observer on the rotating Earth: at 18^h local time, the observer is on the rear side of the Earth's orbital motion. At 6^h local time, the observer is on the front side.

the sporadic meteors seen on a 'non-shower' night are actually from this source (Hughes, 1990). In addition, the distribution of sporadic meteoroid orbits will be affected to some degree by the positioning of their former stream orbits. This in turn should lead to an increased concentration of sporadic radiants in certain areas of the sky, notably near the ecliptic plane, as the vast majority of parent bodies have low-inclination orbits.

1.4.1 Diurnal and annual variation

In examining the total sporadic flux encountered by the Earth, we find it to be a remarkably coherent type of activity despite its disparate sources, whether evaluated over short intervals or at longer timescales of up to a few years. A mean value for the population index $r = 3.0$ (see Section 7.2 on page 139) for sporadic meteors is often assumed in texts, and this is confirmed by recent observational results: an analysis of visual data collected over many years yields $r = 2.95 \pm 0.05$ (Figure 1.12) with a small annual variation (Rendtel, 2004). Sporadic rates do show two regular cycles however, one diurnal and the other annual.

During the course of the night, sporadic rates show a generally increasing trend from the early evening hours (around 18^h local time) to peak near dawn (roughly 6^h) as the observer's position rotates from the rear side to the front side of the Earth with respect to its orbital motion around the Sun (Figure 1.13). The rear side is only reached by meteors approaching the Earth from behind, moving faster than the Earth. The front side collects all meteoroids which are not faster than the Earth. This is apparent in both the northern and southern hemispheres. For radar meteors, the factor between the lowest and the highest rates varies between 2.3 at 69° N, 4.6 at 54° N and 6.4 at 22° S (Singer et al., 2005). At most locations, visual observers can follow only a part of this variation because the observing period is usually less than 12 hours. Usually, the times of the lowest and highest sporadic rates are not covered. Visual data from about 50° N, collected between 20^h and 04^h local time, yield a factor of only 1.4 for February and 1.2 in September.

In the northern hemisphere, sporadic activity slowly decreases in the first half of the year, reaching an ill-defined low around June before increasing again in July, and maintaining a generally rising pattern with some variations to reach a peak in October–December. Southern observers record the highest level in the first half of the year reaching the maximum in July followed by a steep decrease down to the minimum of September–October (Keay & Ellyett, 1969). The total flux as derived from radar observations shows no clear maximum. An analysis of visual data mainly including the (north) apex source (cf. Section 1.4.2), shows several maxima in the sporadic rate corrected for the zenith distance of the apex (Figure 1.15). These diurnal and annual variations are caused by the changing position of the sporadic sources over time.

1.4.2 Sporadic radiant distribution

Results from radar observations have demonstrated that the true distribution of sporadic radiants in the sky is rather complex, and occurs by a convoluted interplay of the distribution of meteoroid orbits, the Earth's motion relative to these orbits and a number of selection effects (Campbell-Brown & Jones, 2006; Figure 1.16). These selection factors range from the varying probabilities different meteoroids have of actually encountering the Earth in the first place, to how the particle velocities affect the produced meteor brightnesses, which in

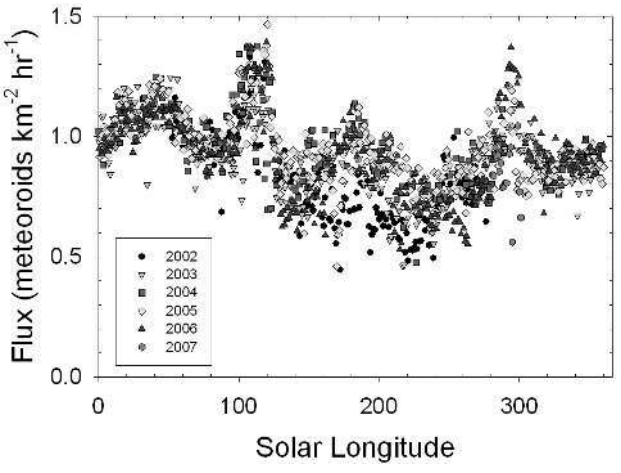


Figure 1.14: Annual variation of the total sporadic flux activity according to radar observations from London, Canada. This is an updated graph similar to Campbell-Brown & Jones (2006) provided by Campbell-Brown in August 2008. Note that the radar meteors represent a different meteoroid population (smaller particles) as compared to optical meteors and thus the times of maxima/minima differ.

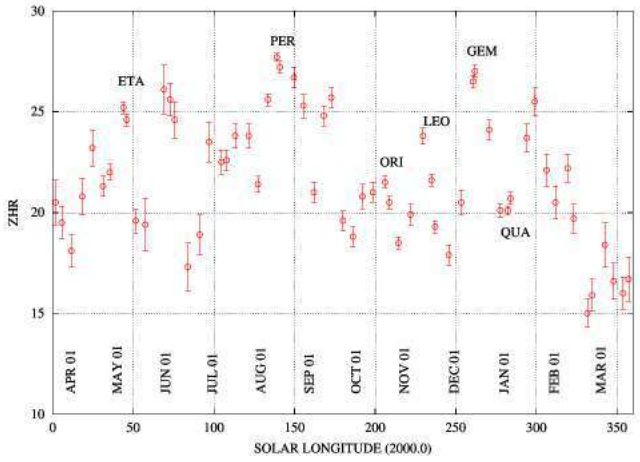


Figure 1.15: ZHR of the meteors labelled as 'SPO' in the Visual Meteor DataBase, which are representative of the activity mainly of the north apex source (Rendtel, 2006). The sample includes visual data from 1984 to 2005. Peaks of some showers, especially those with high inclinations, obviously 'pollute' the sample. Periods in the immediate vicinity of major shower peaks have been excluded.

turn makes some objects more likely to be observed than others.

In the centre of the all-sky plot (Figure 1.16), the apex source is clear. The double structure of its most active regions is caused by something of a lack of suitable meteoroid orbits with almost zero inclination. The apex sources originate from Halley-Family comets. The η-Aquariid (north apex) and Orionid (south apex) showers have radiants in the apex sources, as does the Leonid shower (north apex). All the mentioned sources

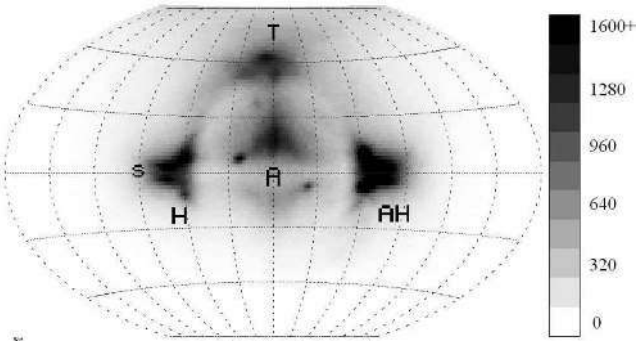


Figure 1.16: Density-distribution of sporadic meteor radiants with respect to ecliptic coordinates derived from observations of the UWO radar in London, Canada. The different sources are clearly visible: A–Apex, H–Helion, AH–Antihelion, and T–Northern Torodial source. Due to a lack of data the southern part of the sky with the Southern Torodial source was not plotted. S is the position of the Sun.

are also clearly distinguishable in the video meteor data (Molau, 2007).

On the ecliptic and symmetrically positioned to either side of the Apex are the Helion and Antihelion sources. The Helion source lies close to the Sun, and occasional meteors belonging to this group may sometimes be seen in the morning sky shortly before sunrise. The Antihelion source culminates about one hour after local midnight and is thus nearly opposite the Sun in the sky. Both sources are connected as their associated meteoroid orbits are similar (Stohl, 1986). Most of these orbits have low inclinations, high eccentricities and relatively small perihelion distances (≤ 0.6 au). An example of the combination of vectors resulting in the Helion and Antihelion sources is shown in Figure 1.17. The radiant of a meteor from these sources lies in the Antihelion region if its collision with the Earth's atmosphere takes place before it reaches perihelion, and in the Helion area if the event occurs after perihelion. Jupiter family comets are the dominant contributors to these sources. All of the daytime showers (see the respective Chapter in the *Meteor Shower Workbook* have radiants in the Helion source, while many major showers like the Geminids, the δ-Aquariids and the Taurids have radiants in the Antihelion source.

The Toroidal sources are also roughly symmetrically-placed with respect to the Apex, but due north and south of its centre some 50° away from the ecliptic. These are produced by high orbital inclination sporadics. A study of the sources of sporadic meteors and their strength is given by Jones & Brown (1994) and Campbell-Brown & Jones (2006). The parent bodies of the Toroidal source may include prograde Halley-Family comets and some near-Earth asteroids (Wiegert et al., 2009). The only major shower with a radiant in the north Toroidal region is the Quadrantid shower.

The Helion source seems to be most active from about

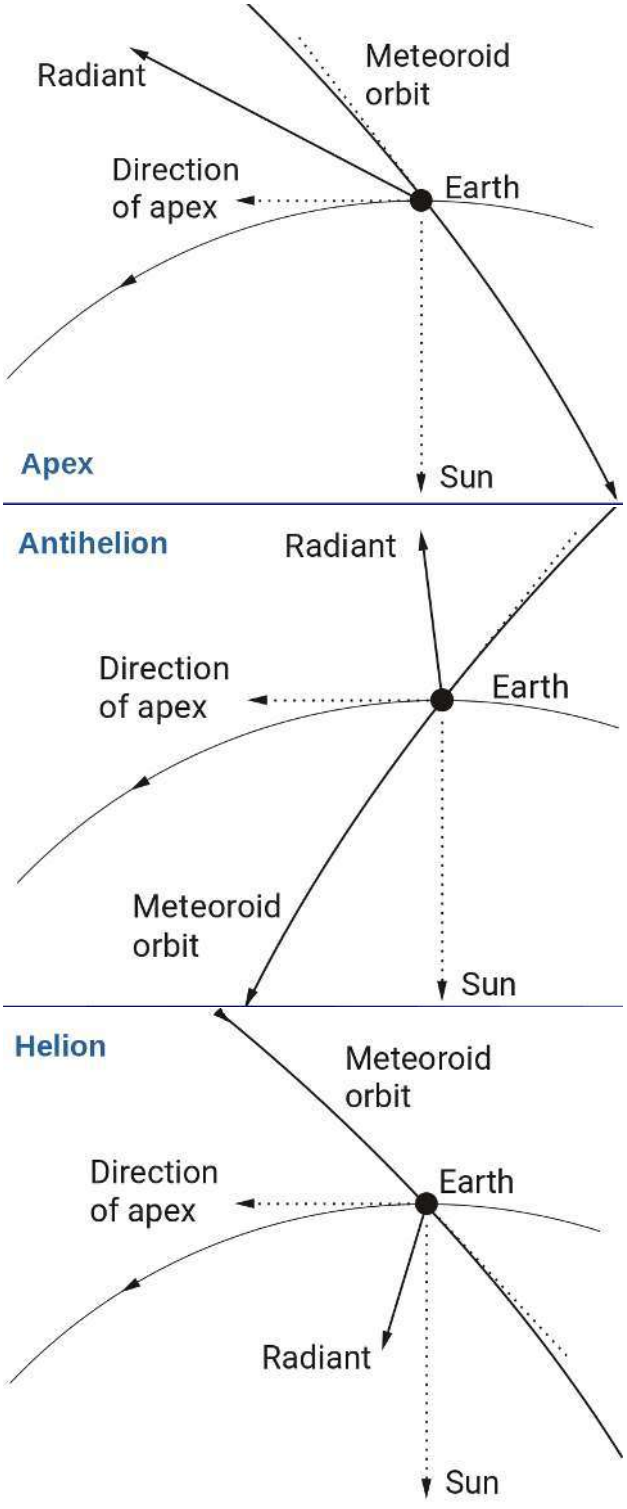


Figure 1.17: Vector subtraction of heliocentric meteor velocities and the velocity of the Earth. The resulting vectors pointing towards the radiant are directly opposite to the geocentric velocities of the meteors. Compared to the heliocentric radiant, the geocentric radiant is always turned towards the apex of the Earth's motion. The meteoroids in the top graph move on a retrograde orbit while those in the middle and lower graphs have direct orbits with small inclination and perihelion distance. The middle graph shows how the radiant is placed near the antihelion direction, the top panel shows how the radiant is placed near the apex, and the lower panel shows how the radiant is placed near the helion direction.

May to June, with the Antihelion most distinct between October to December, and it is interesting that these periods coincide approximately with the daytime ζ-Perseids and β-Taurids of June and the night-time Taurids of October–November, all of which are associated with a group of objects having orbits similar to that of Comet 2P/Encke (see the Taurids and daytime showers sections in the *Meteor Shower Workbook*). This group is thus probably the greatest originator of meteoric material in the near-Earth environment. It must be remembered however that not all sporadic meteors will radiate from one of these sources.

1.4.3 Sporadic sources: brightness correlations

A variation in population indexes r of sporadics from the various sources is apparent. There appears to be a correlation between orbital type and observed magnitude distribution (and thus also mass distribution) for the sporadics.

Compared to short-period orbits the proportion of bright meteors is higher for long-period orbits. For faint meteors the situation is reversed. The relative lack of orbits of inclination $\approx 90°$ is due to the reduced probability of these objects colliding with Earth's atmosphere.

In practical terms, the Toroidal Sources have the highest population indexes, while the Apex Source has the lowest, which means the Apex tends to dominate in photographic and to some extent visual results, though visual data from the Antihelion Source is usually more plentiful. The Torodial Sources are essentially the province of the video and radar observer. Naturally, this has an effect on what sporadic variations are seen. For example, brighter visual meteors are often noted in the post-midnight hours while rates of faint meteors may show little diurnal change at all.

1.5 Parent bodies

The first attempts to compare individual meteoroid orbits with those of other Solar System objects were made in the 1860s, when several authors published works that established comets as the originating bodies for the then-known main meteor showers, as we will discuss in Section 1.9. Initially, this was a largely theoretical link, but confirmation came in spectacular form in late November 1872.

Back in 1826, Captain Wilhelm von Biela of the Austrian army discovered a comet, now known as 3D/Biela. This was the same as a comet seen in 1805, recognised even then (by Friedrich Bessel) as the same as a faint telescopic comet seen in 1772. Von Biela and others computed it as having a very short orbital revolution, of just 6.7 years. It returned again in 1832, but was missed in 1839 due to an unfavourable geometry with the Sun. At its return of late 1845 into early 1846, it was seen to have split into two separate comets (Figure 1.18). Both these fragments were observed for the last time

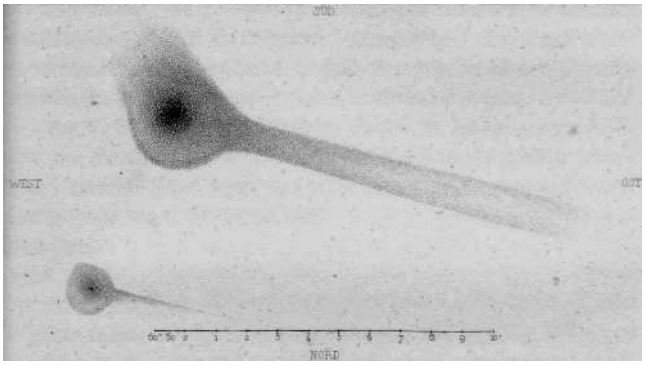


Figure 1.18: Biela's comet in 1846. This is a drawing after an observation of O. Struve on 1846 February 19 (Arago, 1856), the return at which it was seen to have broken up.

in 1852 at a large relative distance, about 1.5 million kilometres, to one another. Returns were expected in 1859 and 1865, but the comet(s) were not recovered, and have never been seen since. In 1867, astronomers Edmund Weiss, an Austrian, and Heinrich d'Arrest, a German, independently realised that occasionally very strong meteor showers, seen in early December since the late 18th century, came from the radiant in Andromeda that meteors associated with Comet Biela would have. Such Andromedid (also called 'Bielid') events, sometimes seen lasting for several nights, were reported on various dates between November 24 and December 10, when anything happened at all, probably beginning in 1741. This work by Weiss and d'Arrest led to a prediction of strong Andromedid rates for November 1872, when the Earth would pass closest to the comet's orbit, and indeed, a marvellous meteor storm was seen from Europe on November 27. A further Andromedid storm occurred, again largely over Europe, in late November 1885. Unfortunately, perturbations by the major planets have disturbed the orbit so that the dense part of the stream no longer meets the Earth's orbit. Other connections between showers and their originating bodies are described in the *Meteor Shower Workbook.*

1.6 Meteoroid stream evolution

Having linked cometary bodies with meteor showers and meteoroid streams, we now need to consider what happens to a meteoroid stream in space from the time it forms, because this has implications for how meteor showers may behave as observed from Earth. Many aspects of this discussion are theoretical, and some are either unknown or subject of debate. We must also exercise our imaginations to help us visualise what might happen to such a stream once it is exposed to the various forces at work within the Solar System.

As a comet approaches the Sun, the increased solar radiation causes the frozen ices of the nucleus's surface to sublimate to gas, liberating the dust inclusions held in the icy matrix. According to observations made by the Giotto spacecraft, there are active areas which cover about 20% of the surface of comet 1P/Halley, and it is these regions which produce all the observed cometary activity. Indeed, close-up images of the comets 1P/Halley, 19P/Borrelly, 81P/Wild, and 9P/Tempel suggest very isolated active areas on the comets' surfaces. These are likely to be the places where also meteoroid dust is released. The impactor of the space probe Deep Impact created such an active area on comet 9P/Tempel showing a jet of enormous dust production. Still, there are many unsolved questions here, such as the dust-ice ratio in cometary nuclei, the structure of nucleus surfaces, or the possible existence of amorphous water-ice and its probable transformation into (normal) crystalline ice setting free some energy which may cause the bursts of activity observed in several comets at large heliocentric distances.

The rotation of the comet's nucleus is a further reason why the release of meteoroids is an asymmetrical process. It is also not yet completely clear what velocities can be reached due to the sublimation and subsequent ejection process into vacuum. At least a fraction of the particles are able to leave the nucleus entirely while others fall back down to the surface, helping to augment the dark outer crust. For a cometary nucleus of 10 km diameter the escape velocity is of the order of 3 m/s, and ejection velocities may be of the order of 0.5–1 km/s. These values are much higher than Whipple's model (1950) suggests, and the escape process remains debatable. Ejection velocities are greater for smaller, 'fluffier', particles, for particles from larger comets, and for particles ejected closer to the Sun.

After its release from the nucleus, each particle becomes an independent body with an orbit that differs from that of the comet in two main respects. The first of these is due to the slight velocity difference which has allowed the particle's escape, the second is due to radiation pressure from the Sun, which acts as an outward force on especially tiny, low mass, objects. As material is released during a major fraction of the near-perihelion part of the comet's orbit, many effects are superimposed and cause a spreading of the individual meteoroid orbits away from the original cometary one. The ejection process may be more intense after perihelion passage, due to the cumulative heating and heat-retention of the nucleus.

The scatter in ejection velocities means meteoroid particles will both lead and lag the comet. The radiation pressure has the same dynamical effect as reducing the gravitational pull by the Sun, and the particles tend to move on larger orbits than the parent comet. The particles are thus biased to lag the comet on average. The deviations from the motion of the comet will eventually come to form a continuous belt after a certain number of revolutions. The time taken for this to occur, called the 'loop-formation time', is a function of the particle size, the size of the comet's nucleus, its perihelion distance, and the size of its orbit. Table 1.1 gives the loop-formation times for radio meteors. The mean meteoroid masses which produce radio-detectable meteors are of the order of 2 mg. The loop-formation times for visual meteors with a typical mass of ≈ 0.5 g would be roughly $2\frac{1}{2}$ times as long.

Table 1.1: Loop-formation times for selected meteoroid streams, from Hughes (1978) and McIntosh (1991). The values from the latter source are calculated for particles ejected at 1 au at 10 m/s. The figures of both papers are of the same order. (Rev. – number of revolutions)

	Hughes (1978)			McIntosh (1991)	
	Radio met. (2 mg)		Visual (0.5 g)		
Stream	Rev.	Years	Years	Rev.	Years
Geminids	11	16	40	12	18
Quadrantids	62	330	820	120	650
Orionids				9	675
Leonids				35	1100
Perseids	35	4400	8800		

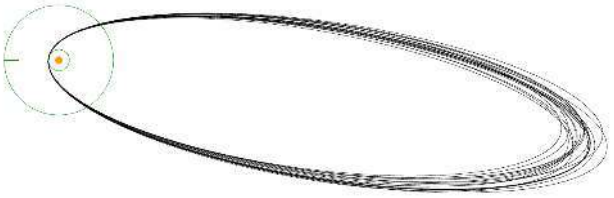


Figure 1.19: Graph of 19 averaged Perseid orbits representing a total of 10^5 orbits (modelled by Jérémie Vaubaillon) ejected in 59AD, projected into the orbital plane of comet 109P/Swift-Tuttle. The orbits of Earth and Jupiter are highly inclined in this frame. The circles are circles at equivalent distances, not Earth and Jupiter orbits themselves. The point of vernal equinox is also highly inclined to this plane but it *projects* on to the direction shown. The dispersion in the nodes Ω are smaller than the observed ones shown in Figure 1.20. The observed Ω-dispersion could result after many thousand years of evolution.

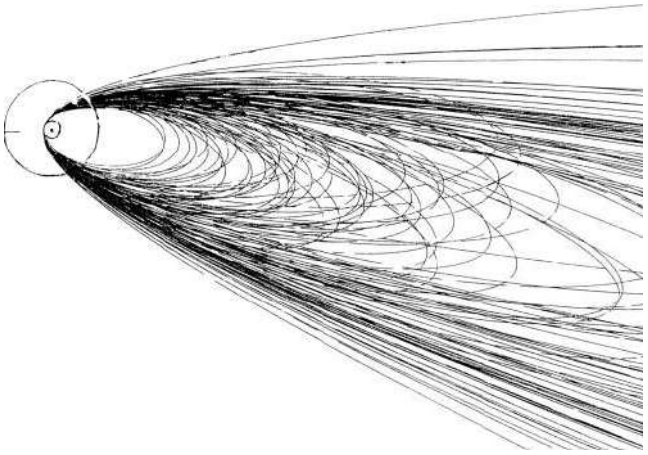


Figure 1.20: Observed Perseid orbits, from Hughes (1993).

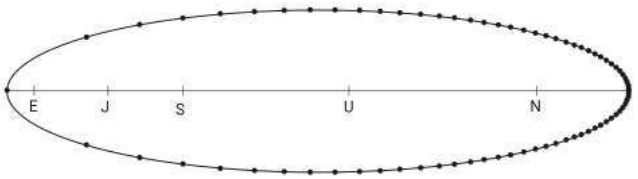


Figure 1.21: Distribution of particles along orbit after Hughes (1993). The letters denote the distances of the planets Earth to Neptune.

Modelling the evolution of a shower starts from the ejection and includes the scatter of ejection velocities and the subsequent disturbances. A result of *modelling* Perseid meteoroids ejected in 59 AD is shown in Figure 1.19. The dispersion in the nodes Ω is expected to become larger after further evolution.

Once we have established a complete loop of material along a meteoroid stream's orbit, typical distributions of orbits and of particles along average orbits emerge. An example for the *observed* Perseid orbital distribution is shown in Figure 1.20. Since the observed orbits are a superposition of meteoroids ejected during numerous periods, the dispersion of Ω, corresponding to the shower's observed duration, is larger than the modelled case.

The distribution along the average orbit is not uniform in space. Because every body in the Solar System moves slower near the aphelion of its orbit than near its perihelion, more particles travel at the far end of the orbit than at the perihelion end at any given time. This is illustrated in a schematic way in Figure 1.21.

Apart from this general fact, we might still expect to find a greater concentration of particles, many quite recently released, in the comet's vicinity, leading to enhanced meteor showers on Earth in years when the comet is near perihelion. This is the case with the Leonids for example, which can produce very strong showers for several years around their parent comet's perihelion passage, but whose average activity in other years is a much more modest trickle of meteors.

As a comet grows less active over time, while the various gravitational and radiative forces continue to operate on the meteoroid stream, we can envisage that the stream will broaden, and particles will be lost from it, but not replaced by fresh ones. The effects seen from Earth will be a decline in meteor numbers from such a source, but meteors from that shower might be detectable for a longer time each year—weeks instead of days, perhaps. Consequently, we can devise an evolutionary scheme whereby a 'young' meteor shower from a meteoroid stream still forming would produce high to very high observed rates for a few hours whenever the parent comet was nearby, but nothing at other times or in other years. At the other extreme, an 'old' shower might show low activity regularly persisting annually for a month or two, and with only slight (or even no) signs of a days-long annual enhancement in rates when the Earth was closest to the main stream's orbit, regardless of whether its parent body was at perihelion or not.

This is a simplified scheme of course, and reality tends to be more complex. Rather than be scattered evenly about the mean orbit, selection and perturbation processes cause most of the meteoroids to end up on a stream inside the comet's orbit (Vaubaillon et al., 2005a, 2005b; Jenniskens, 2006; Asher, 2008). Because of variations in the timing of these processes and fresh cometary input, each meteoroid stream is a superposition of older and younger components, which may be more or less perturbed. Some apparently older streams, including the Perseids, may show stronger coherent 'currents' of greater meteoroid density within their stream at times, due to phases of more recent cometary activity. These currents we call 'filaments', since they will not persist over more than a small fraction of the overall stream's orbit.

The 'ageing' of a meteoroid stream is not simply time-dependent. It can be accelerated or retarded depending on whether the stream has been subjected to repeated gravitational perturbations, or not. A stream with a relatively short-period, low-inclination orbit will suffer more such effects, and 'age' relatively faster than one in a longer-period, higher-inclination orbit. So we can find showers producing 'young' types of activity which have been observed at times for thousands of years, such as the Lyrids, whose orbital inclination is $\approx 80°$, and whose first probable strong activity was in 687 BC. Another effect seen with low-inclination streams is to split the observed showers into multiple—often northerly and southerly—branches, with radiants near the ecliptic (Porubčan & Očenáš, 1992). This is described in some detail for the Taurid complex in the *Meteor Shower Workbook.*

Some showers are closely related and as considered as meteoroid stream complexes. The most famous complex is the Taurid complex (see also the discussion in the Taurids section in the *Meteor Shower Workbook*). In this complex of objects on related orbits we find both nighttime and daytime showers. In this case (nighttime) Taurids are related with the ζ-Perseids (172 ZPE) and the β-Taurids (173 BTA). Further, the Sextantids (221 DSX) are part of the Phaethon-Geminid complex (Ohtsuka et al., 2006). Another complex is formed by the comet 96P/Machholz 1 and the minor planet (196 256) 2003 EH_1. This stream complex includes four well-known meteor showers (Daytime Arietids (171 ARI), Southern δ-Aquariids (005 SDA), Quadrantids (010 QUA), and the Northern δ-Aquariids (026 NDA). The stream filaments corresponding to the 171 ARI and two Aquariids (005 SDA, 026 NDA) constitute the ecliptical component, and those corresponding to the 010 QUA and their southern counterpart constitute the toroidal component of the complex (Neslušan, Kaňuchová & Tomko, 2013; Neslušan, Hajduková & Jakubík, 2013). This is also discussed in the Quadrantid section of the *Meteor Shower Workbook.* Modelled meteor showers of a group of six near-Earth asteroids with related orbits were found to be identical. They could be recognised as two nighttime showers in the Antihelion radiant area (χ- and δ-Scorpiids) and two daytime showers (β- and σ-Librids). Babadzhanov et al. (2013) assume that this complex is a result of the fragmentation of an unknown comet several millennia ago. A similar complex of Earth crossing minor planets (2008 BO_{16}, 2011 EC_{41} and 2013 CT_{36}) and four theoretical showers has been analysed by Babadzhanov, Kokhirova & Khamroev (2014). The four radiants – two nighttime and two daytime – should be in Capricornus (among them the Sagittariids/Capricornids, 115 DSC). Two further objects (2101) Adonis and 1995 CS are assumed to be related with the (nighttime) Capricornids. The authors suggest that all five objects may be fragments of a former large comet.

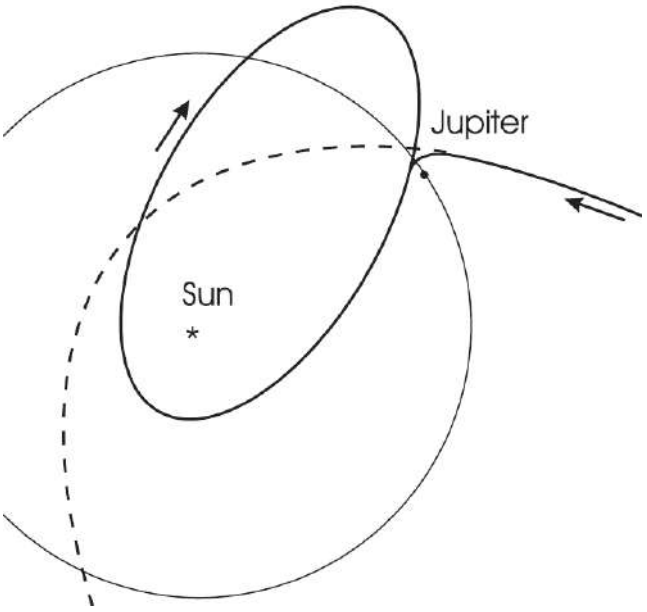
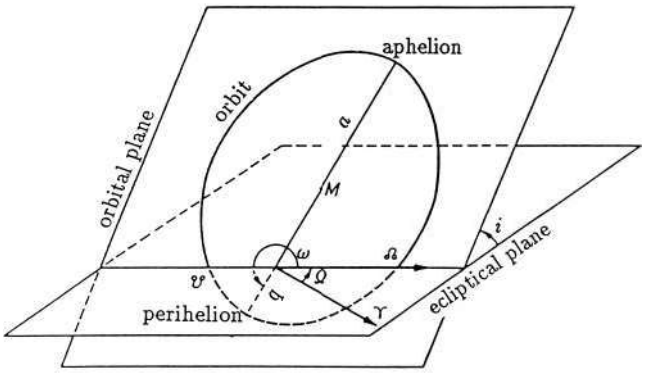


Figure 1.22: Orbital perturbations by Jupiter may change the orbit of a nearby passing object completely.

Gravitational perturbations occur the most when an object passes close to a planetary body. The larger the planet, the greater and more widespread its effect will be. In the Solar System, the strongest such planetary influence is wielded by the gas giant Jupiter (Figure 1.22). Jupiter may readily alter cometary orbits so much that they can become capable of creating entirely new meteoroid streams which the Earth can meet, but it may operate more subtly too, over longer timescales. Despite its much smaller mass, the Earth is an important perturber, too, as every observable meteoroid stream naturally passes very near the Earth – we would not see a meteor shower otherwise!

A typical phenomenon of orbital evolution is the motion (precession) of the line of nodes (that is, the line along which the stream's orbital plane intersects the ecliptic—see Figure 1.23). This motion will be retrograde if the orbital inclination is less than 90° (Figure 1.24) and prograde otherwise. Through this effect the Earth will meet the stream earlier (respectively later) and the shower maximum will occur earlier (respectively later) over the course of the centuries. A further long-term adjustment to the calendar date of the shower is due to the 'precession of the equinoxes' from the changing orientation of the Earth's spin axis.



– direction to the vernal equinox
– direction to the ascending node
i – inclination
Ω – longitude of ascending node
ω – argument of perihelion
a – semi-major axis
q – perihelion distance
e – eccentricity, $e = 1 - q/a$
π – longitude of perihelion, $\pi = \omega + \Omega$

Figure 1.23: Orbital elements.

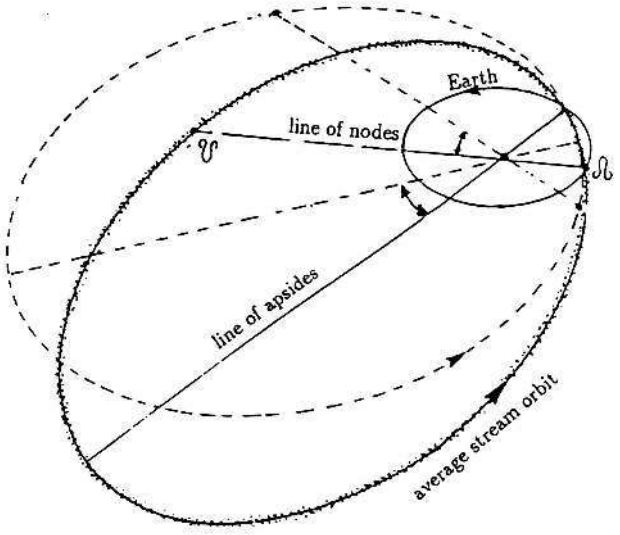


Figure 1.24: Nodal regression, how the line of nodes may be altered by gravitational perturbations over a long period, changing the whole geometry of the orbit in the Solar System. The *line of apsides* is the orbit's major axis, connecting the perihelion and aphelion points.

The orbit's inclination can be altered along with the line of apsides. (This line is shown in Figure 1.24.) These perturbations can be strong enough to increase the distance between the Earth's orbit and that of the stream, leaving no possibility of any further encounters. After several centuries or millennia, the Earth may again intersect the stream as the polar axis of the stream's orbit precesses. This is almost certainly why we did not see any Quadrantids before 1830 and why we will probably cease to see the Geminids in a few centuries from now.

So far, we have discussed the situation for an individual body, but it is clear that gravitational action will not affect all the particles in a torus of meteoroids in the same way. Imagine the case where Jupiter approaches a stream's orbit. The particles passing closest to the planet will be most affected, while those in the opposite sector of the stream's orbit will not suffer at all from this encounter. Where a very close encounter occurs, wholly unexpected situations may arise, for instance the apparent link between the Quadrantids and the Southern δ-Aquariids, dealt with in the *Meteor Shower Workbook.*

Another force which changes the orbits of interplanetary dust particles is radiation pressure, which we met earlier. As we learnt then, it results from the action of photons of light from the Sun impacting on the very smallest meteoroids. These collisions cause the photons to impart their momentum to the impacted particles, and the effect is to gradually push the affected meteoroids away from the Sun. This force increases with the particle's surface area, and since smaller meteoroids have a greater surface area to mass ratio, is extremely important for particles smaller than a few microns across. The smallest dust grains are thus ultimately 'blown out' of the Solar System, and removed from the meteoroid complex entirely. The force becomes less important for larger particles, although at millimeter sizes is still significant in the long-term orbital evolution of the stream.

Two other forces due to light and heat also affect meteoroids: Poynting-Robertson and Yarkovsky-Radzievskii. In the Poynting-Robertson Effect, photons from the Sun are absorbed by the particle, warming it up. This radiation is then re-emitted by the dust grain in various directions. Photons re-emitted in the grain's orbital direction are slightly blue-shifted by the Doppler effect, while photons emitted towards the rear are slightly red-shifted. The tiny momentum difference from the Doppler shift effectively causes a braking force which over long periods of time will cause the object to spiral in towards the Sun.

The Yarkovsky-Radzievskii Effect, which can act as either an accelerating or a retarding force, occurs for spinning particles which are not in thermal equilibrium. This means different amounts of radiation are emitted in different directions, and depending on how the particle is spinning in relation to its orbital motion, this may either increase or decrease its orbital energy, increasing or decreasing its orbital size as a result. This can effect the fine structure and orbital dispersion within a stream (Lyytinen et al., 2001).

All of these effects contribute to gradually disperse a meteoroid stream, and until it finally becomes entirely unrecognisable as such. From the timescales on which these processes operate, the conclusion is that the age of most meteor streams is likely to be of the order of 10 000 years or so, which is surprisingly short, given the current age of the Solar System of about 4600 million years.

The observable meteor population therefore is a composition made of meteoroids forming streams with particles all along the average orbit, probably with numerous dust trails (annual showers), widely dispersed meteoroids (outer regions or heavily disturbed streams) as

well as narrow regions with higher spatial meteoroid density (fresh ejecta or 'focused' meteoroids e.g. by resonant motion effects). This implies that we may observe activity from one source annually, regularly (periodic) or just on one occasion.

1.7 Fireballs

1.7.1 Fireball magnitudes

For a visual watcher, most meteors seen during an observing session will be faint. This is because, in general, meteor brightnesses relate to meteoroid sizes: the larger the meteoroid, the brighter the meteor. However, the meteoroid population is dominated by small to very small bodies. Just a tiny fraction of meteoroids are large enough to produce meteors of visual magnitude zero or brighter – and even those objects are predominantly only a few millimetres in size. Statistics suggest roughly 1 in 1200 observed meteors attains magnitude -5 or more, while just 1 in 12 000 achieves magnitude -8 (Rendtel & Knöfel, 1989). Such very brilliant meteors are called *fireballs.*

The defining minimum magnitude for a visual fireball varies somewhat arbitrarily in the literature, between approximately magnitudes -2 to -6. International agreement on a minimum value of magnitude -3 was accomplished following the IMO's formation in 1988, and this is now widely accepted. The same value of -3 defines video fireballs too, but because video systems may have a variable spectral sensitivity compared to the human eye (in particular, many such systems are more sensitive to infra-red radiation), this is usually stated as a 'video magnitude', which may be brighter, perhaps by a magnitude or so, to what a visual observer would have seen. Various definitions based on received signal strength and duration have been attempted to give an equivalent classification for radio fireballs, but since it is not possible to state a simple relationship between a meteor's true brightness and the radio reflection it produces, the best we can achieve is to suggest that a strong, long-duration radio echo may have been due to a radio fireball. Sometimes, it is possible to use such a radio echo timing to correlate the event with a visual fireball, but even this does not guarantee the two were due to the same event.

1.7.2 Superbolides

Two other fireball definitions may be found in the literature, *bolide* and *superbolide*. There is no specific definition as to what constitutes a 'bolide' (which derives from the Greek 'bolis' a throwing-dart or spear), other than it can be applied to any especially bright fireball, or sometimes a fireball which also produces sounds audible at the Earth's surface. 'Superbolides' are those exceptionally rare and brilliant fireballs which can be observed from Earth-orbiting spacecraft equipped with suitable sensors, which spacecraft are normally employed to check for compliance with nuclear bomb test



Figure 1.25: One of literally thousands of images showing the bright fireball which appeared shortly after sunrise on 2013 February 15.

treaties. As such, the minimum magnitude for a superbolide is -17 mag (Ceplecha et al., 1999). The most prominent recent example was the Chelyabinsk superbolide of 2013 February 15 (Borovička et al., 2013; Brown et al., 2013).

The remarkable Chelyabinsk event (Figure 1.25) was observed from the ground (more than 400 video cameras at ranges up to 700 km away). Further data include infrasound, seismic and US government sensors. The airblast (shock wave travelling through the air from an explosion) shattered thousands of windows in and around Chelyabinsk, Russia, with broken glass injuring many residents. The peak brightness was equivalent to an absolute astronomical magnitude of -28 (Brown et al., 2013). For an observer directly under this point the bolide appeared 30 times brighter than the Sun. The data yield an estimated energy equivalent of about 530 kt of TNT. In this respect, the Chelyabinsk superbolide belongs to the strongest airblasts on record, and it certainly is the best documented event of this class. Table 1.2 gives an overview of airblasts observed since the famous "Tunguska-event" in 1908.

The data of the Chelyabinsk bolide allow us to analyse atmospheric processes in great detail (see page 1.7.4). Very obvious was a huge dust train which was left in the atmosphere after the bolide passage (Figure 1.26). The southern and bottom sides of the trail were illuminated by the rising Sun. From northern sites the trail appeared thin because only the illuminated bottom was visible (except for the first seconds, when the trail was self-luminous). The trail started at an altitude of 68 km. Between 60 and 26 km, the trail was thick, with a radius of 1.0–1.8 km. The lower parts were thinner and continued down to 18 km. The total volume of the trail was of order 600 km^3. The lower edge of the thick trail was almost stationary immediately after the passage of the bolide but then moved forwards in two waves as the material originally released at greater heights arrived. About 15 s after the bolide passage, splitting of the trail into two parallel tracks became apparent, an effect seen in high-altitude luminous meteor

Table 1.2: Selected airblasts recorded between 1908 and 2021 (as of December 2021). We list very large events and some which are of special interest for astronomical reasons such as the entries of 2008 TC_3 (2008 Oct 7), the first minor planet detected before impacting Earth, the 3 m-sized 2019 MO (2019 Jun 22) and another 8 m-object on 2020 Dec 22.
The approximate total radiated energy in the atmosphere represents the kinetic energy of the object and is given in Joule (J). An event with an energy equivalent of 1000 t TNT is called a "kiloton event", where 1 kt (TNT) = 4.185 TJ.

Date	Location	Energy released	Explosion height	Reference
1908 Jun 30	Tunguska, Russia 60°53′09″N, 101°53′40″E	10–15 Mt TNT 42 000–63 000 TJ	8.5 km	Napier & Asher, 2009
1930 Aug 13	Curu cá, Brazil 5°11′S, 71°38′W	9–5000 kt TNT 38–20 920 TJ		Corderoa & Poveda, 2011
1932 Dec 8	Arroyomolinos de León, Spain 38°1′N, 6°25′W	190 kt TNT 790 TJ	15.7 km	Madiedo & Trigo-Rodriguez, 2011
1947 Feb 12	Sikhote-Alin Mts., Russia 46°9′36″N, 134°39′12″E	10 kt TNT 42 TJ		Fesenkov & Krinov, 1959
1963 Aug 3	Prince Edward Islands 51°S, 24°E	176–356 kt TNT 740–1490 TJ		Edwards et al., 2006
2002 Jun 6	230 km NNE of Benghazi, Libya 34°N, 21°E	12–26 kt TNT 50–109 TJ		Brown et al., 2002
2008 Oct 7	Almahata Sitta, Sudan 20°48′N, 32°12′E	0.9–2.1 kt TNT 3.8–8.8 TJ	37 km	Yeomans, 2008
2009 Oct 8	South Sulawesi, Indonesia 4°30′S, 120°E	31–50 kt TNT 130–210 TJ	25 km	Silber et al., 2011
2013 Feb 15	Chelyabinsk, Russia 54°30′N, 61°30′E	530 kt TNT 2100 TJ	30–45 km	see text
2013 Apr 30	SW of the Azores 35°30′N, 30°42′W	10 kt TNT 42 TJ	21 km	`cneos.jpl.nasa.gov/fireballs/`
2016 Feb 06	NW of Tristan da Cunha island 30°24′S, 25°30′W	13 kt TNT 45 TJ	31 km	`cneos.jpl.nasa.gov/fireballs/`
2017 Dec 15	Kamchatka, Russia 60°12′S, 170°0′E	6.4 kt TNT 27 TJ	20 km	`cneos.jpl.nasa.gov/fireballs/`
2018 Dec 18	Bering Sea / Kamchatka, Russia 56°54′N, 172°24′E	49 kt TNT 205 TJ	26 km	`cneos.jpl.nasa.gov/fireballs/`
2019 Jun 22	Caribbean Sea 14°54′N, 66°12′W	6 kt TNT 25 TJ	32 km	`cneos.jpl.nasa.gov/fireballs/`
2020 Dec 22	Qinghai province, China 31°54′N, 96°12′E	9.5 kt TNT 40 TJ	36 km	`cneos.jpl.nasa.gov/fireballs/`
2021 Jul 05	North Pacific, S. of Alaska 44°18′N, 164°12′W	1.8 kt TNT 8 TJ	43 km	`cneos.jpl.nasa.gov/fireballs/`



Figure 1.26: Composite image of the Chelyabinsk dust train showing the sunlit part as well as the far side (to the right) partly shaded generated from a video taken by Gregor Grimm (location 55 °.110894N, 61 °.409514E). Composite from P. Brown, UWO, London, Canada.

trails and caused by convective instability leading to vortices.

Satellite measurements allowed the detection of aerosols in the mid-stratosphere (25–45 km altitude) released from the Chelyabinsk event. The plume spread withpropagation speeds up to 85 m/s and subsequently formed a circumpolar layer by February 19 comprised of the faster, higher portion of the plume. A detectable belt of bolide dust persisted around the planet for at least three months (Gorkavyi et al., 2013).

1.7.3 Fireball rates

As with other meteor activities, fireball rates vary too. Some annual meteor showers, such as the Perseids, produce more bright meteors than the sporadic background, including a higher proportion of fireballs. The Perseids consistently show three to four times more fireballs (around $1.0 \pm 0.2\%$) than the sporadics in IMO statistics (McBeath, 1999). Sporadic fireball rates, as sporadic activity in general (as we found in Section 1.4), vary annually and diurnally as well. Oddly though, the annual sporadic fireball 'peak' happens near the vernal equinox in the northern hemisphere, when hourly sporadic counts for the year are at their lowest. Fireball rates then are statistically around three times their level at the northern autumnal equinox for mid-latitude visual and photographic meteors (Rendtel & Knöfel, 1989). This ratio holds true for the subset of fireballs which drop meteorites (Halliday & Griffin, 1982). The diurnal sporadic fireball "peak" also has a similar antiphase relationship to the total sporadic activity, with a statistical high at about 18^{h} local time, and a low roughly twelve hours later, around 6^{h} local time. For visual and photographic sporadics, the likelihood of a fireball occurring in the local evening, compared to the morning, hours is 4:1 (Rendtel & Knöfel, 1989). For meteorite falls, this ratio is between 2:1 (mid-latitudes; Halliday & Griffin, 1982) to 3:1 (all latitudes; Hughes, 1981).

Part of these variations results from the non-uniform distribution of the sporadic meteoroids the Earth orbit encounters at different times of year. However, there are theoretical considerations beyond such anisotropies. Normally, we would expect a faster meteoroid of a given size to produce a brighter meteor than a slower one. There is a counter-argument to this as we move to larger particles, up to potential meteorite-dropping objects, because faster meteoroids ablate higher in the atmosphere. A slower velocity object starts ablating somewhat lower, and with a larger particle, there will be more material to ablate, which means in turn the particle may continue ablating deeper into the atmosphere. The increasing atmospheric density closer to the surface increases the efficiency of the energy transformation for an incoming meteoroid, and consequently produces a brighter meteor. Meteoroids which are travelling through space in roughly the same direction as the Earth arrive with the lowest relative velocities, as we learnt earlier (Section 1.2). This 'antiapex' region is on the ecliptic about 90° east of the Sun, so it follows that it will be highest in the sky towards 18^{h} local time daily, and in the spring annually. This certainly seems to fit with the observed sporadic fireball distributions for the northern hemisphere. Southern hemisphere observations to check whether the same pattern holds true there have not yet been made in sufficient quantity. The same problem exists for checking data from tropical and polar regions. From what we have discussed here, in theory, fireball rates should show a much stronger diurnal, but a weaker annual, variation from the tropics, and a significantly lower diurnal, but greater annual, change towards the poles. These comments assume that the antiapex effect dominates, but we must bear in mind that the anisotropy of sporadic particles may play a greater role. Caution is also due not to confuse the antiapex concept with an 'antiapex radiation area'; the antiapex is actually the point with the least probability to be the radiant of any meteoroid. A concentration of radiation points around the antiapex does not exist.

Some authors, including Astapovich & Terentjeva (1968) and Dall'Olmo (1978), have suggested that regular fireball showers were observed in the past. It is not clear if such early records were of just ordinary bright meteors (e.g., of magnitudes from +2 to −2), or were of modernly-recognised fireballs, however. It is curious that, if such fireball showers were prevalent at times 500 to 2000 years ago, there are none seen today. This may have implications for comet-meteoroid stream evolution, if correct. Occasionally though, we do get unusually strong returns of other meteor showers with many fireballs, the most recent example of which was the 1998 Leonids over Europe, when a superb display of bright meteors was seen on November 16-17. Around 15 to 20% of Leonids that night were fireballs! Enhanced fireball rates have also been observed from the Taurids in years when the Earth encountered a dense region called "Taurid swarm" (Spurný et al., 2017); the next such encounter is due end October / early November 2022.

In the IMO, we regard meteors of at least zenithal magnitude −3 as fireballs. By *zenithal magnitude* we mean the brightness the meteor would have if it had appeared in the zenith of the observing site. As an example, a meteor *appearing* as −1 may actually be a fireball if it moves only a few degrees above the horizon. The apparent brightness decreases with the square of the distance between object and observer, and further-

more, the absorption of the light is proportional to the optical pathlength as well. In the case of a near-horizon meteor, the distance to the observer is very large resulting in a strong reduction of the apparent brightness.

To put this the other way round: a fireball of −6 zenithal magnitude terminating about 50 km above Earth's surface will appear as a meteor of magnitude −1 at an elevation of 5° above the horizon for an observer 600 km from the event.

The zenithal magnitude for visual observations can be calculated using the formula:

$$M = m + 5 \log \sin h \tag{1.1}$$

where M is the zenithal magnitude, m the apparent magnitude and h the elevation of the event above the horizon.

Annual variations of fireball frequencies to be seen from the equator must be caused by variations of the meteoroid distribution along the Earth's orbit. In case of an isotropic distribution, there would be no annual variation at all. The reason for this is the geometry of the apex / antiapex positions. Both rising and setting of near-ecliptic regions means that they appear or disappear almost vertically at the horizon. This is independent of the seasons. The only change is an alteration of the azimuth of the rising or setting point, but this does not cause any real difference. On the other hand, the very steep rising of the apex during the night causes a very strong diurnal variation. At the poles we find the opposite. Virtually no diurnal variation will occur at all since any celestial point circles the sky at a constant altitude. But there will be a significant annual variation. For half the year the apex / antiapex are situated below and above the horizon respectively. At mid-latitudes we find an increasing effect of annual, but a decreasing effect of diurnal, variations. Superimposed on this is a gentle decrease of fireball frequency towards the poles, because the orbits of the meteoroids responsible for producing these meteors are concentrated near the ecliptic. Consequently the expected rates will be highest between the tropics where the ecliptic reaches its highest positions in the sky. As already pointed out, this is valid only if we assume an isotropic distribution of meteoroid orbits in the plane of the ecliptic.

1.7.4 Fireballs and meteorite falls

Only very few fireballs are connected with meteorite falls. A meteorite may survive its atmospheric flight and may perhaps then be found if at least part of the body is decelerated from its entry velocity down to its free-fall terminal velocity of about 100 m/s. According to the models in use (see Wetherill and ReVelle (1981) and references therein) and using the ablation coefficient derived from the Příbram, Lost City and Innisfree falls, less than 50% of the remaining mass will be ablated as soon as the velocity falls below 8 km/s.

Another destructive process which may work against the fall of a meteorite is fragmentation of the meteoroid. The peak pressures these bodies can stand, as derived from large bodies such as recovered meteorites, were found to be about 10^6 N/m^2 (1 MPa). This is much less than the crushing stress of about 10^8 N/m^2 found in laboratory measurements. The reason may be in the earlier history of the meteorite parent bodies. Obviously, a very large fraction of meteoroids undergoes a breakup when entering the atmosphere. This was visually observed in the past, but becomes very obvious from fireball photographs (e.g., the Lost City images (McCrosky et al., 1971) and other meteor images (Babadzhanov & Kramer, 1968)) and the video recordings taken of the Peekskill meteorite fall on 1992 October 9 (Brown et al., 1994). More details are available for the Chelyabinsk meteoroid (see subsection 1.7.2). Here, the first significant mass loss occurred at an altitude of about 45 km, under a dynamic pressure of 7×10^5 N/m^2 (Borovička et al., 2013). The most severe fragmentations occurred between 40 and 30 km ($1–5 \times 10^6$ N/m^2). By 29 km, the object had already fragmented into about 20 large boulders. Deceleration data hint at a mass of the leading boulder (main body) of approximately 2×10^4 kg. It remained intact until an altitude of 22 km, before severe disintegration began at a pressure of 18×10^6 N/m^2. The main mass of 654 kg caused a circular hole of about 6 m diameter in the ice cover of the nearby Chebarkul lake. The chunk was detected and finally recovered in September 2013 from the ground of the lake.

The fragmentation history shows that the bulk strength of the Chelyabinsk asteroid was about 10^6 N/m^2 (1 MPa), a value typical for smaller meteoroids, confirming that for near-Earth objects there is little correlation between strength and size on scales from centimetres to tens of metres. Only the very strongest parts, representing less than 1% of the original mass, had strength > 15 MPa.

We may then assume that a successful passage of the atmosphere will occur if the object enters at less than 23 km/s and survives to reach a velocity of less than 8 km/s without serious disruption. All of these values were derived from ordinary chondrites however and are likely to be valid only for comparable materials. Even so, the above is only true up to a certain mass. Very large objects of several meters in diameter, which may cause meteorite craters, are not decelerated very much (Ceplecha 1991).

After the transformation of its kinetic energy and its total deceleration, the surviving meteorite falls only by the Earth's gravitation without the emission of light, a period known as dark flight. During this phase the wind's force and direction have an important influence, and the surviving body may drift away from its original course. The effect can be considerable because both the free-falling meteorite and the wind have comparable velocities. Furthermore the dark flight trajectory is affected by the shape of the meteorite.

All the parameters characterising a bright fireball—its entry velocity, initial mass, angle of entry, the final

height of its luminous trail and its brightness—are put together in the PE-criterion (Ceplecha and McCrosky, 1976) or similar criteria (Wetherill and ReVelle, 1981). The PE-criterion is an empirical definition for the meteor's end height, weighted by terms for the initial mass, initial velocity, and direction of flight with respect to the vertical. The PE-criterion is related to different types of material and thus may help decide whether a meteorite fall is probable or not. The types are:

- Type I: ordinary chondrite, relatively strong material, density about 3.7 g/cm^3, asteroidal material (Příbram, Lost City, Innisfree), frequency 29%.
- Type II: carbonaceous chondrite, density 1.9 – 2.1 g/cm^3, asteroidal material, frequency 33%.
- Type IIIA: cometary material, weak, density 0.6 – 0.9 g/cm^3, frequency 29%.
- Type IIIB: very weak cometary material, density 0.2 – 0.34 g/cm^3, appearing in the Draconids or the Sumava fireball (Nemtchinov et al., 1999) for example, frequency 9%.

The frequencies of occurrence are taken from an analysis of photographic fireball networks by Ceplecha (1991). This has been further investigated by Ceplecha (1994) – see Table 1.3. The statistics behind this contains several hundred photographed meteors. The 'characteristic orbits' give some idea about the source region of the meteoroid, but are not meant as an average with a known scatter; the individual orbits may significantly differ from each other. Of course, our knowledge has increased a lot due to many well recorded events. Figure 1.27 shows the currently calculated orbits of meteorite dropping fireballs. Tables with details of 13 analysed events are given by Popova et al. (2011).

The orbits of all currently known meteorite dropping fireballs originate from objects with an aphelion in the main asteroid belt. Some resemble each other very closely, such as the Příbram and Neuschwanstein meteoroids, but the material of the two meteorites—H5 and EL6 chondrites—is different. Opposite to this, one minor body can be composed of different meteorite materials as well: the Chelyabinsk meteorites include a wide variety of LL5 chondritic material, and the Almahata Sitta meteorites (from a smaller object than the Chelyabinsk fall) include achondritic anomalous Ureilites as well as EH and EL chondritic portions (Bischoff et al., 2010); see Figure 1.28 at page 28).

The analysis of photographs and/or video recordings of meteorite-producing fireballs yielded end heights for the luminous path of about 21 km. In the case of the very shallow trajectory of the Peekskill meteorite (Brown et al., 1994), the last point measured on the video records corresponds to a height of 33.6 km, but this is not the end of the luminous path.

To reach the ground from this height, a meteorite needs about 3 to 4 minutes in free-fall, so there will normally be a delay of this duration between sightings of the end of the track and reports of impact noises being heard. If there is information about such impact noises, a systematic search for meteorites is recommended. Impact noises were important for recovering the Salzwedel (Hohenlangenbeck) meteorite which fell on 1985 November 14, the Trebbin (1988 March 1) and the Glatton (1991 May 5) daylight meteorite falls, for instance. Sounds also gave valuable hints to recover the Villalbeto de la Peña (2004 January 4; Trigo-Rodriguez et al., 2006) and La Mancha (2007 May 10) meteorites.

Table 1.3: Characteristics of photographic fireballs according to Ceplecha (1994). Densities ϱ are in g/cm^3, semi-major axes a in au.

Type	Bulk density ϱ	Characteristic orbit for 0.1 – 1 m size a	e	i	Assumed composition
I	3.7	2.4	0.68	6°	stony
II	2.0	2.3	0.61	5°	carbonaceous
IIIA	0.75	2.4	0.82	4°	cometary
IIIAi	0.75	$\approx \infty$	0.99	any	cometary
IIIA	0.75	2.7	0.67	any	cometary
[CIII]					
IIIB	0.27	3.0	0.70	13°	soft cometary

The identification of a meteorite is in many cases not indisputable. A freshly-fallen meteorite usually has a black and relatively smooth melted crust a few tenths of a millimeter thick. This crust may crumble away and be lost on a short time-scale, dependent on the material involved. Carbonaceous chondrites are especially susceptible to this effect. The interior may be very different, and unambiguous identification is only possible using analytical methods such as looking at a specially-prepared transparent thin-section of the rock, and searching for chondrules (characteristic inclusions in chondritic meteorites, these are millimeter-sized spherules of fine-grained silicate rock), or etching a cut and polished plane with acid to find the so-called Widmannstätten patterns in iron meteorites (Section 1.8). In the case of fresh meteorite falls, an isotope analysis should be made as soon as possible after the event. During recovery searches for meteorites, all meteorite-like material should be collected—it is better to include a lot of terrestrial material than to miss a real meteorite (McSween, 1987).

1.8 Meteorites

As Figure 1.1 and a consideration of the basic physics involved might suggest, recovering meteoroidal material intact for study in the laboratory is extremely difficult. Micrometeorites, the very fine meteoroidal dust particles, about 10 000 tonnes per year of which rain down to the surface, have been collected from deep sea sediments since the 1880s. Dust samples from other surface environments were checked during the 20th century too, with greater (e.g., the permanent ice-caps or remote beaches and deserts) or lesser (such as rainwater

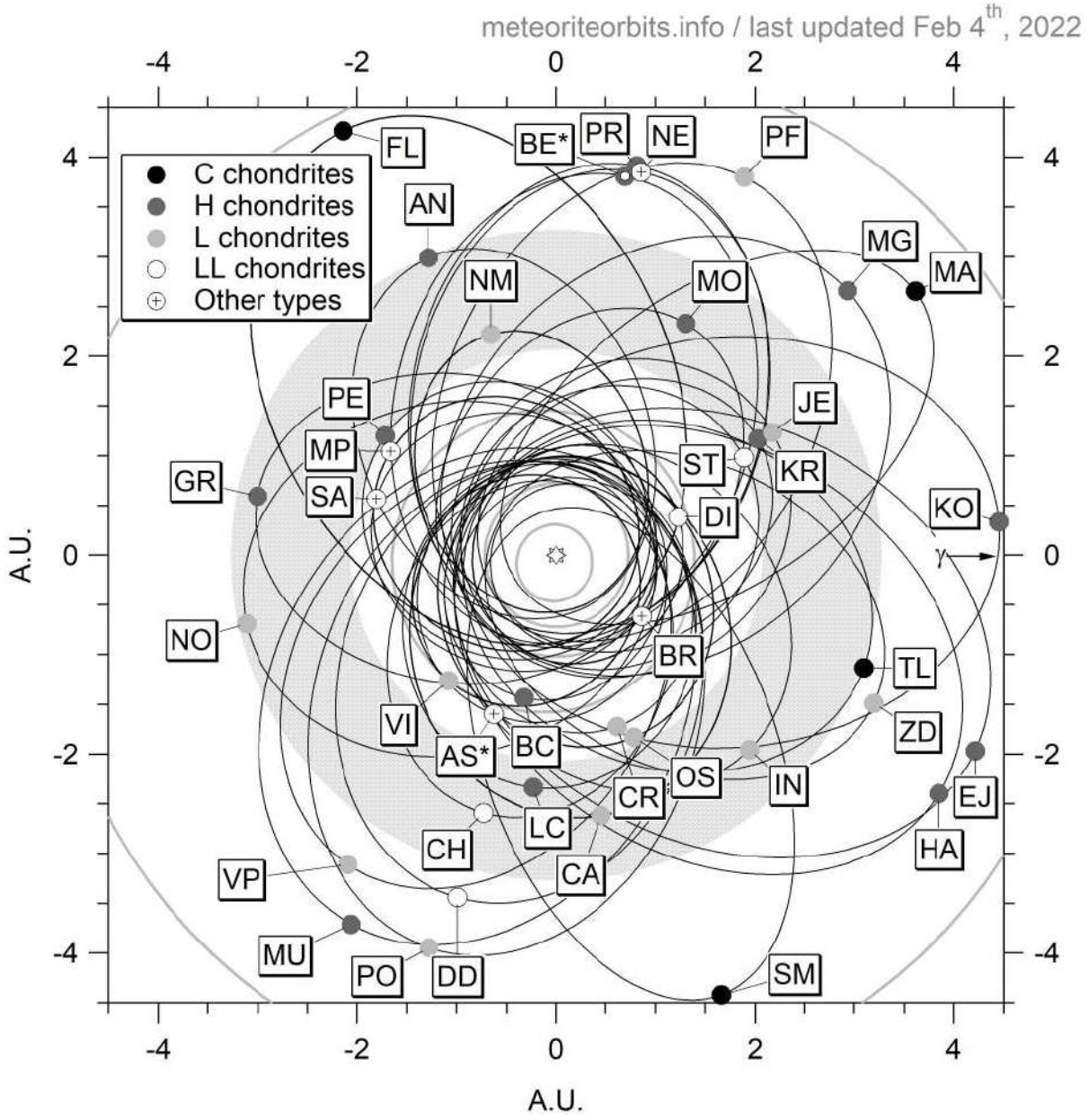


Figure 1.27: Orbits of the meteorite dropping meteoroids observed with different optical methods, *projected on the ecliptic plane.* Name and date of fall and inclination of the orbit. (Graph kindly provided by Matthias M. M. Meier, Naturmuseum, St. Gallen, Switzerland.) A publication of the orbital data for the 40th fall to be included in this list, Winchcombe, UK (2021 Feb. 28), is under preparation.

AN – Annama, Russia (2014/04/18; 14 °.6); AS – Almahata Sitta, Sudan (2008/10/07; 2 °.5)
BC – Buzzard Coulee, Canada (2008/11/21; 25 °.0); BE – Benešov, Czech Republic (1991/05/07; 24 °.0)
BR – Bunburra Rockhole, Australia (2007/07/20; 9 °.0); CA – Cavezzo, Italy (2020/01/01; 4 °.0)
CH – Chelyabinsk, Russia (2013/02/15; 5 °.0); CR – Creston, USA (2015/10/24; 4 °.2)
DD – Dingle Dell, Australia (2016/10/31; 4 °.1); DI – Dishchii'bikoh, USA (2016/06/02; 21 °.2)
EJ – Ejby, Denmark (2016/02/06; 1 °.0); FL – Flensburg, Germany (2019/09/12; 6 °.8)
GR – Grimsby, Canada (2009/09/26; 28 °.1); HA – Hamburg, USA (2018/01/17; 0 °.6
IN – Innisfree, Canada (1977/02/06; 12 °.3); JE – Jesenice, Slovenia (2009/04/09; 9 °.6)
KO – Košice, Slovakia (2010/02/28; 2 °.0); KR – Križevci, Croatia (2011/02/04; 0 °.6)
LC – Lost City, USA (1970/01/04; 12°); MA – Maribo, Denmark (2009/01/17; 0 °.1)
MG – Mason Gully, Australia (2010/04/13; 0 °.83); MO – Morávka, Czech Republic (2000/05/06; 32 °.2)
MP – Motopi Pan, Botswana (2018/06/02; 4 °.3); MU – Murrili, Australia (2015/10/27; 3 °.6)
NE – Neuschwanstein, Germany (2002/04/06; 11 °.4); NM – Novo Mesto, Slovenia (2020/02/28; 8 °.8)
NO – Novato, USA (2012/10/18; 5 °.5); OS – Osceola, USA (2016/01/24; 13 °.2)
PE – Peekskill, USA (1992/10/09; 4 °.9); PF – Park Forest, USA (2003/03/27; 3 °.2)
PO – Porangaba, Brazil (2015/01/09; 8 °.6); PR – Příbram, Czech Republic (1959/04/07; 10 °.5)
SA – Sariçiçek, Turkey (2015/09/02; 22 °.6); SM – Sutter's Mill, USA (2012/04/22; 2 °.4)
ST – Stubenberg, Germany (2016/03/06; 2 °.1); TL – Tagish Lake, Canada (2000/01/18; 1 °.4)
VI – Viñales, Cuba (2019/02/01; 11 °.5; VP – Villalbeto de la Peña, Spain (2004/01/04; 0 °.0)
ZD – Žd'ár nad Sázavou, Czech Republic (2014/12/09; 2 °.8)

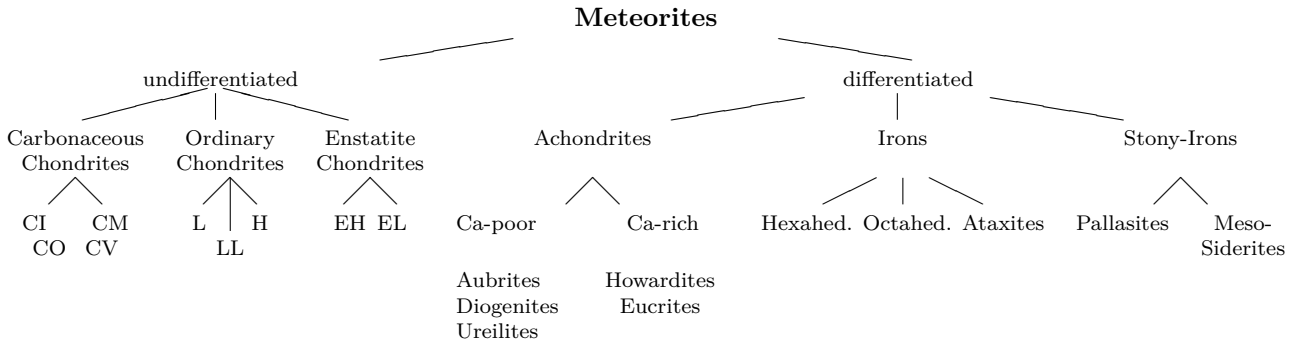


Figure 1.28: Classification scheme of meteorites with the main categories. CI are carbonaceous chondrites with about 3.5% carbon and 18–22% water (also called C1); CM are carbonaceous chondrites with about 2.5% carbon and 6–16% water (also called C2). Chondrites of type L have a low abundance of iron, type LL has an extremely low iron abundance, while type H has a high iron abundance. Among the achondrites, Ureilites have relatively high carbon abundance and show microscopic diamonds. Meteorites from Mars and the Moon also belong to the achondrites. Pallasites have about equal amount of silicates and iron, a sponge of nickel-iron is filled with troilite and olivine. Mesosiderites have a larger fraction of silicates forming a matrix in which nickel-iron is finely distributed.

collections or lake sediments) success in finding micrometeorites, and separating them from terrestrial contaminants. Sticky traps, plates covered in very viscous oil, intended to catch extraterrestrial particles in mid-air, have been deployed at various levels in the atmosphere from high hills and mountains, through stratospheric aircraft and high altitude balloons, to sounding rockets.

The particles amassed intact by the intra-atmospheric methods are a mixture of largely unaltered aggregates of smaller grains, held together in more or less porous 'clumps', or once-molten particles with a more solid, rounded form, often spherical or spheroidal, some of which may have resulted from meteoroidal ablation in the atmosphere. Their sizes range from a few microns up to ~ 100 μm. Chemically, about 60% of the high-altitude aircraft particles collected between 1974 and 1976 were made up of iron, magnesium, silicon, carbon, sulphur, calcium, nickel, and other elements in lesser proportions generally, with some of the carbon in an organic form. Of the rest, 30% were iron-sulphur-nickel composites (with very little nickel overall), and 10% were made of iron-magnesium minerals. Though around 30 years old now, this classification scheme (Figure 1.28) generally speaking is still valid today (Norton, 2002).

In addition to the micrometeorites, we also have the far larger, if far rarer, 'ordinary' meteorites available for study, to provide evidence for the nature of meteoroids. Their larger sizes and much more robust structures after all—they have each survived a very violent atmospheric flight inside a brilliant fireball before we can collect them—mean they are not the same as the particles producing the more usual range of observed meteors. However, their chemical characteristics are similar to the examined micrometeorites, and they give us good data concerning processes going back to the formation of the Solar System. So, they are a vital aspect of meteor and meteoroid science.

With respect to their composition, we distinguish three broad classes of meteorites: stones, largely made up of silicate minerals, often with some metal; irons, chiefly composed of nickel-iron alloys; and stony-irons, a transitional mix of materials between the two extremes.

Most stony meteorites contain small spherical bodies called 'chondrules'. These may be visible only with a microscope. Such meteorites are called 'chondrites', and are chemically similar to the largest class of the high-altitude aircraft micrometeorites. A small proportion of these are especially fragile, and contain organic compounds of carbon, hydrogen, oxygen and nitrogen. They are called 'carbonaceous chondrites'. The majority of meteorites seen to fall are chondrites. Immediately after they have landed, they usually have a very thin, black, outer fusion crust a few tenths of a millimetre thick (Figure 1.29), created when their outermost layer melted and rapidly re-solidified during the object's atmospheric flight. However, they rapidly weather on the Earth's surface to become indistinguishable from terrestrial rocks, and, in a relatively short while, may disintegrate completely into soil. This is partly why we need rapid accumulation and analysis of accurate fireball data, in case the fireball dropped meteorites, which we might then recover. A speedy retrieval of any meteorites also helps cut down on potential terrestrial contamination of the sample as well.

Chondrites only retain their internal chondrules because the rocks have not been significantly heated after their formation. Any stony meteorites which have been so heated, to the point of re-melting, lose their chondrules, and are called, logically enough, 'achondrites'. About 5% of the stony meteorites are achondrites, with varying mineralogies, though most were once-molten rocks, like igneous basalt lavas on Earth. A small fraction of these have chemistries and structures very similar to rocks returned to Earth from the Moon, while a still tinier percentage have properties which strongly suggest an origin on Mars.



Figure 1.29: This L6-chondrite fell on 2019 Feb 1 near Viñales on Cuba. The fresh fusion crust is just about 0.2–0.3 mm thick which is easily visible at the parts where the crust chipped off when this 9.1 g meteorite hit the ground (J. Rendtel).



Figure 1.30: Widmanstätten pattern in a slice of a Muonionalusta meteorite (J. Rendtel).

Iron meteorites are very robust, and can survive intact on the Earth's surface for millennia after landing. Though only a relatively minor constituent of the overall meteorite flux, this longevity, plus the fact that many are strongly magnetic, makes irons much easier to find, so most meteorites recovered that were not seen to fall are irons. Many iron meteorites seem to have cooled and solidified from their once-molten state slowly, and those with ~ 6 to ~ 17 weight-percent nickel often show the results of this in the Widmanstätten pattern (Figure 1.30). This pattern cannot be achieved in terrestrial laboratories yet on macroscopic scales, and is revealed when a cut face of an iron meteorite is etched in a weak acid. It is due to the intergrowth of crystals of two phases of nickel-iron, kamacite (low nickel content) and taenite (high nickel content). Meteorites which show the cross-hatched Widmanstätten pattern are called 'octahedrites'. Irons with only kamacite, the 'hexahedrites', do not show this, but instead may display fine striations, called Neumann lines (Figure 1.31). Taenite-rich irons show no obvious crystal structure, and are called 'ataxites'.



Figure 1.31: Neumann lines in a slice of a Seymchan meteorite (J. Rendtel).

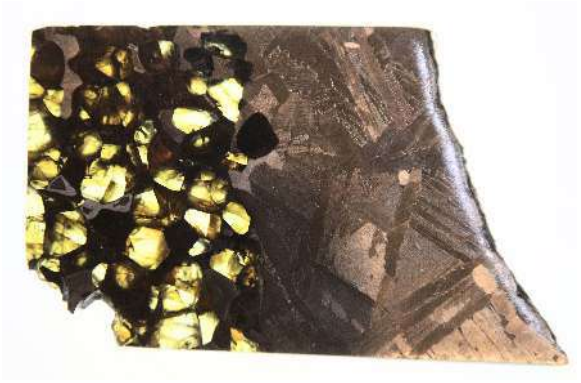


Figure 1.32: This polished slice of a Seymchan meteorite shows both the translucent olivine crystals and the iron part with Widmanstätten structure (J. Rendtel).

Stony-irons are the rarest class of meteorites, with roughly equal proportions of silicate and metallic components. There are two chief subtypes. 'Pallasites' are those where crystals of olivine sit in a metallic matrix (Figure 1.32). Both parts of these must have cooled slowly together from a molten original state, as the olivine crystals can be large, and the metal often shows Widmanstätten structure. The other kind



Figure 1.33: Structure of a Mesosiderit, visible in a polished slice of NWA 13623 (J. Rendtel).

are 'mesosiderites' (Figure 1.33), mixtures of angular achondritic fragments, metal chunks (each of which may show its own Widmanstätten pattern), glass and metal veins. This implies the mesosiderites were subjected to variable heating regimes, and probable partial breakup after their creation. Further information on meteorites, and the complexities of their more detailed classification, can be found, e.g., in Norton (2002).

Meteorite samples can also be approximately dated, both as to when they last solidified from being molten, and as to how long they were exposed to cosmic rays in space after being broken off their parent body. Most show last-molten ages of the order of the current age of the Solar System of just over 4500 million years. When combined with studies for the very few meteorites whose orbits have been established, and other considerations, this suggests many meteorites originated in asteroids. Some, such as the stony-irons and achondrites, must have formed in bodies large enough to allow gravitational pressure heating, differentiation, and slow cooling, thus probably at least 200 km in diameter. A very few of the carbonaceous chondrites show evidence for a formation with some liquid water present, which may imply a cometary origin. Formation ages for the lunar achondrites can be as young as 3900 million years, while for the potential Martian meteorites, this can be as geologically recent as 1300 million years ago. Caution is sometimes needed in interpreting these values, as partial melting and recrystallization can occur during and even after the impact/fragmentation which freed the meteorite, and which can give a very much smaller age for its (re-)formation (Norton, 2002).

One other type of object related to Earth-impact events should be noted here, the 'tektites'. As the name, derived from the Greek 'tektos' = 'melted', suggests, these are small, glassy, once-liquid stones. They vary in colour and texture from smooth transparent or translucent green, to a rough, dull, opaque, black. They are found in strewn fields in various parts of the world, often in relation to identifiable impact structures. They seem to be composed mostly of terrestrial material melted by the impact of a huge meteorite (one not decelerated below cosmic velocity by the atmosphere), and violently flung away through the air as droplets, so cooling very rapidly as glass, and rounded by air friction. By the time they landed, most seem to have been at least semi-solid again. For more information, see McCall (2001).

1.9 History of post-medieval meteor astronomy

1.9.1 The 17th and 18th centuries

From ancient times through to the 19th century, the term 'meteor' was also used for other atmospheric phenomena such as lightning, aurorae, rain, hail, snow, cloud formations, and rainbows. Some people thought meteors were associated with volcanic activity, strong winds, or were due to the ignition of atmospheric gases. The idea that meteors were due to purely atmospheric phenomena persisted into the 19th century, though a few scientists had already suggested an astronomical origin for fireballs much earlier.

Schickard (1624) published a first attempt to calculate the trajectory of a fireball observed over Germany on 1623 November 17. Schickard was not able to prove a non-terrestrial origin, however. In 1676, Montanari calculated the trajectory of a bright fireball (May 21) from sightings by witnesses at several different sites around the Adriatic Sea, which led him to the conclusion that an extraterrestrial origin was indicated (Chladni, 1794). Edmond Halley concluded that the upper limit of the Earth's atmosphere was at an altitude of 72 km in 1686. Some years later he proposed an extraterrestrial origin for shooting stars. A brilliant fireball that was observed from several locations on the evening of 1719 March 19 enabled Halley to compute its altitude as 119 km and its speed as 8 km/s (Halley, 1719). The same bolide was accompanied by rattling noises, and it was very difficult to explain how sound could be transmitted through almost vacuous space. E.F.F. Chladni was the first to deal with this phenomenon systematically, and he proved theoretically the extraterrestrial origin of meteorites and fireballs in 1794, but the idea was not accepted widely.

Even Alexander von Humboldt, who observed the famous 1799 Leonid shower from South America, doubted this extraterrestrial origin in his work "Kosmos" (1845).

Many small steps were necessary before a rather more complete picture of the meteor phenomenon could be established. The simultaneous observation of identical meteors from two sites by the German students Brandes and Benzenberg in 1798 belongs to these steps. Between 1798 September 11 and November 4 they did some double-station meteor watches. They were able to compute 22 atmospheric trajectories for meteor paths, leading to the conclusion that the meteors were of extraterrestrial origin (Benzenberg & Brandes, 1800). Their results spread among the scientific community only some years later, as the general opinion of meteors then prevailing excluded the possibility that meteorites fell from the heavens.

1.9.2 The 19th century

Unfortunately, the spectacular Leonid return of 1799 failed to trigger any further real interest in, or systematic investigations of, the occurrence of shooting stars, despite its having been seen from places across Europe. Although regarded as an interesting curiosity then, and later, the fact that nobody seemed willing to investigate it says a lot for the state of science around 1800! But then, on 1803 April 26, several widely seen meteorites fell near the village of L'Aigle in France, and this finally did force the scientists to reconsider their views.

After this catalyst, a further 21 years elapsed before the first truly systematic meteor work by astronomers began. Some European astronomers, such as A. Quételet, organised new multiple station observations. Quételet's (1841) catalogue of shooting stars is one of the very few publications containing any meteor observing results from the mid-19th century. Quételet



Figure 1.34: Woodcut of the 1833 Leonid meteor storm.

collected many articles and reports from other meteor workers of that time.

The great Leonid meteor storm of 1833 November 13 (Figure 1.34) turned much popular attention towards meteors. This exceptional shower and the annual return of the Perseids in August (recognised as such within five years of the 1833 Leonids) supported the theory of a non-earthly origin for meteors, though until 1863 doubts remained about their possible atmospheric character. H. A. Newton concluded that the Leonids were caused by the Earth passing through a stream of particles that were in orbit around the Sun. Newton and Olbers predicted a spectacular display for the Leonids in 1866, a prediction that was confirmed by observations. In 1866 the Leonids enabled scientists to study upper atmospheric winds by describing persistent meteor trains; the different colours led chemists to ask questions about the chemical composition of meteoroids. The first spectroscopic meteor work was done with direct vision prisms. Despite the patience required for this visual spectroscopic work, quite a lot of results were obtained in the mid-19th century in this field.

The 1866 Leonids also encouraged the first amateur astronomers to specialise in meteor observing. In 1861, Kirkwood had stated that meteoroid streams were the debris of ancient but disintegrated comets. Then in 1867, Peters, Schiaparelli and Oppolzer concluded independently that the calculated orbit of 55P/Tempel-Tuttle (1866 I) was similar to the orbit of the November Leonids. Schiaparelli (1871) came to the same conclusion for the Perseid orbit and that of Comet 109P/Swift-Tuttle (1862 III).

As a side-note, Quételet's cataloguing of meteoric events was continued and expanded upon after 1840 by the British Association for the Advancement of Science (BAAS). Though the BAAS was founded in 1831, it was only in 1840 that the first report on meteors was included. It summarised the prominence of the strong 1832 Leonid display, as seen from places in central Russia, west across Arabia and most of Europe, with additional references to stronger activity at the same time of year from 1799, 1822 and 1831, then in 1833 over America, and gave notes on all subsequent years through to 1839 (with a very brief footnote on the lack of any unusual observations from a limited geographic area for 1840). It includes references to all the more significant European and North American publications on the source up to 1840. With respect to the Perseids, it mentions the lesser, but still easily noticeable, prominence of meteor activity in the August 10–15 period, with references to Quételet and Arago.

1.9.3 Continuous observations of meteors

The first scientific amateur work on meteors dates to the early 19th century too. Good work was done in Europe, particularly in Great Britain, Italy and Germany. The most famous amateur meteor worker that ever lived was beyond doubt William Frederick Denning (1848–1931). His first observations date back to the 1860s (Beech, 1998). As he was a visual observer, he was probably the first to identify many meteor showers (Denning, 1899). Unfortunately, Denning was not aware of the complex, apparently random, nature of meteor radiants within the omnipresent sporadic activity, and he compiled long lists of radiants, many of which have turned out to be spurious. He believed that up to 50 meteor showers were active on every single night of the year. Although more recent investigations suggest this may be true, all but a tiny minority of these showers have such low activity that they cannot be observed by the visual techniques he employed. Another of his theories defended the concept of stationary radiants, and this kept a (sometimes heated) discussion going for over 50 years. Even in recent times, Denning's theories have misled some amateurs into trying to observe all these imaginary radiants. Despite this unfortunate point of view, Denning deserves much respect as the most dedicated observer, who even gave up his professional career to spend over 65 years of his life on meteor astronomy. Denning published hundreds of articles about meteors and inspired many other people with his enthusiastic support of meteor observing.

Since Denning's interest was mainly aimed at the discovery of meteor radiants, visual work paid little attention to any kind of investigation of the activity levels of

even the more active meteor streams. There is, for instance, not one usable report from the 19th century that would enable us to accurately reconstruct the activity profile of a shower in that era. Our current knowledge of the particle distribution in the cross-sections of the various meteoroid streams is thus very recent.

When studying 19th-century publications on meteor observing, it is clear that the observers were often discouraged by their mutually contradictory impressions of the various stream strengths. These reports are descriptive, and very subjective, accounts by observers who were not used to reporting meteor data in a way that could be used for any later numerical analyses. We cannot blame these observers today, as nobody had any experience in analysing data of this sort more than a century ago. From the vague descriptions provided, we can guess that some meteor showers must have behaved in a remarkable way. It is unfortunate that all the observing efforts from the second half of the 19th century cannot help to give us a definite picture of the particle distribution's evolution in the various streams. A compilation of Leonid observational data with an attempt to construct the particle distribution about 55P/Tempel-Tuttle can be found in Brown (1999). We can at least learn from this how very important it is to have a thoroughly well-defined standard to follow when making our observations today, so that such analyses are possible.

Lockyer (1890) assumed that the continuous infall of meteoritic material to the Sun was the source of the Sun's energy, because the other available explanation at that time, that of a gradual gravitational collapse, allowed only an astronomically brief stellar lifetime. Variable stars were taken to be nothing less than meteoroid swarms rushing through each other producing collisions and variations in luminosity. Scientists must be allowed to bring up unlikely theories as well as more plausible ones in order to make progress. These stranger ideas may hold a grain of truth, or may spark off a chain of thought which comes up with the actual reasons behind an event. In retrospect, these cases show how funny some such ideas may look later on, but only hindsight gives us this perspective. These examples also show how careful researchers have to be. The best attitude is to put question marks after any theory that is not fully proven, and to assume that any current 'truth' is only as good as its evidence.

1.9.4 Early photography and radar observations

The first meteor photograph was obtained in 1885 during the Andromedid display of that year by L. Weinek in Czechoslovakia (Weinek, 1886). It was not until 1894, however, that meteor photography started to yield useful results. A rotating shutter was introduced in 1898 by W.L. Elkin at Yale (Elkin, 1899). Photographic work was initially very expensive and not very successful due to the poor quality of both the optics and film stock used. Improvements to both aspects came as the 20th century progressed. Photographic meteor spectroscopy was successful accidentally as early as 1897. Harvard cameras provided stellar spectra for the Henry Draper Catalog and, by chance, some meteor trails appeared on these plates. By 1932, Peter Millman had eight spectra from that project at hand when he started a meteor spectroscopy program and laid the basis of our current knowledge of this subject. However, it was not until after World War II that meteor photography became widely used in meteor science.

In 1929, a further technique was added to the meteor astronomers' repertoire. When H. Nagaoka was using radio to study the ionised layers of the upper atmosphere, he noticed unexpected echoes, which he was soon able to associate with meteors. The first deliberate observing attempt was in 1931 by A.M. Skellett in Iowa, for the Leonids. Radio meteor observations thus became possible, but like photography, this method was developed fully only after 1945, based on technological improvements made possible during the war.

The period between the two World Wars was additionally characterised by the 'hyperbolic versus elliptic orbits' debate. Meteoroids on elliptical orbits clearly belong to the Solar System, while those with hyperbolic orbits must have come from outside, if their orbits were really hyperbolic and not result of perturbations. A special Harvard expedition to Arizona (1931–1933) was organised to examine this theory. Öpik had developed an ingenious apparatus known as the "rocking-mirror" which showed a meteor in the sky as a curved trail in the mirror (Öpik, 1934). The shape and length of the curved trail enabled him to compute the meteoroid's velocity. The rather large errors introduced by this technique were ignored and 60% of the meteors seemed to be hyperbolic. Further examination, and the eventual resolution, of this topic had to wait until post-1945, however. Actually, the debate is not yet concluded as the orbit calculation strongly depends on the accuracy of velocity measurements.

1.9.5 Amateur organisations

The amateur community too kept up a steady activity into the 20th century. Around 1900 a number of amateur meteor groups became established in several parts of the world. The Meteor Section of the British Astronomical Association had produced regular reports since 1890, for instance, and in 1911 the American Meteor Society was founded (Olivier, 1955). Until circa 1939, amateur meteor work was the business of individuals, although some societies were established on a national basis. The lack of well-coordinated observing programs and the absence of specialised observing instructions were the most important limitations to the achievements of that period. During World War II, all activities, including astronomical ones, suffered. Beginning in the 1950-ies, the start of space exploration created interest in astronomy.

However, meteor astronomy got little attention by amateurs. Even the famous 1966 Leonid return had no significant effect on the number of systematic meteor observations in general. Observations with telescopes

and astrophotography obviously were more attractive than naked-eye meteor watching.

Local and national groups of meteor observers have been established later in the 1970-ies. An International Meteor Weekend was held in 1979 near Bonn, Germany, followed by similar meetings in Belgium, Germany and the Netherlands. The 1986 and 1988 meetings even saw professional attendance. In parallel, the journal *WGN* (originally "Werkgroepnieuws", a circular in Dutch) became an international journal in English with contributions from all over the world. During the *International Meteor Conference (IMC)* in Oldenzaal, the Netherlands, in March 1988 the foundation of the *International Meteor Organization (IMO)* with WGN as its principal journal was decided. In less than a year, about 100 meteor workers from Europe, North America, the former Soviet Union, Australia and Japan, were prepared to act as founding members for this organisation. In order to guarantee its truly international character, the IMO got legal status as an international scientific non-profit organisation; the constitution was approved at the IMC in October 1989 in Balatonfölvár, Hungary.

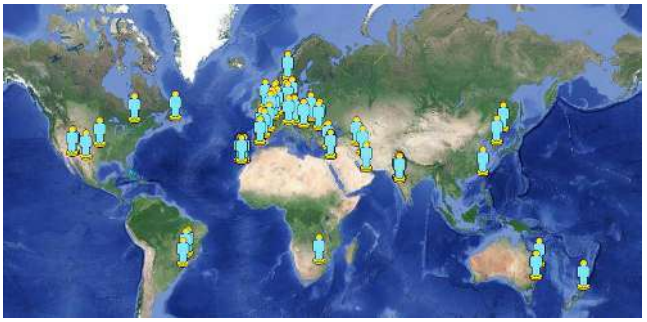


Figure 1.35: Positions of visual observers who submitted data during the 2018 Geminid campaign. Observers of a national group can cover a few hours at best. In the global sample, only the wide Ocean longitudes often remain incomplete.

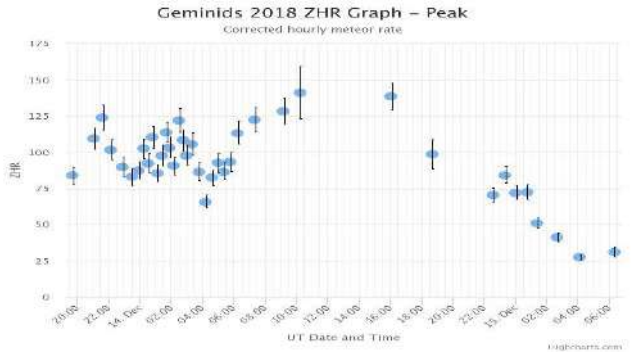


Figure 1.36: Activity profile of the 2018 Geminid peak period between December 13, 20^{h}UT and December 15, 06^{h}UT, i.e. 34 hours.

One major aim in the beginning was the development of standardised observing methods and analysing procedures. It started with visual meteor observations which were carried out by many observers. One great advantage of the worldwide collection of consistent data over nearly all longitudes is the possibility to obtain full activity profiles for many meteor shower returns. Figures 1.35 and 1.36 from the Geminid campaign 2018 are shown as an example of the observer contribution and the result.

Such a data collection included to establish an archive of all data which is available for research; in this case the Visual Meteor DataBase (VMDB) which can be accessed from the IMO web page (see Chapter 2).

In the subsequent years, an increasing amount of data was collected by video meteor cameras (Chapter 4), covering activity data as well as precise meteor shower radiants and meteoroid orbits. Nevertheless, it is important to continue with both visual and video observations for some time in parallel to ensure a calibration of the results and this way to extend our data base concerning shower evolution over a long period.

Radio observations (Chapter 6) have the great advantage that we can record meteor activity also during daylight and bad weather conditions.

1.10 Modern meteor science

1.10.1 Photographic, radar and video observations

After 1945, a revolution occurred with regard to the instrumental observing techniques in meteor astronomy (Jacchia et al., 1965). A tremendous improvement came in 1950 with the Super-Schmidt Cameras which were able to photograph meteors down to +3.5 mag (Whipple, 1951). Hundreds of precisely determined meteor orbits were computed, and it became clear that if a hyperbolic component existed at all, the number of hyperbolic meteor orbits was very low.

Major meteor showers were studied in great detail, though the many minor showers in which amateur observers had believed proved to be undetectable in the reliable statistics taken from accurate photographic results. Some sub-radiants such those as of the various Aquariids in August, were resolved for the first time, where amateur visual work had failed to determine any sub-radiants before. Indeed, the accuracy of visual plots turned out to have been over-estimated. Unfortunately, many amateurs preferred to stop meteor observing altogether rather than change their observing programs. Until the 1950-ies, very little was done to study features such as activity variations in the regular, reliable meteor showers. Most reports only gave popular descriptions of shower activity, ignoring important, relevant information on sky conditions and observing methods, and thus have no real value for modern statistical analyses.

Photographic networks have been established in Europe, North America and Australia. They permitted the calculation of the orbit of a meteoroid, and thus of meteorite producing bodies (see Section 5.3 on page 105).

The development of radar meteor observing was very important to meteor science. Radiants and meteor



Figure 1.37: Fragmentation of a bright fireball seen on 2009 October 13 near 17^{h}UT from Groningen, the Netherlands. (Images taken by Robert Mikaelyan, `https://www.robertmikaelyan.com/astronomy/meteor/`).

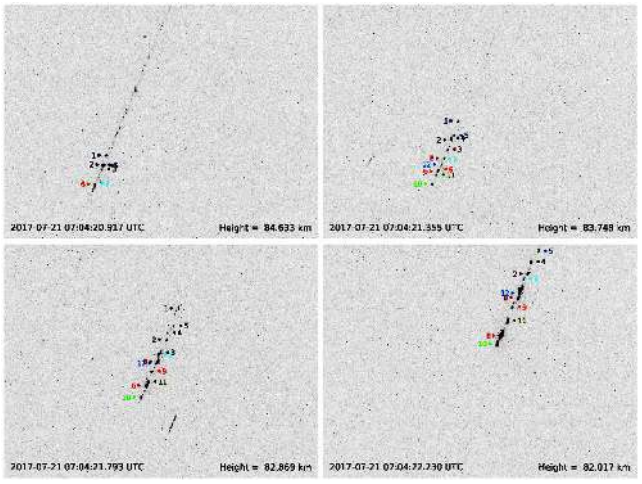


Figure 1.38: Fragmentation of a meteor observed on 2017 July 21 by the Canadian Automated Meteor Observatory, CAMO (Vida et al., 2021) showing the separation of fragments.

orbits—down to the range of faint telescopic meteors (magnitude $\leq +13.5$ mag)—were established. The first daytime meteoroid streams were discovered and long-term studies enabled researchers to continuously follow meteor activity throughout the day.

First video observations were made in the 1960-ies (Spalding, 1963), but only after the addition of image intensifiers the sensitivity increased and made the systems useful for meteor research. Nowadays, numerous video meteor camera systems are operational. These allow us to record physical meteor parameters (Chapter 4). The great advantage of video meteor observations for studies of meteoroids in the atmosphere is the temporal resolution. For example, the fragmentation of meteoroids in the atmosphere can only partly studied from (series of) still images (Figure 1.37) but video recordings cover all phases. A specially designed video system CAMO (Vida et al., 2021) is able to turn a high resolution camera to a meteor and to follow the meteor continuously (Figure 1.38), taking 100 frames per second. The sensitivity of modern cameras allows us to investigate also atmospheric trajectories and spectra of faint meteors with information about atmospheric parameters and meteoroid composition (Vojaček and Borovička, 2017; Borovička et al., 2019).

Video meteor networks provide us with precise orbital data so that the structure of meteoroid streams can be derived (extension of streams, evolution and relation of orbits, association to possible parent objects).

Even accidental fireball video recordings have been used to calculate orbits and trajectories of meteorite dropping events (Figure 1.27). This was the case with the Chelyabinsk fall. Another recent example is the Flensburg (Germany) daylight fireball on 2019 September 12 at $12^{h}50^{m}$UT. The meteorite was found on the ground soon after the event and the orbit has been calculated (Borovička et al., 2021).

1.10.2 Lidar observations, lunar and other impacts

Lidar systems which are primarily used for studies of the atmosphere have been used for meteor research as well. These systems excite metal atoms or ions at resonant wavelengths in the upper atmosphere and provide information about the abundance of metal in meteor trains and also about velocities in the meteor level (von Zahn, 2001).

Modern video techniques can also be used to check for impacts of meteoroids onto the lunar surface. Technical details are described by Cudnik (2009), results are discussed by Bouley et al. (2012) and a summary of observations was given at the 2014 Lunar and Planetary Science Conference (Thompson et al., 2014). The current observational and technical status of lunar meteoroid impacts is described by Madiedo et al. (2019) in a section of the 2019 "Meteoroids" book.

Recent research also includes extra-terrestrial meteors, i.e. the observation of meteors in the atmosphere of other planets with different density structures and encountering different dust (Christou et al., 2019).

1.10.3 Airborne observations, artificial meteors

Airborne observations with many instruments mounted on a platform onboard of an airplane or balloon have a number of advantages over ground-based observations: the recordings are not disturbed by clouds, the air mass to look through is much smaller (less extinction) and the observable spectral range is extended into the infrared and ultraviolet range. Such airplane campaigns were organised for peculiar events: for the Leonid storms in 1999 (Jenniskens, Butow & Fonda, 1998) and in 2002 (Jenniskens, 2002), for the 2007 Aurigids (Vaubaillon & Jenniskens, 2007), the 2008 Quadrantids (Gray, 2008) and the 2011 Draconids (Vaubaillon et al., 2015). More recently, the Geminids 2016 have been observed from

video equipment on a balloon platform (Vaubaillon et al., 2019).



Figure 1.39: Image from the video taken during the re-entry of the Hayabusa spacecraft and capsule over Southern Australia on 2010 June 13, 13:52 UT. Credit: NASA/JPL-Caltech/SETI Institute, `http://hayabusa.seti.org/`.

The entry of spacecraft capsulae returning from interplanetary missions cause "artificial meteoroids", although at lower velocity (about 12–13 km/s) than most meteoroids. Since the encounter time and location are precisely known, complex observing equipment can be placed. Examples of such returning spacecraft capsulae which produced "man made fireballs" entering the atmosphere at higher than the Earth's escape velocity are listed in Table 1.4.

Table 1.4: Data of the observed interplanetary spacecraft reentry capsulae; references see in the text below the Table.

	Genesis	Stardust	Hayabusa	Hayabusa2
Date	2004 Sep 08	2006 Jan 15	2010 Jun 13	2020 Dec 06
Time	09:54 MDT	03:00 MST	23:22 CST	04:20 CDT
UT	15:54	10:00	13:52	17:50 (Dec 5)
Mass	225 kg	45.8 kg	18 kg	16 kg
Diam.	1.52 m	0.81 m	0.40 m	0.40 m
Vel.	11.0 km/s	12.9 km/s	12.1 km/s	12.0 km/s
Site	Utah, USA	Utah, USA	S. Australia	S. Australia

Details can be found here: for the Genesis mission in 2004 (Jenniskens et al., 2004), Stardust in 2006 (ReVelle & Edwards, 2007), Hayabusa in 2010 (Ishihara et al., 2010; Borovička et al., 2011) – see Figure 1.39 – and Hayabusa2 on 2020 December 6 (`https://dfn.gfo.rocks/hayabusa.html`).

Detailed observations of the re-entries allowed to derive the trajectories and velocities of the spacecraft, its fragments, and the capsule and to test models and physical parameters (ablation, luminous efficiency etc.) as the structure and composition for each of the capsules is known precisely.

However, in our book we concentrate on the interaction between interplanetary meteoroids and the Earth's atmosphere and the related ground-based observations.

1.11 Meteor observations

Meteor observations can provide a lot of valuable information about the spatial distribution, origin, evolution, and decay of meteoroids. As we have seen, the meteoric complex shows a strong relationship to minor planets as well as to comets, thus meteor astronomy also contributes to our ideas about the origin, evolution and structure of our Solar System. Comparing meteor observation with other fields of astronomical observation, there are many differences. A major one is caused by the phenomenon itself. Only the final stage of a particle's trajectory through the Earth's atmosphere can be observed, when the path has already been substantially disturbed by the Earth itself. It is also necessary to obtain a large sample of meteor events before any conclusions can be drawn. Each individual observing session thus has to last for a relatively long time. For instance, it is possible to gather several tens of magnitude estimates for different variable stars during a night, while a single useful interval for visual meteor observing lasts from one to three hours.

This Handbook provides guidance for making ground-based meteor observations by the methods generally available to unpaid volunteer observers, including visual, video, photographic and forward-scatter radio techniques. It contains details on what makes observations scientifically valuable, enabling your data to contribute to the larger whole of how we can better understand part of our Universe.

Acknowledgements

Special thanks to David J. Asher who supported me with detailed hints and recommendations which helped to improve the contents and readability of this Chapter and also created graphs. Jérémie Vaubaillon provided me with meteoroid stream modelling results. Information concerning sources of sporadic meteors was given by Margaret Campbell-Brown. Some graphs have been created by Rainer Arlt.

References:

Arago F., 1856: Populäre Astronomie, 2. Band. O. Wiegand, Leipzig.

Asher D.J., 2008: Meteor outburst profiles and cometary ejection models. *EMP* **102,** 27–33.

Astapovich I.S., Terentjeva A.K., 1968: Fireball radiants of the 1st-15th centuries. In: *L. Kresák, P.M. Millman (eds.), Physics and dynamics of meteors. IAU Symp. 33,* Reidel, 308–319.

Babadzhanov P., Kramer E.N., 1968: Some results of investigations of instantaneous meteor photographs. In: *L. Kresák, P.M. Millman (eds.), Physics and dynamics of meteors. IAU Symp. 33,* Reidel, 128–142.

Babadzhanov P.B., Kokhirova G.I., Khamroev U.Kh., 2014: The Capricornids asteroid-meteoroid complex. In: *T.J. Jopek, F.J.M. Rietmeijer, J. Watanabe, I.P. Williams (eds.), Meteoroids 2013, Proc. Int. Conf. Poznań, Poland,* Adam Mickiewicz Univ. Press, 199–204.

Babadzhanov P.B., Williams I.P., Kokhirova G.I., 2013: Near-Earth asteroids among the Scorpiids meteoroid complex. *A & A* **556,** A25.

Beech M., 1990: William Frederick Denning: in quest of meteors. *J. Roy. Astr. Soc. Can.* **84,** 383–396.

Beech M., 1998: The makings of meteor astronomy: part XV. W.F. Denning—the doyen of amateur astronomers. *WGN* **26,** 19–34.

Benzenberg J.F., Brandes H.W., 1800: Versuche, die Entfernung, die Geschwindigkeit und die Bahnen der Sternschnuppen zu bestimmen. Peters, Hamburg.

Bischoff A., Horstmann M., Pack A., Laubenstein M., Haberer S., 2010: Asteroid 2008 TC3–Almahata Sitta: a spectacular breccia containing many different ureilitic and chondritic lithologies. *MAPS* **45,** 1638–1656.

Borovička J., Abe S., Shrbený L., Spurný P., Bland P.A., 2011: Photographic and radiometric observations of the HAYABUSA re-entry.. *Publ. Astron. Soc. Japan* **63,** 1003–1009.

Borovička J., Spurný P., Brown P., Wiegert P., Kalenda P., Clark D., Shrbený L., 2013: The trajectory, structure and origin of the Chelyabinsk asteroidal impactor. *Nature* **503,** 235–237.

Borovička J., Macke R.J., Campbell-Brown M.D., Levasseur-Regourd A.-C., Rietmeijer F.J.M., Kohout T., 2019: Physical and chemical properties of meteoroids. In: *G.O. Ryabova, D.J. Asher, M.D. Campbell-Brown (eds.), Meteoroids. Sources of meteors on Earth and beyond.* Cambridge Univ. Press, 136–158.

Borovička J., Bettonvil F., Baumgarten G., Strunk J., Hankey M., Spurný P., Heinlein D., 2021: Trajectory and orbit of the unique carbonaceous meteorite Flensburg. *MAPS* **56,** accepted.

Bouley S., Baratoux D., Vaubaillon J, Mocquet A., Le Feuvre M., Colas F., Benkhaldoun Z., Daassou A., Sabil M., Lognonné P., 2012: Power and duration of impact flashes on the Moon: implication for the cause of radiation. *Icarus* **218,** 115–124.

Brandes H.W., 1825: Beobachtungen über die Sternschnuppen, angestellt von mehreren Naturforschern. *Unterhaltungen für Freunde der Physik und Astronomie* **1,** Leipzig.

Brown P., 1999: The Leonid meteor shower: historical visual observations. *Icarus* **138,** 287–308.

Brown P., Ceplecha Z., Hawkes R.L., Wetherill G.W., Beech M., Mossman K., 1994: Orbit and atmospheric trajectory of the Peekskill meteorite from video-records. *Nature* **367,** 624–626.

Brown P., Spalding R.E., ReVelle D.O., Tagliaferri E., Worden S.P., 2002: The flux of small near-Earth objects colliding with the Earth. *Nature* **420,** 294–296.

Brown P.G. and 32 co-authors, 2013: A 500-kiloton airburst over Chelyabinsk and an enhanced hazard from small impactors. *Nature* **503,** 238–241.

Campbell-Brown M., Jones J., 2006: Annual variation of sporadic meteor rates. *MNRAS* **367,** 709–716.

Ceplecha Z., 1991: Meteors depend on meteoroids. In: *D. Heinlein, D. Koschny (eds.), Proc. IMC 1990, Violau,* Veitsbronn, 13–21.

Ceplecha Z., 1994: Impacts of meteoroids larger than 1 m into the Earth's atmosphere. *A & A* **286,** 967–970.

Ceplecha Z., McCrosky R.E., 1976: Fireball end heights: a diagnostic for the structure of meteoritic material. *J. Geophys. Res.* **81,** 6257–6275.

Ceplecha Z., Spalding R.E., Jacobs C., ReVelle D.O., Tagliaferri E., Brown P., 1999: Superbolides. In: *W.J. Baggaley, V. Porubčan (eds.), Meteoroids 1998,* Astron. Inst. Slovak Academy Sci., Bratislava, 37–54.

Chladni E.F.F., 1794: Über den Ursprung der von Pallas gefundenen und anderer ihr ähnlicher Eisenmassen und über einige damit in Verbindung stehende Naturerscheinungen. Leipzig and Riga.

Chladni E.F.F., 1819: Über Feuermeteore und die mit denselben herabgefallenen Massen. Wien.

Christou A., Vaubaillon J., Withers P., Huesco R., Killen, R., 2019: Extra-terrestrial meteors. In: *G.O. Ryabova, D.J. Asher, M.D. Campbell-Brown (eds.), Meteoroids. Sources of meteors on Earth and beyond.* Cambridge Univ. Press, 119–135.

Corderoa G., Poveda A., 2011: Curuça 1930: A probable mini-Tunguska?. *Planet. Space Sci.* **59,** 10–16.

Cudnik B., 2009: Lunar meteoroid impacts and how to observe them. Series: Astronomers' Observing Guides, Springer, 256pp.

Dall'Olmo W., 1978: Meteors, meteor showers and meteorites in the middle age: from European medieval sources. *J. Hist. Astron.* **IX,** 123–134.

Denning F.W., 1899: General catalogue of the radiant points of meteoric showers and of fireballs and shooting stars observed at more than one station. *Mem. Roy. Astron. Soc.* **53,** 203–292.

Denning F.W., 1905: Value of meteoric radiants based on three paths. *MNRAS* **65,** 592–593.

Drolshagen E., Ott T., Koschny D., Drolshagen G., Colas F., Jeanne S., Vaubaillon J., Poppe B., 2020: The luminous efficiency determination and its difficulties. *WGN* **48,** 177–180.

Edwards W.N., Brown P.G., ReVelle D.O., 2006: Estimates of meteoroid kinetic energies from observations of infrasonic airwaves. *JATP* **68,** 1136–1160.

Elkin W.L., 1899: The velocity of meteors from photographs. *Astron. J.* **20,** 102.

Fesenkov V.G., Krinov E.L., 1959: The Sikhote-Alin iron meteorite shower. vol. 1, 1959; vol. 2, 1963; Publishing House, Academy of Sciences USSR, Moscow.

Gorkavyi N., Rault D.F., Newman P.A., Silva A.M., Dudorov A.E., 2013: New stratospheric dust belt due to the Chelyabinsk bolide. *Geophys. Res. Lett.* **40,** 4728–4733.

Gray R., 2008: The Quadrantid Multi-Instrument Aircraft Campaign (MAC) or observing the Quadrantids from 47,000 feet. *Journal of the Association of Lunar & Planetary Observers, The Strolling Astronomer* **50,** 25–26.

Halley, E., 1719: An account of the extraordinary meteor seen all over England, on the 19th of March 1718/9 with a demonstration of the uncommon height thereof. *Phil. Transactions (1683–1775 series)* **30,** 978–990.

Halliday I., Griffin A.A., 1982: A study of the relative

rates of meteorite falls on the Earth's surface. *Meteoritics* **17,** 31–46.

Hoffmeister C., 1949: Meteorströme. J.A. Barth, Leipzig.

Humboldt A.v., 1845: Kosmos (vol. 1). Stuttgart and Tübingen.

Hughes D.W., 1978: Meteors. In: *J.A.M. McDonnell (ed.), Cosmic dust,* Wiley, Chichester, 123–185.

Hughes D.W., 1981: Meteorite falls and finds: some statistics. *Meteoritics* **16,** 269–281.

Hughes D.W., 1990: The mass distribution of comets and meteoroid streams and the shower/sporadic ratio in the incident visual meteoroid flux. *MNRAS* **245,** 198–203.

Hughes D.W., 1993: Illustrating a meteoroid stream. *WGN* **21,** 254–258.

Ishihara Y., Yamamoto M., Hiramatsu Y., Furumoto M., Fujita K., 2010: Ground observation of the Hayabusa reentry: the third opportunity of man-made fireball from interplanetary orbit. *American Geophysical Union, Fall Meeting 2010*, abstract id.P13A-1364

Jacchia L., Verniani F, Briggs R., 1965: An analysis of the atmospheric trajectories of 413 precisely reduced photographic meteors. SAO Special Report 175.

Jenniskens P., 2002: The 2002 Leonid MAC airborne mission: first results. *WGN* **30,** 218–224.

Jenniskens P., 2006: Meteor showers and their parent comets. Cambridge Univ. Press.

Jenniskens P., 2014: Camelopardalids (IAU 451) from comet 209P/LINEAR. *WGN* **42,** 98–105.

Jenniskens P., Barentsen G., Yrjölä I., 2011: Draconids 2011. *CBET* **,** No. 2862, 1 (2011). Edited by D.W.E. Green.

Jenniskens P., Butow S.J., Fonda M., 1998: The 1999 Leonid Multi-Instrument Aircraft Campaign – an early review. *EMP* **82/83,** 1–26.

Jenniskens P., Nénon Q., Gural P.S., Albers J., Haberman B., Johnson B., Morales R., Grigsby B.J., Samuels D., Johannink C., 2016: CAMS newly detected meteor showers and the sporadic background. *Icarus* **266,** 384–409.

Jenniskens P., Wercinski P., Olejniczak J., Allen G., Desai P.N., Raiche G., Kontinos D., Revelle D., Hatton J., Baker R.L., Russell R.W., Taylor M., Rietmeijer F., 2004: Preparing for hyperseed MAC: an observing campaign to monitor the entry of the Genesis sample return capsule. *EMP* **95,** 339–360.

Jones J., Brown P., 1994: The radiant distribution of sporadic meteors. *Planet. Space Sci.* **42,** 123–126.

Keay C.S.L., Ellyett, C.D., 1969: Southern hemisphere meteor rates. *Mem. Roy. Astron. Soc.* **72,** 185–232.

Kirkwood D., 1867: Meteoric astronomy, a treatise on shooting-stars, fireballs and aerolithes. Philadelphia.

Koseki M., 2016: Research on the IAU meteor shower datbase. *WGN* **44,** 151–169.

Lockyer J.N., 1890: The meteoritic hypothesis. Macmillan & Co, London.

Lyytinen E., Nissinen M., Van Flandern T., 2001: Improved 2001 Leonid storm predictions from a refined model. *WGN* **29,** 110–118.

Madiedo J.M., Ortiz J.L., Yanagisawa M., Aceituno J., Aceituno F., 2019: Impact flashes of meteoroids on the Moon. In: *G.O. Ryabova, D.J. Asher, M.D. Campbell-Brown (eds.), Meteoroids. Sources of meteors on Earth and beyond.* Cambridge Univ. Press, 136–158.

Madiedo J.M., Trigo-Rodríguez J.M., 2011: Historical records of δ-Arietids superfireballs over Spain. *42nd Lunar and Planetary Science Conference,* 1368.

McBeath A., 1999: On the occurrence of bright Taurids. *WGN* **27,** 53–56.

McCall J., 2001: Tektites in the geological record: showers of glass from the sky. Geological Society, London.

McCrosky R.E., Posen A., Schwartz G., Shao C.Y., 1971: Lost City meteorite—its recovery and a comparison with other fireballs. *J. Geophys. Res.* **76,** 4090–4108.

McIntosh B.A., 1991: Debris from comets: the evolution of meteor streams. In: *R.L. Newburn Jr, M. Neugebauer, J. Rahe (eds.), Comets in the post-Halley era, Vol. 1,* Astrophysics and Space Science Library Volume 167, Kluwer, 557–591.

McSween jr. H.Y., 1987: Meteorites and their parent planets. Cambridge Univ. Press.

Millman P.M., 1963: Terminology in meteoritic astronomy. *Meteoritics* **2,** 7–11.

Molau S., 2007: How good is the IMO working list of meteor showers? A complete analysis of the IMO video meteor database. In: *F. Bettonvil, J. Kac (eds.), Proc. IMC 2006, Roden,* IMO, 38–54.

Molau S., Rendtel J., 2009: A comprehensive list of meteor showers obtained from 10 years of observations with the IMO Video Meteor Network. *WGN* **37,** 98–121.

Napier B., Asher D., 2009: The Tunguska impact event and beyond. *Astronomy & Geophysics* **50 (1),** 18–26.

Nemtchinov I.V., Kuzmicheva M.Yu., Shuvalov V.V., Golub' A.P., Popova O.P., Kosarev I.B., Borovička J., 1999: Šumava meteoroid – was it a small comet? In: *J. Svoren, E.M. Pittich, H. Rickman (eds.), Evolution and source regions of asteroids and comets, Proc. 173 IAU Coll.,* Astronomical Institute, Tatranska Lomnica, Slovak Republic, 51–56.

Neslušan L., Kaňuchová Z., Tomko D., 2013: The meteor-shower complex of 96P/Machholz revisited. *A & A* **551,** A87, 14 pp.; DOI: 10.1051/0004-6361/201220299).

Neslušan L., Hajduková M., 2017: Separation and confirmation of showers. *A & A* **598,** id. A40, 21 pp.; DOI: 10.1051/0004-6361/201629659.

Neslušan L., Hajduková jr. M., Jakubík M., 2013: Meteor-shower complex of asteroid 2003 EH1 compared with that of comet 96P/Machholz. *A & A* **560,** A47, 10 pp.; DOI: 10.1051/0004-6361/201322228.

Norton O.R., 2002: The Cambridge encyclopedia of meteorites. Cambridge Univ. Press.

Ohtsuka K., Sekiguchi T., Kinoshita D., Watanabe J.-I., Ito T., Arakida H., Kasuga T., 2006: Apollo asteroid 2005 UD: split nucleus of (3200) Phaethon?. *A & A* **450,** L25–L28.

Olivier C.P., 1955: The American Meteor Society. *Bull. No. 17.*

Öpik E.J., 1934: Results of the Arizona expedition for the study of meteors. III. Velocities of meteors observed visually. *Harvard College Circ.* no. 389.

Popova O., Borovička J., Campbell-Brown M.D., 2019: Modelling the entry of meteoroids. In: *G.O. Ryabova, D.J. Asher, M.D. Campbell-Brown (eds.), Meteoroids. Sources of meteors on Earth and beyond.* Cambridge Univ. Press, 9–36.

Popova O., Borovička J., Hartmann W.K., Spurný P., Gnos E., Nemtchinov I., Trigo-Rodríguez J.M., 2011: Very low strengths of interplanetary meteoroids and small asteroids. *MAPS* **46,** 1525–1550; DOI: 10.1111/j.1945-5100.2011.01247.x.

Porubčan V., Očenáš D., 1992. The Taurid meteor complex. In: *J. Rendtel, R. Arlt (eds.), Proc. IMC 1991, Potsdam,* IMO, 7–13.

Quételet A., 1841: Nouveau catalogue des principales apparitions d'étoiles filantes. Bruxelles.

Rendtel J., 2004: The population index of sporadic meteors. In: *M. Triglav-Čekada, C. Trayner (eds.), Proc. IMC 2003, Bollmannsruh*, IMO, 114–122.

Rendtel J., 2006: Visual sporadic meteor rates. *WGN* **34,** 71–76.

Rendtel J., 2007: Visual observations of the Aurigid peak on 2007 September 1. *WGN* **35,** 108–112.

Rendtel J., 2020a: Die α-Monocerotiden 2019. *Meteoros* **23,** 4–5.

Rendtel J., 2020b: Minor meteor shower anomalies 2018: predictions and observations. In: *U. Pajer, J. Rendtel, M. Gyssens and C. Verbeeck (eds.) Proc. IMC 2019, Bollmannsruh*, IMO, 63–68

Rendtel J., Brown P., Molau S., 1996: The 1995 outburst and the possible origin of the α-Monocerotid meteoroid stream. *MNRAS* **279,** L31–L36.

Rendtel J., Knöfel, A., 1989: Analysis of annual and diurnal variation of fireball rates and the population index of fireballs from different compilations of visual observations. *BAIC* **40,** 53–63.

Rendtel J., Koschack R., 2021: Aurigid outburst on 2021 August 31. *WGN* **49,** 73–75.

Rendtel J., Lyytinen E., Molau S., Barentsen G., 2014: Peculiar activity of the September ε-Perseids on 2013 September 9. *WGN* **42,** 40–47.

Rendtel J., Molau S., 2010: Meteor activity from the Perseus-Auriga region in September and October. *WGN* **38,** 161–166.

Rendtel J., Molau S., 2018: October Camelopardalid outburst 2018 October 6. *WGN* **46,** 173–175.

ReVelle D.O., Edwards W.N., 2006: Stardust – an artificial, low-velocity "meteor" fall and recovery: 15 January 2006. *MAPS*

, Schiaparelli J.V., 1871: Entwurf einer Astronomischen Theorie der Sternschnuppen. (German translation by Boguslawski) Stettin..

Schickard W., 1624: Theopyroscopia theologico-physica. Das ist: Geistlich vnd natürliche Betrachtung, dess Anno 1623. den 17. Nov. vom Himmel gefallenen Fewers. Dero jehne, Durch M. Wolffg. Jacob Christmann, Evangel. Predigern in Augspurg. Diese aber, Durch Herrn Wilhelm Schickhardten, Hebr. Sprach Professorn zu Tübingen, Vnd M. Petrum Meyderlinum Collegii August. Annaei Ephorum gestellet. J. Schultes, Tübingen (includes first attempt of a fireball trajectory calculation).

Silber E.A., Le Pichon A., Brown P., 2011: Infrasonic detection of a near-Earth object impact over Indonesia on 8 October 2009. *Geophys. Res. Lett.* **38,** L12201, 5 pp.

Singer W., von Zahn U., Batista P.P., Fuller B., Latteck R., 2005: Diurnal and annual variations of meteor rates at latitudes between 69°N and 35°S. In: *B. Warmbein (ed.), 17th ESA Symposium on European Rocket and Balloon Programmes and Related Research, 30 May - 2 June 2005, Sandefjord, Norway. ESA SP-590,* ESA, Noordwijk, 151–156.

Spalding J., 1963: Image-orthicon photographs of meteors. *Smithsonian Contributions to Astrophysics* **7,** 237–238.

Spurný P., Borovička J., Mucke H., Svoreň J., 2017: Discovery of a new branch of the Taurid meteoroid stream as a real source of potentially hazardous bodies. *A & A* **605,** id.A68, 25 pp.; DOI: 10.1051/0004-6361/201730787.

Stohl J., 1986: The distribution of sporadic meteor radiants and orbits. In: *Asteroids, comets, meteors II, Proceedings of the International Meeting, Uppsala, Sweden, June 3–6, 1985).* Uppsala, Sweden, Astronomiska Observatoriet, 565–574.

Thompson S.D., Bowles Z.R., Povilaitis R.Z., Daubar I.J., Robinson M.S., 2014: Recent impacts on the moon. *45th Lunar and Planetary Science Conference,* LPI Contribution No. 1777, 2769.

Trigo-Rodríguez J.M., Borovička J., Spurný P., Ortiz J.L., Docobo J.A., Castro-Tirado A.J., Llorca J., 2006: The Villalbeto de la Peña meteorite fall: II. Determination of atmospheric trajectory and orbit. *MAPS* **41,** 505–517.

Vaubaillon J., Caillou A., Deverchere P., Colomer C., Zilkova1 D., Christou A., Laskar J., Baratoux D., Fouchard M., Colas F., Maquet L., Birlan M., Bouley S., Vernazza P., Carry B., Beck P., 2019: Optimisation of double-station balloon flights for meteorobservation. In: *R. Rudawska, J. Rendtel, C. Powell, R. Lunsford, C. Verbeeck, A. Knöfel (eds.): Proceedings of the International Meteor Conference Pezinok-Modra, Slovakia, 2018*, 151–154

Vaubaillon J., Colas F., Jorda L., 2005a: A new method to predict meteor showers. I. Description of the model. *A & A* **439,** 751–760.

Vaubaillon J., Colas F., Jorda L., 2005b: A new method to predict meteor showers. II. Application to the Leonids. *A & A* **439,** 761–770.

Vaubaillon J., Jenniskens P., 2007: First results from the Aurigids 2007 Multi-instrument Aircraft Campaign. *American Astronomical Society, DPS meeting #39, id.59.07; Bulletin of the American Astronomical Society* **39,** 535.

Vaubaillon J., Koten P., Margonis A., Toth J., Rudawska R., Gritsevich M., Zender J., McAuliffe J., Pautet P.-D., Jenniskens P., Koschny D., Colas

F., Bouley S., Maquet L., Leroy A., Lecacheux J., Borovicka J., Watanabe J., Oberst J., 2015: The 2011 Draconids: the first European airborne meteor observation campaign. *EMP* **114,** 137–157; DOI: 10.1007/s11038-014-9455-5.

Vaubaillon J., Maquet L., Soja R., 2014: Meteor hurricane at Mars on 2014 October 19 from comet C/2013 A1. *MNRAS* **439,** 3294–3299.

Vida D., Brown P.G., Campbell-Brown M., Weryk R.J., Stober G., McCormack J.P., 2021: High precision meteor observations with the Canadian Automated Meteor Observatory. *Icarus* **354,** article id. 114097; DOI: 10.1016/j.icarus.2020.114097.

Vojaček V., Borovička J., 2018: Properties of faint meteors derived from video observations. In: *Gyssens M., Rault J.-L. (eds.), Proc. IMC 2017, Petnica, Serbia*, 109–114

von Zahn U., 2001: Lidar observations of meteor trails: evidence for fragmentation of meteoroids and their subsequent differential ablation. In: *Warmbein B. (ed.), Proc. Meteoroids 2001. ESA SP-495,* ESA, Noordwijk, 303–314.

Weinek L., 1866: Beobachtung des Sternschnuppenfalls auf der k.k. Sternwarte in Prag. *Astr. Nachr.* **113,** 374–380.

Wetherill G.W., ReVelle D.O., 1981: Which fireballs are meteorites? A study of the Prairie Network photographic meteor data. *Icarus* **40,** 308-328.

Whipple F.L., 1950: A comet model. I. The acceleration of comet Encke. *Astrophys. J.* **111,** 375–394.

Whipple F.L., 1951: The Baker super-Schmidt meteor cameras. *Astronomical J.* **56,** 144–145.

Wiegert P., Vaubaillon J., Campbell-Brown M., 2009: A dynamical model of the sporadic meteoroid complex. *Icarus* **201,** 295–310.

Williams I.P., Jopek T.J., Rudawska R., Tóth J., Kornoš L., 2019: Minor meteor showers and the sporadic background. In: *G.O. Ryabova, D.J. Asher, M.D. Campbell-Brown (eds.), Meteoroids. Sources of meteors on Earth and beyond.* Cambridge Univ. Press, 210–234

Yeomans d., 2008: Impact of Asteroid 2008 TC3 Confirmed. NASA, Near Earth Object Program. 2008-10-07 `neo.jpl.nasa.gov/news/news160.html`

2 | Visual Meteor Observations

Jürgen Rendtel, Rainer Arlt, Ralf Koschack

2.1 Aims

One important purpose of visual meteor observing is principally to obtain data which can be used to compare with past meteor reports made by other naked-eye observers. Such previous observations may have been made last week, last year, last century, or even several millennia ago. The comparison may be made for any number of reasons, but it mostly involves looking for patterns, whether similar or different, in what visual meteor activity was like, to help us better understand meteor showers, and to see how we can model a given meteoroid stream, to predict what might be seen in future.

One great advantage of visual observing is that it has been carried out for a very long time. The earliest datable records of individual meteors and probable meteor showers come from ancient Mesopotamia and China, beginning in the early second millennium BC (Zhang, 1977; Bjorkman, 1973). This material is rarely as detailed as even the more basic modern reports until recent centuries, but useful information can sometimes be extracted from earlier times even so.

For several studies of the evolution of meteoroid streams we successfully transcribed past meteor reports from publications into modern format, this way extending the time line to a century or more. Of course, this is possible only for showers which were recognised in the past. Examples are the Leonids, Geminids and the Orionids.

The other key advantage of visual meteor work is that it is very easy to do. Anyone with normal eyesight can go outdoors under a clear, dark sky at night and look for meteors. The essential things are to know what to look for, when, and what to record and report from your observing. This is what we discuss in this chapter, including the two chief techniques of meteor counting (suitable for nights of stronger meteor activity up to meteor storm level) and meteor plotting (for when meteors are less frequent).

2.2 General advice

2.2.1 When to organise an observation

If you have never observed meteors before, you should choose a period around the maximum of one of the major showers, when more than 15–20 meteors are visible per hour. Not only it is much more fun to see lots of meteors, it is also important to see plenty in order to get sufficient practice of recording data, and to become familiar with the appearance of meteors generally. If you practise on an average night, only a few meteors will appear, and there will be insufficient opportunities to make brightness estimates, etc. However, major shower activity is not the sole determinant of how many meteors can be expected. There are at least two other circumstances to be taken into account.

As shown in Figure 1.8, lower radiant elevations mean fewer meteors are observable. The Zenithal Hourly Rate (ZHR) of a shower gives a measure of that shower's activity, and is the number of shower meteors per hour an observer might count under perfect sky conditions with the radiant at the zenith (for a detailed explanation see Chapter 7; major showers have maximum ZHRs of more than 20). Table 2.1 gives the number of meteors an observer might expect to see for different radiant elevations if the ZHR amounted to the impressive value of 100. Now you can imagine what you would see with a radiant elevation of 10° if the ZHR was not as impressive as 100!

Table 2.1: The number of meteors visible per hour for a ZHR = 100 shower, at different radiant elevations, h_{Rad}, based on geometric considerations alone, and assuming a perfectly clear, ideally transparent, sky with the reference limiting magnitude of +6.5 and no obstructions in your field of view.

h_{Rad}	90°	70°	50°	40°	30°	20°	10°
n	100	94	77	64	50	34	17

Consequently, when planning your watch, you should prefer periods when the radiant has a suitable elevation of 20° or more for your whole observation. Special events (outbursts) and showers with peculiar geometry (e.g. daytime showers) may require observations with the radiant lower in the sky.

The ZHR refers to perfect sky conditions, although these may not be always available. If there is haze, clouds or any kind of sky illumination (the Moon, ar-

tificial lights, twilight) the observable numbers of meteors will decrease, since a considerable fraction of the fainter meteors will be missed. Haze and clouds cannot be foreseen in planning an observation, but twilight and the Moon can.

- The Sun should be at least 12° below the horizon (the definition of when nautical twilight begins or ends). The respective times can be found in almanacs or listings on various web pages or can be calculated using planetarium programs.

- Moonlight problems strongly depend on the Moon's phase and the transparency of the air (i.e., the amount of scattered light). Moonlight is negligible if the Moon is a crescent, or very low in the sky, but the well-risen gibbous to full Moon reduces the observed meteor numbers by up to a factor of ten!

Of course, it can be of interest to collect data of an outburst or shower activity during "poor conditions". In such cases it is important to find a place where the direct light is shielded (blocked by a tree or a building, for example) and to record the observing conditions carefully. Checking for possible meteors of daytime showers (radiants $\leq 30°$ away from the Sun position) requires to watch into twilight. In such cases arrange your field centre in a way that the radiant is still near the edge of your field of view but the centre is not in the direction of the brightest twilight segment.

2.3 Observing location

Before starting any observations you should look for a dark-sky site, since this will considerably improve your observations. Your backyard might do. Try to choose a place where you will not be disturbed by direct lights, such as streetlamps or lit windows. Urban dwellers may have to travel to the countryside. This may involve transport problems, and possible problems with accommodation. Camping or staying with friends are possible solutions. Such organised watches with others can be ideal occasions for astronomical camps. Young people may find this especially enjoyable.

Note however, that if you do observe with a group like this, it is essential that each person observes independently of the others. Data from different observers must not be combined.

This is because such joint results cannot be properly analysed, as everyone's eyesight and visual acuity is different. Consequently, each observer must maintain his or her own separate notes and observational reports.

After the watch you should get plenty of rest, and avoid any unnecessary travelling. This is particularly important if you will probably not be able to use public transport to return from your observing site.



Figure 2.1: Mountain expedition clothing may be a good choice when observing under cold conditions (group photo from the 1998 Leonid expedition to Mongolia where the temperatures dropped to −35°C during the observations).

2.4 Observing equipment

2.4.1 Check list

As we have seen already, it is important to plan ahead for your observations. One key element in that is to plot out onto star charts the positions of any active meteor shower radiants for the night(s) you intend to observe. The daily drift of each radiant must be allowed for. This information can also be found in the annual IMO Meteor Shower Calendar. You can then work out, using star charts, a planisphere, a computer program or online-planetarium, when the radiant will be at a suitable elevation of at least 20° for your observing location – except for observations of outbursts, peak activity, or showers with radiants close to the horizon during all available intervals.

Memorise the magnitudes of a number of stars from the region of sky you will be watching, so you have a complete scale from magnitude 0 to +6 available that you can use to estimate the magnitudes of the meteors you see. You should learn too the areas in this region you will need to work out the sky's limiting magnitude (see Section 2.5.3).

Another essential element in preparing for good observations is comfort. Cold and damp nights are at best unpleasant for the unprotected observer, and at worse can be very dangerous if prolonged exposure to conditions like these occurs. Observers living in cold regions have their experiences, of course. Meteor observing implies being out in (very) cold conditions and not moving for some time. Mountain expedition clothing has been found useful e.g. during some past Leonid campaigns (Figure 2.1). For 'regular' sessions, some ordinary things can help. You might find the following useful:

- a deck chair, camp bed, or air mattress;

- a sleeping bag or blanket (even in summer);

- warm clothes—not tight-fitting ones: many thin layers are better than a few thick ones, as the air trapped between the layers is a good insulator;

- a cushion or pillow with a damp-proof cover, to raise your head if lying on an air mattress or camp bed;
- a cover to keep the dew and/or frost off bedding and equipment;
- food and drinks to consume during observing breaks; do not have hot drinks – they expand the blood vessels to better radiate the excess heat, thus making you feel colder.

The essential observing equipment consists of

- an accurately set, or better: radio controlled watch, ideally a digital one or a speaking watch (avoids looking at a display and re-focusing);
- a dim red torch enabling you to read or write, without ruining your dark adaptation;
- a small flip-over notepad or a roll of paper and at least two pencils, or a portable digital or cassette recorder. Smartphones may also provide a useful recording function (make sure this does not cause disturbing light).

If you are intending to use a digital or tape recorder, you should be aware of its limitations, and plan for potential problems by practising with it under field conditions before you observe. Difficulties such as pressing the right buttons, learning about probable battery lifetimes, how sensitive the microphone is, or even how to change the tape or the batteries in the dark, are better worked-through before you encounter them during a real meteor watch.

The recorder should be easily usable in the dark and should have a one-touch recording button preferably. Do not use the pause switch since this is generally very small, and the recorder may slowly decharge the battery when set to paused recording. The use of a voice actuator is not recommendable either as the first syllables may be lost before the tape starts running, and you cannot check if the device is really recording, without looking down. Recorders storing the time of speaking can be very helpful; however, note that it may take the recorder some 30 seconds until the complete time information is stored.

2.4.2 Preparing to observe

Shortly before you start to observe, check that your torch and any recording device used are working correctly, and spend a few minutes refreshing your memories of

- the radiant positions you plotted out earlier;
- the magnitudes of the meteor-comparison stars that will be in your field of view;
- the limiting magnitude fields near the area you will be observing.

A good observer has a pair of vigilant eyes, as fast, often faint, meteors require a good perception also off the line of sight. Lack of vitamin A, as well as the side-effects from alcohol and nicotine consumption, all negatively affect visual perception. Smokers must realise that their eyes will not dark-adapt completely, even if they stop smoking for a while.

The time to reach full dark adaptation varies from person to person. When going into the dark, the pupil size increases immediately. The rods and cones of the retina both become more sensitive during the first few minutes, and after 5 to 10 minutes the cones reach their maximum sensitivity. After this rods become more sensitive than cones. This increase of sensitivity will continue over the next few hours because the rods regenerate a receptor protein called rhodopsin[1]. After about 30 minutes, the observer is roughly 90% dark-adapted. The slow improvement beyond this point is difficult to recognise. Your planning must allow for the slow process of dark adaption, but you may reduce the time by partially dark adapting while collecting equipment and getting dressed before going out to observe. It also means that light should be avoided during breaks. The rods are most sensitive to bluish-green (maximum at about 500 nm) and almost not sensitive to red light (beyond approximately 580 nm – hence a red torch is recommended for checking anything or taking notes; best if deep red with 600 nm or more). Key points to remember include the following:

- always use a red torch to see by when you have dark adapted and avoid looking at screens of mobile phones with their bluish light!;
- allow plenty of time for your eyes to fully dark adapt.

Once at your site and ready to observe, carefully choose the direction you are going to face, so that:

- your field of view will not be obscured by surface objects such as trees or bushes;
- you will not be facing artificial lights, or the Moon, or any illuminated surfaces (even Venus may be a disturbing object);
- you can comfortably centre your field of view at 50° to 70° elevation;
- you will not be directly facing a shower radiant; the optimal radiant distance to observe meteors from a given shower is about 20° to 40°).

Then arrange your equipment according to the direction chosen. As the centre of your field of view must be given

[1] Vogel & Siebert (2001) show that opsin, if formed after a light event from activated rhodopsin is weakly active and makes the photoreceptor cell "see" virtual light even in complete darkness. This way it prevents complete dark adaptation. Only after about 30 minutes, opsin is completely regenerated to inactive rhodopsin, then allowing complete dark adaptation. This means that the switching-off of the activity of opsin is the main effect to achieve dark adaption. The increase of the total amount of rhodopsin by regeneration adds only to a very minor degree.

in your observing report, remember to record it when you start your watch, and at any time later when you need to change it.

2.5 Visual counting observations

Meteor counting watches are suitable for all observers from beginners to experts, at any time of year, but as it provides only limited information on the probable source of each meteor, its value for examining lower-activity meteor sources is equally limited. For minor shower investigations, once you have some familiarity with meteor observing generally, we recommend visual plotting observations as described in Chapter 3. However, if the observed meteor rate from all sources is 20 an hour or more on any given night, you should concentrate solely on counting observations, otherwise you will probably miss more meteors than you see! Note too that as many details are the same for both types of watch, familiarity with the counting technique is essential for plotting observations.

2.5.1 What to record

It is important to record your observations correctly at the time. This can be done by storing all the information on a tape or digital recorder, or by writing it onto scrap paper without taking your eyes off the sky. The notes you take must cover all the following details about the observation:

- the times the watch began and ended at, any breaks, and time labels at least every 15 minutes; *give all times in Universal Time*, UT, sometimes called UTC (Section 2.5.2);
- the limiting magnitude and any changes to it during your watch (Section 2.5.3);
- details of any cloud cover present (Section 2.5.4);
- the centre of your field of view, in right ascension, α, and declination, δ (Section 2.5.5);
- the details for all meteors seen (Section 2.5.6).

2.5.2 Timings for the watch

Timings of each meteor's appearance are not required as we want to derive information of the *number of meteors per source and time interval.* Apart from the times you started and stopped watching (including any break timings) a record of time labels at least every 15 minutes is required. It is not necessary to note these labels exactly at the quarters of each hour, but they should occur at about 15 minute intervals. Near any major shower's maximum, or at other times when activity is unusually high, time labels should be more frequent, at least every 5 minutes or so.

Universal Time, UT, has four slight variants, of which the one we use is UTC, coordinated UT, though we commonly call this just 'UT' for simplicity. This is the time base for all precise broadcast time signals or the signal for the radio driven clocks, so is easily accessible worldwide, providing the correct allowance is made to convert local time to UT. As UT is valid for 0° geographical longitude, it is sometimes known as Greenwich Mean Time, GMT, named from the Greenwich meridian. From this, it follows that if you divide your own longitude in degrees by 15, you will have a guide to the correction in hours you must apply to your local time to find UT, subtracting this amount if east of the Greenwich meridian, adding it if west.

Table 2.2: Table with corrections for converting local times to UT for some selected places. 'ST' gives the difference for the standard time zone, while 'DS' gives the difference when normal 'daylight saving' or 'summer' time is in operation.

Place	ST	DS
Australia, east	−10	−11
Australia, central	−9.5	−10.5
Australia, west	−8	−9
Austria	−1	−2
Belarus	−2	−3
Benelux	−1	−2
Brasil, west	+3	+2
Bulgaria	−2	−3
China	−8	−9
Croatia	−1	−2
Czech Republic	−1	−2
Finland	−2	−3
France	−1	−2
Germany	−1	−2
Hungary	−1	−2
Italy	−1	−2
India	−5.5	−6.5
Japan	−9	−10
Jordan	−2	−3
Malta	−1	−2
New Zealand	−12	−13
Norway	−1	−2
Pakistan	−5	−6
Portugal	−1	−2
Romania	−2	−3
Russia (European part)	−3	−4
Slovakia	−1	−2
Slovenia	−1	−2
South Africa	−2	−3
Spain	−1	−2
Sweden	−1	−2
UK	−0	−1
Ukraine	−2	−3
USA/Canada AST/ADT	+4	+3
USA/Canada EST/EDT	+5	+4
USA/Canada CST/CDT	+6	+5
USA/Canada MST/MDT	+7	+6
USA/Canada PST/PDT	+8	+7
USA, Alaskan time	+9	+10
USA, Hawaiian time	+10	n/a

However, time zones often follow political or administrative boundaries which may deviate significantly from the theoretical ones. Additionally, allowance must be made for other local deviations, such as summertime whole number of hours (such as in India, where standard clock time is 5^h30^m ahead of UT, or in central Australia, where Northern Territory and South Australia are 9^h30^m ahead of UT). Table 2.2 gives some selected time conversions.

Your watch should last as long as possible, under the constraints already outlined—in effect, as long as the observing conditions or fatigue will allow. The longer you observe, the more meteors you will see. A larger sample usually reduces the error margins for derived quantities. Furthermore, the part of the activity profile you cover widens. Perhaps if you stop too early you may miss the best activity! The minimum useful watch length is one hour. Of course, in the vicinity of peaks or outbursts, one may use shorter cloud-free intervals to record unusual activity. This requires a careful documentation of the probably varying observing conditions.

2.5.3 Determination of the limiting magnitude

The darker and more transparent the sky and the more sensitive your eyes, the more meteors you can see. To use your observations for scientific analyses, a quantitative characterisation of these factors needs to be established. The limiting magnitude (which is defined as the magnitude of the faintest star near the zenith that the observer can detect using the slightly averted naked eye) defines both the condition of the sky's clarity and the quality of the observer's eyes. Please note, the limiting magnitude is an *observer-specific* quantity. Do not be surprised if other observers at the same site obtain different limiting magnitudes than you. This is the rule, rather than the exception. Only record your own values! There are several methods for determining the limiting magnitude. We describe and recommend one which is favoured by many meteor observers.

In the star charts printed at the end of this Chapter (pages 60 to 60) star fields are marked by dashed lines. During the observation, the number of stars visible in (some of) these areas are counted, including the corner stars. After the observation, these numbers of stars can be converted into the limiting magnitude by using Table 2.6 on page 59 and following page. Do not increase your attention artificially when obtaining the limiting magnitude since it should characterise your average eye-state during your observation. Determine the limiting magnitude in a way as shown in Figure 2.2 at the start of the watch, whenever a variation occurs (e.g. haze occurs or twilight begins), and generally every 30–45 minutes, even if there is no obvious or considerable change. In this way you will reduce the random errors in the procedure. Variations of the limiting magnitude should be considered for the choice of intervals.

You should preferentially use fields in your observing direction, and use at least two, or better three, fields for each determination. This is necessary because there

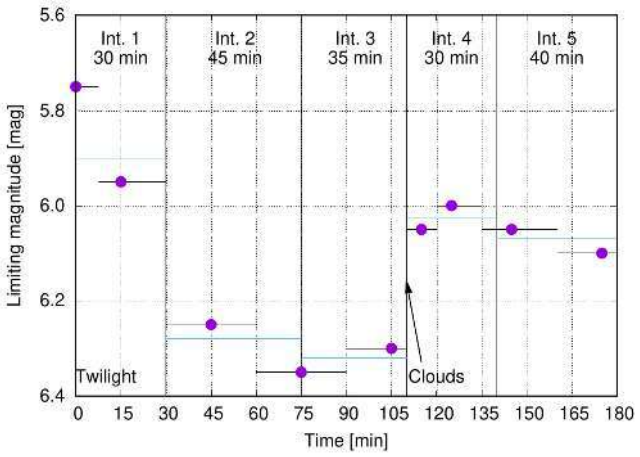


Figure 2.2: It is recommended to determine the limiting magnitude at the beginning of a session, repeatedly during the watch and especially of changes occur. In this example we start with some remaining twilight brightening (interval 1), followed by improving conditions until the limiting magnitude decreases suddenly due to incoming clouds or haze. The dots give the averages for the counts, the adjacent lines show the validity of the count (half time to the neighbouring count) and the thicker lines represent the averages for each interval. A detailed example follows in section 2.6 on page 47.

may be larger magnitude steps in the sequence of stars in some fields. It is advised to have a look into the Table 2.6 to identify such large steps. Using more star counts will help to reduce random errors as well. The fields should have an elevation of more than 40°. Remember to note the time, field number, and the number of stars counted.

2.5.4 Obstruction of the field of view

Your observations should be carried out with an unrestricted field of view. If a fraction of the field is covered by clouds, you will miss a certain number of meteors. To calculate how many meteors you might have observed had your field been completely clear, we use a factor based on the number of meteors missed as being proportional to the field fraction obscured.

Although we always refer to an unrestricted field of view, due to the properties of the human eye, about 98% of all meteors are witnessed within an almost circular field of around 50° radius. We call this field the *effective field of view*. Whenever clouds cover your effective field (not another part of the sky!) record the time in your notes.

Clearly, it would take a very major effort to record every change in the percentage of cloud cover. Remember that you are outside first and foremost to observe meteors rather than to record cloud obscuration. Instead of recording every change, report the average cloud percentage during the past 10–15 minutes of your watch, until your field is cloudless again or you stop observing. Note the begin of the cloud cover and average the ob-

struction percentage unless it does not change severely as in the example observation in Figure 2.4 on page 47.

At first glance, this method seems to be useful for any value of cloud cover. But let us think one step further. Imagine a hole of about 40° radius in the clouds. Observing through this hole, about 50% of the area of your effective field is covered. In order to obtain the number of meteors you would have observed in an unrestricted field you have to multiply the number you observed within the partially covered field by a factor of 2. But owing to the construction of the human eye, most meteors are seen in the centre of your field of view. In our example you would miss only 10% of the meteors instead of 50%. This example may be an artificial one, but the situation is similar to many other real cases of cloud cover. Please therefore note that the cloud correction is an approximation only, which works primarily with small amounts of cloud cover. *Thus, you should take a break as soon as cloud cover exceeds 20%*, unless you are monitoring an unusual event or a meteor storm.

2.5.5 Field of view

It is recommended that, while observing, you should follow the motion of the sky, and thus you will become more familiar with certain regions. If the position of the field becomes unfavourable (e.g. elevation less than 50°) you should choose another field, and then record the centre of the new field in your notes.

2.5.6 When a meteor appears

Having read to this point you may have got the impression that meteor observing consists mainly of recording lots of odd data unconnected with meteors. But that is not the case. Now we reach our main subject: What do you have to do when a meteor appears? The most important thing is to remain calm so that you can record what you have just seen as objectively as possible. Keep looking at the region of sky where you saw the meteor in order to memorise the following data in this order:

2.5.6.1 Meteor's path

The most important information is its direction rather than the exact length and start/end points. Memorise it with respect to the background stars.

2.5.6.2 Shower association

Members of a given meteor shower seem to originate from one small area of sky; the radiant. Since you memorised the radiant's position in the sky before the start of the watch, you can trace back the meteor's path as an imaginary straight line, to see whether it intersects with the radiant. Now it becomes clear why it is best to look not too far from the radiant. Tracing back the meteor's path over a large distance is difficult and brings in greater uncertainties. If the path can be traced back to the radiant, the meteor was a shower meteor, otherwise it was a sporadic. Please note additionally two general rules:

- Shower meteors appear faster the larger their distance from the radiant (up to 90°) and the higher their elevation above the horizon. Near the radiant or near the horizon shower meteors generally seem slower.
- The apparent path length shows a similar behaviour to the angular velocity. Near the radiant or near the horizon meteor paths are generally short, while they are longer with increasing distance from the radiant and nearer to the zenith.

This means that even if the trail came from the radiant, a meteor in the vicinity of the shower radiant does not belong to the shower if it was very fast and/or very long. A detailed explanation of the reasons for this can be found in Section 3.6.

2.5.6.3 Maximum magnitude

Estimate this by comparing the meteor with the brightness of nearby stars you memorised prior to the start of the watch. If you are very certain of the sighting, i.e., if it occurred in the centre of your viewing field, estimate it to the nearest 0.5 mag, e.g., 3.5 mag or 1.0 mag; otherwise estimate it to the nearest whole magnitude, e.g. 3 mag or 1 mag. Later we are interested in the distribution of meteor brightnesses per shower, not in the magnitude of each single meteor. If, for example, a meteor appeared at the edge of the field, you may also note a .5-value: if you say it was *between +2 and +3*, note +2.5.

2.5.6.4 Persistent train

If you observed a train that persisted after the meteor had disappeared give its duration in seconds. If you detected a train persisting only for a few tenth of a second you may note a "+" as an indication of a so-called wake.

2.5.6.5 Colour and other data

Note that it should theoretically be impossible to detect colours for meteors fainter than magnitude +2 mag. This information is of least value of all the data and can be omitted.

Unless you are going to photograph meteors or a fireball appears, the time of individual meteors is of little interest, since you set time labels for each ≈ 15 minutes (or shorter) into your notes.

The duration of a meteor is usually less than one second. This requires exceptional concentration and quick reactions on the part of the observer. This is also the reason why the observer sees only a fraction of the meteors that actually appear.

After storing all the data in your memory you can transfer them to your record. If you are using a voice recorder you start the device and report the data in a format like this: *'Perseid, magnitude +0.5, train 3 seconds, white'*. Then stop recording until the next meteor appears or you want to record limiting magnitudes, etc. On a paper roll (shown in Figure 2.3) a record such

as that in Figure 2.4 can be made. The corresponding record to the taped version will look like: *'P 0.5 3s w'*.

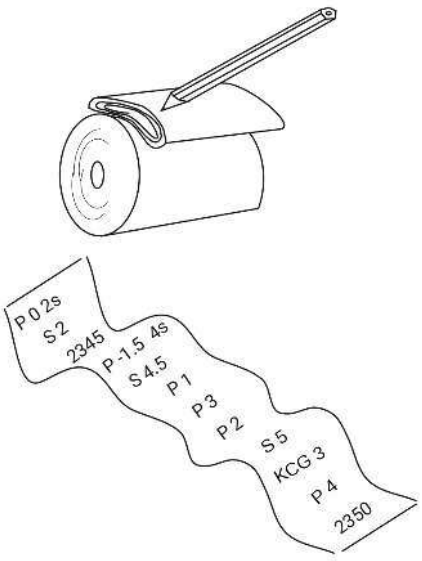


Figure 2.3: Use of a paper record.

In both recording techniques, you you do not want interrupt your observation by looking at what you are doing. You have to use the tape or the paper 'blind'. The tape should provide no problems but writing blind onto paper requires a little experience. It avoids problems with low batteries, however. Important: be consistent within your notes, use a coherent and short writing. For example, four digits XXXX is always a time ('2345' = $23^{h}45^{m}$), numbers with a slash XX/XX is reserved for star counts in lm-fields ('7/18' = field 7: 18 stars), letter + number NX for meteors of shower N with brightness X ('S3' is a sporadic meteor of magnitude +3) and so on.

2.5.7 How long should the watch last?

As already mentioned, meteor observing requires great concentration and quick reflexes. Your whole attention must be paid to your observation. Avoid talking or listening to music. As soon as you get tired take a break to walk around or to consume some food. In most cases this will fend off tiredness, and you will be able to continue the watch. If you do become too tired, you should stop observing and retire to bed, since the accuracy of your data will reduce as fatigue takes hold, meaning that you will miss many meteors. Thorough preparation before observing includes ensuring that you are sufficiently rested, as this is the one factor which may stop you watching that you can control, unlike, for instance, the weather.

Generally, if your observation period lasted longer than 2 hours, you should divide it into intervals of roughly 1 hour duration. The interval boundaries must coincide with any time labels reported in your notes (breaks included). There is no need to report intervals of exactly 1 hour duration. If circumstances change considerably and quickly (e.g., change of limiting magnitude by more than $0\overset{m}{.}5$) take the time of such a change as an interval boundary.

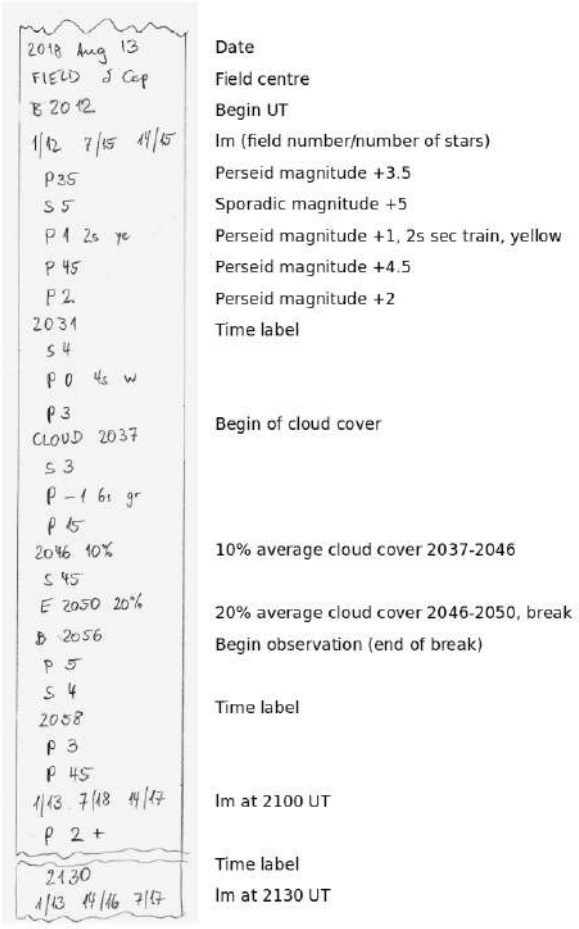


Figure 2.4: An example of an observation record on a paper roll. The same information could have been spoken onto a tape or other recording device instead.

If you do not report on a major shower maximum, periods of about 1 hour are suitable.
If you report on a maximum of a major shower, 15-minute periods are recommended.
Shorter interval lengths ($\leq$ 5 min) are required if an outburst occurs or a peak is predicted.
Interval lengths may be adopted to the activity: give short intervals during high rates and slightly longer intervals before and/or after. Generally it is better to choose shorter intervals than too long ones.

2.6 Reporting data of a visual observation

In order to carry out a scientific analysis of meteor activity on a global scale, the IMO needs to store observational data in the Visual Meteor Data Base (VMDB). Submission of data is easily done via the input form on

the IMO website which asks all the necessary meteor and watch data we need for later analyses step by step. This way we try to ensure that the data for each session is complete. It is vital that this input is done very carefully. The incoming reports are checked by a team to find possible errors and are subsequently approved.

To illustrate the steps from the observation to the final report, we created an example which may answer regularly occurring questions and has some recommendations. The (modelled) observation in the evening of October 8 includes a short activity outburst (October Draconids), the late rise of another radiant (Orionids) and variable parameters. According to the shower working list, we may expect meteors of four showers:
Draconids (DRA; we further shorten it for our 'blind' notes to D)
Orionids (ORI, or O)
δ-Aurigids (DAU, A)
Southern Taurids (STA, T)
as well as sporadic meteors (S).
Figure 2.5 shows the 'original notes' (which may be paper notes or the script of the notes from a voice recorder) as well as the translation into the input data for the VMDB.

2.6.1 Dividing the observation period into intervals

In our example, we start at 2003 (UT), note the field centre (α Cep at RA=$21^{\mathrm{h}}19^{\mathrm{m}}$=320° De=63°) and start with lm counts. The sequence of meteors is relatively low. We note a first time label after nearly half an hour (2030) defining our first interval. The second interval has a nice series of DRA towards 2045 which may indicate an increase of activity – hence we choose our next time stamp as interval boundary. At this time we add another lm count and see DRA in higher cadence (at one instance we note three almost together – shown here in one line) and take time stamps closer now (2050, 2056). If you go for short intervals, make sure that the stamps mark the exact minute MM (MM:00). In case of 30-minute intervals the difference of half a minute does not matter. Now the meteors occur frequently, and we continue with time labels every 5 minutes. At 2109 clouds start to move in; we note 20% at 2124, add another lm count and stop at 2138 (with 30% cloud cover in the last minutes).

Later the clouds move away and we start another interval at 2212, now with the field centre near α Lac (RA=$22^{\mathrm{h}}31^{\mathrm{m}}$=338° De=50°– the nearest 10° value is sufficient). The last interval of our session ends at 23:00 UT.

The useful intervals are indicated in Figure 2.5. Now we need to prepare the raw data for the input form.

Net observed time T_{eff}

This is the time we effectively observed. Any breaks need to be subtracted (operating a camera, looking for something fallen to ground, ...). In the on line report form, the total time between start and end of an interval is displayed. Be careful if a correction is needed.

Limiting magnitude

Using the conversion Table 2.6 (page 59) we have to find the corresponding limiting magnitude (lm). In some of the fields there are quite large jumps in the sequences. As an example, we find that the 10th star in field 1 is of magnitude 5.3 and the 11th one of magnitude 6.0. If the lm actually is 5.8, we cannot see the 11th star and obtain a value of 5.3 which is far off the true lm (and affects the average). Hence it is recommended to count the stars in more than two fields so that you can omit lm values at such large step widths. Whenever the limiting magnitude lies in a 'gap' wider than 0.3 mag, one should ignore this field.

When all the limiting magnitudes have been determined, we can calculate the weighted averages ($\mathrm{lm}_{\mathrm{avg}}$ for each interval. Do *not* compute the average number of stars: only magnitudes themselves can be averaged.

$$\mathrm{lm}_{\mathrm{avg}} = \frac{\sum_{i=1}^{n} \mathrm{lm}_i \times t_i}{\sum_{i=1}^{n} t_i}$$

where t_i is the time for which lm_i is valid. The lm values for the first interval in our example are:
$\mathrm{lm}_1 = 6.10$ (at the start), valid until the middle to the next lm count (2030), which is 27/2 = 14 minutes after the start, i.e. 2017. So for the remaining 14 min, the lm is 6.21. This gives for interval 1:

$$\mathrm{lm}_{\mathrm{avg}} = \frac{6.10 \times 13\,\mathrm{min} \;+\; 6.21 \times 14\,\mathrm{min}}{13\,\mathrm{min} + 14\,\mathrm{min}} = 6.16$$

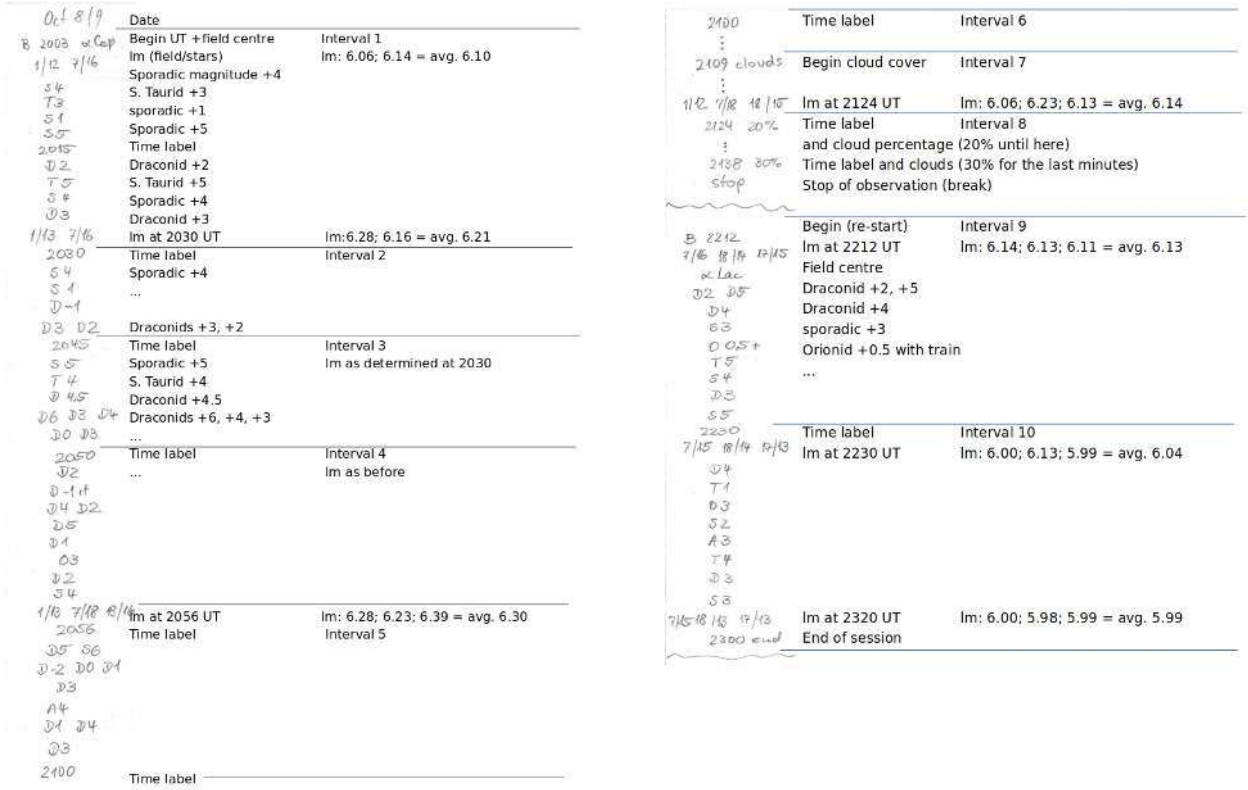
and in the same way for interval 2:

$$\mathrm{lm}_{\mathrm{avg}} = \frac{6.21 \times 13\,\mathrm{min} \;+\; 6.30 \times 2\,\mathrm{min}}{13\,\mathrm{min} + 2\,\mathrm{min}} = 6.22$$

This procedure may appear somewhat cumbersome, especially where the lm is very variable, but simple averaging is usually possible in most cases (see interval 1) and as we also see for the rest of our model session.

For all intervals in our example we may summarise the lm values as follows:

Int.	Interval (UT)	Period (min) lm	$\mathrm{lm}_{\mathrm{avg}}$
1	2003–2030	2003–2016 (13) 6.10 2016–2030 (14) 6.21	6.16
2	2030–2045	2030–2043 (13) 6.21 2043–2045 (2) 6.30	6.22
3	2045–2050	6.30	6.30
4	2050–2056	6.30	6.30
5	2056–2100	6.30	6.30
6	2100–2109	6.30	6.30
7	2109–2124	6.14 (with clouds)	6.14
8	2124–2138	6.14 (with clouds)	6.14
9	2212–2230	2212–2221 (9) 6.13 2221–2230 (9) 6.04	6.09
10	2230–2300	2230–2245 (15) 6.04 2245–2300 (15) 5.99	6.02



Date	
Begin UT +field centre	Interval 1
lm (field/stars)	lm: 6.06; 6.14 = avg. 6.10
Sporadic magnitude +4	
S. Taurid +3	
sporadic +1	
Sporadic +5	
Time label	
Draconid +2	
S. Taurid +5	
Sporadic +4	
Draconid +3	
lm at 2030 UT	lm:6.28; 6.16 = avg. 6.21
Time label	Interval 2
Sporadic +4	
...	
Draconids +3, +2	
Time label	Interval 3
Sporadic +5	lm as determined at 2030
S. Taurid +4	
Draconid +4.5	
Draconids +6, +4, +3	
...	
Time label	Interval 4
...	lm as before
lm at 2056 UT	lm: 6.28; 6.23; 6.39 = avg. 6.30
Time label	Interval 5
Time label	

Time label	Interval 6
Begin cloud cover	Interval 7
lm at 2124 UT	lm: 6.06; 6.23; 6.13 = avg. 6.14
Time label	Interval 8
and cloud percentage (20% until here)	
Time label and clouds (30% for the last minutes)	
Stop of observation (break)	
Begin (re-start)	Interval 9
lm at 2212 UT	lm: 6.14; 6.13; 6.11 = avg. 6.13
Field centre	
Draconid +2, +5	
Draconid +4	
sporadic +3	
Orionid +0.5 with train	
...	
Time label	Interval 10
lm at 2230 UT	lm: 6.00; 6.13; 5.99 = avg. 6.04
lm at 2320 UT	lm: 6.00; 5.98; 5.99 = avg. 5.99
End of session	

Figure 2.5: Notes from an (artificial) observation and preparation steps for the report. Left are the 'original notes', the explanation and suggested interval choice.

Cloud cover

We need to compute the weighted average cloud cover. Multiply every percentage k by its corresponding time interval in minutes. These products are then totalled, and their sum is divided by the total observing time, also in minutes, and by 100 to give a percentage.

$$k = \frac{\sum_{i=1}^{n} k_i \times t_i}{t_{\text{total}} \times 100\%}$$

In our example we prefer short intervals so that we only use the cloud cover values estimated for the two affected intervals. If we had combined the intervals 7 and 8 (2109–2138, t_{total} 29 min), we had to compute:

$$k = \frac{20\% \times 15\,\text{min} + 30\% \times 14\,\text{min}}{29\,\text{min} \times 100\%} = 0.248$$

k is the average part of the field covered by clouds during the entire watch. The final correction factor results from:

$$F = \frac{1}{1-k}$$

In our example:

$$F = \frac{1}{1-0.248} = 1.33$$

.

If possible, avoid observations with cloud interference because it is very difficult to estimate the loss of effective observing field as most of the meteors will be seen close to the field centre and by applying corrections we introduce additional uncertainties. In our example, the observed high DRA activity rectifies a continuation with the clouds. During peaks, outbursts or other peculiar events, data obtained under disturbed conditions may be of interest. In Figure 2.6 we show an example with parts of the sky being cloudy but an undisturbed field of more than 90° diameter remains free.

Analyses of dedicated visual observations (Koschack & Rendtel, 1990) show that a visual observer notes about 96 percent of all meteors within 52° radius around the viewing direction. (Hence the recommendation to have the field centre at least 50° above the horizon.) Figure 2.7 shows the relative amount of meteors over the field of view and various effects of the cloud cover to the perception of meteors. This emphasises that an appropriate field correction is not a simple geometric effect (as for video meteor observations – see Nikolić, Schröder and Tešić, 2018) but a kind of weighted field correction which can be done with limited accuracy only.

2.6.2 The online report form

Be prepared to enter the following data after having logged on to the IMO website:

- Location: There is a map option to identify your observing location. You may also give the geographic coordinates directly.



Figure 2.6: Partly cloudy sky during a Geminid watch (slightly enhanced contrast to increase the visibility of clouds). In such a case no correction factor > 1.0 is necessary because a large enough field is free of clouds.

- Date: be careful with the Local Time / UT conversion issue. This especially holds for the period when daylight saving time / summer time is applied. We recommend to use UT generally to avoid problems. (How long do you assume you remember which 'official' time was in use at a certain date?)
- Start/end: start and end of each interval.
- The IMO three-letter codes of the showers observed.
- Period (UT): report the start and end of the interval (in UT). Once filled the line, the form automatically offers the continuation. Needs to be modified in case of a break.
- Field: fill in the coordinates of the centre of your field of view with a accuracy of about 10°.
- T_{eff}, F, lm: fill in the quantities obtained during the interval analysis. F has the option to show the factor for cover percentages.
- M: observing method. Fill in 'C' for 'counting' if you 'counted' the meteors without plotting them onto charts or recording their sky coordinates. Use 'P' if you were plotting meteors, 'R' if you reported positions relative to the stars (see notes in section 3.4, page 85).
- N: number of shower meteors observed during the interval.

If there was more than one interval to your watch, fill in the data from the subsequent intervals in the subsequent lines. You may add more lines for further intervals.

For our session shown in Figure 2.5 we show some of the input steps. After the input of the location and date/start time (UT), we select the showers from a drop down menu (Figure 2.8).

The next step is the input of magnitude data. The standard is to give the magnitudes per shower and per interval. However, for many analyses we do not go into very short intervals and magnitude data can be merged for several intervals or for the entire session. This can also be handled different for an active shower and the other data. In our example we give the DRA data per interval (as it documents a peak) while we merge all other data into one distribution, except the sporadic data because the sample contains more than 20 meteors. So we first merge also SPO, but select then the splitting symbol, choose 2 intervals (which we identify with the data before and after the break). This appears as shown in Figure 2.12

Important Notes:

(1) If the number of meteors for the most active shower exceeds 20 for the whole observation, you should report a series of separate magnitude distributions, rather than the global one. If a high temporal resolution of an r-profile is required (e.g. close to an activity peak), we need to restrict to data which is given for short intervals. Otherwise, we smear out data defining possible variations. Therefore, it is better to provide magnitude data also for intervals similar to the count data (numbers per shower). The analysing procedures can easily accumulate data of intervals in a given step-size, while a later splitting is impossible. Do not worry if the number of shower meteors seems low per interval. A combination of data from many observers will allow reliable calculations.

(2) If the limiting magnitude of two adjacent intervals differs by more than 0.5 magnitudes, you should not incorporate the meteors seen into one magnitude distribution. In this case, it is more useful to report a separate magnitude distribution for each interval.

Reporting visual data using the on-line form on the IMO's internet page `http://www.imo.net/members/imo_observation/add_observation` soon after your session is of great interest: during the activity of major showers and in periods when unusual activity is expected, a live graph is produced on the IMO web page and allows you to follow the activity profile – including your own data – immediately.

Data can also be submitted using the 'CSV version' especially when the session has more than 35 meteors and/or in case of a slow internet connection.

You do not need to create an IMO account for all the observers when you submit visual reports for other observers.

We provide you with hints to add visual data to the VMDB here: `https://www.imo.net/members/imo_observation/add_observation`

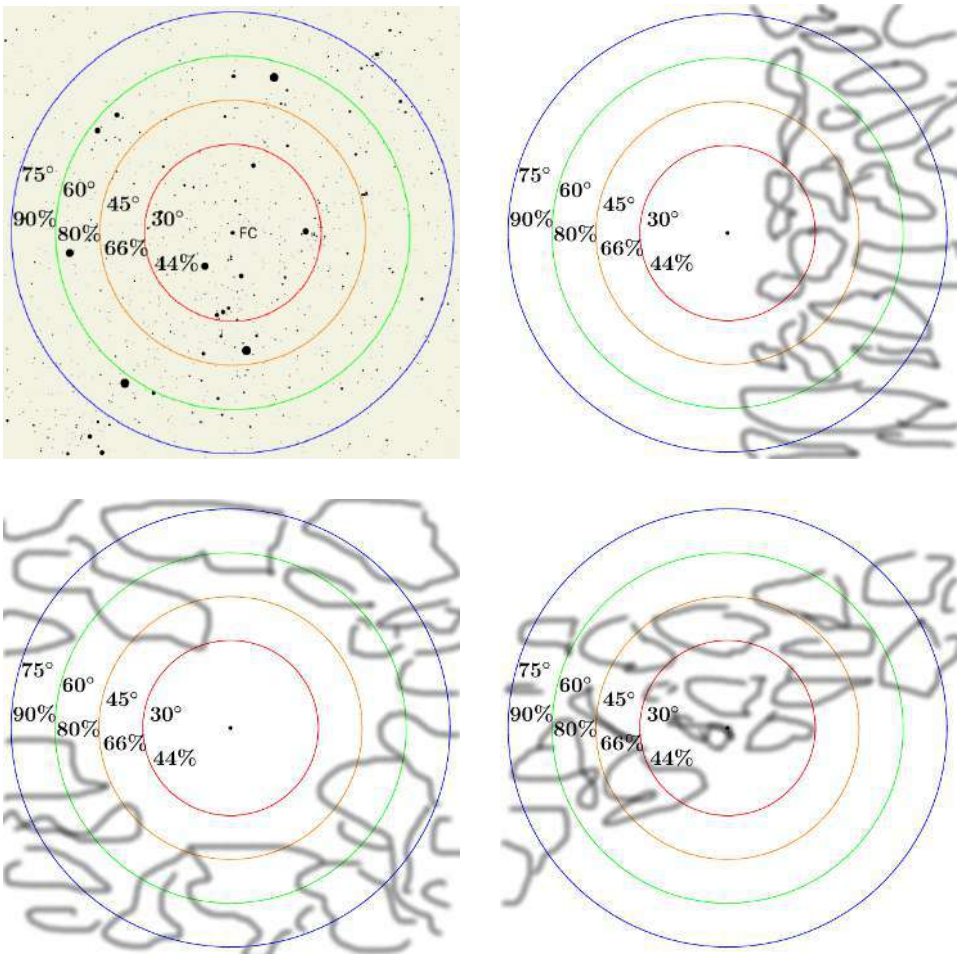


Figure 2.7: **Top left:** meteors in the field of view of a visual observer. (The background stars are shown as an example to illustrate the field size; FC – field centre.) 44% of the meteors are detected inside the central field within 30° diameter, a field with 45° diameter yields 66% of the meteors etc. (Numerical values from Koschack & Rendtel, 1990). **Top right:** In the case of clouds covering part of the sky, the factor will work well for a kind of incoming cloud front. **Bottom left:** a free field centre has relatively little effect as most meteors are probably seen. So continuing if the clouds have large enough 'holes' may be appropriate. **Bottom right:** clouds passing the central field will badly affect the result and an observation should be stopped.

2.7 Meteor shower peaks

The climax of observing a major shower is its maximum. During these times, the counting method is the only appropriate way to record the activity. As we have experienced during the Leonids 1998 to 2002, rates exceeding 500 observed meteors per hour are well within the limits of this method. If the meteor shower becomes so strong that you do not feel able to record all the data anymore, you should leave out some of the information per meteor. Details like colour and persistent train can be omitted first. The magnitude of the meteor should *not* be missed but it is sufficient to estimate whole magnitudes only. You can leave out indicating shower association and only qualify meteors which do not belong to the major shower by '*S*'. Attempts have also made to use handheld computers (Lüthen, 2001).

In case of high activity, the observation has to be broken up into intervals shorter than 1 hour. The interval length depends on the number of meteors seen. In order to study the small-scale structure of the stream, we need short intervals in the order of 5–10 minutes.

- Give time labels every 5 minutes in your observation record (it is necessary to be precise with the full minute timing – otherwise the lengths may vary between 4 and 6 minutes).
- Give the numbers of shower and non-shower meteors only.
- Magnitude distributions should not cover more than about 20 minutes.
- Estimate meteor brightnesses as integers.

2.8 Observation at storm level

2.8.1 Visual observations

With an increasing meteor rate, the main problem with trying to record the activity using the standard counting method is that the time available for recording the data

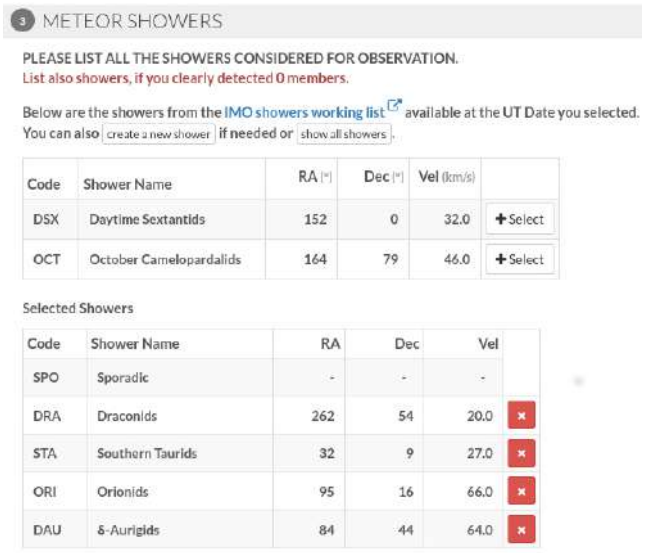


Figure 2.8: Shower selection: the showers of the IMO working list which are active are shown. Since the shower appears 3 days before and after the nominal period, we select just those we considered in our observation. The option to define a "new shower" is meant for unknown radiants (e.g. from the weekly shower news).

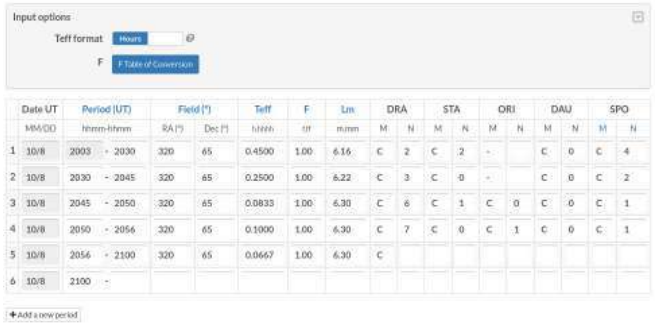


Figure 2.9: Next we type the interval count data. Since the ORI radiant was below or just at the horizon in the first two intervals, we change the method from 'C' to '–' and leave the number of shower meteors (N) column empty.

for each meteor is greatly reduced. As more meteors appear, information recording should be restricted to the most important data only. The most vital information about a visually observed meteor is its brightness. When activity is very high, determining shower association is much less important, as only a very small fraction of the meteors seen will not belong to the shower. To achieve maximum recording speed, you should just speak the magnitudes (estimated only to the nearest whole magnitude) onto tape. If there is an obvious sporadic then add this information. All other magnitudes can be assumed to belong to shower meteors. Do not forget to put enough time labels into your tape recording. Here, time labels should be given every 5 minutes or even every 2 minutes. The importance of having the magnitude for each meteor recorded cannot be stressed too much. Simple counts made without estimating the magnitudes are almost completely useless for analyses.

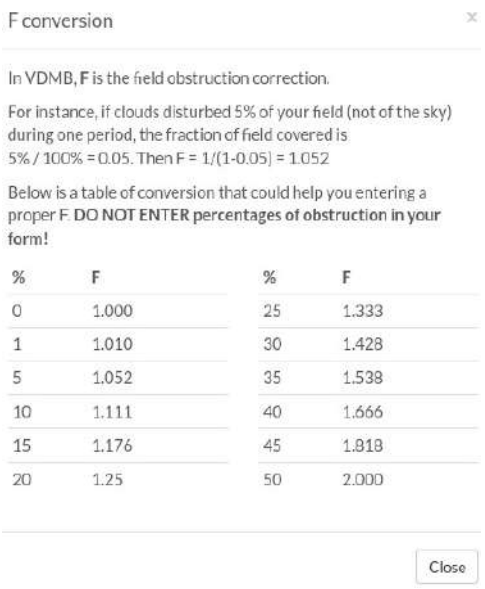


Figure 2.10: If you have just the percentage of field covered by clouds, you can get the F correction value from the drop down menu 'F Table of conversation'.



Figure 2.11: The input program offers a continuation of the session so that the end of one interval is the start of the next one. In case of a break you have to modify the start time of the respective interval.

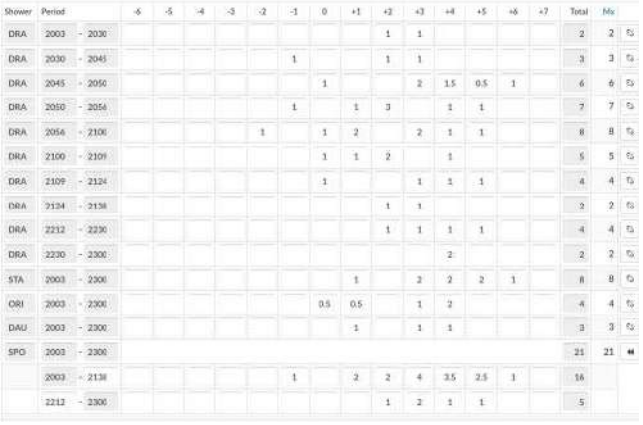


Figure 2.12: Input of magnitude data: DRA data for each interval, SPO for the period before/after the break and the others merged into one magnitude distribution for the entire session.

During the Leonid meteor storms, however, it has been proven that bursts up to a few meteors *per second* and continuous sequences of about 60 meteors per minute can be handled by the traditional recording methods. In any case it is important to note also changes in the observing method or recording scheme to allow analyses of the data.

As soon as possible after the event, you should report the complete record of your observation (i.e., the meteor list plus the time labels in between the meteors, start, end and break times, and information about clouds and limiting magnitude) to the VMDB input officer or – as far as possible – via the on-line form (comments). Also enclose a short report including any special circumstances, remarkable properties of the meteors (e.g. persistent trains), etc. Data of bright fireballs should be reported via the on-line fireball form.

2.8.2 Photographic observations

Details for the meteor photographer are given in Chapter 5. Here, we restrict to a few notes for the case of extraordinary high rates. The visual observing technique has the advantage of being able to analyse meteors down to magnitude +5 or +6. Thanks to this, the sample, that is the number of meteors the analysis is based on, is large, which in turn results in more accurate overall results, despite the generally subjective character of visual watching. Photography on film or with digital cameras, although a more objective technique, suffers due to its poor meteor limiting magnitude, which is roughly $+1^{\mathrm{m}}$ and its restricted field of view. Even during a 'normal' major shower maximum, rather few meteors are likely to be caught by a single camera. This sample is so small that it is difficult to easily analyse rates and magnitude distributions. For very high activity levels, however, this restriction is no longer valid. On a 3-minute film exposure taken during the great Leonid storm in 1966, some 40 meteor tracks were recorded, for instance! By contrast, the higher the activity, the less certain visual results become, since here there is a far greater chance of meteor data being incorrectly recorded, or meteors missed entirely. This means that for the monitoring of very high rates, video is clearly favoured.

However, such events are well suited for photography. Detailed information are given in Chapter 5. At this point we just briefly summarise a few hints:

35-mm SLR-cameras, medium format cameras (6 cm × 6 cm, 6 cm × 9 cm) or particularly digital SLR cameras are recommended. Using a wide-angle or fish-eye lens will increase the chance of catching bright meteors,

Black-and-white films of ISO 400–3200 are preferable. The sensitivity of a digital camera should be set to a high value (at least ISO 1600 for most sites). Note that the noise reduction of the camera needs to be deactivated, because it will require a dark exposure after each image.

The exposure times should be kept short. In the case of film, we recommend 5 minutes as a maximum (allowing about 3 hours of photography on one standard film). With digital cameras, 1 minute exposures are well suited for analyses and a "natural" appearance of meteors in the sky. In this case, the star trails are just $0\overset{\circ}{.}25$ long, quite precise positions are possible to measure even from unguided photographs, e.g. to determine radiant positions. However, the exposure times need to be recorded exactly. Hence the use of an automatic cable release with timer is highly recommended. Typically, camera batteries will allow to operate a digital camera for about three hours. So it is necessary to have replacement batteries at hand or to use a power-supply based adaptor (available for astronomy applications.

Table 2.3: Optimum elevation h of the field centre (camera with standard lens) depending on the radiant elevation h_{R}.

h_{R}	0°	20°	40°	60°	90°
h	90°	80°	70°	60°	45°

Do not change the camera direction if not necessary to keep the conditions constant. Point the camera field to the darkest region of the sky, but preferably not too far from the radiant. A true fish-eye camera should naturally be pointed close to the zenith. Optimum camera elevations are given in Table 2.3.

The analysis of the photographs to derive activity information requires a refined procedure. For each image (scanned or obtained with digital cameras), the following information should be available:

- date;
- start and end of the exposure in UT;
- approximate field centre (in α, δ);
- site (geographical coordinates);
- observer;
- focal length and effective speed of the lens;
- format of the negative or camera sensor;
- sensitivity setting.

2.8.3 Use of a video camera

Here, we refer to the specific chapter on video observations (Chapter 4). The great advantage of video recordings is the possibility of precise timing and the frame by frame analysis. Normal camcorders will of course have several limitations, but may yield interesting data of outbursts or meteor storms.

Use the largest aperture possible with your video camera lens. If it is a zoom lens, you will need to adjust it to a fairly wide angle. Once you have selected a 'zoom' setting, do not change it during the course of the observations. Set the focus to 'manual' at infinity, as some types of automatic focus mechanisms will not operate properly when aimed at a dark sky. For most purposes, you should not use the electronic shutter available on CCD video cameras since the unit's sensitivity will be further impaired. Some observers may,

however, want to use this feature to specifically look for meteor trains—in this case be sure to note the electronic shutter speed used (e.g., 1/1000 s).

Turn the time display to 'on' and set it to the shortest time increment possible. Synchronise your video clock time to a standard time signal. If no video time signal is possible with your camera, briefly blank the picture (by covering the lens) at several separately recorded times. Recording a short-wave radio time signal on the audio track of the video recording offers another timing option (or more simply, use a microphone to place time markers on the audio track according to the time indicated on an accurately calibrated clock).

Unless a clock-driven equatorial mount is available, use a firm tripod with a fixed direction. Select an observing direction in the same way as suggested for photographic work, but adjust it as necessary to make sure that a minimum of 3 stars is visible in your field of view.

It will assist with photometric corrections if, at the beginning or end of your observing period, you record several minutes with the same camera settings but with the camera skewed at angular rates which roughly correspond to that of the expected shower. Identify the stars used in the test.

The analysis of the tape can be done with the MetRec software described in Chapter 4. Hints for the analysis can be obtained from the Video Commission Director.

2.9 Fireball observations

2.9.1 Important data

A bright fireball is an impressive event. Even well-trained observers may be overwhelmed so much by the appearance that they forget what data to record; the impression dominates and data can remain uncertain. Of course, it is impossible to do fireball-observing exercises, as the objects are totally unpredictable in appearance and are also relatively uncommon. In the case of bright meteors, one tends to note more information than usual, so it is useful to have a standard way of recording fireball data, and to know which data are important to note down.

Immediately after the fireball's appearance you should look at a watch or clock of any sort to **determine the time**, preferably to an accuracy of one second. Later, this watch or clock should be compared with an official time signal. In some regions, special time signal transmitters exist (e.g. in Western Europe there is the DCF-77 transmitter on 77.5 kHz). Radio controlled clocks and wrist-watches are widely available. Also the satellites of the Global Positioning System (GPS) give the exact time worldwide on a GPS-receiver.

Next, the **apparent path** determined by the first and last sightings of the trail should be immediately recorded, before the exact data begin to fade in your memory. If you store your observational data on tape, or if you witness a fireball when not carrying out a meteor watch, you should note at least 3 prominent points of its trail. Positions can be given relative to background stars but also relative to terrestrial reference points. In the latter case, the exact own position needs to be recorded, too, for later calculation of coordinates.

Only then should you note **additional data** such as fragmentation, colour, apparent velocity, flares and any sounds. Lastly, note the apparent magnitude, as this information can usually be remembered best. The certainty of the magnitude is likely to be lower in the case of very bright fireballs, those which are brighter than the quarter moon (about -9 mag or -10 mag). You may use comparisons where these are helpful, such as 'brighter than the full moon', or intervals (e.g., between -11 and -14 mag). If possible, you should note any magnitude variations (the light curve) too.

Reports of fireball observations are collected by the IMO. On our web page you find a form (in many languages) to submit data of your sighting. Quite soon after your report has been processed you will see whether there were further reports which allow to calculate a trajectory.

2.9.2 Meteor sound

Meteor sounds are noticed only on rare occasions, but they are important. The *'regular' sounds* are audible only after a few minutes have elapsed since the optical observation, as sound travels through air far slower than light. While recording the data described above, you should be listening for these sounds. Meteor noises can reach the surface from any point of the trajectory lower than about 60 km and may consist of bangs or swishing sounds, or possibly other noises.

Meteoroids move through the atmosphere at multiples of the sound speed. Hence the supersonic pressure wave generated along the trajectory effectively has the form of a cylinder with the wave expanding vertical to the meteoroid motion (see, e.g. Ens et al., 2012; Silber, 2018). In case of fragmentations, additional pressure waves are generated, which as a rough approximation can be considered as point-like explosions with additional roughly radially expanding pressure waves (responsible for noises like bangs or gunfire). Depending on the position of an observer relative to the trajectory, the noises can arrive at the location in various sequence. Depending on the size of the entering meteoroid, the effects of the overpressure can cause severe damages particularly to light and large structures. In the case of the Chelyabinsk super bolide this caused several thousand injuries mainly due to braking glass (Brown, 2013; Popova, 2013). If a bright fireball occurs, it may be a good idea to go outside a building. Not only to avoid pressure caused effects, but also to have the chance to witness further details related to the possible meteorite fall(s). For example, the observation of a witness led to the find of the small Salzwedel (Hohenlangenbeck, Germany) meteorite in November 1975.

However, there may also be noises heard *simultaneously* with the meteor's optical appearance. These are certainly not hallucinations! A compilation has been

published by Keay (1994b) as part of the WGN Report Series. Such anomalous sounds appear to propagate via very low frequency (VLF) radio-waves, and seem to be generated especially in the upper part of the trajectory. These waves, of course, propagate with the velocity of light and, if there are dielectric media near the surface, such as massive objects or atmospheric electrical activity, they can then be converted into sound waves (Ceplecha et al., 2004; Keay, 1994a; Keay & Ceplecha, 1994). Meteor sounds may usually be expected if a fireball is brighter than -8^{m} (visual). It is essential to identify and exclude other possible sources for supposed meteor noises, for example, motors, airplanes, other technical sources, or animals. In 2000, the Global Electrophonic Fireball Survey, GEFS, was initiated to systematically investigate all reports of simultaneous meteor sounds in a standard way (Vinković, 2000). Vinković (2002) has more details, some first results, and all the essential earlier references.

Photographic fireball networks provide useful information, but even here visual data are also necessary. Only a few photographic stations operate a pair of guided / unguided cameras or have an electronic time registration (Bland et al., 2006; Spurný et al., 2007), and exact timings are vital for further calculations. Furthermore, a photograph gives little or no information about the real colour, persistent train or sounds, and fragmentation data are difficult to derive from a still picture.

2.9.3 Meteor trains

The collision of the meteoroid with atmospheric particles causes ablation, and thereby ionisation, of both atmospheric and meteoroid constituents. While most of these excited states exist for about 10^{-8} seconds only, there are also some atomic states which may persist for times exceeding several seconds (metastable levels). The emissions from such levels may be visible for variable amounts of time, and are designated as persistent trains. They appear bright in the night sky after the meteor itself has disappeared.

The old (1961) IAU definition of 'train' concerned *anything (such as light or ionisation) left along the trajectory of the meteor after the head of the meteor has passed.* In principle, the formation of a meteor train depends on the mass, velocity, and composition of the meteoroid, on the status of the atmosphere (diurnal changes and solar activity influences), and on the height of the deposition of meteoritic energy and mass. Therefore several types of trains may or may not occur. Borovička (2006) described *four different types.*

1. Wake means a luminosity just behind the meteor head and moves with the meteor and forms a kind of tail. This is often present in bright fireballs. The length can exceed 1 km. It is strongest above 55 km and its duration is usually less than 0.1 s.

The spectrum consists mainly of low excitation lines (not in thermal equilibrium) and the gas responsible for the wake radiation comes from the meteor head (ablation of dust particles from the meteoroid).

2. Green trains are short-duration (maximum 3 s) trains exclusively formed by the green oxygen line at 557.7 nm (Borovička, 2006) which is typical for high-velocity meteors of medium and low brightness. It can be seen visually for 1–2 seconds after the disappearance of the meteor (though the colour is hard to recognise).

Their maximum brightness and duration occurs near 105 km, and their brightness is not correlated with the meteor ablation rate. The green line is a forbidden line; the upper (excited) level is metastable with a radiative lifetime of 0.75 s.

3. Persistent trains are self-luminous and can be visible for tens of minutes after the meteor. They are produced only by bright high-velocity fireballs. They always form in the region of maximum meteor brightness. Hence, their luminosity is driven by the energy and material deposited by the meteoroid. Three distinct phases have been identified by Borovička & Koten (2003) called the afterglow, recombination and continuum phases.

4. Reflection trains (dust trains) are somewhat similar in appearance to persistent trains. They can be formed by the explosion of bright bolides in the atmosphere. These trains are not self-luminous and hence visible only in daylight or twilight. They represent dust particles left in the train after the meteoroid disruption and can remain visible for hours.

Besides allowing a direct comparison with photographic data or even adding to them, visual recordings indicate the existence of a complex picture of fireball appearances and rates as was described above. Observations of fireballs of at least apparent magnitude -3 mag or zenithal magnitude -4 mag should be sent as soon as possible on a fireball report form to the person responsible for collecting data for the VMDB in your area or submit it on-line to the IMO's web page using `http://www.imo.net/fireball/report`

Here are some guidelines concerning filling in the forms:

- Date, Time: Use UT (UTC/GMT) only; please pay attention to the date—remember it changes at midnight.
- Location of observation, geographic coordinates: Name of the location in the original language, adding state, country, district or similar information later. Be as precise as possible with geographic coordinates.
- Path, coordinates of first/last sighting: Note right ascension α (in degrees) and declination δ of first and last point.
- Magnitude: If possible, give the apparent magnitude, or, if not known exactly, a magnitude interval (e.g., -5 to -8 mag).
- Duration: Give the estimated or measured duration of the luminous flight in seconds.
- Colour: Give the colour seen and any variations, referring preferably to pure colours, not, for exam-

ple, 'bluish' or 'bluish-green' (use 'blue' or 'blue and green' instead).

- Trains: Note appearance and, if known, colour and shape (see the different types explained above).
- Fragmentation: Give the number of fragments, their brightness, colour and position on the trajectory. Note also any sparks in this section.
- Persistent train: Note the duration, colour, shape and any variations.
- Angular velocity: Note this in degrees per second, or using the appropriate scale number: 0 = stationary, 1 = very slow, 2 = slow, 3 = medium, 4 = fast, 5 = very fast.
- Sounds: Describe the sounds (compare with supersonic sounds, like an avalanche, swishing, whistling, etc.) and the time between the optical and audible observations.
- Observer: Name and, if possible, postal or e-mail address, in case there are any queries about the report.
- Source, reviewer: This should be given if observations of other people are reported or the information about the fireball is from local astronomical or other journals. Note the address of the reviewer to allow queries.

2.10 Telescopic Observations

The telescopic observer sees meteors fainter than those recorded by the unaided eye, and can plot meteor paths more accurately. These in turn opened up new areas of research. Generally when one observes a telescopic meteor it is the result of a meteoroid of extremely low mass burning up in the upper atmosphere: the mass may be several orders of magnitude less than meteoroids which cause naked-eye meteors. Most are the result of micrometeoroids with masses in the range 10^{-4} to 10^{-10} kg. They are exceedingly numerous. They make up the bulk of the meteor particles entering Earth's atmosphere. For example, the hourly rate of magnitude +9 meteors is about 10 000. The majority of telescopic meteors are sporadic. This is even true during the activity period of major showers. The prominent visual showers have relatively fewer meteors than the sporadics progressively to fainter magnitudes. It is only by studying interplanetary debris over a wide range of the mass spectrum, that we learn the physics of meteoroid streams. Thus photographic, visual, video, radio/radar, and telescopic observations of meteors are complementary.

Telescopic plotting has a few advantages over the visual (wide field) observation. First of all, if there were no other factors, magnification reduces the displacement *pro rata*. So for a typical magnification of 10× would pinpoint the meteor trail to about ±20 arcminutes. However, there's more. A typical viewing diameter for a visual observer is at least 100°. Contrast that with 55° for the telescopic observer with a wide-field eyepiece. That's only 30% of the area. So a higher proportion of meteors are seen directly rather than with averted vision. This markedly improves the plotting errors. Exactly how much is debatable, but a factor of two is certainly not out of the question. This leads to a typical displacement at the radiant of about a degree. It then becomes possible to detect weak minor showers, because pollution by sporadic meteors is reduced. Also probing shower radiants for substructure and measuring radiant motion become feasible.

However, the technical evolution particularly of the video technique over the last decade has completely replaced the visual telescopic observations. To access fainter magnitude meteors as with the visual telescopic observations, it would be a good idea to mount a sensitive video camera to a lens with longer focal length (see page 91).

2.11 VMDB – the Visual Meteor Database

Currently, the IMO's VMDB contains data of more than 4,000,000 meteors obtained by using standardised observing methods which were collected during the last ≈ 40 years. Since the visual data may provide us with information about the long-term behaviour of meteor showers, we encourage observers as well as readers of "old" papers with respective data to submit these to the VMDB. Certainly, we cannot completely establish reports according to our current standard. But within some error margins we may derive rates from observations made before the standards have been defined. If you are uncertain, you may contact the Visual Commission Director.

Extracts of the VMDB can be downloaded from `http://www.imo.net/members/imo_vmdb`.
We encourage interested people to use the data for own analyses and studies. An example of a Perseid analysis was subject of a workshop associated to the 2018 International Meteor Conference (IMC) in Pezinok-Modra, Slovakia. The Perseid analysis with many details is published in Rendtel et al. (2019); general advise and procedure description for a software package can be found in the IMC 2018 Proceedings (Velkovic et al., 2019).

For the input of visual meteor data
please use the on-line form at
`http://www.imo.net/members/imo_observation/add_observation`

2.12 The IMO Meteor Shower Working List

Details for meteor showers including historic events and past activity are given in the *Meteor Shower Workbook* published by the IMO. On page 58 we provide the list as of January 2022 to complete the information for the visual observations required to fill in the report form and also as a reference for the minor shower observing aspects described in the following Chapter.

References

Arlt R., 1999: New limiting magnitude tables. *WGN* **27,** 6–18.

Bland P.A., Spurný P., Bevan A.W.R., Towner M.C., McClafferty T., Deacon G., 2006: First Light for the Desert Fireball Network. *MAPS* **41,** 5197.

Borovička J., 2006: Meteor trains—terminology and physical interpretation. *J.Royal Astr. Soc. Canada* **100,** 194–198.

Borovička J., Koten P., 2003: Three phases in the evolution of Leonid meteor trains. In: *H. Yano, S. Abe, M. Yoshikawa (eds.): Proceedings of the 2002 International Science Symposium on the Leonid Meteor Storms*, Inst. Space Astronaut. Sci., Sagamihara, Japan. ISAS Report SP 15, pp. 165–173.

Borovička J., Spurný P., Brown P., Wiegert P., Kalenda P., Clark D., Shrbený L., 2013: The trajectory, structure and origin of the Chelyabinsk asteroidal impactor. *Nature* **503,** Issue 7475, 235–237..

Bjorkman J., 1973: Meteors and Meteorites in the Ancient Near East. *Meteoritics* **8,** 89–130.

Brown P. (and 32 co-authors), 2013: A 500-kiloton airburst over Chelyabinsk and an enhanced hazard from small impactors. *Nature* **503,** Issue 7475, 238–241.

Ceplecha Z., Borovička J., Elford W.G., ReVelle D.O., Hawkes R.L., Porubčan V., Šimek M., 2004: Meteor phenomena and bodies. *Space Sci. Rev.* **84,** 327–471.

Ens T.A., Brown P.G., Edwards W.N., Silber E.A., 2012: Infrasound production by bolides: A global statistical study. *JATP* **80,** 208–229..

Keay C.S.L., 1994a: Audible fireballs and geophysical electrophonics. *Proc. Astr. Soc. Australia* **11,** 12–15.

Keay C., 1994b: Electrophonic sounds catalog. *WGN Report Series* **6,** 151–172.

Keay C.S.L., Ceplecha Z., 1994: Rate of observation of electrophonic meteor fireballs. *J. Geophys. Res.* **99,** 13163–13165.

Koschack R., Rendtel J., 1990: Determination of spatial number density and mass index from visual meteor observations (I). *WGN* **18,** 44–58.

Lüthen H., 2001: Counting meteors using a handheld computer. *WGN* **29,** 218–223.

Nikolić V., Schröder L., Tešić A., 2018: Cloudiness estimation for video meteor observations. In: *Gyssens M. and Rault J.-L. (eds.) Proceedings of the IMC Petnica, Serbia, 2017*, 228–230.

Popova O.P., Jenniskens P., Emel´yanenko V., and 56 more authors (the Chelyabinsk Airburst Consortium), 2013: Chelyabinsk airburst, damage assessment, meteorite recovery, and characterization. *Science* **342,** 1069–1073.

Rendtel J., Velkovic K., Weiland T., Verbeeck C., Knöfel A., 2019: Perseids 2018 – Analysis of global visual data. *WGN* **47,** 18–25..

Silber E.A., 2018: Infrasound observations of bright meteors: the fundamentals. *WGN* **46,** 52–61..

Spurný P., Borovička J., Shrbený L., 2007: Automation of the Czech part of the European fireball network: equipment, methods and first results. In: *G.B. Valsecchi and D. Vokrouhlický (eds.): Near Earth Objects, our Celestial Neighbors: Opportunity and Risk,* Proc. IAU Symposium 236. Cambridge: Cambr. Univ. Press, pp. 121–130.

Velkovic K., Rendtel J., Verbeeck C., Weiland T., Knöfel A., 2019: Tricks of the trade: global analysis of visual meteor observations using VMDB and MetFns – an example. In: *R. Rudawska, J. Rendtel, C. Powell, R. Lunsford, C. Verbeeck, A. Knöfel (eds.): Proceedings of the International Meteor Conference Pezinok-Modra, Slovakia, 2018*, pp. 57–63.

Vinković D., Andreić Z., Garaj S., Kovacić D., Mladinov M., Zgrablić G., 2000: Global Electrophonic Fireball Survey. *WGN* **28,** 48–53.

Vinković D., Garaj S., Lim P.L., Kovavić D., Zgrablić G., Andreić V.Z., 2002: Global Electrophonic Fireball Survey: a Review of Witness Reports – I. *WGN* **30,** 244-257.

Vogel R., Siebert F., 2001: Conformations of the active and inactive states of opsin. *J. Biological Chemistry* **276,** 38487–38493.

Zhuang T.-S., 1977: Ancient Chinese records of meteor showers. *Chinese Astronomy* **1,** 197–220.

2.13 Tables and charts

On the following pages you find

- the IMO meteor shower working list (page 58)
- the fields for the determination of the limiting magnitude (page 59)
- the conversion tables for the limiting magnitude (page 59)
- Atlas Brno charts with the lm-fields (page 60)

Table 2.4: IMO meteor shower working list. After the shower designation we add the IAU code, the start, end and (average) maximum dates, the solar longitude of the maximum, the radiant at the maximum date, the atmospheric entry velocity and the average population index. Note that a certain solar longitude may correspond to different dates due to the leap year changes. The radiant of the Antihelion Source is an extended area about 12°east of the solar opposition point (size roughly 30° in right ascension and 15° in declination). It has no IAU code as it is a collective description of numerous minor showers near the ecliptic. The list is subject of permanent updates depending on incoming data.

Shower	Activity	Maximum		Radiant		v_∞	r	ZHR
		Date	$\lambda_\odot$	α	δ	km/s		
Antihelion Source (ANT)	Dec 10–Sep 10	March–April,	see caption			30	3.0	4
	–	late May, late June						
Quadrantids (010 QUA)	Dec 28–Jan 12	Jan 03	283.°15	230°	+49°	41	2.1	110
γ-Ursae Minorids (404 GUM)	Jan 10–Jan 22	Jan 19	298°	228°	+67°	31	3.0	3
α-Centaurids (102 ACE)	Jan 31–Feb 20	Feb 08	319.°2	210°	−59°	58	2.0	6
γ-Normids (118 GNO)	Feb 25–Mar 28	Mar 14	354°	239°	−50°	56	2.4	6
Lyrids (006 LYR)	Apr 14–Apr 30	Apr 22	32.°32	271°	+34°	49	2.1	18
π-Puppids (137 PPU)	Apr 15–Apr 28	Apr 23	33.°5	110°	−45°	18	2.0	Var
η-Aquariids (031 ETA)	Apr 19–May 28	May 05	45.°5	338°	−01°	66	2.4	50
η-Lyrids (145 ELY)	May 03–May 14	May 08	48.°0	287°	+44°	43	3.0	3
Dayt. Arietids (171 ARI)	May 14–Jun 24	Jun 07	76.°6	44°	+24°	38	2.8	30
June Bootids (170 JBO)	Jun 22–Jul 02	Jun 27	95.°7	224°	+48°	18	2.2	Var
Piscis Austr. (183 PAU)	Jul 15–Aug 10	Jul 29	125°	341°	−30°	35	3.2	5
S. δ-Aquariids (005 SDA)	Jul 12–Aug 23	Jul 30	127°	340°	−16°	41	2.5	25
α-Capricornids (001 CAP)	Jul 03–Aug 15	Jul 30	127°	307°	−10°	23	2.5	5
July Pegasids (175 JPE)	Jul 04–Jul 09	Jul 14	107.°5	340°	+15°	61	3.0	5
Perseids (007 PER)	Jul 17–Aug 24	Aug 12	140.°0	48°	+58°	59	2.2	100
July γ-Draconids (184 GDR)	Jul 25–Jul 28	Jul 31	125.°3	280°	+51°	27	3.0	5
κ-Cygnids (012 KCG)	Aug 03–Aug 25	Aug 17	145°	286°	+59°	25	3.0	3
Aurigids (206 AUR)	Aug 28–Sep 05	Sep 01	158.°6	91°	+39°	66	2.5	6
Sep. ε-Perseids (208 SPE)	Sep 05–Sep 21	Sep 09	166.°7	48°	+40°	64	3.0	5
Dayt. Sextantids (221 DSX)	Sep 09–Oct 09	Sep 27	184.°3	152°	+00°	32	2.5	5
Oct. Camelopardalids (281 OCT)	Oct 05–Oct 06	Oct 05	192.°58	164°	+79°	47	2.5	5
Oct. Draconids (009 DRA)	Oct 06–Oct 10	Oct 08	195.°4	262°	+54°	20	2.6	10
S. Taurids (002 STA)	Sep 10–Nov 20	Oct 10	197°	32°	+09°	27	2.3	5
δ-Aurigids (224 DAU)	Oct 10–Oct 18	Oct 11	198°	84°	+44°	64	3.0	2
ε-Geminids (023 EGE)	Oct 14–Oct 27	Oct 18	205°	102°	+27°	70	3.0	3
Orionids (008 ORI)	Oct 02–Nov 07	Oct 21	208°	95°	+16°	66	2.5	20
Leonis Minorids (022 LMI)	Oct 19–Oct 27	Oct 24	211°	162°	+37°	62	3.0	2
N. Taurids (017 NTA)	Oct 20–Dec 10	Nov 12	230°	58°	+22°	29	2.3	5
Leonids (013 LEO)	Nov 06–Nov 30	Nov 17	235.°27	152°	+22°	71	2.5	10
α-Monocerotids (246 AMO)	Nov 15–Nov 25	Nov 21	239.°32	117°	+01°	65	2.4	Var
Nov. Orionids (250 NOO)	Nov 13–Dec 06	Nov 28	246°	91°	+16°	44	3.0	3
Phoenicids (254 PHO)	Nov 28–Dec 09	Dec 02	250.°0	18°	−53°	18	2.8	Var
Puppid-Velids (301 PUP)	Dec 01–Dec 15	(Dec 07)	(255°)	123°	−45°	40	2.9	10
Monocerotids (019 MON)	Dec 05–Dec 20	Dec 09	257°	100°	+08°	41	3.0	3
σ-Hydrids (016 HYD)	Dec 03–Dec 20	Dec 09	257°	125°	+02°	58	3.0	7
Geminids (004 GEM)	Dec 04–Dec 20	Dec 14	262.°2	112°	+33°	35	2.6	150
Comae Berenicids (020 COM)	Dec 12–Dec 23	Dec 16	264°	175°	+18°	65	3.0	3
Dec. Leonis Minorids (032 DLM)	Dec 05–Feb 04	Dec 19	268°	161°	+30°	64	3.0	5
Ursids (015 URS)	Dec 17–Dec 26	Dec 22	270.°7	217°	+76°	33	3.0	10

Table 2.5: Corner stars of the fields for the determination of the limiting magnitude. The fields are marked in the charts shown at the following pages.

Field	Corner stars		
1	χ Dra – ζ Dra – δ Dra – ξ Dra	16	α CVn – ε UMa – η UMa
2	β Per – δ Per – ζ Per	17	ε Aur – ϑ Aur – δ Aur
3	23 UMa – ϑ UMa – β UMa	18	μ And – γ And – φ And
4	α Gem – ε Gem – β Gem	19	κ Dra – α Dra – β UMi
5	ζ Aql – γ Aql – δ Aql	20	42 Cam – β Cam – γ Cam
6	α And – γ Peg – α Peg	21	α PsA – 98 Aqr – δ Aqr
7	α Cep – β Cep – δ Cep	22	β Lep – β Ori – 53 Eri
8	α Tau – β Tau – ζ Tau	23	δ Crv – γ Crv – ε Crv – β Crv
9	α Leo – β Leo – γ Leo – δ Leo	24	β Lib – γ Lib – σ Lib – α Lib
10	α Vir – ζ Vir – γ Vir	25	α Sco – ε Sco – χ Lup
11	α CrB – γ Boo – α Boo	26	γ TrA – α TrA – η Ara – α Cen
12	α Ser – β Lib – δ Oph	27	β Cen – α Cru – γ Cru
13	β Lyr – ζ Lyr – ϑ Her – ν Her	28	β Car – ε Car – ι Car
14	ε Cyg – η Cyg – γ Cyg	29	γ Hyd – α Hyd – β Hyd
15	β Dra – τ Her – π Her	30	α Tuc – α Pav – ε Pav

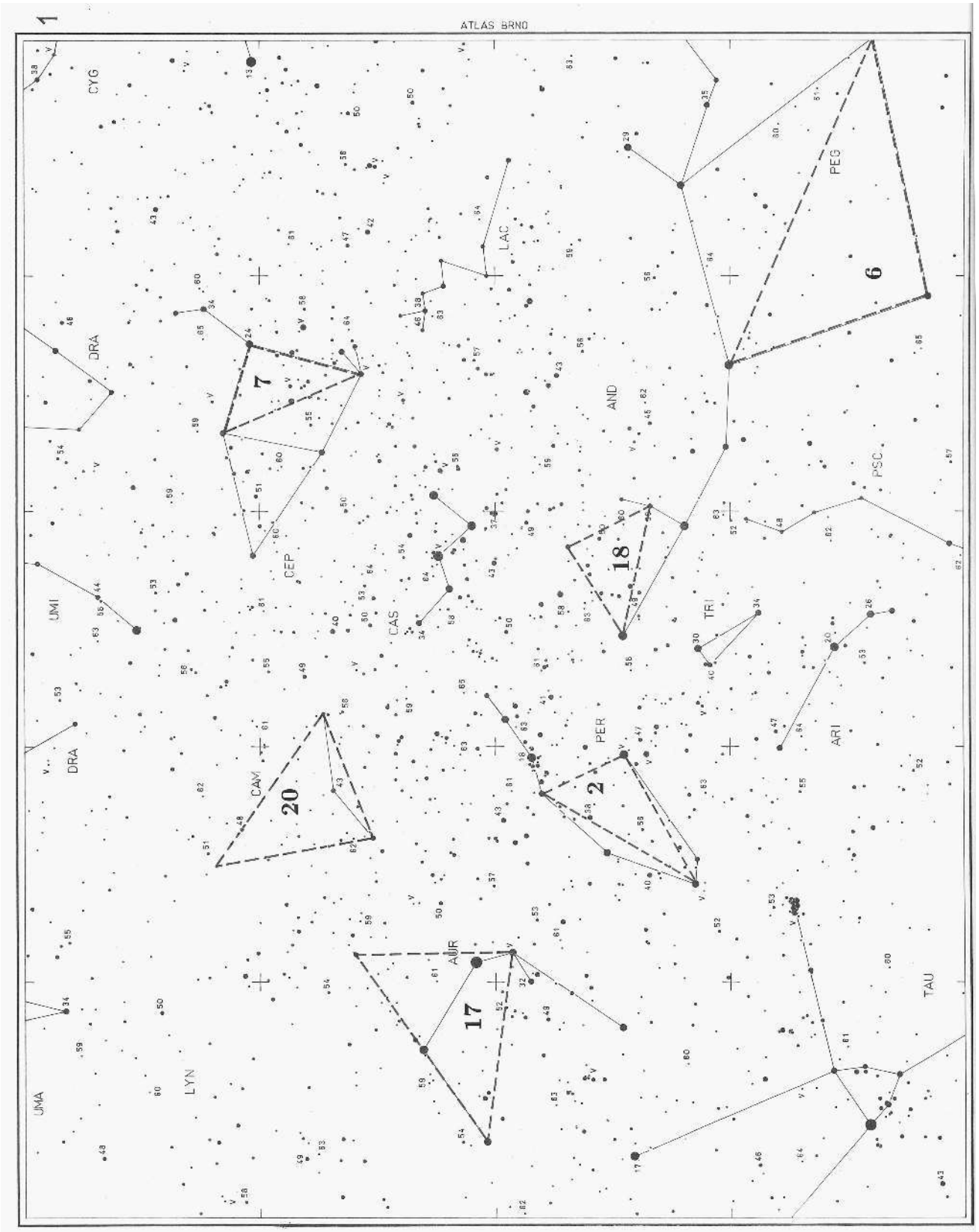
Table 2.6: The number of stars seen in one of the star fields (given in Table 2.5) including the corner stars correspond to a limiting magnitude (lm) listed below. If you encounter gaps of more than $0^{\mathrm{m}}.3$ between two rows, use this magnitude value only if you do not have another estimate for the same period. The complete list extending to brighter and fainter values of lm can be found on the IMO's web page or in Arlt (1999).

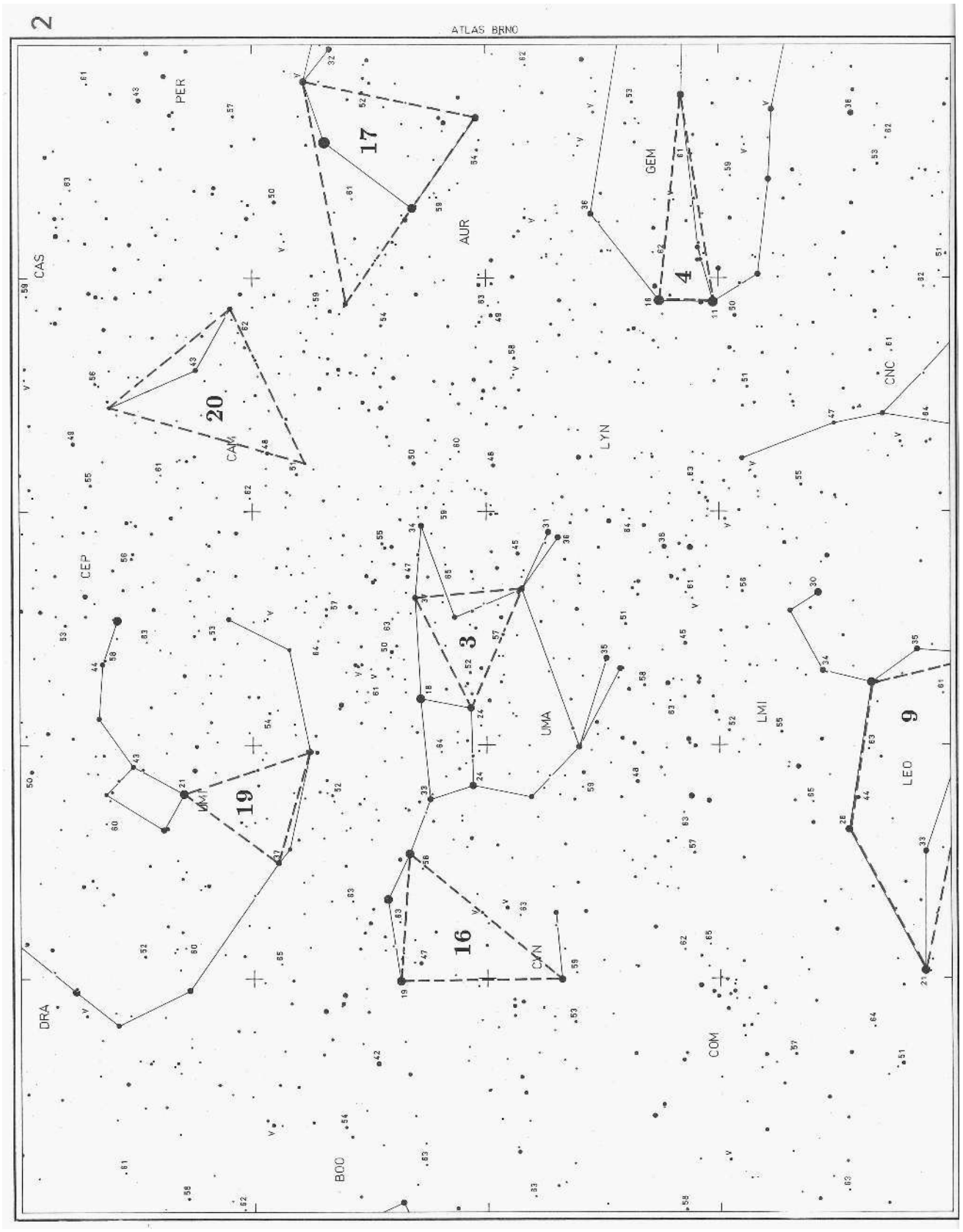
N	1 (Dra) lm	2 (Per) lm	3 (UMa) lm	4 (Gem) lm	5 (Aql) lm	6 (Peg) lm	7 (Cep) lm	8 (Tau) lm	9 (Leo) lm	10 (Vir) lm	N
4	3.74	3.78	3.78	3.79	4.45	4.66	4.23	4.62	2.56	4.39	4
5	4.23	4.95	4.48	5.01	5.16	5.08	4.79	4.88	3.33	5.77	5
6	4.78	5.15	4.56	5.07	5.30	5.49	5.12	4.95	4.41	5.80	6
7	4.83	5.55	4.83	5.34	5.53	5.56	5.17	5.09	4.78	5.86	7
8	5.00	5.60	5.13	5.75	5.98	5.80	5.26	5.29	5.42	5.92	8
9	5.08	5.79	5.16	5.76	6.02	6.13	5.29	5.43	5.44	5.97	9
10	5.25	5.80	5.49	5.78	6.31	6.14	5.36	5.51	5.48	5.99	10
11	5.96	5.98	5.66	6.20	6.36	6.17	5.42	5.73	5.50	6.12	11
12	6.06	6.01	5.72	6.37	6.71	6.25	5.73	5.84	5.58	6.41	12
13	6.28	6.07	5.79	6.47	6.72	6.25	5.95	6.10	5.73	6.44	13
14	6.42	6.40	5.97	6.54	6.77	6.26	5.96	6.19	5.92	6.63	14
15	6.50	6.41	6.19	6.67	6.80	6.29	6.00	6.27	6.14	6.64	15
16	6.60	6.45	6.30	6.76	6.90	6.44	6.14	6.29	6.17	6.65	16
17	6.63	6.50	6.35	6.80	6.91	6.47	6.19	6.36	6.27	6.69	17
18	6.65	6.51	6.41	6.99	6.96	6.50	6.23	6.50	6.27	6.83	18
19	6.66	6.54	6.49	7.00	7.00	6.50	6.44	6.55	6.31	6.90	19
20	6.68	6.60	6.49	7.02	7.05	6.57	6.47	6.71	6.40	7.04	20
21	6.68	6.61	6.54	7.10	7.06	6.59	6.48	6.76	6.43	7.06	21
22	6.70	6.66	6.59	7.12	7.07	6.59	6.63	6.77	6.52	7.08	22
23	6.79	6.72	6.72	7.17	7.09	6.60	6.69	6.87	6.61	7.16	23
24	6.86	6.73	6.77	7.22	7.10	6.60	6.70	6.88	6.64	7.19	24
25	6.86	6.75	6.83	7.43	7.11	6.67	6.71	6.95	6.78	7.20	25
26	6.86	6.78	6.85	7.45	7.27	6.68	6.72	7.15	6.81	7.24	26
27	6.86	6.85	6.99	7.46	7.28	6.68	6.84	7.17	6.84	7.25	27
28	6.87	6.89	7.01	7.46	7.38	6.69	6.88	7.19	6.85	7.25	28
29	6.89	6.90	7.06	7.47	7.39	6.72	6.92	7.21	6.95	7.32	29
30	6.92	7.02	7.12		7.40	6.73	6.93	7.30	7.00	7.33	30

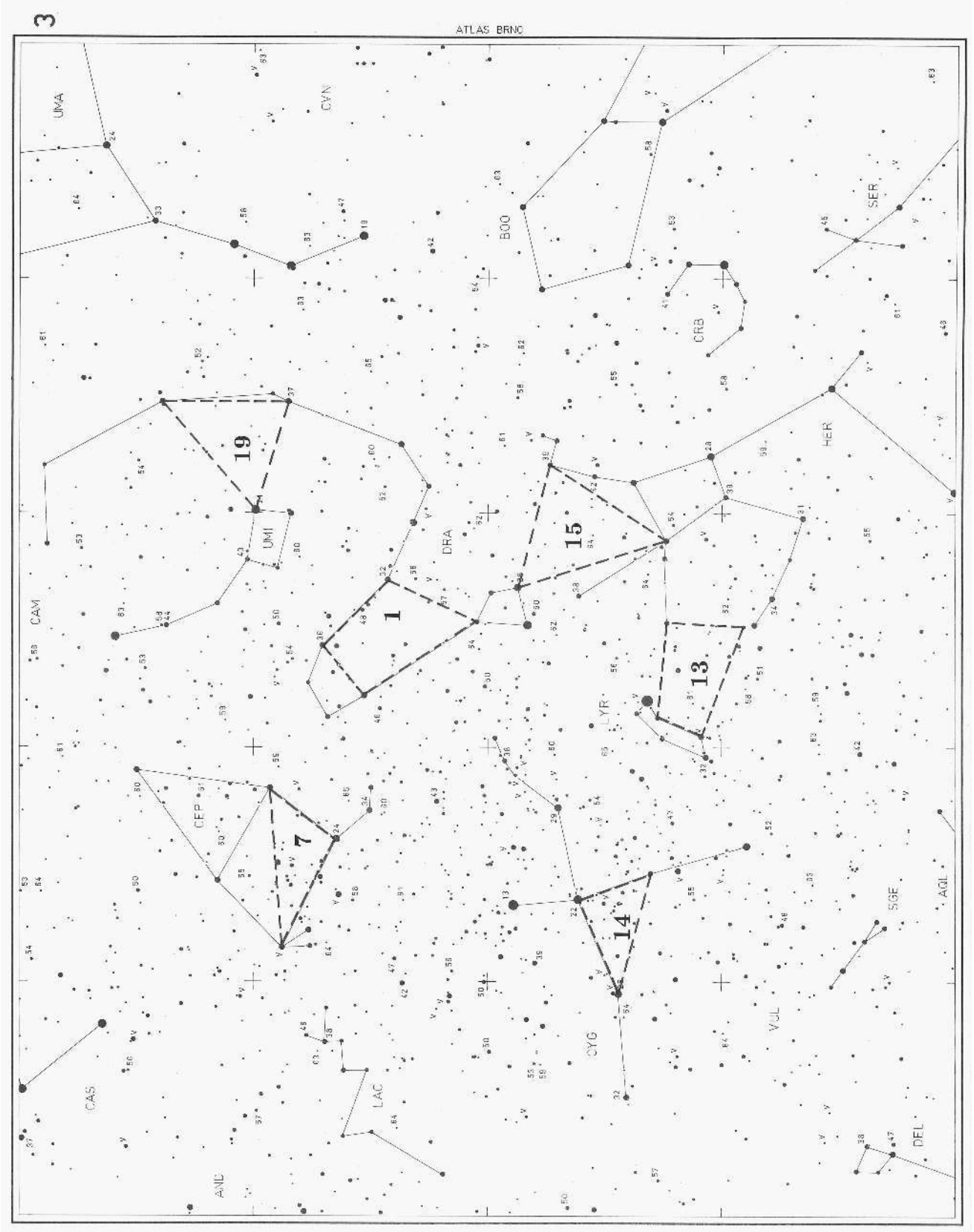
N	11 (Boo) lm	12 (Ser) lm	13 (Lyr) lm	14 (Cyg) lm	15 (Her) lm	16 (CVn) lm	17 (Aur) lm	18 (And) lm	19 (UMi) lm	20 (Cam) lm	N
4	3.04	3.55	4.34	4.65	4.82	4.67	3.03	4.26	5.19	4.77	4
5	3.57	5.10	4.41	4.73	5.07	5.15	3.73	4.83	5.50	5.14	5
6	4.47	5.23	4.98	4.79	5.50	5.64	3.97	4.87	5.81	5.44	6
7	4.51	5.39	5.42	4.94	5.67	5.79	4.33	4.96	6.20	5.47	7
8	4.79	5.39	5.49	5.06	5.82	5.85	4.52	5.01	6.33	5.62	8
9	4.81	5.51	5.56	5.39	5.92	5.88	5.21	5.04	6.40	5.63	9
10	4.93	5.53	5.72	5.58	5.98	6.11	5.46	5.64	6.53	6.00	10
11	5.28	5.57	5.99	5.64	6.06	6.42	5.64	5.67	6.70	6.04	11
12	5.51	5.87	6.01	5.87	6.11	6.48	5.91	5.94	7.00	6.17	12
13	5.67	6.25	6.03	5.91	6.16	6.55	5.99	5.98	7.17	6.17	13
14	5.79	6.34	6.05	6.04	6.17	6.70	6.09	6.13	7.22	6.20	14
15	5.81	6.51	6.10	6.25	6.29	6.79	6.11	6.13	7.25	6.21	15
16	5.88	6.52	6.17	6.29	6.34	6.80	6.23	6.39	7.30	6.24	16
17	5.90	6.54	6.47	6.31	6.36	6.81	6.30	6.42	7.33	6.25	17
18	6.00	6.71	6.59	6.34	6.36	6.84	6.30	6.52	7.41	6.35	18
19	6.01	6.85	6.62	6.38	6.45	6.96	6.41	6.55	7.45	6.36	19
20	6.04	6.87	6.67	6.47	6.46	6.98	6.44	6.58	7.49	6.38	20
21	6.06	6.88	6.70	6.48	6.58	6.98	6.47	6.60		6.43	21
22	6.13	6.95	6.89	6.60	6.66	7.05	6.48	6.64		6.49	22
23	6.13	6.96	6.93	6.73	6.66	7.06	6.51	6.65		6.61	23
24	6.22	6.97	7.00	6.74	6.74	7.23	6.54	6.68		6.62	24
25	6.27	7.04	7.01	6.82	6.78	7.26	6.56	6.68		6.63	25
26	6.32	7.13	7.02	6.87	6.82	7.28	6.57	6.77		6.64	26
27	6.38	7.16	7.02	6.90	6.85	7.33	6.58	6.77		6.64	27
28	6.38	7.16	7.03	6.96	6.87	7.38	6.58	6.84		6.66	28
29	6.40	7.19	7.04	7.00	6.87	7.47	6.59	6.90		6.69	29
30	6.40	7.21	7.06	7.02	7.00	7.48	6.60	6.95		6.71	30

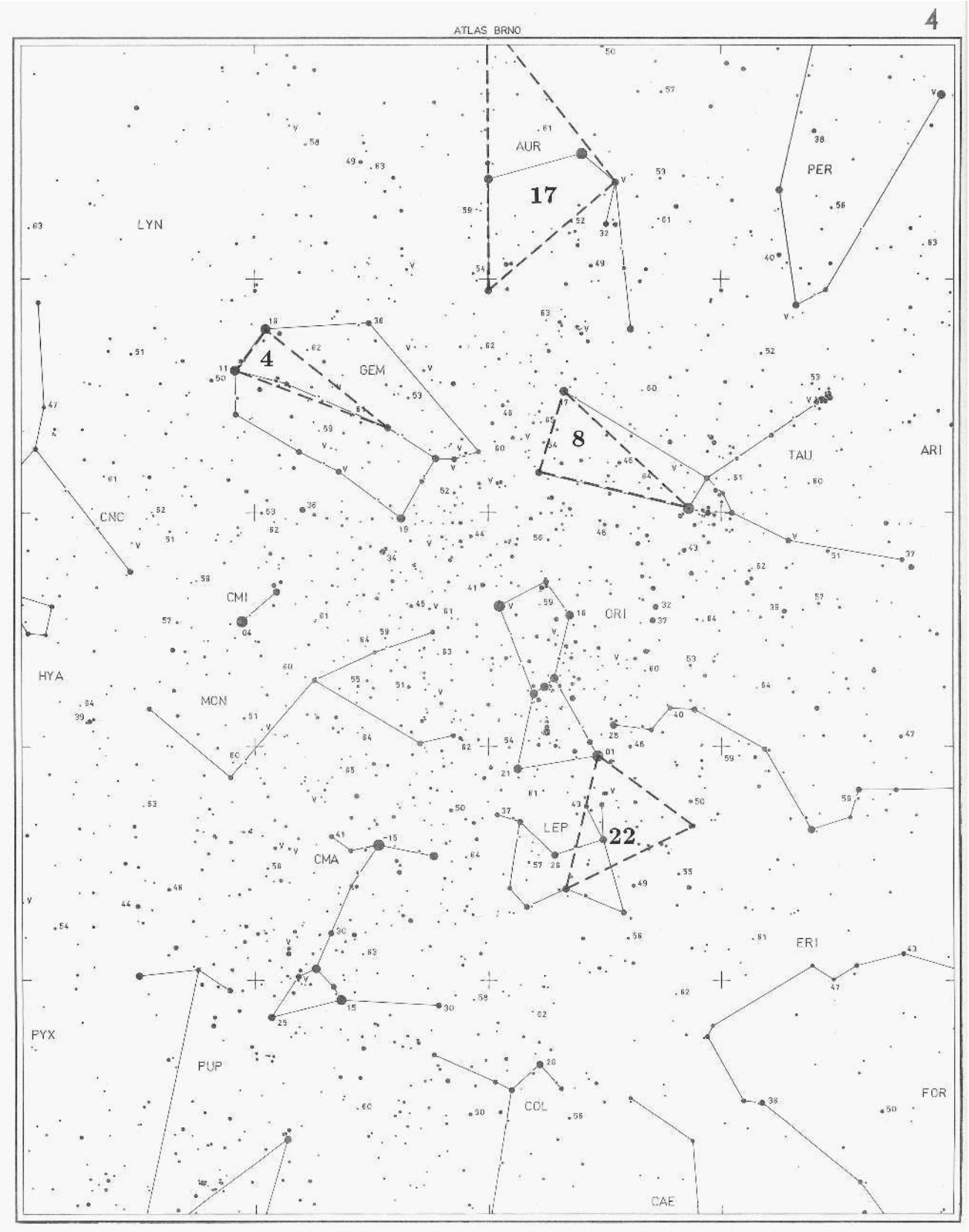
N	21 (Aqr) lm	22 (Lep) lm	23 (Crv) lm	24 (Lib) lm	25 (Sco) lm	26 (TrA) lm	27 (Cru) lm	28 (Car) lm	29 (Hyd) lm	30 (Pav) lm	N
4	3.96	3.87	3.01	3.92	5.26	2.88	1.65	3.84	4.08	3.65	4
5	4.48	4.28	5.21	4.56	5.40	3.76	4.31	3.96	4.69	3.95	5
6	4.72	4.43	5.81	5.19	5.50	3.85	4.56	4.00	4.74	4.23	6
7	5.54	4.47	5.95	5.64	5.84	4.11	4.59	4.33	5.51	4.76	7
8	5.66	4.78	6.40	5.72	5.92	4.85	4.61	5.46	5.57	4.86	8
9	5.98	5.46	6.62	6.08	6.00	5.08	4.69	5.54	5.67	5.12	9
10	6.28	5.49	6.84	6.14	6.09	5.10	4.92	5.78	5.99	5.15	10
11	6.30	5.68	7.06	6.15	6.15	5.11	5.50	5.79	6.09	5.18	11
12	6.35	5.68	7.25	6.17	6.32	5.17	5.75	6.36	6.36	5.61	12
13	6.79	5.69	7.30	6.19	6.41	5.18	5.82	6.36	6.43	5.62	13
14	6.82	5.72	7.41	6.41	6.47	5.29	6.04	6.49	6.57	5.76	14
15	6.97	5.82	7.44	6.46	6.56	5.50	6.20	6.54	6.59	5.92	15
16	7.05	5.96	7.44	6.50	6.56	5.72	6.20	6.63	6.65	6.09	16
17	7.25	5.96	7.46	6.63	6.62	5.75	6.23	6.72	6.66	6.22	17
18	7.42	6.05		6.64	6.85	5.77	6.42	6.85	6.69	6.22	18
19	7.45	6.15		6.67	6.90	5.89	6.61	6.90	6.69	6.28	19
20	7.46	6.23		6.75	6.97	5.89	6.61	6.93	6.71	6.33	20
21	7.48	6.27		6.76	6.98	5.95	6.66	6.99	6.77	6.35	21
22	7.50	6.35		6.76	7.01	5.95	6.69	7.04	6.81	6.36	22
23		6.40		6.80	7.07	6.02	6.73	7.08	6.84	6.40	23
24		6.42		6.87	7.13	6.07	6.74	7.14	6.85	6.50	24
25		6.46		6.94	7.14	6.12	6.75	7.15	6.86	6.59	25
26		6.47		7.07	7.15	6.14	6.92	7.16	6.88	6.70	26
27		6.54		7.14	7.26	6.16	6.93	7.18	6.89	6.70	27
28		6.68		7.16	7.40	6.17	6.96	7.19	6.89	6.73	28
29		6.71		7.19	7.46	6.20	6.98	7.25	6.91	6.77	29
30		6.73		7.20		6.20	7.07	7.29	6.94	6.83	30

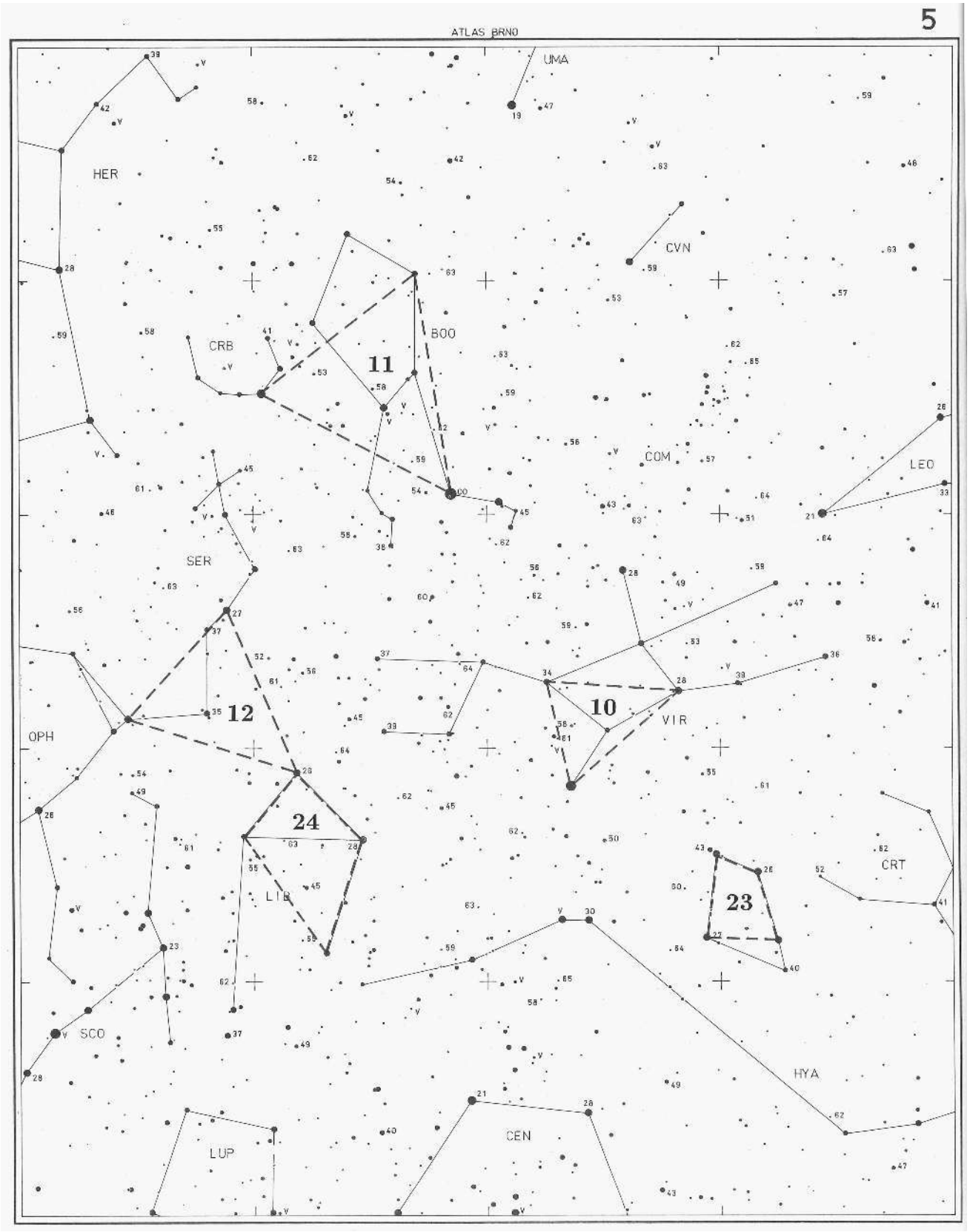
The following pages 60 to 60 show the charts of Atlas Brno (layout and use described in Section 3.5 on page 86) with the borders of the fields listed above for lm determination (dashed lines).

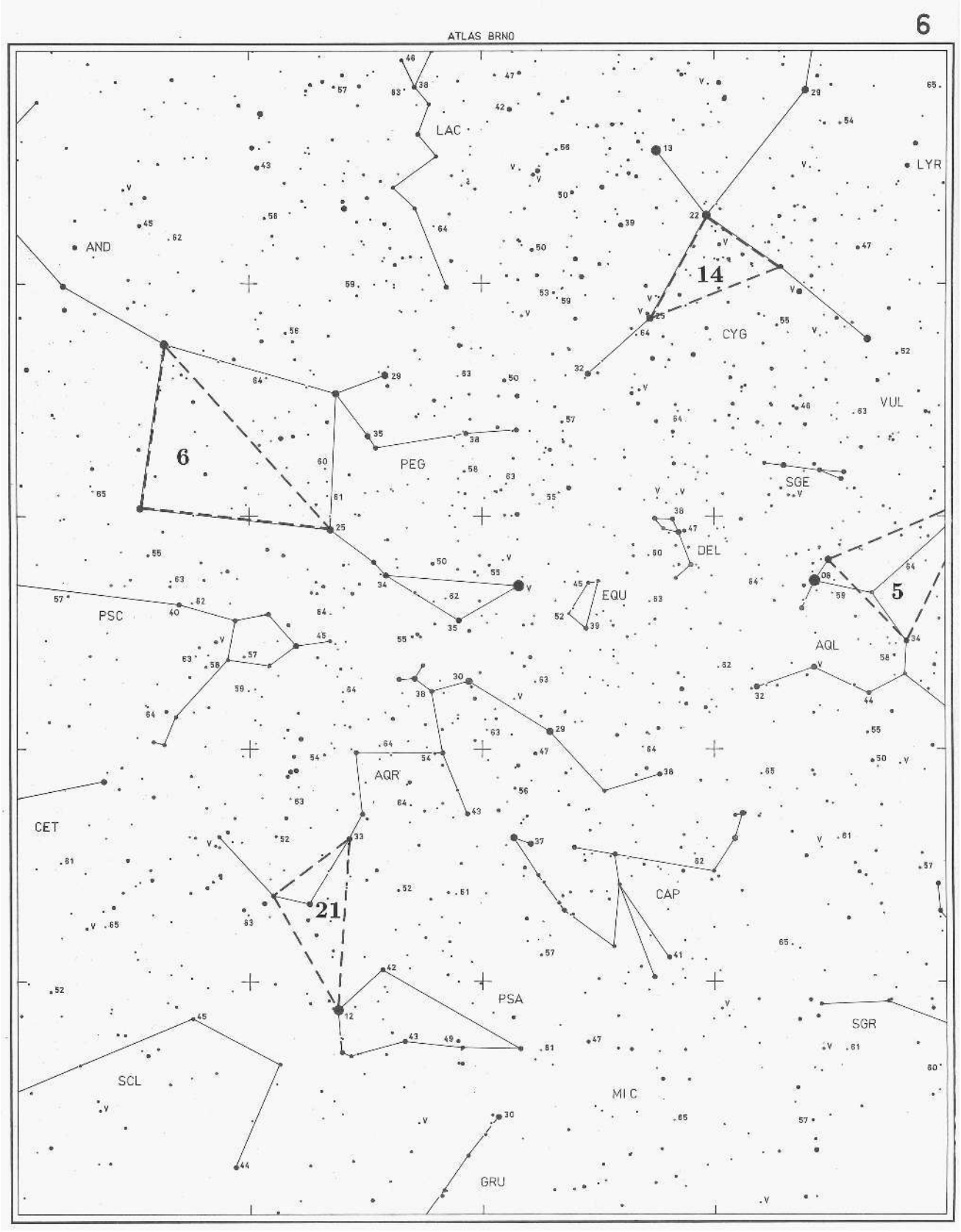

1
ATLAS BRNO
CYG
DRA
UMI
DRA
UMA
LYN
CEP
CAS
CAM
LAC
AND
PEG
PSC
TRI
ARI
PER
AUR
TAU
7
20
2
17
18
6

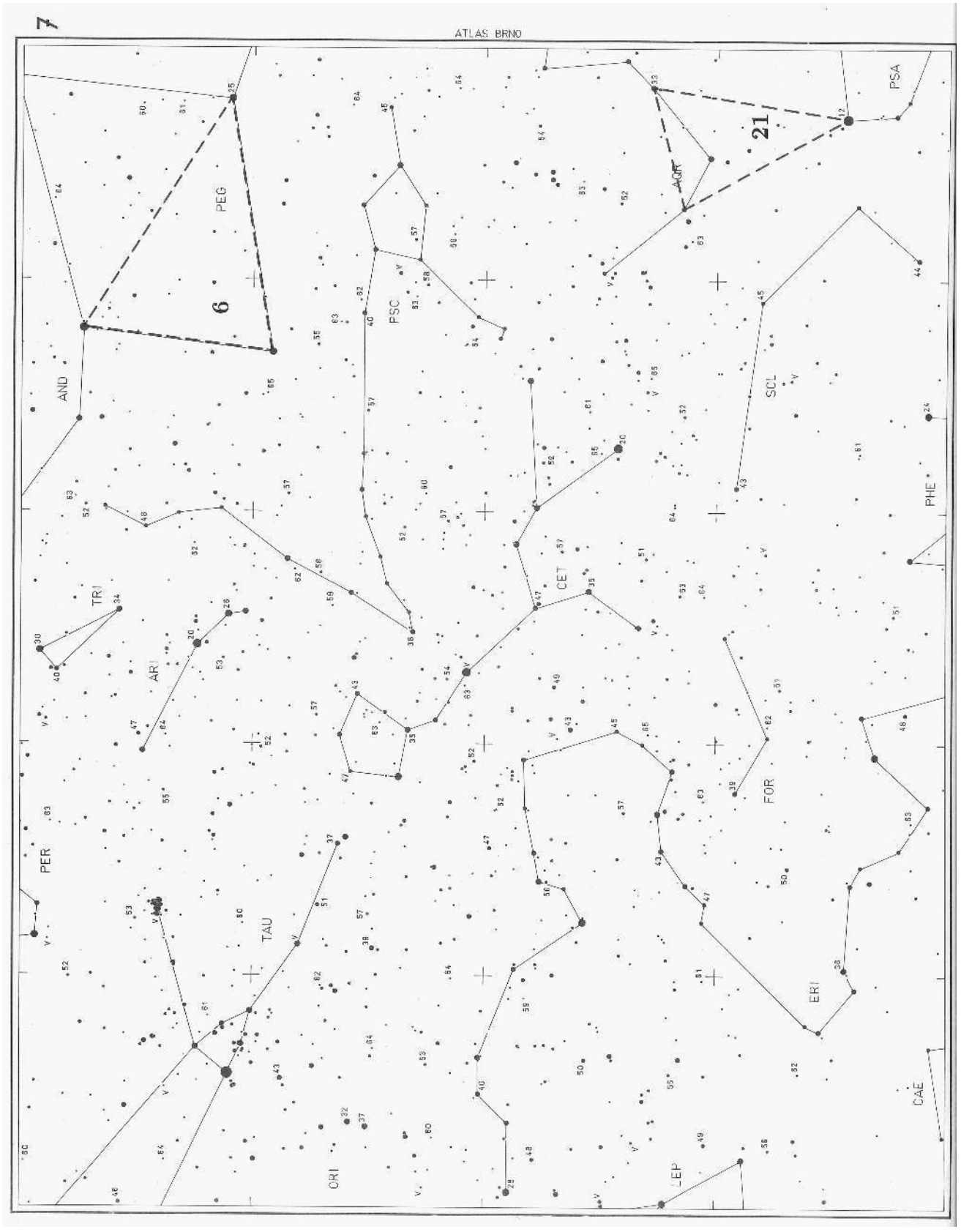

2
ATLAS BRNO
PER
CAS
17
AUR
GEM
4
20
CAM
LYN
CNC
CEP
3
UMA
LMI
9
LEO
19
UMI
16
CVN
DRA
COM
BOO

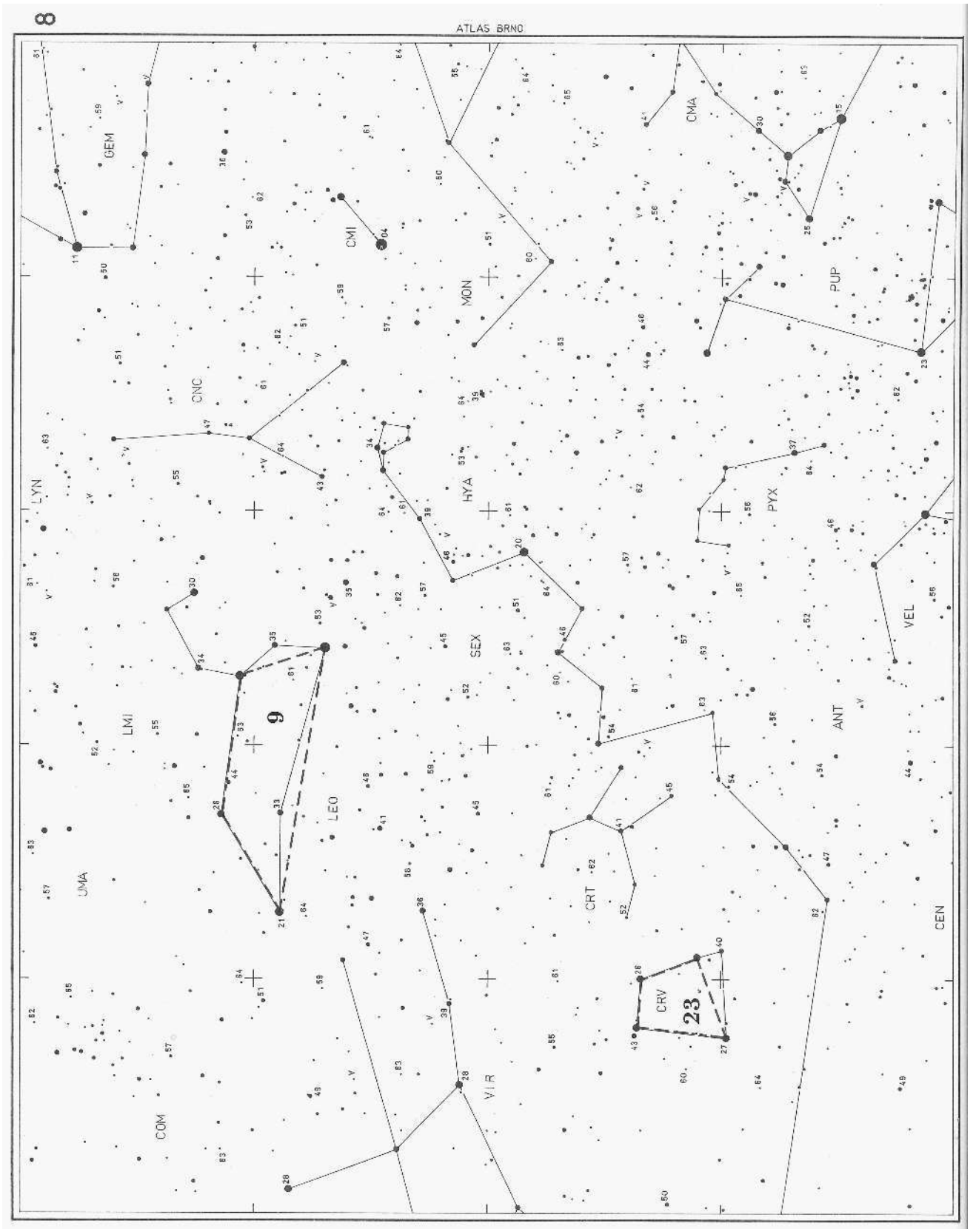

3
ATLAS BRNO
UMA
CYN
BOO
SER
CRB
HER
DRA
UMI
CAM
CEP
LYR
CAS
LAC
CYG
VUL
SGE
AQL
DEL
AND
19
1
15
13
7
14

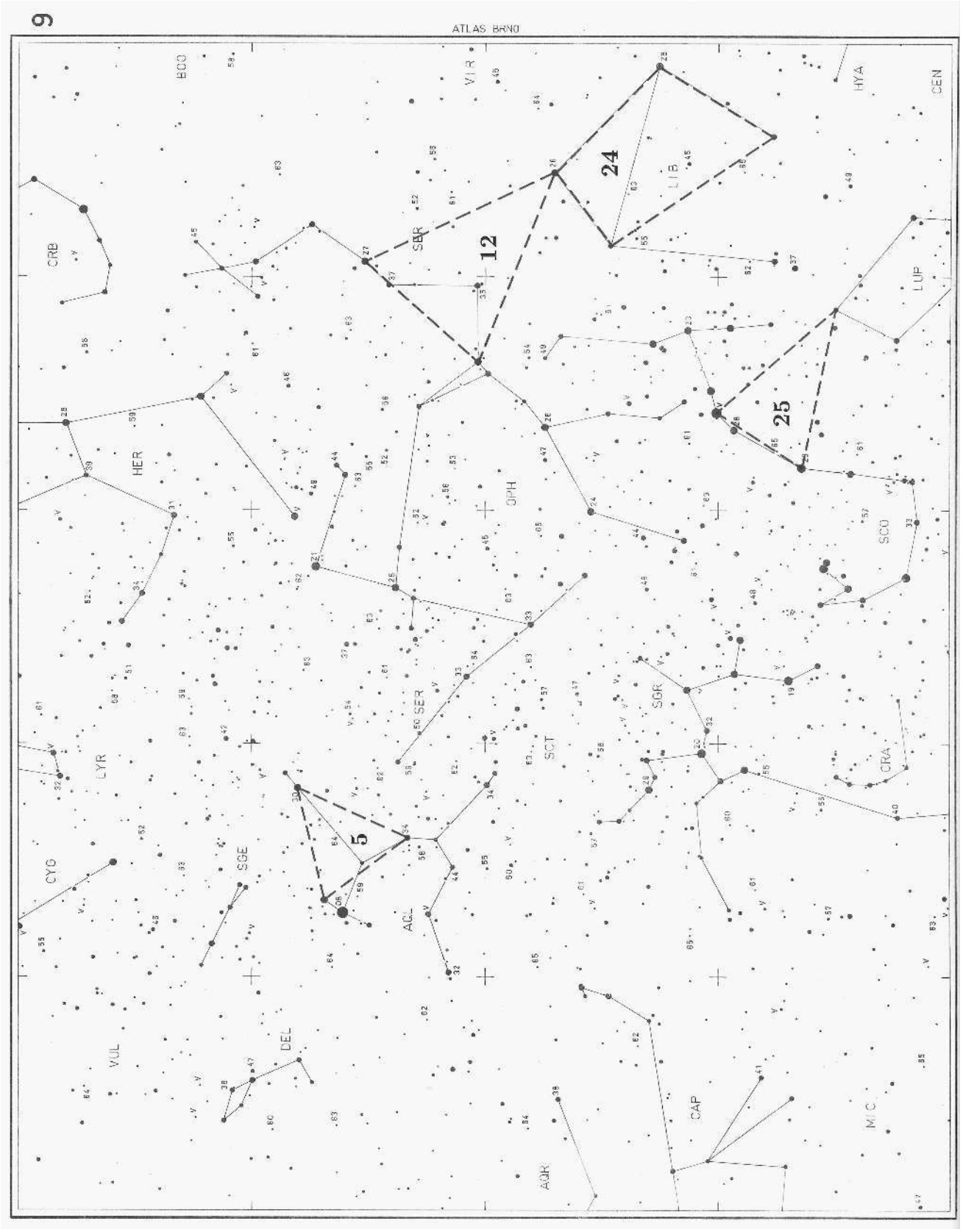

ATLAS BRNO
4
AUR
17
PER
LYN
4
GEM
8
TAU
ARI
CNC
CMI
ORI
HYA
MON
LEP
22
CMA
ERI
PYX
PUP
COL
FOR
CAE

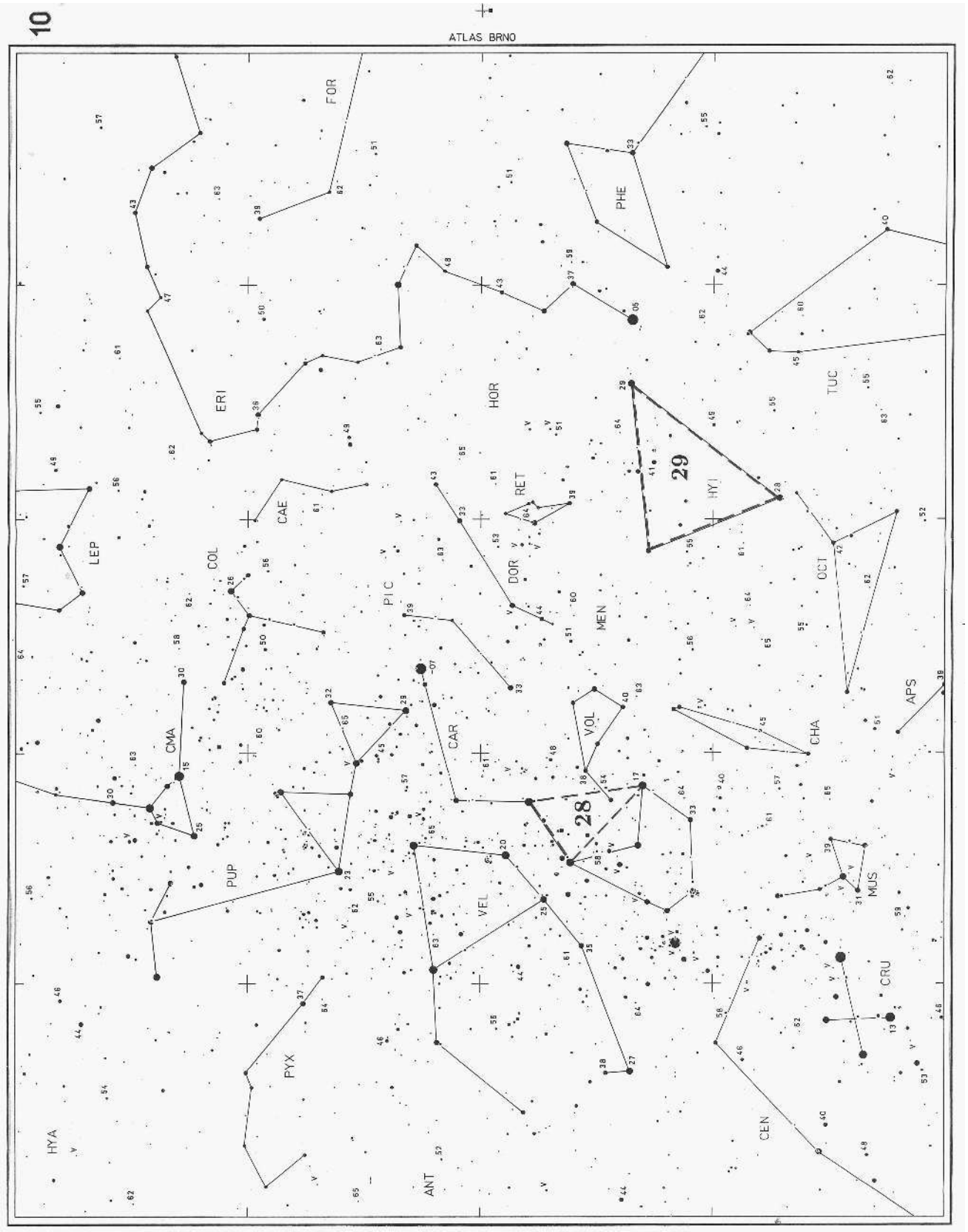

5
ATLAS BRNO
UMA
HER
CVN
CRB
BOO
11
COM
LEO
SER
12
10
VIR
OPH
24
LIB
23
CRT
SCO
HYA
CEN
LUP

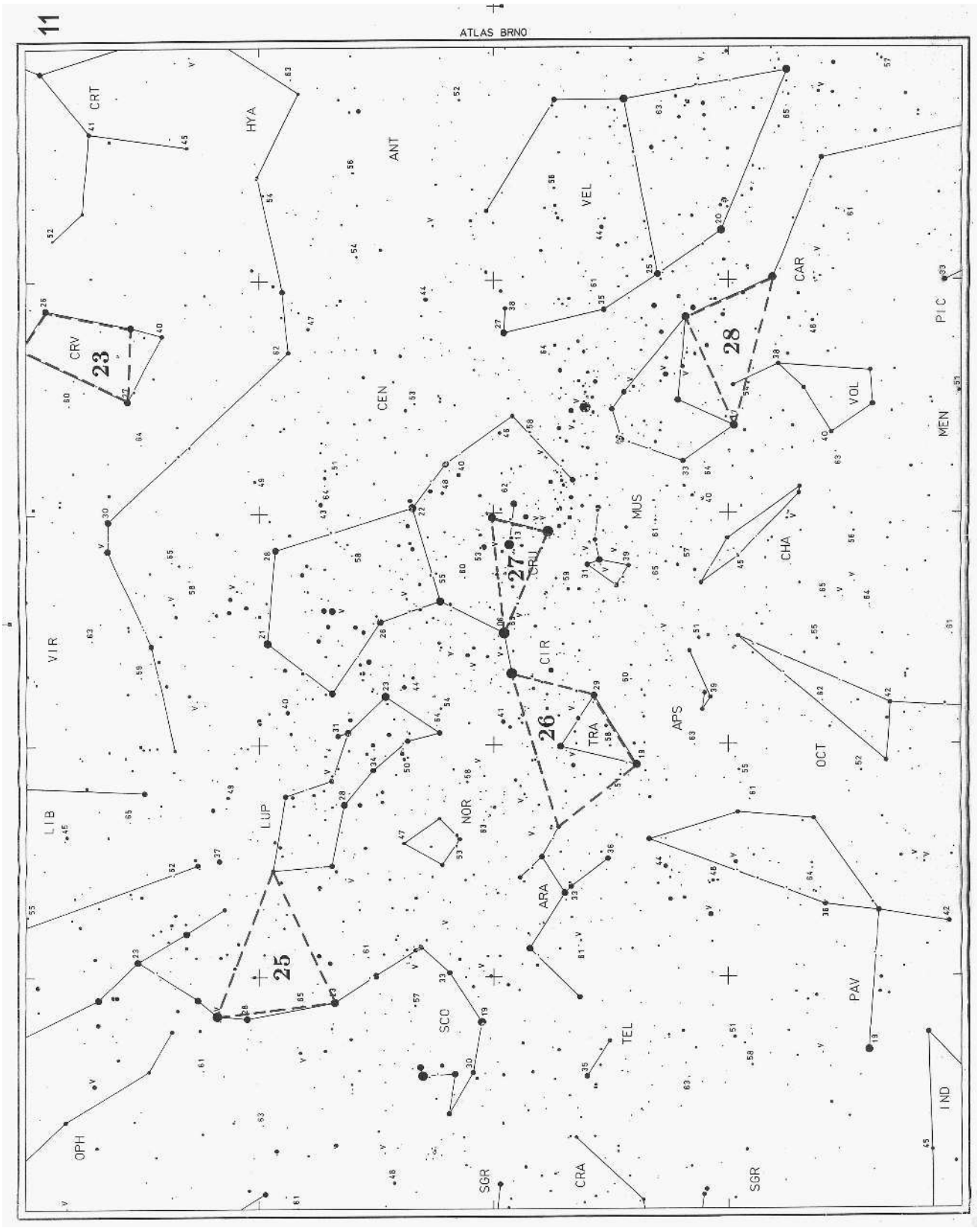

ATLAS BRNO
6
LAC
LYR
AND
14
CYG
6
PEG
VUL
SGE
DEL
EQU
5
PSC
AQL
AQR
CET
21
CAP
PSA
SGR
SCL
MIC
GRU

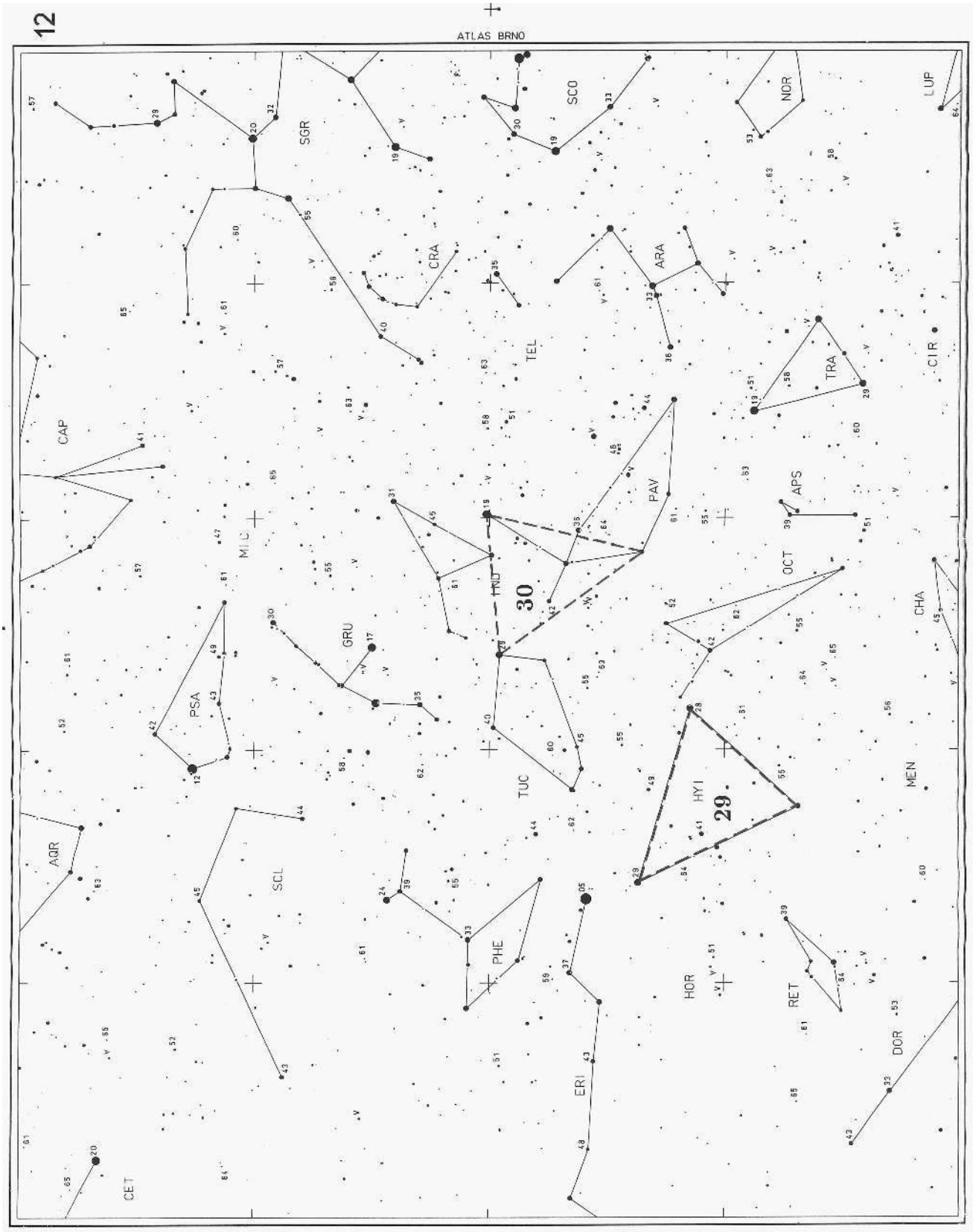

7
ATLAS BRNO
PEG
6
21
AQR
PSA
PSC
AND
SCL
PHE
CET
TRI
ARI
FOR
PER
TAU
ERI
CAE
CRT
LEP


8
ATLAS BRNO
GEM
CMI
MON
CMA
PUP
CNC
LYN
HYA
PYX
VEL
SEX
ANT
LMI
9
LEO
UMA
CRT
CEN
CRV
23
VIR
COM


9
ATLAS BRNO
BOO
VIR
HYA
CEN
CRB
SER
12
24
LIB
LUP
25
HER
OPH
SCO
LYR
SER
SGR
SCT
CRA
5
CYG
SGE
AQL
VUL
DEL
CAP
M C
AQR


10
ATLAS BRNO
FOR
ERI
PHE
TUC
HOR
RET
HYI
29
LEP
COL
CAE
DOR
PIC
MEN
OCT
CMA
CAR
VOL
CHA
APS
28
PUP
VEL
MUS
CRU
PYX
HYA
ANT
CEN


11
ATLAS BRNO
CRT
HYA
ANT
VEL
CAR
PIC
CRV
23
28
CEN
VOL
MEN
MUS
27
CRU
CHA
VIR
CIR
26
TRA
APS
OCT
LIB
LUP
NOR
ARA
25
SCO
TEL
PAV
OPH
SGR
CRA
SGR
IND


12
ATLAS BRNO
SGR
SCO
NOR
LUP
CRA
ARA
TEL
CIR
TRA
CAP
PAV
APS
MIC
OCT
CHA
PSA
GRU
IND
30
TUC
HYI
29
MEN
AQR
SCL
PHE
HOR
RET
ERI
DOR
CET

3 | Visual Observations of Minor Showers

Rainer Arlt, Jürgen Rendtel, Ralf Koschack

3.1 Plotting meteor trails

During most nights of the year, the meteor rates are far below those of major shower peak periods. Generally, visual data suffer from observing errors. Meteors of the strongest source which are not correctly associated tend to 'pollute' the weaker sources more than the other way round. This effect is of little importance near major shower peaks, but increases if rates become low. Therefore it is essential to associate meteors with their radiants correctly.

The suggested procedure is to plot the apparent meteor trails seen in the sky on a suitable map and to note the other data of each meteor (mainly magnitude and angular velocity) during the observation. The shower association is done after the observation at the desk.

3.1.1 Plotting meteors

When a meteor appears, try to store the phenomenon as a whole in your memory. Then keep looking at the sky in order to memorise the following data (in this order):

1. **The path.**
   The most important information is its *direction* rather than the exact start/end points. Memorise it with respect to the background stars, e.g., in between which stars the meteor passed or to which ones it can be traced back or prolonged.

2. **Maximum magnitude.**
   Estimate this by comparing it to the brightness of the stars you memorised at the beginning of the watch (see Chapter 2).

3. **Angular velocity.**
   In order to have a quantity that can be compared to an expected value for shower association, you should estimate this in degrees per second (°/s): in your imagination you make the meteor move for one second. The path length in degrees the meteor would have reached after moving for one second is its angular velocity in °/s. With some experience, you will have the scale fixed in your memory and can then estimate the angular velocity directly.

While the apparent path is plotted into a gnomonic map (see below), the other meteor data are recorded either on a tape or on a list with an identification number given to each entry. The Atlas Brno with the charts shown on pages 60 to 60 (reduced size) is a set gnomonic maps for meteor plotting. Details of the Atlas are given in section 3.5 on page 86.

3.1.2 Shower association

Meteor plotting allows shower association by more objective criteria after your observation than the simple imaginary back-prolongation of paths under the sky. Meteors plotted on gnomonic maps can be traced back to their (most probable) radiants by extending their straight line paths. If a radiant lies on another chart, you need to find common stars on both charts to do this correctly. An example is provided in section 3.3.

Table 3.1: Optimum radiant diameters to be assumed for shower association of minor-shower meteors as a function of the distance D between the radiant and the meteor.

Distance D	Optimum diameter
15°	14°
30°	17°
50°	20°
70°	23°

How large a radiant should be assumed for shower association? The real physical radiant size is very small, but plotting errors cause many true shower meteors to miss the real radiant area. Thus, we have to assume a larger effective radiant to allow for these errors. Unfortunately, as we enlarge the radiant, more and more spo-

Table 3.2: Error limits for the angular velocity.

Angular velocity [°/s]	5	10	15	20	30
Permitted error [°/s]	3	5	6	7	8

Table 3.3: Angular velocity ω (in °/s) as a function of the elevation of the meteor's beginning point h_b and the distance D between the end point and the radiant for various values of a stream's geocentric velocity v_∞ and the altitude H_b of the meteor's beginning point above the Earth's surface. The values of H_b are averages for the given velocities v_∞.

	$V_\infty = 20$ km/s $H_b = 100$ km					$V_\infty = 25$ km/s $H_b = 100$ km				
h_b=	10°	20°	40°	60°	90°	10°	20°	40°	60°	90°
$D = 5°$	0.2	0.3	0.6	0.9	1.0	0.2	0.4	0.8	1.1	1.3
10°	0.3	0.7	1.3	1.7	2.0	0.4	0.9	1.6	2.2	2.5
20°	0.7	1.3	2.5	3.4	3.9	0.9	1.7	3.2	4.3	4.9
40°	1.3	2.5	4.7	6.3	7.3	1.6	3.2	5.9	8.0	9.3
60°	1.7	3.4	6.3	8.5	9.8	2.2	4.3	8.0	11	13
90°	2.0	3.9	7.3	9.8	11	2.5	4.9	9.3	13	14
	$V_\infty = 30$ km/s $H_b = 100$ km					$V_\infty = 35$ km/s $H_b = 100$ km				
h_b=	10°	20°	40°	60°	90°	10°	20°	40°	60°	90°
$D = 5°$	0.3	0.5	1.0	1.4	1.6	0.3	0.6	1.1	1.5	1.7
10°	0.5	1.1	2.0	2.7	3.1	0.6	1.2	2.2	3.0	3.4
20°	1.1	2.1	4.0	5.3	6.2	1.2	2.3	4.3	5.8	6.7
40°	2.0	4.0	7.4	10	12	2.2	4.3	8.2	11	13
60°	2.7	5.3	10	14	16	3.0	5.8	11	15	17
90°	3.1	6.2	12	16	18	3.4	6.7	13	17	20
	$V_\infty = 40$ km/s $H_b = 100$ km					$V_\infty = 50$ km/s $H_b = 110$ km				
h_b=	10°	20°	40°	60°	90°	10°	20°	40°	60°	90°
$D = 5°$	0.3	0.7	1.3	1.7	2.0	0.4	0.8	1.5	2.0	2.3
10°	0.7	1.4	2.6	3.5	4.0	0.8	1.6	2.9	3.9	4.6
20°	1.4	2.7	5.0	6.8	7.9	1.6	3.1	5.8	7.8	9.0
40°	2.6	5.0	9.5	13	15	2.9	5.8	11	15	17
60°	3.5	6.8	13	17	20	3.9	7.8	15	20	23
90°	4.0	7.9	15	20	23	4.6	9.0	17	23	26
	$V_\infty = 60$ km/s $H_b = 115$ km					$V_\infty = 66$ km/s $H_b = 115$ km				
h_b=	10°	20°	40°	60°	90°	10°	20°	40°	60°	90°
$D = 5°$	0.5	0.9	1.7	2.3	2.6	0.5	1.0	1.9	2.5	2.9
10°	0.9	1.8	3.4	4.5	5.2	1.0	2.0	3.7	5.0	5.8
20°	1.8	3.5	6.7	9.0	10	2.0	3.9	7.3	10	11
40°	3.7	6.7	13	17	20	3.7	7.3	14	18	21
60°	4.6	9.0	17	23	26	5.0	10	18	25	29
90°	5.3	10	20	26	30	5.8	11	21	29	33
	$V_\infty = 70$ km/s $H_b = 126$ km									
h_b=	10°	20°	40°	60°	90°					
$D = 5°$	0.5	0.9	1.8	2.4	2.8					
10°	1.0	1.9	3.6	4.8	5.5					
20°	1.9	3.7	7.0	9.4	11					
40°	3.6	7.0	13	18	21					
60°	4.8	9.4	18	24	28					
90°	5.5	11	21	28	32					

Examples:

1. Geminid $V_\infty = 35$ km/s $h_b = 60°$ $D = 40°$ $\omega = 11°/s$
2. Orionid $V_\infty = 66$ km/s $h_b = 30°$ $D = 60°$ $\omega \approx 14°/s$
3. Ursid $V_\infty = 33$ km/s $h_b = 50°$ $D = 30°$ $\omega \approx 7°/s$

radic meteors (and a few of other showers) will appear to line up accidentally with this region. Hence, we have to apply an optimum radiant diameter to compensate for the loss due to plotting errors without introducing too much sporadic meteor pollution. Table 3.1 gives this optimum diameter as a function of the distance of the meteor from the radiant.

The radiant diameter criterion as listed in Table 3.1 applies to all shower radiants *except* those of the Southern and Northern Taurids, and the Antihelion Source, all of which have notably larger radiant areas. The optimum $\alpha \times \delta$ size to be assumed for each radiant of the two Taurid showers is instead $20° \times 10°$, while that for the Antihelion Source is still larger, at $30° \times 15°$.

The angular velocity of a meteor is another important criterion for the shower association: it should match the expected speed of the given shower meteors according to their geocentric velocities. Speeds are in the range 3°/s to 25°/s. Typical errors for such estimates are given in Table 3.2.

The angular velocity of a meteor is another important criterion for the shower association: it should match the expected speed of the given shower meteors according to their geocentric velocities. Speeds are in the range 3°/s to 25°/s. Typical errors for such estimates are given in Table 3.2.

A meteor which passes a radiant within the diameter (Table 3.1) and fits the expected angular velocity (Table 3.3) within the error margins (Table 3.2) very probably belongs to the corresponding shower.

Detailed shower data can be found in the descriptions given in the IMO's *Meteor Shower Workbook* and in the annual *IMO Meteor Shower Calendar*. The current IMO meteor shower working list is also printed as Table 2.4 on page 58.

3.1.3 Enhanced rates: modifying the observing method

If you spend too much time for plotting, the sample may become biased and the observational data become less reliable. This happens if the number of *observed* meteors exceeds about 30 per hour: on average you are busy with plotting every second minute. This may easily happen especially after local midnight between August and December, when several sources contribute to the meteor activity. For example, in October, we find the Orionids as a major source, the ε-Geminids, the Taurids and the Leonis Minorids.

If the cadence of meteors becomes to high, you may combine the counting and plotting procedures: meteors which *could* belong to one of the minor showers are plotted while obvious Orionids and sporadics are counted according to the guidelines described in Chapter 2. Data of the Orionids and sporadics are then recorded without taking your eyes off the sky. This will greatly reduce the amount of dead time and still enables an accurate shower association for the minor sources.

3.1.4 Observing field

Most meteors are witnessed centrally in the field of vision. Thus it is important to choose the field centre such that meteors appearing there can be easily distinguished from sporadics and associated to the shower(s) under study.

In the vicinity of the radiant, shower meteors are slow moving and have short paths while at larger distances from the radiant they resemble sporadics. A field near the radiant seems therefore more favourable. The main criterion, the direction of the path, also applies more accurately for meteors in the vicinity of the radiant.

From the above one could perhaps conclude that it is best to look directly at the radiant. However, motion is the property which distinguishes meteors from stars. We witness faint meteors in between the hundreds of stars in our field due to their motion. If a faint star appeared for one second or less we would not realise it. But that is exactly what happens when a meteor occurs in the immediate vicinity of the radiant! On the other hand, very fast-moving (faint) meteors are easily missed too. Medium velocity is optimal for perception.

Taking into account all the factors discussed above, a distance from the centre of the field of view to the radiant(s) under study of 20° to 40° is optimal. Distances of more than 50° should be avoided.

Besides an elevation of 50° to 70° from the horizon and a radiant distance of 20° to 40°, there is an additional point to be taken into account. If you are going to observe several showers at the same time, as described in our example, you have to take care that their radiants do not lie in one line as seen from your field centre. Otherwise, meteors from these radiants cannot be distinguished by their path directions, and distinguishing them by their angular velocity and path length alone will become difficult and more uncertain (you will experience this problem in our example provided in Section 3.3). Observing, for instance, the Orionids with their radiant near β Ori and the ε-Geminids with their radiant near β Gem, the field centre should be in Taurus/Auriga/Perseus or Canis Minor/Monoceros/Canis Major rather than in Cancer/Ursa Major or Lepus/Eridanus.

When you have chosen the best-situated field you should follow its diurnal motion as long as conditions (elevation of the field about 50°–70°, artificial lights, obstructions, etc.) permit. If you are forced to change

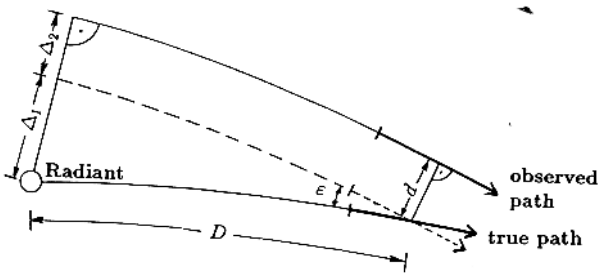


Figure 3.1: Tilt ε and parallel shift d of a meteor appearing at distance D from the radiant result in an error Δ at the radiant. This error consists of $\Delta_1(\varepsilon)$ and $\Delta_2(d)$.

the field, note the time of this change and the new field. For analysis the time of such a change should be identical with the boundary of an observing interval.

3.2 Background of the method

3.2.1 Plotting errors

The path of a meteor which suddenly appears at any position in the field of view will be memorised with some uncertainty. Here, we analyse the plotting errors which affect the shower association. As shown in Figure 3.1, there are two error components: a tilt ε, and a parallel shift d.

Due to these components, the backwards prolongation of the plotted meteor misses its real radiant by a distance Δ. As shown in Figure 3.1, Δ results from the addition (if the real path and the plotted path are convergent) or the subtraction (in the case of divergence) of the components Δ_1 and Δ_2. For small angles ε and shifts d, we may write

$$\Delta_1 \approx \varepsilon \times \sin D;$$

$$\Delta_2 \approx d \times \cos D;$$

$$\Delta = \Delta_1 + \Delta_2,$$

with D being the distance to the radiant.

It can be seen that the resulting error due to a given tilt, Δ_1, increases with increasing radiant distance D (up to 90°), while the situation for the shift is reversed (Δ_2). The histograms in Figures 3.2 and 3.3 show the distribution of both components determined from plots during extensive visual observations done by observers carrying out plotting regularly.

It becomes obvious that the *tilt* is the main component while the shift can be effectively ignored. Thus, shower association will be more accurate for meteors in the vicinity of the radiant. This is illustrated by the distribution of resulting errors at the radiant in Figure 3.4. While most meteors very close to the radiant show small resulting errors, the number of large errors increases considerably with the distance from the radiant. This should be kept in mind during the observation.

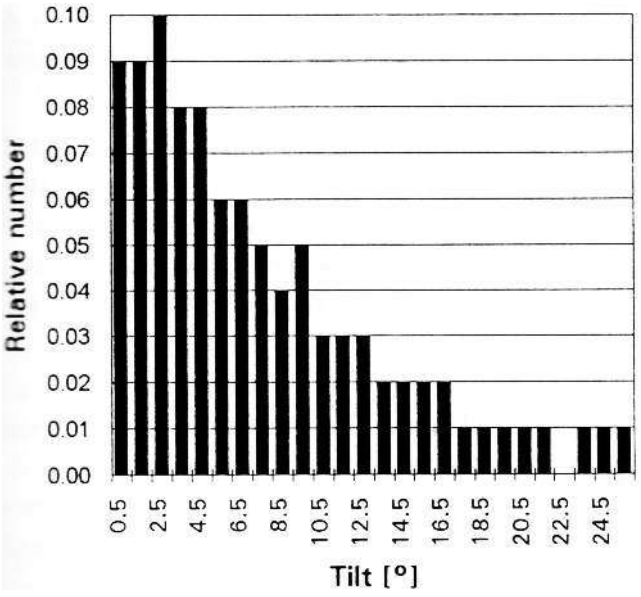


Figure 3.2: Relative numbers of tilts ε obtained from observations of experienced observers (Koschack, 1991).

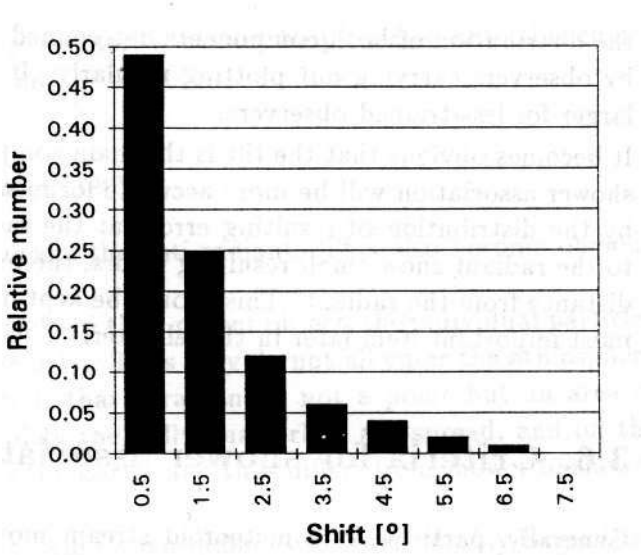


Figure 3.3: Relative numbers of shifts d derived from plottings of experienced observers (Koschack, 1991).

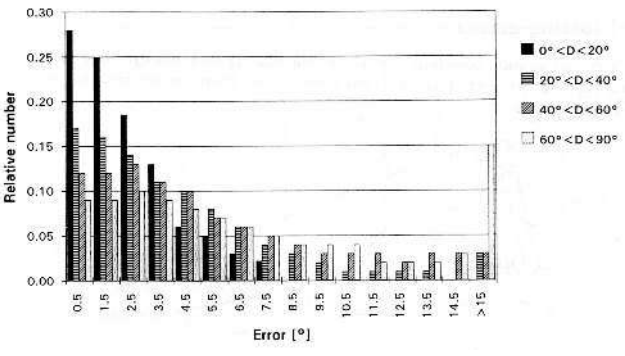


Figure 3.4: Relative numbers of resulting errors Δ for different radiant distances D according to Koschack (1991). The average distances D are: 0–20° (15°), 20–40° (30°), 40–60° (50°), and 60–90° (70°).

3.2.2 Path and radiant

Shower meteors apparently radiate from a certain point or small region in the sky, the radiant. In Figure 3.5, we see how observers at three locations A, B and C project a meteor M onto the sky hemisphere as sections of an arc. They define a great circle. Meteors from the same radiant (same shower) define a number of great circles as shown in Figure 3.6. These great circles of different shower meteors have two poles or intersection points in common: the radiant R (during an observation normally above the horizon) and the anti-radiant AR (below the horizon). The plane perpendicular to the great circles through the centre O marks the points at 90° distance from the radiant.

When the chart's centre P is situated at less than 90° from the radiant (Figure 3.5), the latter may be marked on the same plane as that of the map by use of the usual projection formulae (Section 3.5.1.3). The backward extensions of the shower meteors meet the radiant.

When the radiant is at more than 90° from the map's centre, it cannot be projected onto this chart, but the anti-radiant may be. Its position results from:

$$\begin{aligned} \delta_{AR} &= -\delta_R \\ \alpha_{AR} &= \alpha_R \pm 180^\circ \end{aligned}$$

Now the forward prolongation of the meteor trail meets the anti-radiant. This also becomes obvious from Figure 3.6.

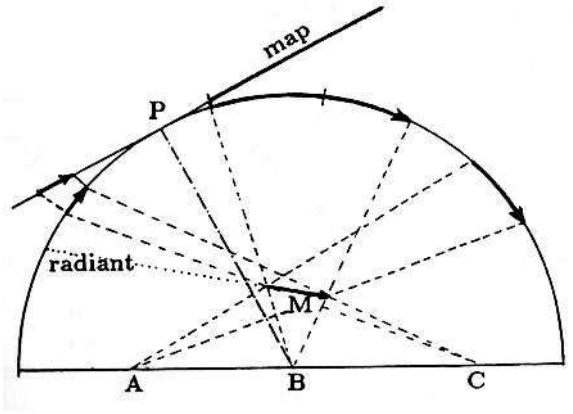


Figure 3.5: Side view of the trajectory being projected on the celestial sphere and on the map. P denotes the map centre (= projection centre), and M is the meteor trajectory.

The backward extensions of plotted meteors will form a radiant area considerably larger than the radius obtained from photographic or video observations due to plotting errors. When trying to decide whether a meteor belongs to a certain shower or not, the question arises as to how large a radiant area can safely be assumed. Making it too large means the sporadic pollution becomes too strong, i.e. several sporadic meteors will meet the radiant accidentally. If the radiant area is too small a certain number of shower meteors will be classified as sporadics because of the plotting errors. This leads to the suggested optimum radiant diameters given in Table 3.1 and for which we will give further details below.

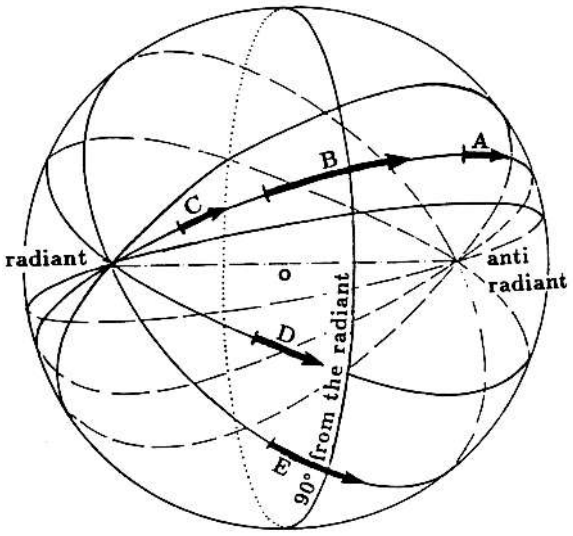


Figure 3.6: View of the celestial sphere on which the meteor's trajectory was projected from different places. Observers A, B, and C are situated on the same meridian (great circle). Other observers (D, E) may see it on other great circles.

3.2.3 Accuracy of velocity estimates

The method to estimate the angular velocity of a meteor may seem rough, but yields acceptable results. A detailed analysis of such estimates was done with the results summarised in Figure 3.7. These error limits for the angular velocity lead to the values given in Table 3.2.

Meteors of a given shower enter the Earth's atmosphere with almost the same velocity, and they start to emit light at similar heights above the Earth's surface. The deceleration along the luminous path through the atmosphere can be neglected for ordinary meteors; their velocity is reduced by a few percent only. For our purposes, we can assume that shower meteors move parallel to each other with a constant velocity.

Thus, the apparent angular velocity ω of a shower meteor (in degrees per second) can be calculated. It depends on the pre-atmospheric velocity V_∞ (km/s), the elevation h_b (degrees) and altitude H_b (km) of its start point, and the angular distance between its end point and the radiant D (degrees).

From Figure 3.8 we find the true length of the luminous path s as

$$s = \frac{H_b \times \sin l}{\sin h_b \times \sin D_e},$$

with l being the apparent path length of the meteor in the sky. The angular velocity ω is

$$\omega = \frac{l \times V_\infty}{s} = \frac{l \times V_\infty \times \sin h_b \times \sin D_e}{H_b \times \sin l}.$$

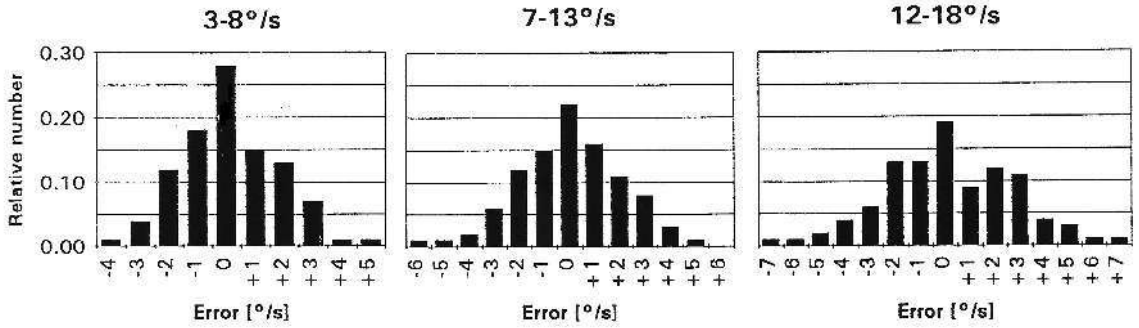


Figure 3.7: Relative error numbers of experienced observers' velocity estimates for different ranges of angular velocity, according to Koschack (1991).

For apparent path lengths l shorter than $\approx 30°$ we find

$$\frac{l}{\sin l} \approx \text{constant} = 1 \text{ rad} \simeq 57.^{\circ}3.$$

Finally, we can write ([1])

$$\omega = \frac{57.3° \times V_\infty \times \sin h_b \times \sin D_e}{H_b}.$$

The result of these calculations leads to Table 3.3 which allows to find the expected angular velocities for the given range of geocentric velocities. This table can also be used if you want to 'calibrate' your angular velocity estimates. When observing meteors of a shower (with known geocentric velocity V_∞), the expected angular velocities of shower meteors in the respective distances from the radiant and elevations above the horizon can be compared with the table. For example, the Perseids ($V_\infty \approx 60$ km/s) should produce meteors with the characteristics shown in Table 3.4. A Perseid 20° from the radiant and 40° above the horizon should appear with $\omega = 7°$/s, etc.

3.2.4 Pollution balance

If we had only meteors from one shower and no sporadics, no shower association is necessary. As soon as there are sporadic meteors, the situation changes and becomes more problematic the more sporadics appear, or, more precisely, the more the ratio *shower meteors/sporadics* reduces. It therefore becomes necessary to distinguish shower meteors from sporadic meteors. This is done by applying the criteria for shower membership, the most important of which is the direction of the path, followed by the meteor's angular velocity and its path length. As visual observations are affected by certain errors, the question arises as to how strictly the criteria have to be applied, in other words, which errors are still acceptable with respect to the expected values.

[1]This holds for the average angular velocity which is estimated by an observer. The instantaneous angular velocity of a meteor is described in detail by Gural (1999). The equations given there need to be considered for analyses of meteors recorded by photographic and video cameras.

Table 3.4: Angular velocity ω (in °/s) as a function of the elevation of the meteor's beginning point h_b and the distance D_e between the end point and the radiant for a geocentric velocity $V_\infty = 60$ km/s. H_b is the altitude of the meteor's beginning point above the Earth's surface.

	$V_\infty = 60$ km/s			$H_b = 115$ km	
$h_b =$	10°	20°	40°	60°	90°
$D = 5°$	0.5	0.9	1.7	2.3	2.6
10°	0.9	1.8	3.4	4.5	5.2
20°	1.8	3.5	6.7	9.0	10
40°	3.7	6.7	13	17	20
60°	4.6	9.0	17	23	26
90°	5.3	10	20	26	30

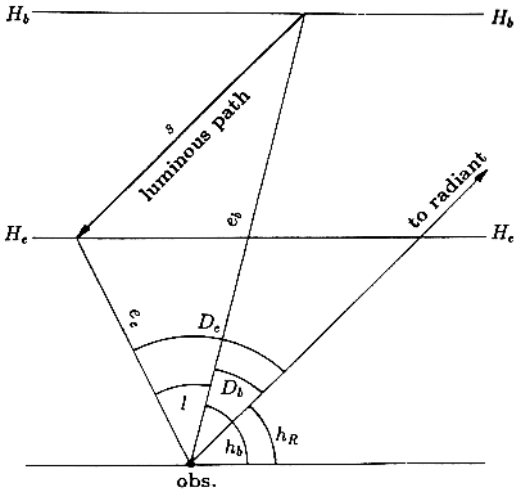


Figure 3.8: The path of a meteor in the atmosphere. From this geometric situation we can determine the angular velocity ω of a shower meteor with a known atmospheric entry velocity V_∞.

It is obvious that the answer must depend on the ratio *shower meteors/sporadics*. Observations around the maximum of a major shower can be approximated by the first situation above, i.e., the criteria can be applied very loosely. The resulting sporadic pollution of

the order of 2 to 4 meteors per hour does not play any significant role where the shower ZHR is more than 10 times higher. For this reason, it is possible to carry out shower association (or, rather, filtering out of obvious sporadics) directly under the sky without plotting the path. For minor-shower observations, where the sporadic pollution can easily reach the order of the shower rate itself, it becomes vital to apply the criteria much more strictly, guided by a solid theory.

The direction of the path is the main criterion for shower membership, thus we have to consider it first and then arrange the other criteria around this in a sensible way. For the path direction, it is necessary to define a radiant diameter suitable for shower association, i.e., a maximum distance by which the backward prolongation of the plotted meteor track is permitted to miss the actual radiant position given in Chapter 8. Choosing too small a diameter will result in a very low level of sporadic pollution but a considerable fraction of the shower meteors will be classified as sporadics due to plotting errors. Conversely, choosing too large a diameter will mean we catch almost all the shower meteors, but also a considerable number of sporadics.

We have to choose the radiant diameter and the error limits for the other criteria such that the loss due to observational errors is compensated for by the sporadic pollution.

The sporadic pollution will depend on the sporadic hourly rate $\mathrm{HR_{spo}}$ which is the number of sporadic meteors per hour corrected for a limiting magnitude of +6.5. The percentage of sporadic meteors meeting a radiant of a certain size and fulfilling accidentally the other criteria, is direct proportional to the radiant's diameter. Furthermore, this percentage depends on the error limits we allow for the other criteria. We have to answer the question which losses we are prepared to accept due to observational errors in the secondary criteria. For this purpose, we have to judge the value of each criterion.

The length of the path is a poorly-defined and approximate criterion only. We do not lose any significant fraction of the shower meteors due to plotting errors in this parameter. The criterion of angular velocity is, by contrast, very well defined. It seems reasonable to choose the error limit for the application of this criterion such that the loss due to the errors of the velocity estimates is about 5%. In Figure 3.9 the error distributions of Figure 3.7 have been plotted cumulatively, considering the absolute value of the error only.

Based on Figure 3.9, the error limits for the angular velocity are determined in terms of the angular velocity itself. This leads to the values given in Table 3.2.

Applying these error limits it was found that 3.75% of sporadic meteors can be associated to any radiant of 10° diameter (Koschack, 1991). For a radiant of 5° diameter this percentage is halved, for 20° it is twice as much, and so on. Mathematically, this relationship is

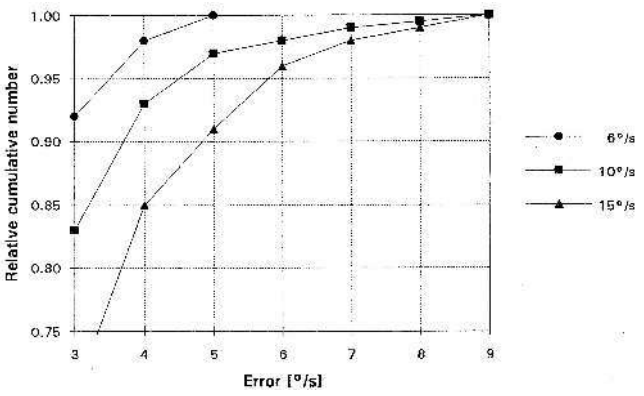


Figure 3.9: Cumulative relative error numbers of angular velocity estimates in the range 3–8°/s (average 6°/s), 7–13°/s (10°/s), and 12–18°/s (15°/s).

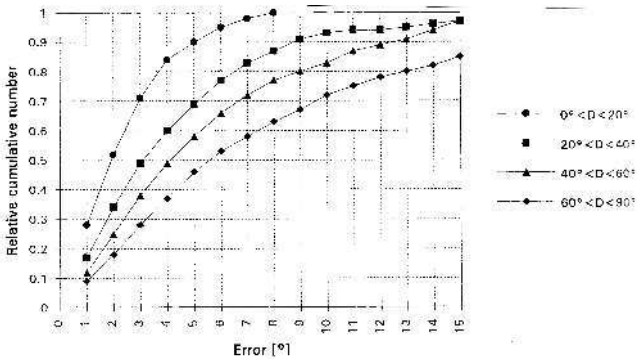


Figure 3.10: Relative cumulative numbers of resulting errors Δ for different radiant distances D according to Koschack (1991). The average distances are: 0–20° (15°), 20–40° (30°), 40–60° (50°), 60–90° (70°).

expressed by

$$\mathrm{sp} = 0.0375 \times \mathrm{HR_{spo}} \times \frac{r_\mathrm{R}}{5°},$$

with sp being the sporadic pollution and r_R the assumed radiant radius. If the direction of the path is applied as the only criterion, the sporadic pollution is more than twice as large (8.25% instead of 3.75%), i.e., the sporadic pollution is halved by the application of the secondary criteria angular velocity and path length in the error limits given above.

The plotting accuracy has already been analysed in Section 3.2.1. Now, we are interested in the percentage of shower meteors which we do not recognise as such, since they do not meet the radiant of a certain diameter due to plotting errors. To obtain this percentage, the distribution of the resulting errors at the radiant (Figure 3.4) has been plotted cumulatively in Figure 3.10.

The diagram should be read as in the following example: 'For radiant distances D less than 20°, 90% of the meteors have resulting errors Δ at the radiant of less than 5°' or, 'If we consider a point-like radiant and assume its radius to be 5° for shower association, 10% of the shower meteors will be classified as sporadics due to plotting errors.' For this example the cumulative relative error number $H(r_\mathrm{R})$ is $H(r_\mathrm{R} = 5°) = 0.90$. Using Figure 3.10, we can obtain the second parameter for

Table 3.5: Optimum radiant radii and the corresponding percentages of sporadics classified as shower members for $HR_{spo} = 10$, different ranges of radiant distances, and different shower hourly rates HR_{sh}.

HR_{sh}	Rad.-dist. [°]	Opt. radius [°]	% spor. met. of HR_{sh}
1	< 20	3.7	25
	20–40	4.7	36
	40–60	5.3	41
	60–120	6.2	47
2	< 20	4.8	16
	20–40	6.4	25
	40–60	7.8	29
	60–120	9.2	35
3	< 20	5.3	13
	20–40	7.6	19
	40–60	9.2	23
	60–120	11.1	28
5	< 20	6.3	9
	20–40	9.0	13
	40–60	11.4	17
	60–120	14.3	21

the determination of the optimum radiant diameter, the loss l due to plotting errors:

$$l = \mathrm{HR_{sh}} \times \big(1 - 0.95 \times H(r_\mathrm{R})\big),$$

with HR_{sh} being the hourly rate of the shower. The factor 0.95 is for the 5% loss due to errors in the estimation of the angular velocity: $H(r_\mathrm{R})$ is the fraction of shower meteors meeting a radiant of radius r_R (if the real radiant is point-like) of which we classify 95% as shower meteors, while the remaining 5% are classified as sporadics due to erroneously estimated angular velocities.

It is our aim to determine the optimum radiant size to be assumed for shower association such that the losses due to observational errors are compensated for by the sporadic pollution. For this optimum radius r_opt the loss l is equal the sporadic pollution sp:

$$\mathrm{sp} = l;$$

$$0.0375 \times \mathrm{HR_{spo}} \times \frac{r_\mathrm{opt}}{5^\circ} = \mathrm{HR_{sh}} \times \big(1 - 0.95 \times H(r_\mathrm{opt})\big).$$

From this equation the optimum radiant radius r_opt follows by iterative computation. For a given radiant distance, i.e., for a given $H(r)$, we have HR_{spo} and HR_{sh} (not the shower ZHR!) as variables. HR_{spo} can be set to 10 for most of the year. The results shown in Table 3.5 were computed with the value of $HR_{spo} = 10$.

If the centre of the field of view is in the vicinity of the radiant, we can assume that the majority of the meteors will have radiant distances in the range of 20° to 40°. For a minor shower with $HR_{sh} = 1$ (which corresponds to a ZHR = 1.6 for 40° radiant elevation), more than one third of the meteors classified as shower members are actually sporadics, so that any computation of the population index, for example, is meaningless. The situation improves with increasing shower HRs. With about one quarter of the shower meteors being sporadics, $HR_{sh} = 2$ (which corresponds to a ZHR = 3 for 40° radiant elevation) we have a situation which can be considered a practical limit, while for higher shower rates the sporadic fraction becomes acceptably small. The high sporadic pollution is one reason for the fact that visual observations of very minor showers with maximum ZHRs of 1 or 2 are of little use. As the shower HR, rather than the ZHR, is decisive for the shower's observability, observers should take care to arrange their watches such that the radiant(s) under study are high in the sky. While a ZHR = 3 shower produces an HR_{sh} of 2 at 40° radiant elevation and can thus still be analysed, the same shower only produces an HR of 1 if the radiant is at 20° elevation.

Table 3.6: Part of Table 3.5 computed with a sporadic pollution of 8.25%, which results from considering the direction of path as the only criterion of shower membership.

HR_{sh}	Rad.-dist. [°]	Opt. radius [°]	% spor. met. of HR_{sh}
1	20–40	3	50
2	20–40	4	37
3	20–40	5	30
5	20–40	6	22

Taking the fraction of 25% sporadics as a limit, it can also be seen that we can analyse weaker showers if we observe closer to the radiant. If the observing field is located in the vicinity of the radiant, the characteristic radiant distance for the shower meteors seen will be 20° to 40°. In this range, the limit of 25% is reached for a shower HR of slightly less than 2. For an observing field at 90° distance to the radiant, most of the shower meteors seen will naturally have this distance. For this radiant distance, the limit is already reached at a shower HR of more than 3. This means that, when observing at large radiant distances, the limit for the HR of showers we can sensibly analyse increases by a factor of 1.5–2, plus there are also increasing problems in distinguishing between neighbouring shower radiants.

It may perhaps be doubted that the additional effort in assigning shower association required by the comparison of the observed angular velocity to the expected value improves the results in an equivalent way. To show the actual effect, Table 3.5 should be compared with Table 3.6.

When considering the percentage of sporadics classified as shower members as the limiting criterion, it becomes obvious that the application of all the criteria enables the useful analysis of weaker showers. Taking 25% for the range $20^\circ < D < 40^\circ$ as the limit of sporadic pollution, we can still analyse showers of $HR \approx 2$

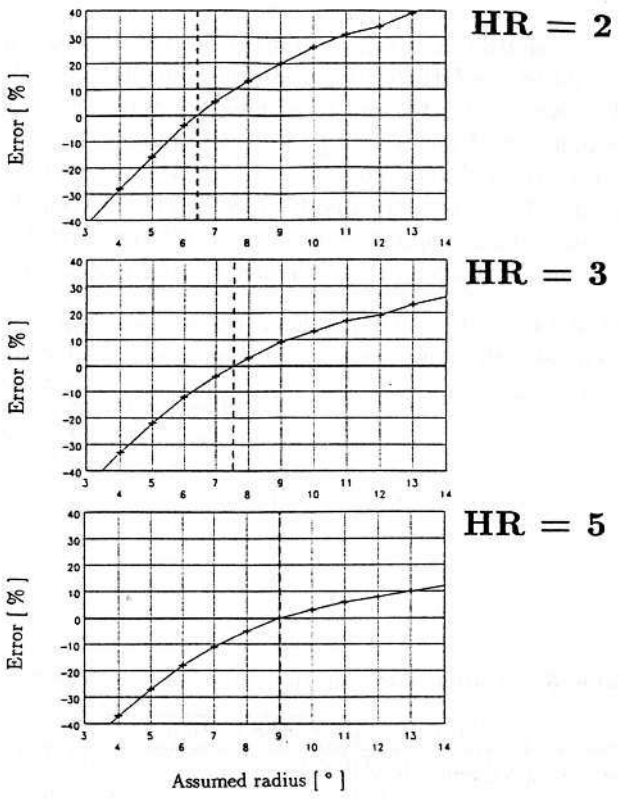


Figure 3.11: ZHR errors depending on the assumed radiant radius for radiant distances in the range 20°–40° and different hourly rates of a shower $HR_{sh} = 2$ (top), $HR_{sh} = 3$ (middle), and $HR_{sh} = 5$ (bottom).

if we apply all criteria (taken from Table 3.5). This limit increases by a factor of about 2 (HR ≈ 4) if only the path direction is used! This means that it is worthwhile to estimate the angular velocity of the observed meteors in degrees per second and then, at the desk, compare these observed values with the expected ones according to Table 3.3. The limit of ZHR = 2 (which corresponds to HR = 1.3 for 40° radiant elevation implying about 30% sporadic meteors) that the IMO sets in the shower list is the absolute minimum when considering all the criteria and assumes observing is carried out in the vicinity of the radiant. Weaker showers than this are simply not suitable for analysis by means of visual observations.

Figure 3.11 shows the errors of the HR (and thus also those of the ZHR) if other radiant sizes than the optimum radii are assumed. Low rates are most sensitive to incorrectly defined diameters. A difference between the assumed radius and the optimum one of 2°, for instance, causes a ZHR error of about 20% for an HR = 2 shower, but one of only about 10% for an HR = 5 shower. At the same time, the ZHR error is less if the radiant is assumed to be too large, than if it is taken to be too small by the same value. The sensitivity to small errors in the assumed radiant diameters is another important reason for the non-observability of very minor showers by visual techniques.

The quantity of 3.75% used for the computation of the sporadic pollution, and thus also for r_{opt}, is a statistical average that shows a considerable scatter, and it depends to some extent on the radiant position and the geocentric velocity of the shower. The sporadic HR was set to 10, which can differ more or less from the actual situation, and the plotting accuracy used for the determination of the loss l will be somewhat different from observer to observer. All this results in the fact that the optimum radiant diameters obtained here are not necessarily optimum in any given situation. Weak showers are most sensitive to this circumstance.

In order to make the practical procedure of shower association not too complicated, it is necessary to define the optimum radiant diameter for minor shower observations depending on the radiant distance of the concerned meteor only. If we additionally consider the shower HR, we come down to an iterative procedure that cannot be handled practically. If we base the optimum diameter on the values for HR = 3, the resulting errors for HR = 2 and HR = 5 (those minor showers within the range we can sensibly analyse) are only 15% at maximum. As soon as the ZHR of an individual shower reaches about 10 (corresponding to an HR ≈ 7 for a radiant elevation of 40°) the observing instructions recommend 'counting', i.e., assigning shower membership directly under the sky without plotting (cf. Chapter 2). In this case the radiant size chosen does not affect the ZHR as strongly as for lower activity. From the bottom diagram of Figure 3.11 (valid for HR = 5 and $20° < D < 40°$) it can be seen that the ZHR error due to incorrect radiant sizes is less than 10% for assumed radiant diameters between 14° and 26° (optimum 18°), and that the error is less if the diameter chosen was too large rather than too small. For higher HRs this range becomes even wider.

There is no problem with the reliability of shower association for ZHR > 10 showers with counting, while for a ZHR ≈ 3 shower it is essential to plot all shower candidates and to assume the optimum radiant diameters.

Up to now we have assumed point-like radiants, but a real radiant is a nearly circular area of a certain radius rather than a point. This fact is taken into account by increasing the optimum diameters obtained for point-like radiants according to the Gaussian error law. This leads to the final optimum *radiant diameters* to be applied for shower association. The values are listed in Table 3.1 at the beginning of this Chapter. For complex radiants, the respective sizes are considerably larger: 20° × 10° for the two Taurid radiants, 30° × 15° for the Antihelion Source.

3.2.5 Shower association in detail

First, select all the showers active on the date of your observation from the IMO's Working List of Meteor Showers (cf. Table 2.12 on page 57, or the annual *IMO*

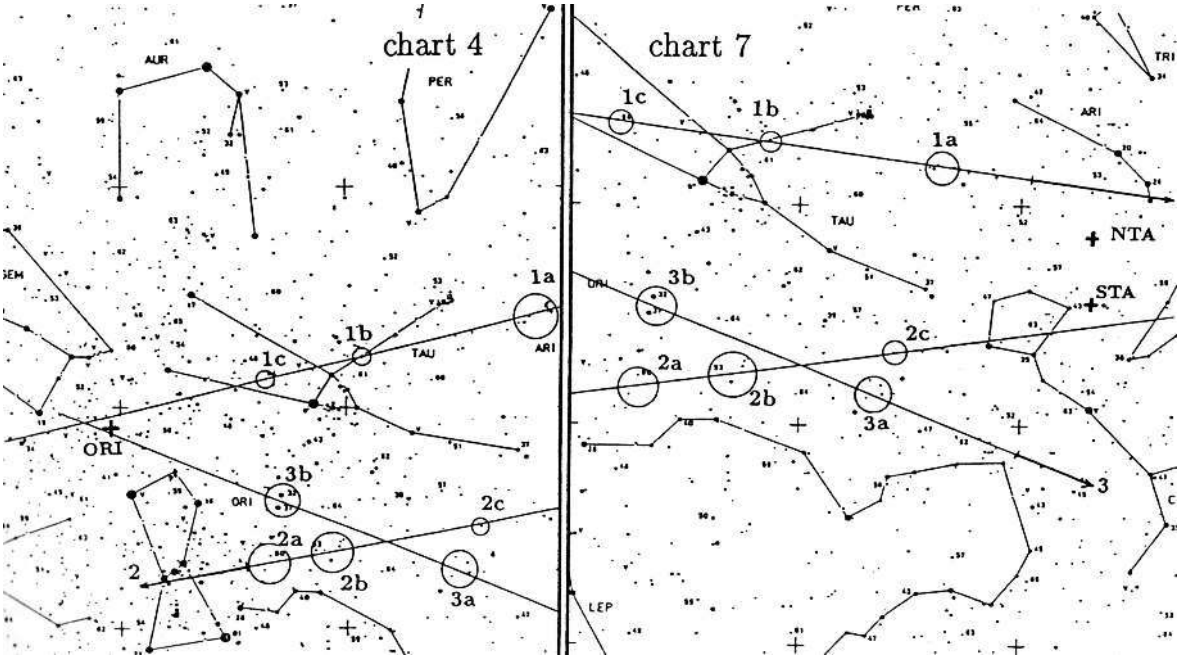


Figure 3.12: Examples for backward extensions of three meteor trails over the boundary of a chart. The reference stars in the overlapping region are marked. In this example we find meteors 1 (in Aries) and 3 (Eridanus–Cetus) were Orionids, and number 2 (in Orion) was a Southern Taurid.

Table 3.7: Scale s in mm/° for different distances d to the centre of the chart (valid for the original projection radius $R = 160.43$ mm).

d [mm]	0	50	100	120	150	170	200	220
s [mm/°]	2.8	3.1	3.9	4.4	5.2	5.9	7.1	8.1

Meteor Shower Calendar) and mark their radiant positions valid for that date onto the chart(s).

The radiant diameters obtained in the previous section are plotted as concentric circles (or ellipses for the complex radiants) onto the chart using the size given in Table 3.1. The scale is not constant over a gnomonic chart: a circle of a given angular diameter in the centre of the chart appears smaller than the same angular diameter near the edge of the chart. Table 3.7 shows the variation of the scale over the chart. As an example, a radiant of 20° diameter at 150 mm distance from the centre of the chart appears as a circle of 104 mm diameter.

Now we check the data of each meteor. If the backward extension meets a radiant area of the corresponding size, the meteor may belong to this shower, i.e., the necessary condition that the 'path can be extended backwards to the radiant' is fulfilled. It may happen that a meteor belongs to a radiant that is plotted on a neighbouring chart. The backward extension is prolonged onto this other chart by using stars which are present on both charts, i.e., stars in the overlapping region. You have to identify stars crossed or closely passed by the line on the neighbouring chart and plot the line in the corresponding position to these stars onto the second chart. Some examples can be seen in Figure 3.12.

Next, we check the condition that 'the path length must be shorter than half the angular distance radiant – start point'. Since this is a rough measure only, we can neglect the variable scale of the chart. The distances are measured using the ruler. If the condition is fulfilled, we can check the next parameter.

It reads 'the angular velocity has to correspond to the expected value within the error limits given in Table 3.3'. To check this condition you may use one of the many planetarium programs to determine the elevation of the start point of the meteor, and Table 3.3. You also need to know the angular distance between the radiant and the end point of the meteor.

Finally, determine the elevation of the meteor start point using a planetarium progam. Table 3.3 allows you to determine the expected angular velocity according to the entry velocity V_∞, radiant distance D and elevation h_b which we just obtained. This value has to be compared to the one you estimated during the observation. If the difference lies within the error limit, the 'angular velocity' condition is fulfilled. The error limits to be used are shown in Table 3.2. The table has to be read as in this example: 'If the angular velocity was expected to be 15°/s, the condition is fulfilled if the estimated value lies in the range 9–21°/s.'

If the meteor fulfills all three criteria it can be considered a shower member. Sometimes it may happen that a meteor fulfills the conditions for shower membership of two different showers. In this case you have to choose the most probable shower association, i.e., that shower the conditions are best fulfilled for. A meteor cannot be a member of two or more different showers. You *must* decide in favour of one shower.

3.3 Example shower association

3.3.1 Shower association – the data

Now we have described the procedures and details for shower association. Next we would like you to deal with an example observation. The meteor list for this exercise is in Table 3.8 and the chart with the meteor plots is provided in Figure 3.13. This chart also shows the radiant positions and the assumed diameters as given in the text with their sizes according to the pollution balance. Strictly, the Antihelion Source should be represented by an elliptical area of 30°× 15° (see Section 3.2.5).

Table 3.8: Meteor list for the exercise "shower association". Shw – shower, Mag – magnitude, Vel – angular velocity, Tr – train. For convenience, the beginning heights h_b above the horizon are given in the list.

Observer: *Otto Meier* **Date:** *2020 Dec 09–10*
Site: *λ =22.°5 E, φ =43.°1 N*

No.	Time [UT]	Shw.	Mag.	Vel. [°/s]	Tr. [s]	h_b [°]
1	*2130*		*3*	*10*		*15*
2	*2142*		*4*	*15*		*80*
3	*2143*		*1.5*	*20*	*2*	*35*
4	*2156*		*3*	*15*		*60*
5	*2201*		*2*	*8*		*30*
6	*2225*		*–0.5*	*10*	*1*	*45*
7	*2238*		*5.5*	*8*		*45*
8	*2253*		*5*	*20*		*50*
9	*2257*		*4*	*25*		*70*
10	*2311*		*0*	*7*	*1*	*40*
11	*2326*		*6*	*8*		*60*
12	*2334*		*1.5*	*10*		*50*
13	*2352*		*4.5*	*7*		*40*
14	*0018*		*1*	*10*		*30*
15	*002314*		*–5*	*10*	*20*	*75*

Finding the shower association allows you to check the procedure and you will also get some practical experience. The solution with a detailed explanation is given in Section 3.3.2. However, we suggest that you go over the list and try to apply the criteria before you read our explanations. Obtaining the heights of the meteors' starting point h_b for the observing location at $\varphi = 43°$ N using a planisphere valid for that latitude or using a planetarium program, we added these numbers in the last column. When analysing your own observations, you have to determine these by using a planisphere valid for your site or use a planetarium program which also gives the horizontal coordinates.

3.3.2 Shower association – the result

In the following explanation we use a number of abbreviations:
D – distance end point of the meteor–radiant;
l – path length of the meteor;
ω_0 – expected angular velocity;
ω – estimated angular velocity.

To recall the data of this observation, we list the essential information, adding the relevant shower parameters and the atmospheric entry velocities as given in the Working List of Meteor Showers and the individual shower descriptions. (These are given and described in detail in the *Meteor Shower Workbook*.)

Date: 2020 December 09/10
Site: $\lambda = 22.°5$ E, $\varphi = 43.°1$ N
Shower, radiant position and V_∞:

GEM	108°, +33°	35 km/s
MON	102°, +8°	43 km/s
ANT	90°, +23°	30 km/s
HYD	126°, +2°	58 km/s

No. 1 – Sporadic.
The backwards prolongation of the path meets the GEM radiant within the error limits. For GEM, $D = 55°$, we find $\omega_0 = 4°$/s. The difference $\omega_0 - \omega$ exceeds the limit of ±3°/s valid for $\omega_0 = 4.°5$/s.

No. 2 – Geminid.
The backwards prolongation of the path meets the GEM radiant within the error limits. l is shorter than half the distance radiant–start point. With $D = 50°$, we get $\omega_0 = 15°$/s. ω corresponds to ω_0. There is no other shower association possible for this meteor.

No. 3 – Sporadic.
The backwards prolongation of the path does not meet the HYD radiant within the error limits valid for 20° distance. l and ω are too large for HYD.

No. 4 – Geminid.
The backwards prolongation of the path meets the radiants GEM and ANT within the error limits. l is shorter than half the distance radiant–start point for both radiants.
ANT: $D = 30°$, $\omega_0 = 7°$/s.
GEM: $D = 45°$, $\omega_0 = 12°$/s.
ω lies within the error limits for GEM only, it is too high for ANT.

No. 5 – Monocerotid.
The backwards prolongation of the path meets the radiants GEM and MON within the error limits. l is shorter than half the distance radiant–start point for both radiants.
GEM: $D = 55°$, $\omega_0 = 8°$/s.
MON: $D = 35°$, $\omega_0 = 7°$/s.
ω corresponds to ω_0 of both radiants with nearly the same accuracy. Since the backwards prolongation passes the MON radiant closer than that of GEM, it is more probable that the meteor belongs to MON.

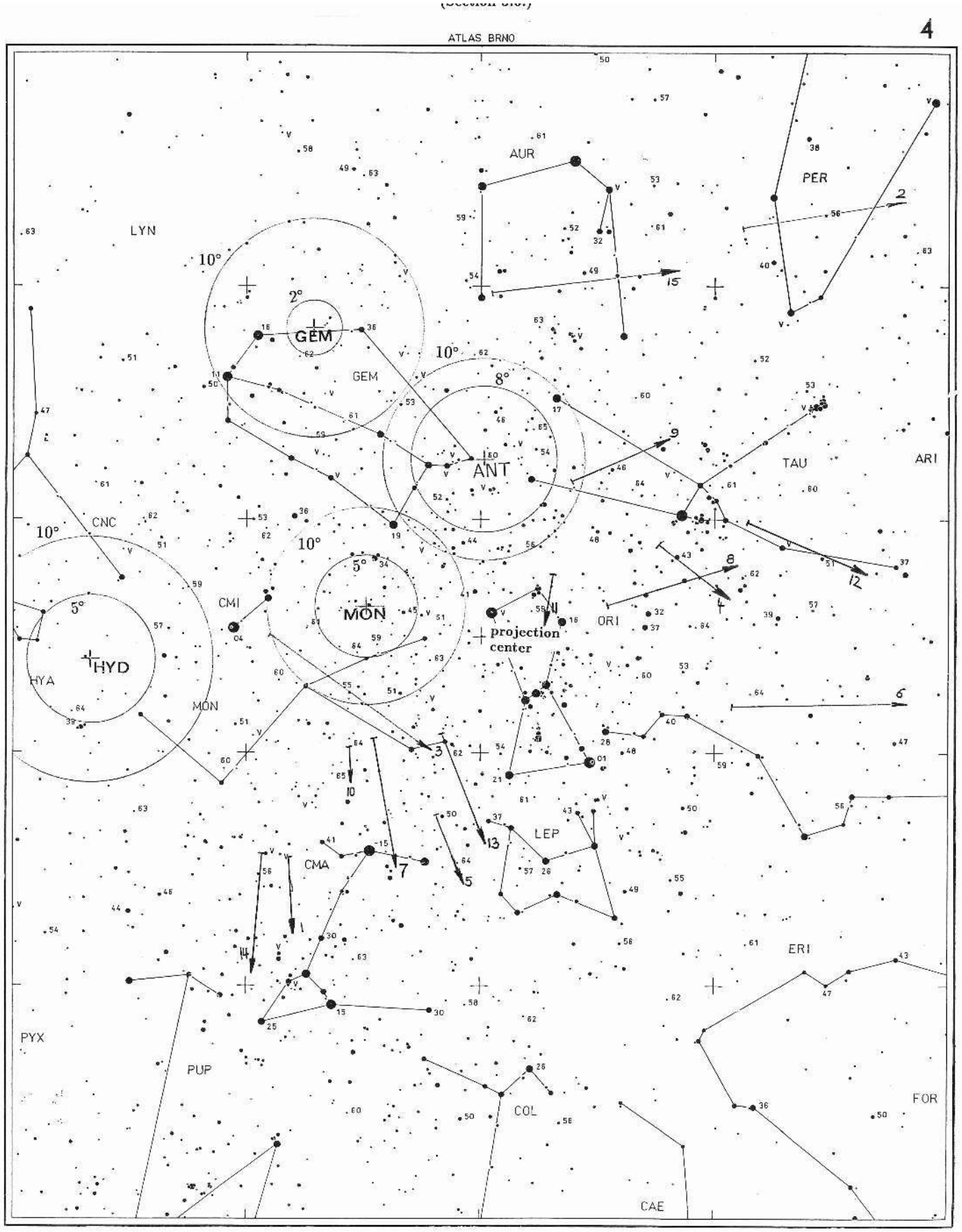


Figure 3.13: Map with the meteor plots referring to Table 3.8, page 83.

No. 6 – Sporadic.
The backwards prolongation of the path meets the radiant HYD within the error limits. l is shorter than half the distance radiant–start point. $D = 80°$, $\omega_0 = 19°/s$. The difference $\omega_0 - \omega$ exceeds the error limit which is $\pm 7°/s$ for $\omega_0 = 19°/s$.

No. 7 – Geminid.
The backwards prolongation of the path meets the radiants GEM and MON within the error limits. l is shorter than half the distance radiant–start point for GEM, but longer for MON.
GEM: $D = 50°$, $\omega_0 = 10°/s$.
MON: $D = 25°$, $\omega_0 = 7°/s$.
ω matches both radiants but since these are more than 30° above the horizon it is improbable that the meteor belongs to MON due to its path length.

No. 8 – σ-Hydrid.
The backwards prolongation of the path meets the radiant within the error limits. l is shorter than half the distance radiant–start point. With $D = 60°$, we get $\omega_0 = 20°/s$. ω matches the expected value very well. There is no other shower association possible for this meteor.

No. 9 – σ-Hydrid.
The backwards prolongation of the path meets the radiants MON and HYD within the error limits. l is shorter than half the distance radiant–start point for both radiants.
MON: $D = 35°$, $\omega_0 = 10°/s$.
HYD: $D = 55°$, $\omega_0 = 23°/s$.
ω lies within the error limits only for HYD.

No. 10 – Monocerotid.
The backwards prolongation of the path meets the radiants GEM and MON within the error limits. l is shorter than half the distance radiant–start point for both radiants.
GEM: $D = 45°$, $\omega_0 = 9°/s$.
MON: $D = 20°$, $\omega_0 = 5°/s$.
ω corresponds with both radiants with nearly the same accuracy. The very small tendency to GEM should not be decisive as long as there are still other criteria. The path of this bright meteor is short, despite the fact that the meteor is high above the horizon. Therefore, it seems more probable that it belongs to the MON radiant which is closer. In this case, the decision is rather uncertain. Deciding for GEM instead of MON does not constitute an error since the 'strong' criteria are fulfilled for both radiants.

No. 11 – Sporadic.
The backwards prolongation of the path just meets the ANT radiant within the error limit for $D \approx 20°$. Furthermore, the meteor is too fast for ANT.

No. 12 – Geminid.
The backwards prolongation of the path meets the radiants GEM and ANT within the error limits. l is shorter than half the distance radiant–start point for both radiants.
GEM: $D = 55°$, $\omega_0 = 12°/s$.
ANT: $D = 35°$, $\omega_0 = 8°/s$.
ω corresponds with both radiants with the same accuracy. Since the backwards prolongation of the path passes the GEM radiant closer than the MON radiant, it is more probable that the meteor belongs to GEM.

No. 13 – Monocerotid
The backwards prolongation of the path meets the radiants GEM and MON within the error limits. l is shorter than half the distance radiant–start point for both radiants.
GEM: $D = 55°$, $\omega_0 = 11°/s$.
MON: $D = 30°$, $\omega_0 = 7°/s$.
ω matches both radiants within the error limits but since the error for MON is remarkably smaller it is more probable that the meteor belongs to MON.

No. 14 – Geminid.
The backwards prolongation of the path meets the GEM radiant exactly. With $D = 60°$, we get $\omega_0 = 8°/s$. ω matches GEM within the error limits. Compare this meteor to meteor No. 1! While both of them have nearly the same position on the chart and the same angular velocity, only the latter one can belong to the GEM shower. The elevation of No. 1 above the horizon is much lower than that of this meteor, and No. 1 must therefore have a lower ω to be a member of GEM. This example demonstrates the use of a planisphere or a planetarium program in determining the elevation of the start point.

No. 15 – Geminid.
The backwards prolongation of the path meets the radiant within the error limits. l is longer than half the distance radiant–start point, but this is possible for fireballs penetrating deeper into the atmosphere than ordinary meteors. With $D = 55°$, we get $\omega_0 = 11°/s$. ω corresponds well with the GEM radiant. There is no other shower possible for this meteor.

3.3.3 Concluding remarks

A real observation will have less difficult cases than our example which was created to explain the steps of shower association in detail. This example demonstrates the limits of visual work, but it also shows that the careful application of the available information improves the value of plots upon the direct shower association when counts are carried out.

3.4 Summary of observing methods

In Chapters 2 and 3 we described techniques of visual meteor observations. Particularly for observations of medium to high rates, the *counting* method is regularly used. If the activity is low and minor showers are

the target of the observation, *plotting* is a recommendation as the uncertainties of single meteor perception are better balanced. A third method, called *reporting* is applied by some experienced observers. The observer gives positions of the start and end point of an apparent meteor path relative to the neighbouring stars or in coordinates, plus an information about the backwards prolongation as well as the angular velocity. This requires a very good knowledge of the sky. For example, meteor 3 in the exercise example (Table 3.8, path in the chart of Figure 3.13 can be described like "2° W αCMi to 1° W βMon, backwards δCnc, 1.5 mag, 20°/s". The accuracy is not meant and not sufficient for deriving radiants, but it allows to associate meteors quite reliably to known radiants and to confirm possible activity detected by other methods (video or radar). Both the *counting* and the *reporting* methods have the advantage that the view is not turned away from the sky while the *plotting* requires to look at the chart and to use a dimmed red torch which introduced dead time. Of course, the methods can be combined as described earlier.

In the report form shown in Figure 2.9 on page 52, the methods are abbreviated:
C – counting,
P – plotting,
R – reporting.

If you combined methods, give the relevant one per shower or interval. For example, you may start plotting all meteors in an October night. After some time it is obvious that the Orionids occur in higher cadence. So you switch to 'count' Orionids and sporadics, while you continue to plot Taurids and ε-Geminids. Then the column 'method' has 'C' for ORI and SPO, 'P' for all others from the respective intervals onwards.

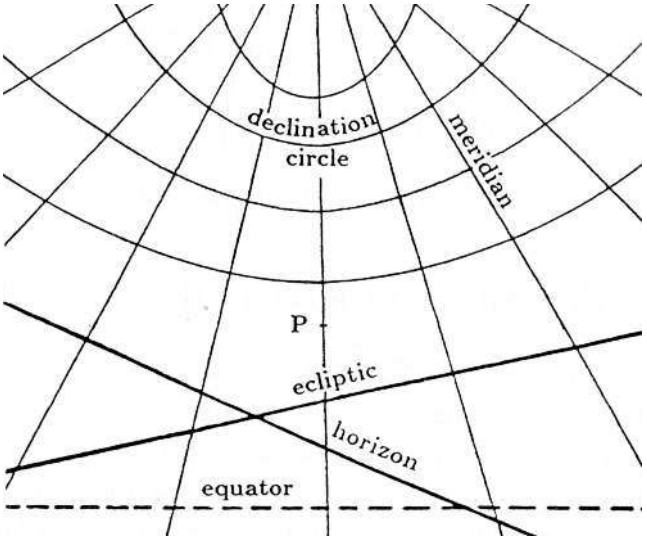


Figure 3.14: Great circles such as the equator, the horizon, all meridians and the ecliptic appear as straight lines on gnomonic maps.

3.5 Gnomonic Atlas Brno 2000.0

3.5.1 Atlas layout

The analysis procedures and plotting hints in this handbook refer to the *Atlas Brno 2000.0.* Due to its large scale and limiting magnitude, this Atlas' charts are the most suitable ones for meteor plotting known to the IMO. Observers are permitted to photocopy the charts for use in their own observations only. Please take care that the original scale remains unchanged when copying. Therefore always use the originals whenever you are going to make copies. For private use, maps can also be downloaded from the IMO's web page `http://www.imo.net/files/data/brno/`.

The following paragraphs describe the details of the Atlas and the mathematical formulae to convert cartesian coordinates in the maps into equatorial ones and vice versa. This is necessary if you wish to measure meteor trail coordinates, but not for the shower association as described above.

The concept of gnomonic projection requires some explanation. It is the only map projection that shows great circles as straight lines (Figure 3.14—thus all meteors can be drawn onto gnomonic charts as straight lines too. On other maps, such as those found in 'Norton's Star Atlas', most meteors would appear as sections of arcs. Figure 3.15 shows what is understood by gnomonic projection. As we mentioned earlier, meteors describe arcs on the celestial sphere that are parts of great circles. Such a circle determines a plane. Plotting a meteor then comes down to determining the intersection between this plane and the plane on which the stars were projected. Figure 3.15 shows two meteors and their great circles on the celestial sphere. Our gnomonic map is the plane tangent to the sphere at point P. The centre of projection is O. From O, all stars on the upper hemisphere are projected onto the plane of the map. On the gnomonic maps, small circles appear as conic sections (Figure 3.16).

3.5.1.1 Stars and constellations

The Atlas contains stars down to magnitude +6.5, according to the SAO Catalog, with the addition of a number of stellar objects not included in this catalog. Since it is mainly designed for use by naked-eye observers, binary and multiple stars are not marked. Objects separated by more than 3′ are recorded separately, while those closer together are depicted as one object, provided their total brightness is over the lower limit of the Atlas. Variable stars are drawn according to their maximum brightness, and where the amplitude of their variations is larger than half a magnitude, they are marked with the letter 'V'.

Reference stars were selected so as to have a small colour index $(B-V)$ in the UBV system; reference stars fainter than +4.5 have $(B-V)$ smaller than half a magnitude $(B-V=0\cdots+0.5)$, but in view of the lack of suitable bright reference stars, the value of this limit increases to $B-V=+1.25$ for stars brighter than magnitude +1.5. The brightness of the reference stars is expressed in units of 0.1 magnitude, without a decimal point. Sirius (α CMa) is noted as '−15' on the Atlas,

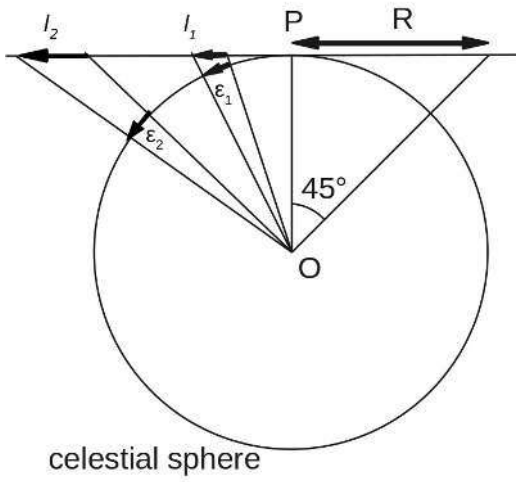


Figure 3.15: Gnomonic projection. The value of R defines the scale of the chart (Atlas Brno charts have $R = 160.43$ mm). P is the centre of projection. The arrows imitate meteors of equal angular length $\epsilon_1 = \epsilon_2$ and their projection onto the chart with different lengths $l_1 < l_2$. If you copy the original maps and perform coordinate measurements, please check the scale. In the original maps the thin crosses mark 70 mm distances.

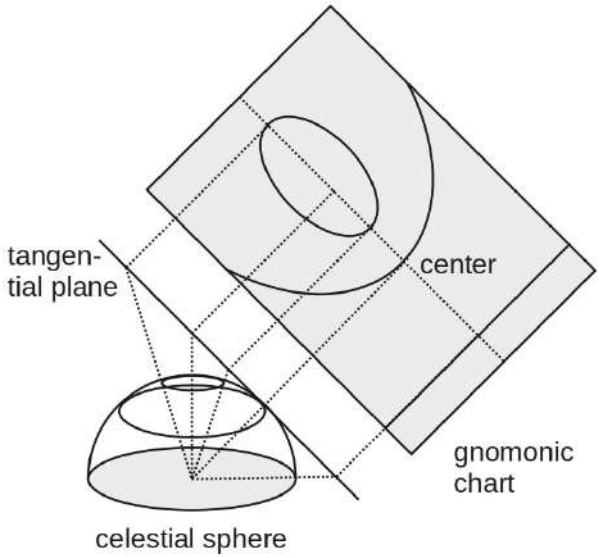


Figure 3.16: The sphere is projected onto a tangential plane. Small circles such as the declination parallels are mapped as conic sections.

which means its magnitude is −1.5. Rigel (β Ori) is '01' (which means +0.1 mag). Variable stars were not used as reference stars, though some of them have quite a low amplitude (e.g., Capella, α Aur).

Star disc diameters on the maps are in units of 0.7 magnitudes, from magnitude +6.5 upwards, in nine classes of magnitude. The positions of all stars was calculated for the epoch 2000.0, taking into account their proper motions.

Most constellations are depicted with the customary alignments joining their stars, as an aid to orientation. Their names are represented by the official three-letter abbreviations, in capital letters.

3.5.1.2 Page arrangement

The Atlas contains 12 pages covering the entire sky. The competing demands for a large-scale atlas, along with an overlap of at least 20° between adjacent maps, has led to a rather unconventional arrangement of pages. The page arrangement is based on a representation of the whole sky as a dodecahedron with one of its apices at the North Pole. The nine 'uppermost' faces were then optimised with regard to position and shape, in view of the rectangular form of the individual maps. It was thus possible to achieve a scale of 2.8 mm/1° at the centre of the maps, with a map size of 280 mm × 350 mm. The whole set of maps was then turned in right ascension, so that most of the radiants of the main meteor showers were closer to the centre of the maps.

3.5.1.3 Coordinates

The atlas contains guidance marks in the form of a set of coordinates at 70-mm intervals (25° according to the scale at the centre of the map). Projection or reading of positions according to these is much more precise than in terms of right ascension and declination. The conversion factors are simple, and, given the present widespread use of calculators and small computers, easy to perform.

From the X and Y coordinates, with their origin at the bottom-left corner of the map (in mm, X-axis to the right, Y-axis upwards), the conversion to standard coordinates (x, y) with regard to the centre of the map goes as follows:

$$x = (X - X_0)/R; \quad (3.1)$$
$$y = (Y - Y_0)/R; \quad (3.2)$$
$$X = X_0 + Rx; \quad (3.3)$$
$$Y = Y_0 + Ry, \quad (3.4)$$

where R is the radius of the projection and (X_0, Y_0) the position of the centre of the map. With a distance of 70 mm between the marks on the map, $R = 160.43$ mm. For maps 1 to 3 and 7 to 12, $X_0 = 175$ mm and $Y_0 = 140$ mm; for maps 4 to 6, $X_0 = 140$ mm and $Y_0 = 175$ mm.

We further define the direction vector of an object by means of the relationships:

$$p = \sin\delta; \quad (3.5)$$
$$q = \cos\delta\sin(\alpha - \alpha_0); \quad (3.6)$$
$$r = \cos\delta\cos(\alpha - \alpha_0), \quad (3.7)$$

where α and δ are the right ascension and declination of the object and α_0 is the right ascension of the centre of the map (given in degrees in Table 3.9).

The calculation of the position of an object on the map starts with the calculation of the direction vector using system (2). Then calculate $s = p\sin\delta_0 + r\cos\delta_0$, with δ_0 the declination of the centre of the map; the

Table 3.9: Right ascension α_0, declination δ_0 and cartesian coordinates X_0 and Y_0 of the centre of each map in the Gnomonic Atlas Brno 2000.0.

Map				1	2	3
α_0				30°	150°	270°
δ_0				55 °.68	55 °.68	55 °.68
X_0				175	175	175
Y_0				140	140	140
Map	4	5	6	7	8	9
α_0	90°	210°	330°	30°	150°	270°
δ_0	4 °.89	4 °.89	4 °.89	−4 °.89	−4 °.89	−4 °.89
X_0	140	140	140	175	175	175
Y_0	175	175	175	140	140	140
Map	10	11	12			
α_0	90°	210°	330°			
δ_0	−59 °.29	−59 °.29	−59 °.29			
X_0	175	175	175			
Y_0	140	140	140			

values of δ_0 are also given in Table 3.9. If $s < 0.582$, the object cannot be drawn on the map. The standard coordinates of the object are then given by the relationship:

$$x = -q/s; \quad (3.8)$$

$$y = (p\cos\delta_0 - r\sin\delta_0)/s, \quad (3.9)$$

from which it is easy to calculate the coordinates (X, Y), using relation (1).

In the other direction, one has to calculate first the standard coordinates using (1) and the polar radius $t = \sqrt{1 + x^2 + y^2}$. The components of the direction vector are then given by:

$$p = (\sin\delta_0 + y\cos\delta_0)/t; \quad (3.10)$$

$$q = -x/t; \quad (3.11)$$

$$r = (\cos\delta_0 - y\sin\delta_0)/t, \quad (3.12)$$

from which the values of α and δ can be determined using the system in (2)

$$\delta = \arcsin p; \quad (3.13)$$

$$\alpha = \begin{cases} \arccos\frac{r}{\cos\delta} + \alpha_0 & (q \geq 0) \\ 360° - \arccos\frac{r}{\cos\delta} + \alpha_0 & (q < 0) \end{cases} \quad (3.14)$$

If you find that $\alpha > 360°$, subtract 360°.

3.5.2 Measuring X, Y coordinates from Atlas Brno

For reporting positional data it is important that the scale of the charts remains unchanged. This means the distance between the thin crosses has to be 70 mm. The origin of the X, Y coordinates is located in the bottom left corner of the chart (X-axis to the right, Y-axis upwards). The reference lines are the *inner* ones, not the thick (outer) lines. Photocopiers often tend to change the original scale. Therefore, use the *originals* you bought whenever you are going to make copies. Otherwise you merely add to the errors. If the scale error exceeds 3 mm over the whole length of the chart (i.e. if the distance between the thin reference lines differs by more than 3 mm from 280 mm for the short side and/or 350 mm for the long one) you should use another device.

In order to minimise the influence of the remaining scale errors, the coordinates for a given meteor must refer to the same coordinate lines. A ruler of at least 35 cm length is recommended. An example is shown and described in Figure 3.17.

3.5.3 Apparent path length

Assuming constant beginning and end altitudes (H_b, H_e) for meteors belonging to a certain shower, one can calculate the expected apparent path length l for members of the shower depending on the elevation of the radiant h_R, the elevation of the start point h_b, and the angular distance between the radiant and the start point D_b:

$$s = \frac{H_b - H_e}{\sin h_R};$$

$$e_b = \frac{H_b}{\sin h_b};$$

$$e_e = \sqrt{e_b^2 + s^2 - (2 \times e_b \times s \times \cos D_b)};$$

$$l = \arcsin\left(\frac{s \times \sin D_b}{e_e}\right).$$

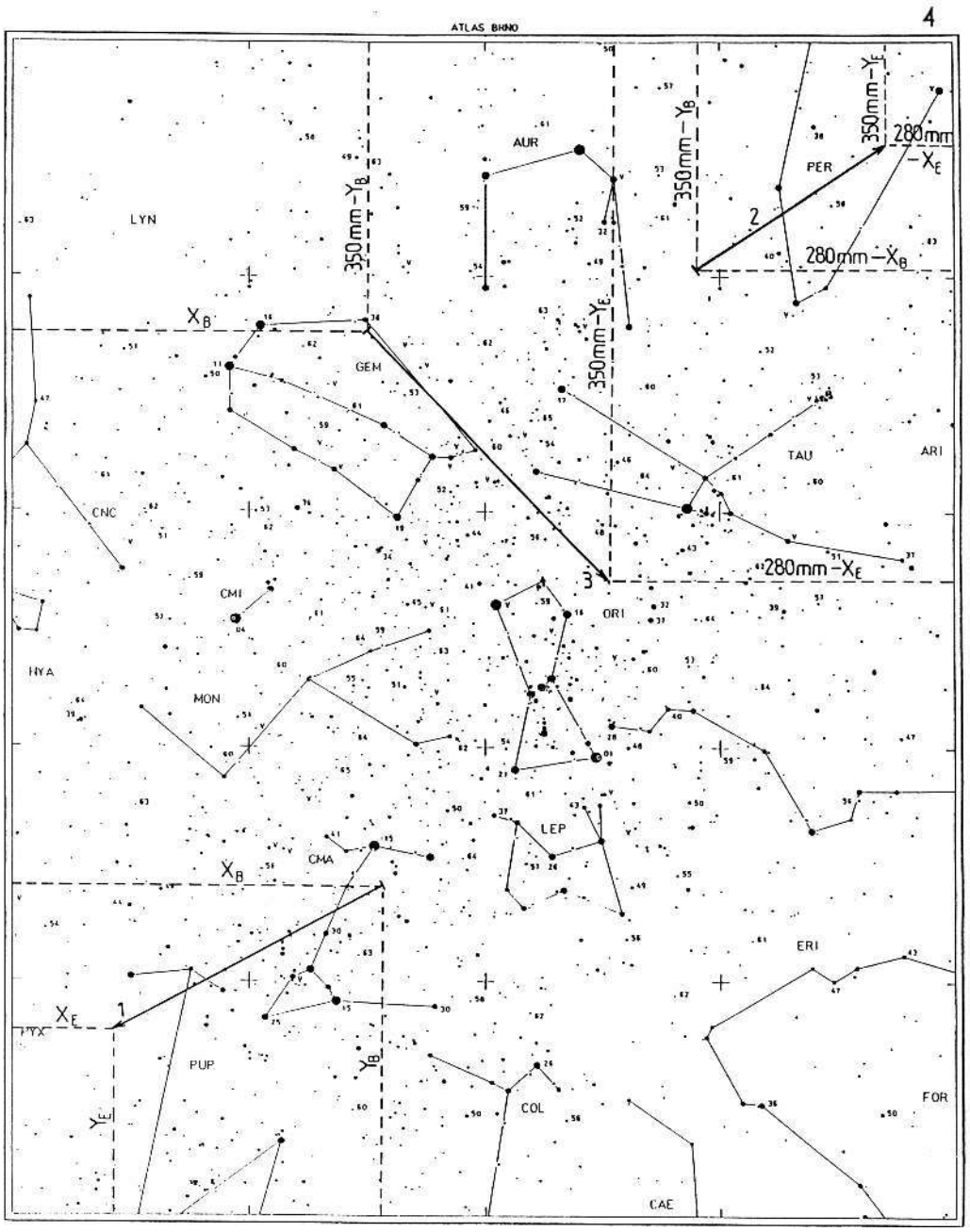


Figure 3.17: Example of coordinate measurements on chart No. 4. Meteor No. 1 was plotted near the bottom-left corner. Here it is opportune to coincide the zero of the ruler with the left vertical reference line and to measure the distance of the start point and the end point to that line (X-coordinates). Measuring of the Y-coordinates is based on the bottom horizontal line. For meteor No. 2 in the upper-right corner it would be useful to coincide the 280 mm label of the ruler with the right vertical reference line (for X-coordinates) and the 350 mm label with the upper horizontal line (for Y-coordinates) in order to avoid measuring long distances. For meteors plotted in the middle of the chart, like meteor No. 3, it is possible to measure, for example, the X-coordinate of the beginning point from the left line and that of the end point from the right one. In the first two cases, a small scale error results in a small parallel shifting of the path which is not important, but in the last case the same small scale error results in a tilt of the path which should be avoided. Thus, both X-coordinates, X_B and X_E, have to refer either to the left or to the right reference line.

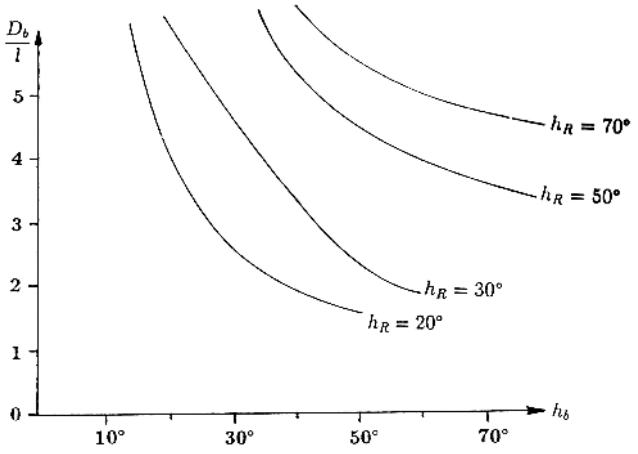


Figure 3.18: The quotient D_b/l for $D_b \leq 30°$ as a function of h_b for several elevations of the radiant h_R. Calculation was carried out using $H_b = 100$ km, and $H_e = 80$ km.

For given beginning and end altitudes, l depends on three quantities: h_R, h_b, and D_b. To visualise this dependence we would have to construct a 4-dimensional diagram which is impossible. This means that the criterion is quite difficult to handle. But calculating l for several combinations of beginning/ending altitudes, one finds

$$\frac{D_b}{l} \approx \text{ constant for } D_b < 30°.$$

This means that the l-criterion can be used favourably in the vicinity of the radiant. In that region, shower meteors distinguish themselves from sporadics by their short paths. Of course, extremely short trails occur only in the immediate vicinity of a radiant: Gural (2002) derived a frequency of one meteor shorter than 5 arcminutes every 10 000 meteors from computer simulations. Bearing in mind that the end altitude depends on the particle mass and material it is opportune to assume it is such that the calculated l is considered to be the upper limit for shower membership. Thus it was assumed $H_b = 100$ km and $H_e = 80$ km. The result is shown in Figure 3.18.

It can be seen that radiants having low elevations produce long meteor paths (small value of D_b/l). The higher the meteor appears in the sky the closer it is to the observer, and thus, the true trail length is seen over a larger angle (apparent path length l). The application of the quantities shown in Figure 3.18 for shower association is problematic since end altitudes can vary greatly and the path length is much more affected by plotting errors than the direction. Therefore, we can establish only a general rule:

For radiant elevations higher than 30°, the distance between radiant and start point of a plotted meteor on the chart has to be at least twice as long as the meteor path itself if the meteor is a suspected shower member.
Bright fireballs generally penetrate deeper into the atmosphere and thus may produce longer paths.

Looking at Figure 3.18, the formulation of the rule seems to be too weak, since factors of 3–5 will be valid for most meteors, but in strengthening the rule there is the danger of classifying a considerable number of shower meteors in the vicinity of the radiant as sporadics, due to short paths being plotted as too long. Experience shows that a factor of two is strong enough for distinguishing sporadic meteors meeting the criteria of path direction and angular velocity, within certain error limits, from real shower meteors.

References

Arlt R., 1992: The software Radiant. *WGN* **20,** 62-70.
Gural P.S., 1999: A rigorous expression for the angular velocity of a meteor. *WGN* **27,** 111–114.
Gural P.S., 2002: On the frequency of pointer meteors and grazers. *WGN* **30,** 149–151.
Koschack R., 1991: Analysis of visual plotting accuracy and sporadic pollution and consequences for shower association. *WGN* **19,** 225–241.
Kresák Ľ., Porubčan V., 1970: The dispersion of meteors in meteor streams. *BAC* **21,** 153–170.

4 | Video observations

Sirko Molau, Pete Gural

4.1 Introduction

Video observation is the youngest and most advanced observing technique in meteor science. Professional astronomers started to use video equipment at the beginning of the nineteen seventies, among amateurs the Japanese (1986) and Dutch (1987) observers have been the first using this technology (Molau et al., 1997). By now, video observations of amateurs have reached a high scientific level and are highly recommended for almost every branch of meteor research. Video systems are of particular interest as they can run continuously on every clear night with an automated computer software pipeline. Such regular monitoring started in Germany in 1999, which later evolved to the IMO Video Meteor Network that has been growing ever since. Other large video networks have also been established in Poland (2004), Japan (2004), in the United States (2010) and in France (2015).

When we talk about video systems, in most cases we refer to recording of a live multi-frame image stream of the sky. In the early years, the term (low light level) TV observations (LLLTV) was used, but the suggested broadcast of television signals is misleading with today's camera technologies and we prefer the word video.

Video observation has a number of advantages over other observing methods, to some extent it combines positive features of other techniques. Video systems have the light-collecting power of a visual or even telescopic observer, but with much higher accuracy and unlimited endurance. All important meteor parameters such as time, position, brightness, colour, velocity and deceleration can be determined with high precision. It is possible to record light curves, meteor spectra, trains, wake, and fragmentation processes of the meteoroid. Due to lower spatial resolution, the positional accuracy of video meteors falls a bit short of photographed meteors, but that can be compensated by using high definition video cameras or operating an array of video cameras, each with smaller fields of view. In addition, video systems obtain several orders of magnitudes more meteors than any photographic camera thanks to the significantly better limiting magnitude. Also the degree of automation is high in the optical domain, which makes this observing method one of the first choices for amateurs doing automated meteor monitoring and data collection.

4.2 Hardware

In the early days, video cameras were too insensitive to be used stand-alone for meteor recording and mainly image-intensified meteor cameras were used. These consisted of three main components: a fast lens, a powerful image intensifier, and a video camera. The lens projects the sky on the sensitive photocatode, and the camera records the amplified image from the intensifier's fluorescent screen.

In the early 2000's, a new generation of CCD cameras reached the consumer market of surveillance cameras and became increasingly popular among amateur astronomers. Thanks to special CCD chips with noise-reduced read-out electronics (some with microlenses on top of each pixel), these cameras were found to be powerful enough to be used directly for meteor observations (unintensified). Typical brands used by amateur astronomers were Mintron and Watec.

In the last few years, there has been a shift from CCD to CMOS technology, which also reached the meteor observer community. The limiting magnitude of the latest CMOS cameras has added an additional one magnitude beyond CCD-based cameras, and typically offer higher high-definition (HD) pixel counts than the PAL/NTSC video standards. Since highly sensitive cameras are required in ever growing quantities in the consumer industry (e.g. for autonomously driving vehicles and night surveillance around facilities), their price has been falling steadily.

A minor drawback of most CMOS-based systems is the so-called "rolling shutter". CCD cameras used a global shutter where the entire focal plane's pixels were exposed at the same time. With a rolling shutter, each row of pixels have a different exposure start and end time, which needs to be corrected for when the video signal is analysed. Fortunately a simple temporal correction method has been developed (Kukic et al., 2018). Intensified and unintensified cameras have certain characteristics which makes them particularly helpful for certain use cases. With respect to sensitivity, intensified cameras have their advantages. Under clear dark skies, an optimised intensified camera system records about a factor of three to four more meteors than an optimised unintensified CCD-based camera. This makes intensified cameras most useful for applications where good limiting magnitudes and high meteor counts are required (e.g. for meteor spectra recordings, flux estimation for small mass meteors, observation of meteor

outbursts and telescopic meteors, meteor cluster analyses, persistent trains – see Figure 4.1). Disadvantages of intensified systems are the limited lifetime of the intensifier tubes (typically between 10^4 and 10^5 hours) and their limited robustness. Image intensifiers can easily be damaged or destroyed by improper handling (e.g. moon inside the field of view, accidental operation in twilight or daylight).

Unintensified cameras are much easier to handle – you only need to care that the Sun never enters the field of view. In fact, even that is not an issue anymore if you have a lens with auto-iris or a fireball camera with a short focal length and a large field of view. Therefore, these cameras are the best choice for long-term automated meteor activity monitoring. In fact, the vast majority of cameras operated in the video meteor networks around the globe are unintensified these days. An unintensified camera is cheaper than an intensified system, but also here the lifetime is limited. It was observed in practice that the camera sensitivity reduces significantly after a few years of operation due to ageing effects.

With the spread of the latest CMOS-based cameras, the days for intensified cameras are numbered. This new camera generation reaches the same sensitivity as intensified cameras, but it comes with all the advantages and robustness of unintensified cameras. Their higher spatial resolution and large dynamic range makes them perfectly suited for meteor studies of any sort.

4.2.1 Intensified cameras

The core components of an intensified video system is the image intensifier. Preferably it should have a gain $> 10\,000$, a photo cathode diameter ≥ 25 mm, and as little noise and image distortion as possible. There are different generations of intensifiers available.

First generation intensifiers often do not have the power required for meteor observation unless they contain three stages of amplification. Even then, they are more noisy than intensifiers of later generations, which is why they are not used for meteor observation anymore.

Second generation intensifiers contain a micro channel plate (MCP) which improves the image quality significantly. They often combine a high gain with small distortion of the field of view and little noise. These devices are well suited for meteor observation. Best experiences were made with the Philips XX1332 tube, which has a photo cathode of 50 mm diameter and a high gain (Figure 4.2). In combination with a fast photographic lens (e.g. $f = 50\,\text{mm}$ $f/1.4$), such a system records more meteors at the same time than a skilled visual observer!

Image intensifiers of generation two and a half are of similar design, but have an extended sensitivity in the infrared range, which is typically not required for meteor observations.

Third generation intensifier use Gallium Arsenide as photoelectric material which gives them higher sensitivity and a much longer lifetime than second generation tubes. They also have a flatter and more even speckle noise response across the sensor. Of course, the better quality has its price which is outside the affordable range for most amateurs.

To get image intensifiers at a reasonable price you should check for military surplus devices, e.g. at Ebay. Beware that export restrictions for military equipment apply, which is why in some countries (e.g. USA) they are not allowed to be sold abroad or even transported round-trip across country borders.

The type of observation you intend to carry out determines the lens to be used. In general, the lens should be as fast as possible for the focal length used. Photographic lenses are a good choice, as there is a large variety of them available at low cost. They were designed for photographic film, which is why vignetting is typically not an issue. However, with today's small $1/3''$ format CMOS cameras, one can use very inexpensive CCTV lenses with $f/1$ focal ratios that are much cheaper than photographic lenses and produce the same quality of image sharpness across the field of view. Just make sure the "format" of the CCTV lens is at least as large as the format of the CMOS or CCD sensor. That is you can use a $1/2''$ format lens on a $1/3''$ format sensor, but not vice versa without suffering vignetting and coma effects.

The longer the focal length of the lens, the smaller the field of view and the fainter the average meteor recorded by the system. The improved limiting magnitude almost compensates for the decreasing field of view diameter, which is why (in the absence of major showers) the meteor count reduces only moderately, as the percentage of sporadic meteors is increasing with the limiting magnitude due to their larger power law population index.

There are only a few constraints for the video camera. In principle every video camera can be used, even simple b/w CCD video surveillance cameras do a good job. Manual gain and brightness control may be of help under certain circumstances but is not a must except for the very sensitive CMOS systems where having gain control is a necessity. The strength of (digital) camcorders is their ability to store the video signal for offline processing, which is helpful in the case of expeditions. In automated observation schemes, however, the video signal is immediately processed by a computer, which makes the requirement for intermediate storage obsolete.

4.2.2 Unintensified cameras

In the meteor observer community, the Mintron 12Vx and Watec 902Hx were the most frequently used until recently. Both of them contain a highly sensitive $1/2''$ ExView HAD CCD chip from Sony and both have a comparable price. The Mintron camera allows to integrate up to 128 frames internally. For meteor observers, two frames integration is the best choice as the temporal resolution is not reduced. The integration time of the Watec camera is fixed at 1/50 s (PAL) respectively 1/60 s (NTSC). In practice, the Watec still seems to be

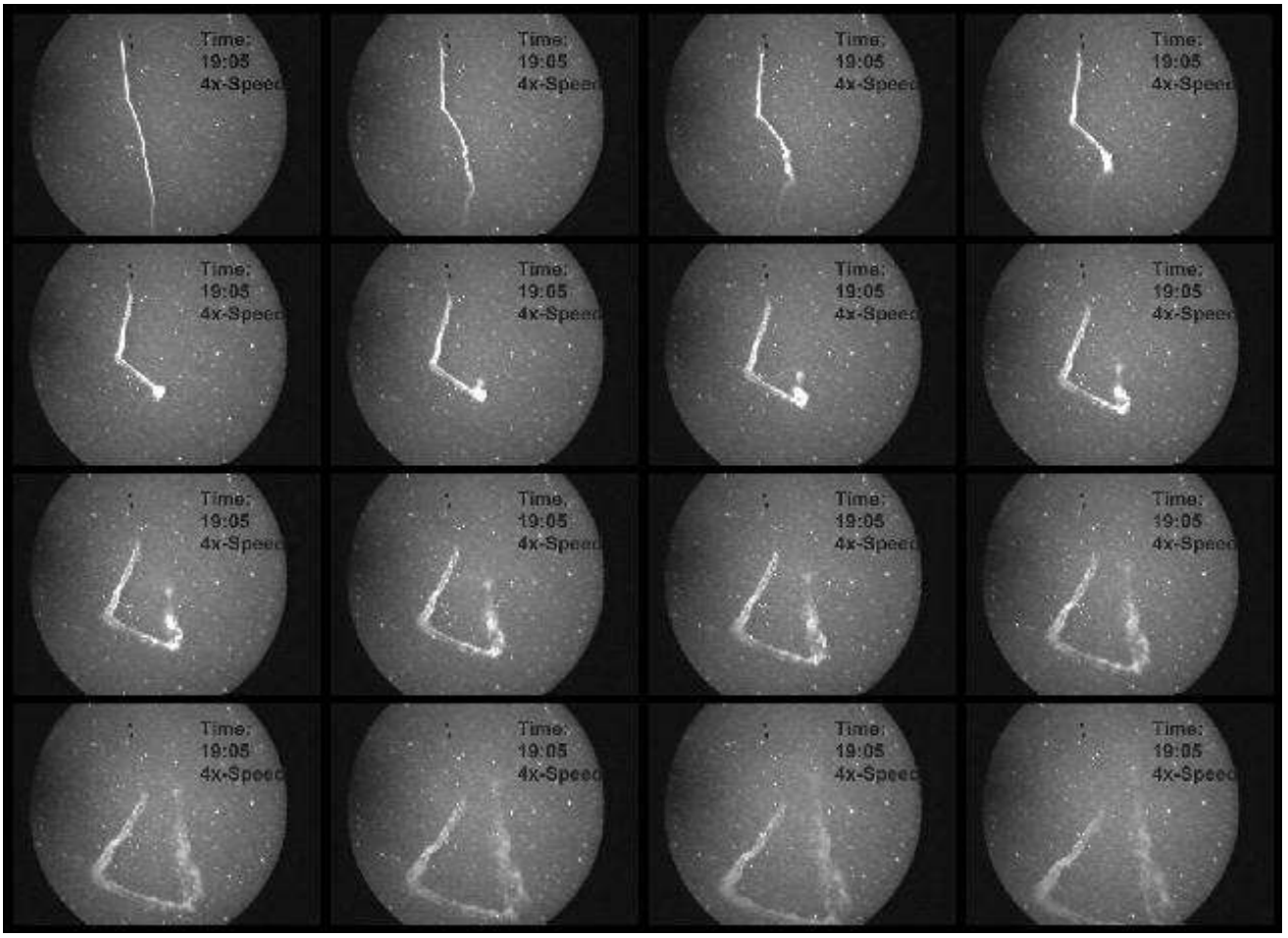


Figure 4.1: The evolution of a persistent train of a fireball recorded during the 1998 Leonids in Mongolia.



Figure 4.2: The Philips XX1332 image intensifier tube.

a bit more sensitive than the Mintron camera. Today, CMOS chips from Sony using (e.g. the IMX 290/291 sensors) are being deployed in meteor systems around the world with greater sensitivity than the Mintron and Watec and one-fifth the cost when they come in a IP board camera form factor.

Around 2015, the first press releases circuited that Sony would cease the manufacture of CCD chips. Though it was not clear if that would only affect the consumer market or also industrial equipment, it soon became difficult to buy new Mintron cameras, for example, which affected different branches of amateur astronomy. In search for a good replacement, the RunCam Night Eagle camera series was found. Their prime field of application is FPV (first person view) for drones and model aircrafts, but thanks to their lightweightness and sensitivity, they were also well suited for astronomical purposes. In fact, there is even an "astro edition" of this camera. First meteor observations with this camera model were conducted in 2018 and proved, that the RunCam outperforms the high-end models of Mintron and Watec, but costs only a fraction of them. So it is the first choice for replacement of old CCD cameras coming to their age.

Any c/cs-mount lens can be used with all of these cameras. The lower the f-stop, the better. Particularly popular is a series of aspherical $1/2''$ c-mount lenses by Computar. They come at different focal lengths (e.g. 3.8 mm, 6 mm, 8 mm, 12 mm) with a fast f-stop of $f/0.8$. Especially the 3.8 mm, 6 mm and 8 mm lenses are frequently used by meteor observers, as they yield a large field of view ($67° \times 89°$ / $43° \times 57°$ / $34° \times 45°$) at a reasonable limiting magnitude (3 to 6 mag). Unfortunately, Computar has discontinued this series of aspherical lenses many years ago, and meanwhile you do not find them even at Ebay anymore. Also the c-

mount lenses from Panasonic with similar parameters are hard to find. For this reason, meteor observers have switched to vari-focal lenses with slightly worse f-stops, but also here things are changing. We have successfully tested fixed-iris machine vision lenses which reach the same limiting magnitude as Computar lenses, but cost only a fifth of their original price.

4.3 Analysis of video observations

Independently whether the video signal is processed online, or whether it is intermediately stored on video tape or hard disc, there are three main stages in the analysis of video data: first the meteors have to be detected and extracted from the video data stream, then they need to be measured in order to determine the basic meteor properties (position, brightness, velocity), and finally the recordings from different stations are combined to calculate the atmospheric trajectory and the orbital elements of the meteoroid. In the early days of video observation, most of this work had to be done manually with only limited support by computers. Later powerful software packages have been developed for the fully automated analysis of video observations. Well-known are the MetRec software (author: S. Molau), the UFO tool suite (author: SonotaCo), and the CAMS software suite of applications for capture through orbital estimation (author: P. Gural).

4.3.1 The MetRec software

MetRec (*Met*eor *Rec*ognizer) is a real-time software package for the automatic detection and analysis of video meteors (Figure 4.3), which was first presented at the 1998 IMC (Molau, 1999). In can be used both offline for the inspection of video tapes and online for an automated video meteor camera. It does the first two stages of meteor processing (meteor detection and measurement) in a single pass, but offers no function to combine observations from different stations for trajectory and orbit calculation. So the prime focus is on single-station meteor observation. There are converter tools that transform the MetRec output such that it can be read by UFOOrbitV2, or to import it to databases like EDMOND. MetRec is primarily used by observers of the IMO Video Meteor Network.

MetRec analyses in real-time half resolution grey scale PAL or NTSC video frames at the full rate of 25/30 frames per second. It stores the appearance time of meteors, a sum image and a sequence from each event. MetRec computes the meteors brightness, its velocity and equatorial coordinates, and determines the meteor shower it belongs to.

Every minute, the software calculates and stores the average limiting magnitude in the field of view. This allows for the determination of meteor shower flux densities on the fly, which are uploaded to the meteorflux website (`https://meteorflux.org`), where both real-time and historic meteor shower flux profiles can be generated (Figure 4.4). As a by-product, the software measures up to over 10^6 individual star positions every night, which leads to highly accurate lens distortion models and allows to track and correct the camera motion during the night (e.g. by thermal instabilities of the mount) down to 1/100th of a pixel.

MetRec is highly flexible – it can be adapted to each individual system with a number of parameters to be set in a configuration file. All output is written into a text logfile. During recognition, the current input signal and the system state is displayed at the computer monitor.

MetRec is complemented by additional tools to efficiently measure reference stars, remove false detections from the data after observation, creating panoramic images from meteor showers and search for radiants and meteor showers by a probabilistic algorithm.

MetRec was originally designed for DOS and later ported to the Windows operating system. It still runs under DOS and any 32-bit version of Windows up to the latest Win 10 release. MetRec is undemanding regarding the required PC hardware, almost any used desktop computer will work. In fact, a number of MetRec instances can run in parallel on the same computer, limited only by the number of PCI slots of the system. To digitise the analog video signal, MetRec requires a Matrox Meteor II frame grabber. These frame grabbers were discontinued after almost ten years of production in 2007, but are still readily available at Ebay, because they were widely used in machine vision and medicine. The data transfer, processing and storage is done uncompressed. MetRec does neither work with TV cards or any frame grabber from a different vendor, nor with digital camera input or pre-recorded video files.

4.3.2 The UFO tool suite

In 2004 a first version of the UFO tool suite was published. The aim of this tool set is the detection and analysis of moving objects like meteors and transient luminous events. The software supports all three stages of meteor analysis, which makes it attractive for dense camera networks with multi-station analysis, but the processing is done stepwise and not in a single pass.

The first tool is UFOCaptureV2 (SonotaCo, 2005), a motion detection program that scans the video stream for moving objects. Each time an object is detected, UFOCapture writes a short AVI sequence from the event to disc. UFOCapture, too, has numerous parameters to control the detection algorithm.

The next tool is UFOAnalyserV2 (SonotaCo, 2007a), which processes the AVI files and determines the type of event that was recorded. If a meteor is detected, UFOAnalyzer does the photometric and astrometric analysis to determine the basic meteor properties and the meteor shower, if applicable.

The last tool is UFOOrbitV2 (SonotaCo, 2007b), which allows to combine observations from different stations and computes precise meteoroid trajectories and orbits (Figure 4.5). UFOOrbit comes with a prolific consistency check that automatically reject meteor pairs with insufficient accuracy or inappropriate geographical

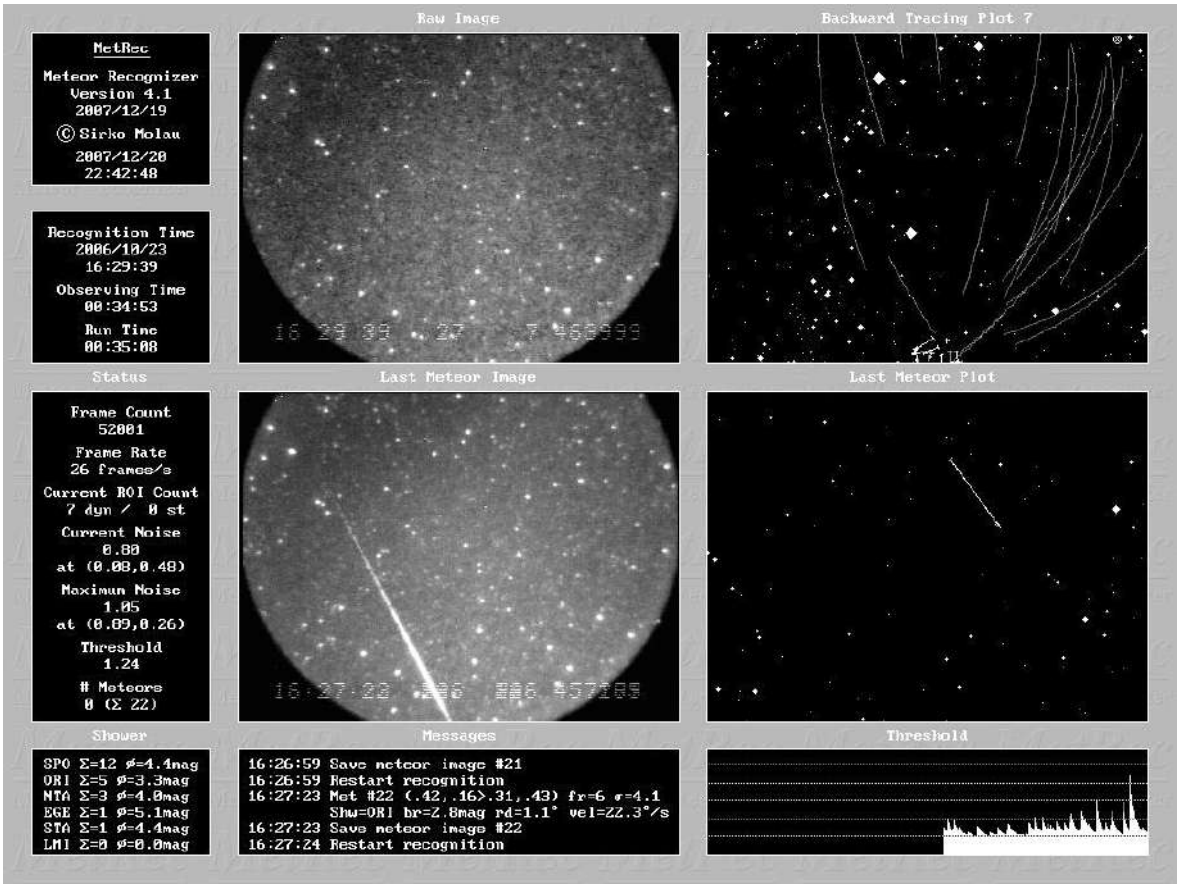


Figure 4.3: Example screen shot for MetRec.

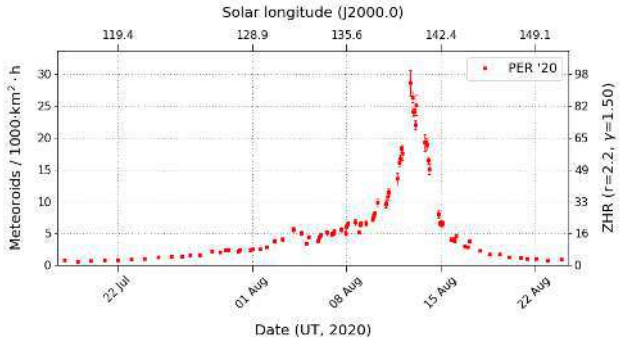


Figure 4.4: Activity profile of the 2020 Perseids, obtained from 30,000 shower meteors uploaded to meteorflux.org

pairing conditions. Hence, high quality data is obtained from the UFOAnalyser output without much further manual interaction.

The UFO tool set supports most DirectShow-compatible video capture device or interfaces for online processing. It allows to use the PCI-Bus, IEEE1394 (Firewire), Card-Bus (PCMCIA), and USB interface, if an "software-encoding type" device is attached that gives an uncompressed video stream to the Windows DirectShow sub system.

For higher resolution video, UFOCaptureHD2 was released at 2013. UFOCaptureHD2 runs on Windows and handles all resolution up to C4K60p (4096×2160, 59.94 fps). Typically, hi-sensitivity mirror-less cameras with normal or wide-angle lens, PCIex bus HDMI capture device, SSD (over 700 MB/s speed), and 8-core CPU is used for 4K/30p colour capturing. Also GigE interface monochrome cameras or USB 3.0 capturing devices are supported by UFOCapture HD2.

The UFO tool suite is used by the SonotaCo network, which is one of the largest existing video meteor network. Furthermore, several hundred individual video meteor observer around the world are using the UFO suite.

4.3.3 The CAMS software suite

The software used by the CAMS Network involves a suite of applications to handle end-to-end processing from imagery capture to orbital parameter estimation developed by Peter Gural. Specifically the major CAMS pipeline components include real-time video frame digitisation to PC memory, compression of 256-frame imagery sequences, astrometric and photometric calibration for each camera, meteor detection processing, multi-camera and multi-site space-time coincidence aggregation of commonly observed tracks, atmospheric trajectory estimation, and finally the computation of Keplerian orbital parameters for each triangulated meteoroid. The detection portion of the processing chain was originally based on the MeteorScan software (Gu-

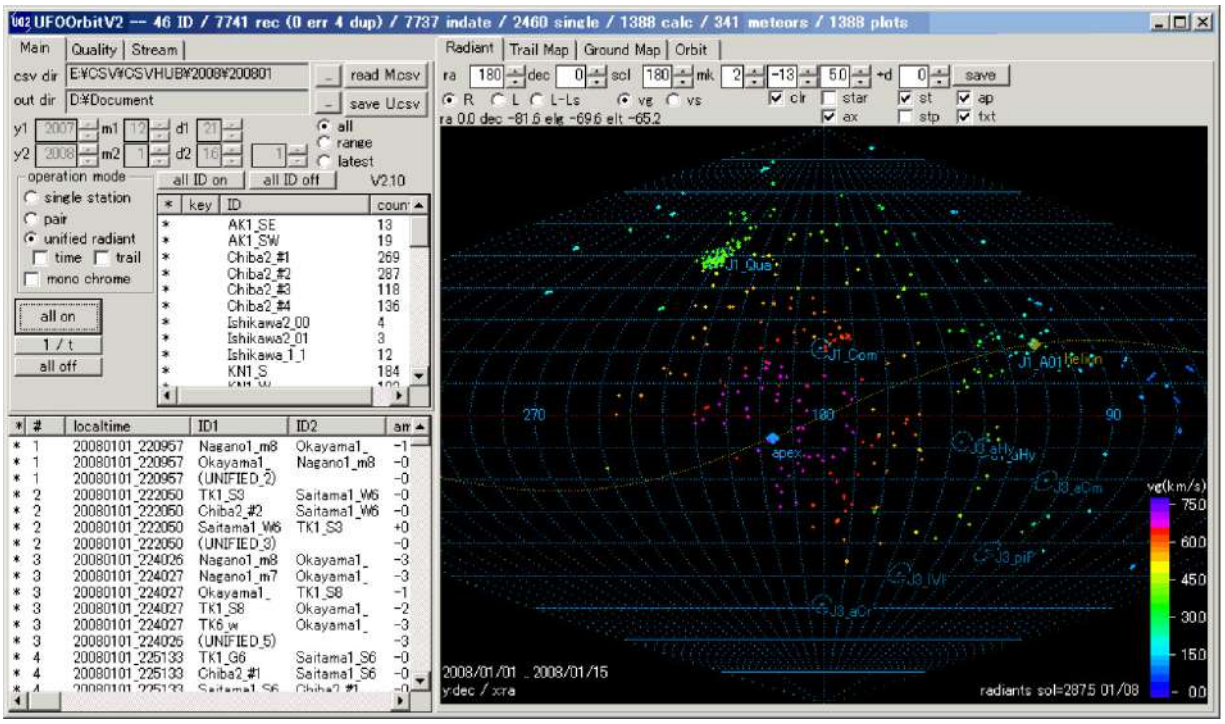


Figure 4.5: Example screen shot for UFOOrbitV2.

ral, 1995, 1997) which utilised the Hough transform, but was replaced with a 40 times faster clustering and tracking algorithm (Gural, 2016). The software also uses a unique imagery compression scheme by merging a sequence of 256 video frames into four images: a maximum pixel value image, an average pixel value image excluding the maximum, a standard deviation pixel value image excluding the maximum, and an image which tracks the frame number of the occurrence of the maximum pixel value. The maximum pixel and frame number of maximum pixel scheme was originally created by Mark Vornhusen, and was extended to this "four frame" (FF) compression content during the development of the CAMS processing pipeline (Figure 4.6). The compression scheme is acceptable for meteors, because they are typically brighter than the background and thus their space-time propagation history (maximum value and associated frame number) can be recorded for each meteor track position. The compression results in a 64:1 compression ratio relative to raw imagery. One disadvantage is that this compression algorithm does not preserve information about wake or short persistent trains, which are fainter than the meteor itself.

The pipeline stages are controlled by configuration files which allows for flexible adaption to specific observing circumstances. While originally developed for professional investigation of minor shower studies by deploying a small number of densely packed camera batteries, as in the old Dutch photographic days, amateurs have become active participants with single and multi-camera sites coordinated to point in overlapping sky regions. For amateurs an EasyCAMS wrapper package was developed to make the user experience easier to set up and run nightly.

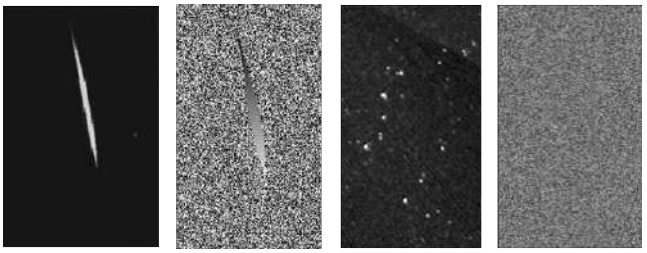


Figure 4.6: Example for "four frame" compression. From left to right: maximum pixel value spanning 256 frames, frame number of maximum pixel value, mean of 256 frames excluding the maximum value, and the standard deviation around the mean.

In the first stage of the pipeline, the video stream is recorded at night and compressed with the four-frame temporal pixel (FTP) algorithm. The second stage of detection processing can be executed in tandom with imagery capture at night, or if CPU horsepower is not sufficient to avoid dropped capture frames, the detection processing can be executed the following morning. The software suite contains modules for movie reconstruction (CameraMovies), all-sky mosaic generation (Mosaic), astrometric calibration (MeteorCal, MeteorCal_AutoUpdate, MeteorCal_Nudge), detection reprocessing (Reprocess). The detection software runs typically with low thresholds that allow for detection of faint events, which can result in a high false alarm rates under partly cloudy conditions. However, during subsequent multi-station coincidence processing, nearly all the false detections are removed.

The third stage of processing involves updating the astrometric and photometric calibration of each cam-

era. The best available frame per night is used for determination of the camera plate constants and pointing direction. For this purpose, third order polynomial plate constants are fitted to typically over hundred reference stars. If the camera orientation has changed, the first few stars have to be identified manually, but then the software automatically identifies more stars and improves the astrometric solution iteratively. In subsequent nights the process happens without manual interaction using the astrometric solution of the previous night for initialisation, or if the camera has shifted for some reason (wind or it got bumped), there is a nudger program that lets the camera operator tweak the star positions into alignment and get the final plate fit. Meteor photometry is obtained by comparing the meteor pixel values against reference stars, taking into account both saturation or spectral response of the cameras. From the light curve and deceleration profile of a meteor, further meteoroid properties like mass density, ablation coefficient and fragmentation properties can be determined.

An optional fourth stage, it to have each camera operator review a night's detection events for real meteors or false alarms. Although this step is not necessary in most circumstances since the next stage of multi-site space-time coincidence weeds out false alarms, many amateur camera operators like to review their meteor captures and this gives them a chance to visually interact with the processing pipeline. There is in development an automated deep learning solution to meteor confirmation processing (Gural, 2019), an approach, which is currently also evaluated by the AllSky7 Meteor Network.

In the fifth stage, all the detection events are centrally combined and processed. Once the data is pooled from multiple sites, a space-time event aggregator and trajectory/orbit estimator application (Coincidence) is run by either a coordination operator for the local camera network, or more typically the data is uploaded to a common server located at the SETI Institute for automated coincidence processing and eventually reporting to the SETI CAMS website. The coincidence software finds all meteor tracks that are spatially and temporally coincident, within a user defined range of time, and employing various geometric constraints to weed out false alarms or bad trajectories. Up until 2012, each meteor trajectory was examined by a human analyst to decide whether a meteor was well estimated. Currently the coincidence and trajectory processing is automated. To obtain meteoroid orbits, the standard transformation formalism from atmospheric trajectory in geocentric to heliocentric Keplerian parameters is used (Ceplecha, 1987). For error calculation, a Monte Carlo approach is taken. The program loops multiple times and adds Gaussian noise to the measurements in order to obtain standard deviations for all the estimated parameters including radiant direction, entry velocity, and deceleration.

4.3.4 How does a video meteor observation look like?

To give an impression of the steps necessary to carry out a video observation, we give a description of a typical observing session of an IMO Video Meteor Network station using MetRec. Similar steps will have to be carried out if other software is used.

If the camera is setup for the first time or if the field of view changed, a reference image needs to be grabbed and the position of a number of reference stars needs to be measured to allow for the equatorial coordinate conversion. With the help of a specialised tool, this takes about ten minutes.

Next you copy and old MetRec configuration file, update a few entries if necessary, and start MetRec. The detection software runs autonomously, but you can interactively check the current recognition status and detection results. The program displays optionally the raw video data stream, different phases of the detection process, a star map with the detected meteors, and the last detected meteor in real time. Raw detection data are uploaded every minute to the `meteorflux.org` server to generate a real-time flux density graph for known meteor showers.

After the observation another tool helps you to browse through the list of detected meteors and to delete false detections in a comfortable way. The data are uploaded to a central server database where they are archived or combined with data from other stations to obtain flux density profiles, trajectories and meteoroid orbits. This takes usually another five to ten minutes per observing night.

In case of a fully automated camera, the computer and the camera are typically activated after sunset by a time switch. The camera is shielded by a weather-proof housing. Optionally, a motor-driven lens cap may open, that protects the camera against the Sun and adverse weather. The software starts automatically and waits until a predefined solar depression is reached before the meteor detection process begins. It then runs all night long and saves the meteors on hard disc. The software quits operation at dawn. Later the camera and the computer are switched off by the time switch, and the optional lens cap closes. The camera operator checks the output maybe once a week or even once in a few months.

4.4 Video Meteor Networks

In the early days, the were just a few video systems around, which were operated occasionally during major showers or exceptional events. With the availability of automated meteor detection software not only the number of video observers steadily increased, but they also organised in observing networks to join forces in creating large meteor and meteoroid orbit databases. Whereas such network stations consisted originally of one or more cameras which recorded only a small fraction of the sky, there has been recently a tendency towards networks of all-sky cameras. Whereas the prime

focus of traditional video meteor network is the analysis of meteor showers, the all-sky camera network are operated at day- and nighttime and focus on fireballs and other types of atmospheric phenomena (e.g. halos, noctilucent clouds, aurorae, sprites). Some of the largest meteor networks shall be introduced here.

4.4.1 IMO Video Meteor Network

The IMO Video Meteor Network (`imonet.org`) is a joint effort of amateur meteor observers mainly located in Europe that started in Germany in March 1999 (Molau, 2001). There is no standard camera type. Even though most stations use Mintron cameras with Computar or Panasonic c-mount lenses, the network comprises a range of different camera types with different properties. Based on the MetRec software, most observers record meteors in any given clear night. The meteor data is centrally collected, quality checked, and archived by the IMO Video Commission. It is made available through the web (`imonet.org`) and other channels.

Since 2011, the network has been collecting meteor flux data in addition. After the quality check by the observer, they are uploaded to a central web site (meteorflux.org), where you can calculate flux density profiles and compare the results for different meteor showers and years. In 2019, the web service was extended by a real-time flux viewer. Thanks to the single-stage processing in MetRec, the IMO Network cameras can upload their data still during the observation to the webserver, which provides a preliminary view of the ongoing meteor shower activity with a lag of less than five minutes.

The IMO network has ever grown since it's formation in 1999, and reached a stable state around 2015. Since then, about 80 cameras are operated by 40 observers in a dozen of countries. Most data are recorded in Germany, Italy and Portugal. Even though the camera density in central Europe has grown such, that most of the sky is covered by more than one camera, the fields of the individual cameras are usually not specifically aligned and the observations can be regarded as single station recordings. At the end of a year, all data are exported to the EDMOND database (Kornos et al., 2013), where they are used for trajectory and orbit determination in conjunction with data from other video meteor networks in Europe.

With the number of meteor cameras, also the collected data set has grown every year. Since 2015, more than 100,000 observing hours are collected by the network every year, and between 400,000 and 500,000 meteors are recorded. Since 2007, there has been not a single night without observations.

By 2006 the overall number of records in the IMO Video Meteor Database had grown to nearly 200,000. That made it worthwhile to analyse the single station data set in detail and search for known and unknown meteor showers based on probabilistic algorithms. The results were presented at the 2006 IMC. The analysis was refined and repeated in 2008, 2009 and 2012, when the database had grown to a million meteors. Over a hundred meteor showers could be detected in the data set [Molau, 2013], among them nearly all meteor showers of the IMO Working List. We could determine detailed meteor shower characteristics (activity period and profile, radiant position and drift) which differed sometimes significantly from the expected values.

4.4.2 SonotaCo Network

The SonotaCo Network (SonotaCo, 2004) – see `sonotaco.jp` – is a night sky video observing network in Japan, that started operation in August 2004. It is operated by amateur meteor observers and professional researchers, that use the UFO tool set. It records nearly 200,000 meteors over Japan per year, and reduces nearly 20,000 orbits per year since 2007 to now (`https://sonotaco.jp/doc/SNM/`). As an example, Figure 4.7 shows the radiant distribution of the data set from one year. There are almost 30 stations and more than 100 cameras deployed. These cameras are almost exclusively non-intensified monochrome video cameras with fields of view between 30 and 90 degrees diameter. There are a number of stations which operate up to 12 cameras simultaneously to cover a wider area with improved accuracy and limiting magnitude. Thus, most of the observational area of the SonotaCo Network is covered by two or more cameras. From 2013, the use of HD and 4K camera has begun in the network. They brought colour precise video images and reduced the measurement error down to 1/6. In focus of the network are not only meteors, but also transient luminous events (TLEs) caused by lightning discharge that appears at almost same altitude as meteors and can therefore be observed with the same equipment.

4.4.3 Polish Fireball Network

The Polish fireball network (`pkim.org`) was established in March 2004 with initially three continuously operating video stations. Over time the network has grown significantly and undergone different hardware changes and upgrades. At first, almost 40 Tayama cameras with $f = 4\,\mathrm{mm}$, $f/1.2$ lenses and $66° \times 50°$ field of view were deployed. Later a series of 16 more sensitive Mintron cameras with different $f/0.8$ Computar lenses and was introduced, which provided a much better limiting magnitude. Finally a series 17 of digital high-definition cameras from DMK with $f = 4\,\mathrm{mm}$ $f/1.2$ lenses were installed, which have a $130° \times 80°$ field of view.

The cameras are located at 40 different sites in Poland. Most of the observers in the fireball network are amateurs who perform the observations from their homes, but some stations are located in astronomical clubs and schools, and also some astronomical institutes and observatories are involved. The cameras are operated fully automated and contain automatic closing devices to shield them from sunlight. Ever since 2015, the network has been recording annually about 80,000 meteors, which yields over 10,000 high quality meteoroid orbits per year (Wisniewski et al., 2018).

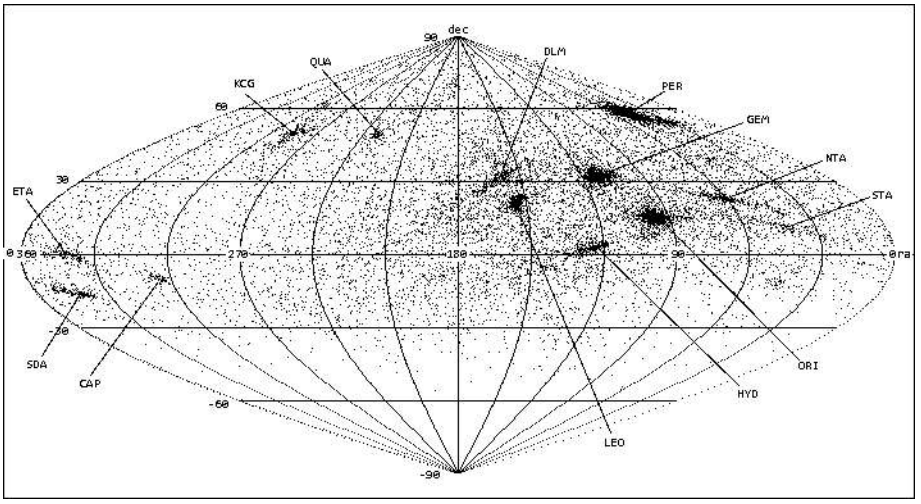


Figure 4.7: Radiants of 18,650 multi-station meteors of the SonotaCo network in 2007 (equatorial coordinates in sinusoidal projection).

The Polish fireball network uses different software stacks. For meteor detection, MetRec, UFOCapture and Freeture is used. Further processing is done by UFOAnalyser, UFOOrbit and software which was developed within the Polish fireball network. It allows for improved astrometric accuracy in cases where only a few reference stars can be measured, and the calculation of meteoroid trajectories and orbits.

4.4.4 CAMS Network

CAMS (Cameras for All-sky Meteor Surveillance / `cams.seti.org`) is an automated video surveillance of the night sky initiated by the NASA in 2010 to validate the IAU Working List of meteor showers (Jenniskens et al., 2011). Before the stations were designed, a study was executed to compare the performance of a variety of video meteor cameras and lenses available circa 2008. Intensified meteor cameras were rejected because of their limited lifetime and expense, and also with respect to lenses a compromise between sensitivity at low f-number and cost for a $1/2''$ format sensor were made. Each CAMS station consists of a battery of 16 to 20 Watec 902H2 Ultimate cameras, which are typically arranged in two rings. They are comprised of a ring of 11 and another ring of 8 cameras with Pentax $f = 12\,\mathrm{mm}$ $f/1.2$ lenses facing at 42° and 63° elevation respectively. Each camera has a $22° \times 30°$ field of view. A zenith camera with $f = 6\,\mathrm{mm}$ $f/1.4$ lens and $29° \times 37°$ field of view completes the sky coverage down to 31° elevation with a stellar limiting magnitude beyond 5 mag (Figure 4.8). Gamma of the Watec cameras is set to 0.45 and fixed gain is used during system operation for periods when the solar elevation angle is 10 degrees below the horizon. The composite interlaced NTSC video signal from 20 cameras was recorded by a battery of video data servers back in 2010 (one server for four cameras) at 60 interleaved frames/s. Currently, CAMS deployment configurations use 16 cameras with two 8-video channel digitising boards from Sensoray, running on a single i7 CPU desktop computer. All cameras are housed in a weather-proofed and heated box with a horizontal 6 mm thick float glass window and a roll-off sun shade.

The first battery of three CAMS systems was deployed in California in 2010. Later also other configurations were designed and implemented, starting from single-camera systems to configuration with 2, 4, 8 and 16 cameras. By early 2021, stations were deployed at 19 locations world-wide, including the US (California, Virginia, Florida), New Zealand, South Africa, Europe, United Arab Emirates, Australia, Chile, Brazil, and Namibia. Thanks to the large global extent, the CAMS network was been every effective in obtaining meteoroid orbits from both northern and southern meteor showers. In 2019 alone, about 360,000 meteoroid orbits had been collected, which outperforms all other current video meteor networks.

4.4.5 FRIPON

FRIPON (Fireball Recovery and Planetary Inter Observation Network / `fripon.org`) has the goal to install and operate a dense fireball camera network in Europe with 100 systems in France alone. They are augmented by 25 radio stations scattered all over France and listening to the Graves beacon. FRIPON was funded by the French National Research Agency in 2013, which did not only pay for the camera systems, but also the development of the corresponding software pipeline. FRIPON is developed and operated by a core-team of nearly 20 professional astronomers and students.

Each FRIPON camera is a monolithic, hermetically sealed system with a single video camera that covers the full sky. The system focuses on robustness and ease-of-use, so that even an unskilled person can install and operate a FRIPON station. The camera delivers a video stream of 1280×960 pixel per frame and yields a resolution of 5 pixels per degree. It has a limiting magnitude of about -4 mag and records of the order of 50 fireballs per year. The camera comes with a pre-configured Mini

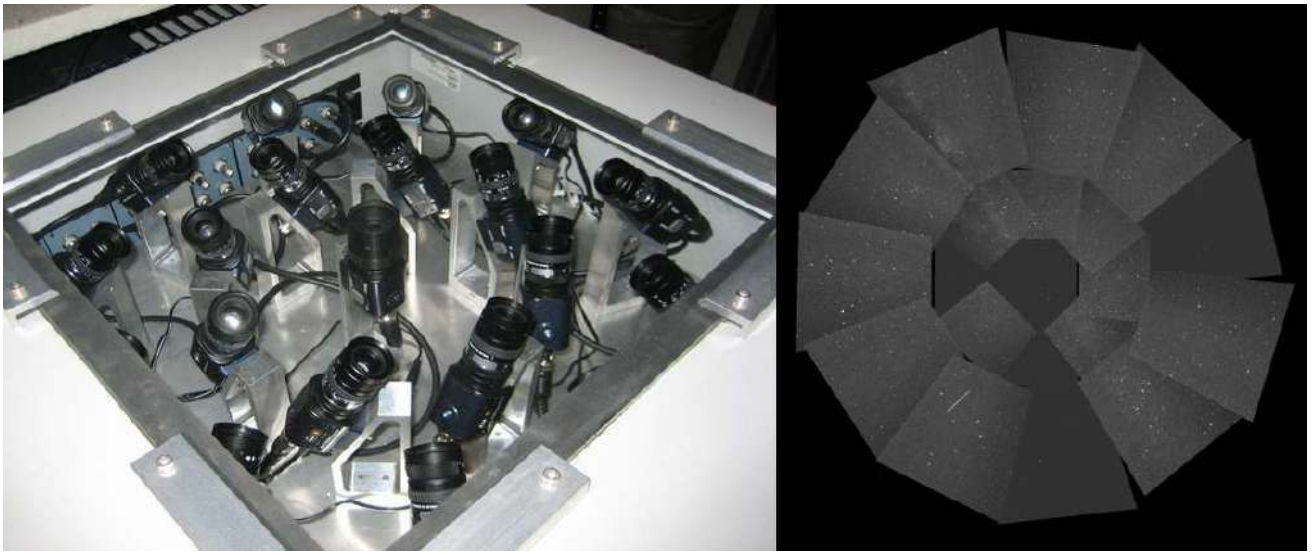


Figure 4.8: Left: Configuration of Watec 902 H2 Ultimate low-light-level cameras at a CAMS station. Right: Corresponding mosaic of video images at one moment in time. The video fields are in gnomonic projection, with the zenith at the centre of the image.



Figure 4.9: Active stations of the FRIPON network in Europe by early 2021.



Figure 4.10: Close-up of an FRIPON (DEMV01) and AllSky7 camera (AMS35) operated side-by-side in Conow, Germany.

Computer in a plug-and-play fashion. You only have to mount the system and attach the cables, and it is ready-to-run.

FRIPON is a closed system. The hardware design is fixed and the computers are interconnected in a private VPN. There are no day-to-day duties for camera operators like checking for false detections. The video data is recorded round the clock. Night-time data are locally processed with the FreeTure pipeline, and detections are uploaded to a central server in France, where multi-station events are automatically searched and analysed.

A web interface allows the camera operator to monitor the camera state and to access the recordings. In case of problems, he can reach out for central support my e-mail. The roll out of FRIPON cameras started in 2014. By early 2021, nearly 200 stations are installed in Europe (Figure 4.9), and the goal to install 100 cameras in France is almost reached. Smaller sub-networks are deployed in Italy, the Netherlands, UK, Germany and Romania. Every year, the FRIPON network collects over thousand orbits from fireball-producing meteoroids, among them less than ten events with a calculated terminal mass $> 100\,\mathrm{g}$. In total, almost 5,000 trajectories have been calculated so far (2021).

4.4.6 AllSky7 Fireball Network

At the 2018 IMC, Mike Hankey presented a new all-sky camera that he had designed: AllSky6 (Hankey at al., 2020). Contrary to FRIPON, it consisted of five cameras pointing in different directions horizontally, and one camera pointing to the zenith (Figure 4.10). Later the design was upgraded to AllSky7, whereby the single zenith camera was replaced by two so that really the full sky was covered from the zenith to the horizon. The AllSky7 system is focusing on low-costs, but still high sensitivity and resolution. Each of the seven cameras covers a field of view of about $84^\circ \times 44^\circ$ and reaches 4th magnitude. The cameras provide a standard resolution (704×576 pixel) and a high resolution (1920×1080 pixel) data stream, which results in a resolution of 25 pixels per degree. The data streams are recorded 24/7 and stored in 1-min chunks on the analysis computer, which is typically shipped together with the camera. An AllSky7 system records about the same number of

meteors per year like a single Mintron camera, which makes it a hybrid meteor and fireball camera. However, it is also be used to observe other types of atmospheric phenomena such as halos, noctilucent clouds, aurorae.

The analysis pipeline of AllSky7 is still in development, but most building blocks are meanwhile available. The first step is a meteor detector, which parses all night-time video chunks and moves them to an extra folder if a meteor was detected. Other data will be overwritten within days. The camera operator can inspect the recordings and delete false detections. Another piece of the analysis pipeline is automatically generating and improving a lens model for each camera, and determining the pointing direction of each camera. Based on this astrometric model, the meteor coordinates are calculated and all data are stored on a central cloud share. In the end, the open-source WMPL trajectory solver (Vida et al., 2019) is used for the final calculation of trajectories and orbit.

AllSky7 is a system with an open, extensible design. It has undergone several hardware revisions before the roll out started, and the software is further developed in short cycles. A neural network classifier is currently designed to reduce the false detection rate of meteors.



Figure 4.11: Stations of the AllSky7 Fireball Network in Germany and neighbour countries in early 2021.

AllSky7 is a pure amateur project, which is driven by a handful of devoted meteor observers and supported by dozens of enthusiasts who bought a camera and operate them. By early 2021, about 70 AllSky7 systems are operated world-wide. The biggest cluster of cameras is the AllSky7 Fireball Network in Europe (`allsky7.net`), which started in 2018, comprises meanwhile nearly 30 stations in Germany and is now extending into the neighbour countries (Figure 4.11). There are further camera clusters at the east and west coast of the United States, and individual systems in other parts of the world.



Figure 4.12: Components of a GMN camera as available from an industrial partner.

4.4.7 GMN

The Global Meteor Network (GMN; `globalmeteornetwork.org`) is another young network to observe meteors at a global scale (Vida, 2020). It was started in 2018 and has meanwhile attracted meteor observers on several continents. By late 2020, over 200 GMN stations have been deployed in 20 countries. In 2019 and 2020, of the order of 100,000 meteoroid orbits could be determined each. So far, most of the cameras are located in North America and Europe, but GMN wants to reach true global coverage in order to record possible meteor shower outburst at any time, but also to observe meteorite dropping fireballs with high precision.

What makes this network different from other is, that you get for small budget a housing that integrates all components including the camera and a Raspberry Pi 4 computer running the necessary video capture and meteor detection software. The cameras are based on the Sony IMX291 sensor and deliver a 1280×720 pixel video stream at 25 frames per second. A range of fast $f/1.0$-lenses starting from $f = 3.6$ mm wide angle lenses reaching a limiting magnitude of 6 mag in about $90 \times 45°$ field of view up to $f = 16$ mm tele lenses with a limiting magnitude of 9 mag in a $20° \times 10°$ field of view are used. The COTS (commercial-of-the-shelf) hardware is easily available everywhere and costs about 200USD,but you can also obtain a pre-configured plug&play system for 450USD from an industrial partner (Figure 4.12).

The GMN software pipeline is fully transparent and open source. On the local computer, the RMS (Raspberry Pi Meteor Station) software is recoding the video, detecting meteors and calibrating the recordings. After

the detections are upload to a central server, the WMPL (Western Meteor Python Library) solver is used for trajectory estimation and orbit calculation. All data (radiants, orbits, magnitudes and masses) are unrestricted and public – they are typically published within 24h in the internet. Particular care is taken for astrometric and photometric calibration in order to obtain high-quality data, which is the basis for good science.

References

Ceplecha Z., 1987: Geometric, dynamic, orbital, and photometric data on meteoroids from photographic fireball networks.. *BAC* **38,** 222–234.

Gural P.S., 1995: Applying state-of-the-art video and computer technology to meteor astronomy. *WGN* **23,** 228–235.

Gural P.S., 1997: An operational autonomous meteor detector: Development issues and early results. *WGN* **25,** 136–140.

Gural P., 2016: A fast meteor detection algorithm, in A. Roggemans, P. Roggemans (eds.), Proc. IMC 2016, Egmond, the Netherlands, 96–104

Gural P.S., 2019: Deep learning algorithms applied to the classification of video meteor detections. *MNRAS* **489,** 5109–5118.

Hankey M., Perlerin V., Meisel D., 2020: The all-sky-6 and the Video Meteor Archive system of the AMS Ltd.. *Planet. Space Sci.* **190,** 105005.

Jenniskens P., Gural P.S., Dynneson L., Grigsby B.J., Newmane K.E., Borden M., Koop M., Holman D., 2011: CAMS: Cameras for Allsky Meteor Surveillance to establish minor meteor showers. *Icarus* **216,** 40–61.

Kornoš J., Koukal J., Piffl R., Tóth J., 2014: The EDMOND meteor database, in: Gyssens, M.; Roggemans, P.; Zoladek, P. (eds.), Proc. IMC 2013, Poznan, Poland, 23–25

Kukic P., Gural P., Vida D., Šegon D., Merlak A., 2018: Correction for meteor centroids observed using rolling shutter cameras. *WGN* **46,** 154–165.

Molau S., 1999: The meteor detection software MetRec, in: R. Arlt, A. Knöfel (eds), Proc. IMC 1998, Stara Lesna, Slovakia, 9–16.

Molau S., Nitschke M., de Lignie M., Hawkes R.L., Rendtel J., 1997: Video observations of meteors: history, current status and future prospects. *WGN* **25,** 15–20.

Molau S., 2001: The AKM video meteor network, in: B. Warmbein (ed.), Proc. Meteoroids 2001 Conference, Kiruna, Sweden. ESA SP-495, 315–318.

Molau S., 2014: Meteor showers identified from a million video meteors, Proceedings of the IMC, Poznan, 2013.

SonotaCo, 2004a: SonotaCo Network Japan. `http://sonotaco.jp/main.php`.

SonotaCo, 2004b: M.CSV Exchange Hub. `http://sonotaco.jp/forum/viewforum.php?f=15`.

SonotaCo, 2005: UFCaptureV2 Users Manual. `http://sonotaco.com/soft/UFO2/help/english/index.html`.

SonotaCo, 2007a: UFOAnalyzerV2. `http://sonotaco.com/soft/download/UA2Manual_EN.pdf`.

SonotaCo, 2007b: UFOOrbitV2 Users Manual. `http://sonotaco.com/soft/UO2/UO21Manual_EN.pdf`.

SonotaCo, 2009: SonotaCo Network Simultaneously Observed Meteor Data Sets, `http://sonotaco.jp/doc/SNM/index.html`

Vida D., Gural P.S., Brown P.G., Campbell-Brown M., Wiegert P., 2019: Estimating trajectories of meteors: an observational Monte Carlo approach I. Theory. *MNRAS* **491,** 2688–2705.

Vida D., 2020: `https://www.youtube.com/watch?v=HNyXB0-stSo&list=PLEypPv_8eK03k5e5wn12OFsuiMf8aUyvp`

Wisniewski M., Zoladek P., Olech A., Raj A., Tyminski Z., Maciejewski M., Fietkiewicz K., Myszkiewicz M., Stolarz M, Gozdalski M., 2018: Results of Polish Fireball Network 2017, Proceedings of the IMC, Pezinok-Modra, 2018, 50–52.

5 | Photographic observations

Jürgen Rendtel, William Ward

5.1 Scientific motivation

5.1.1 Aims of meteor photography

Meteor photography has been revolutionised by digital imaging techniques. Much of the information regarding emulsion based film is no longer relevant. Also, double station/orbit determination photography has been superceded by video techniques (see the appropriate section for more details). The information here is presented for completeness and to provide a context for photographic imaging.

The naked eye is able to detect meteors down to approximately +7 mag under excellent circumstances in the vicinity of the centre of the field of view. Advanced video techniques permit detection of meteors to magnitude +8, and radar meteors as well as telescopic ones may be as faint as magnitude +11. Traditional photography on film as well as with digital sensors can hardly compete with these. But the effort to be spent for the equipment of observation and reduction is much lower than e.g., for video systems. For this reason, photographic observations belong to the standard repertoire of the amateur astronomer.

Photographs not only look nice, they also contain valuable information that can be used for further analysis. Although the method mainly concerns brighter meteors, the great advantage of meteor photography is its accuracy in positions. This allows us to determine the following properties of individual meteoroids or of meteor showers very accurately:

- the trajectory in the atmosphere;
- the radiant;
- the velocity;
- the deceleration. Decelerations vary from hardly measurable (shower meteors) to 50% of the initial velocity (very slow meteors of asteroidal origin);
- the mass which may vary from 0.01 g to thousands of kilograms;
- spectra if a dispersing element (prism or grating) is added.

The deceleration gives information regarding the composition of the meteoroids. From statistical samples of meteor heights, several distinct groups with different genetic origins have been deduced.



Figure 5.1: Camera with a fisheye lens and a remote control which allows semi-automatic image sequences.

The radiant and velocity of a meteoroid yield its heliocentric orbit. This allows to associate meteoroid streams with parent comets.

5.1.2 Basic equipment requirements

The camera body has no great influence overall, since it is effectively only the film holder or sensor cover. Of course, the camera must allow time exposures, and, the easier it is to handle in the dark, the better it is suited for astronomical purposes. In particular, problems may occur with cameras driven by electronics. In this case, it will probably be necessary to switch off most automatic controls (consult the instructions given in the manual first). Long exposures or cold winter nights may cause the operating limits to be exceeded as well.

Long exposures are possible only if the camera shutter has either a **B** or a **T** position. ('B', or bulb, im-

plies that the shutter is open as long as you push the release button; 'T' opens the shutter once you push the release button, and it remains open until you push it again.) If you use 'B' on your camera, you will need a lockable cable release, while 'T' allows exposures without such a device. Modern cameras often allow the use of timer remote controls (Figure 5.1) which are very helpful for (semi-)automatic patrols. For example, a continuous sequence of 1-min-exposures extending over hours can be programmed. Cameras which allow only exposures shorter than 30 seconds and with automatic settings (focus, exposure, flashlight) are not suitable for meteor photography. Modern DSLR (digital single-lens reflex) exclusively use electronic controllers for bulb operations. Care should be exercised to keep the controller free from dew. An improvised cover of some sort can be made and attached to the tripod or mount.

Sometimes, a cable release may cause trouble. Some cable releases are badly affected by humidity or cold, and should be tested before each use. The exposure might otherwise be ended due to a malfunction at an unknown time, and a meteor missed.

5.2 Faint meteors

5.2.1 Lens and film or sensor

The number of meteors that can be photographed depends on the properties of the film or sensor, which may be a CCD (Charged Coupled Device) or a CMOS (Complementary Metal Oxide Semiconductor) chip, respectively. We give hints for both types of cameras. It should be noted, however, that film based techniques have been largely superseded by digital imaging methods now.

5.2.1.1 Photographic film

The limiting magnitude is dependent upon the sensitivity of the emulsion being used (g). Many modern films (colour as well as black-and-white) can be exposed and processed at ISO 1600 (or higher). Using films with ISO below 400 does not make sense except for fireball patrols. The optimal exposure has to be tested for each location, but in general 5 minute exposures should be a suitable choice.

5.2.1.2 Digital sensors

Today, most digital cameras use either a CCD image sensor or a CMOS sensor. Both types of sensor accomplish the same task of capturing light and converting it into electrical signals (Carlson, 2002; Magnan, 2003).

A CCD is an analog device. When light strikes the chip it is held as a small electrical charge in each photo sensor. The charges are converted to voltage one pixel at a time as they are read from the chip. Additional circuitry in the camera converts the voltage into digital information.

A CMOS chip is a type of active pixel sensor made using the CMOS semiconductor process. Extra circuitry next to each photo sensor converts the light energy to a voltage. Additional circuitry on the chip converts the voltage to digital data.

Neither technology has a clear advantage in image quality. CMOS can potentially be implemented with fewer components, uses less power and provide data faster than CCDs. CMOS does not heat up as fast as a CCD and also allows for faster processing. This in turn will result in lower digital noise, because, when a processor heats up, the heat is registered as light and the light as digital noise in a picture. So a CMOS will result in less digital noise than a CCD at the same temperature.

The choice of sensor is important when considering a camera for meteor imaging. As meteors are fast moving objects they spend only a small amount of time illuminating any given pixel.

The relationship between pixel size and sensitivity is generally that the larger the pixel size the better the sensitivity. That is, for any particular size of sensor the one with larger pixels will detect fainter meteors all else being equal. Due to the relationship between the ISO setting, which on DSLR cameras is an expression of gain, and noise it is better to have a sensor with larger pixels and a lower ISO setting than smaller pixels with a higher ISO setting, again all other things being equal.

Some of the latest generation of digital cameras have exceptionally high ISO settings ($\approx$ 500,000 and up). Apart from the general noise issue, these cameras tend to be specialised and are expensive. However as the technology continues to mature these very high ISO's combined with low noise will no doubt start to appear in the consumer market.

Note that you have to switch off the noise reduction as it requires a dark exposure of the same length as the actual exposure which leads to a dead time of 50%. When using a digital camera it is useful to start with a test exposure to check the combination of sensitivity setting and lens's focal ratio and avoid overexposure (under moonlit conditions, hazy skies or in the vicinity of artificial lights). Generally, the image quality (spatial resolution) will be limited for the highest ISO settings.

Whilst offering significant advantage over film based cameras many consumer grade DSLRs are not as robust as film cameras were. Some effort should be made to keep the camera covered during a meteor observing session. This will help prevent dew forming on the body and maximise battery life.

There is also the practical reality of what manufacturers produce for sale. The requirements of ordinary photography are quite different to those of an ideal meteor camera system! Considering the large number of variables involved the most important thing to bear in mind is that just about every modern DSLR will produce good results under the right conditions. Therefore,

use whatever camera and lens combination you have to hand. Using the guidance presented here experiment with ISO settings and exposures to obtain the best results for *YOUR camera!*

5.2.1.3 Lens parameters

The focal length f of the camera lens also plays a role in determining the limiting magnitude. As the focal length increases, the field of view becomes narrower and hence the light of the meteor passes faster over the emulsion grains or image pixels, so the exposure time per pixel decreases—the limiting magnitude is inversely proportional to f. Extreme wide angle or fish eye lenses image the sky and the meteors on very few pixels, resulting in short trails. Here we can easily reach the limit of spatial resolution, that is, we can detect the meteor trail but with very few details along the trajectory.

Finally, the amount of luminosity which enters the camera will depend on the surface area of the lens, hence on the square of the effective diameter of the lens (d^2).

The optical data for a lens is given through its focal ratio or aperture number $A = f/d$ (sometimes also called 'speed') and its focal length f as in $f/2$, $f = 50$ mm. This means that $A = f/d = 2$, or, $d = f/A = 25$ mm. Putting all these factors together in one equation we get

$$\text{efficiency} \propto g f^{-1} d^2,$$

where g is the sensitivity of the emulsion (first number of ISO rating), f is the focal length of the lens (e.g., 50 mm) and d is the effective diameter of the lens (in mm). In general use the fastest lens available. A lens hood is recommended provided it does not impinge on the field of view of wide field lenses. Also some form of dew removal is advisable when conditions dictate.

Modern cameras require electrical power for their operation. Long exposures often are permanently power consuming. Tests are recommended to find out the lifetime of a battery which may be of the order of 2–3 hours in the case of a DSLR camera, and 12 hours for standard (film) SLR cameras. Therefore, some spare batteries should be at hand to avoid that the camera stops working when the meteor activity is high. Alternatively, some cameras provide power-supply based adaptors (designed for astronomy application). As already mentioned, CMOS sensors have the advantage of low power dissipation and camera-on-a-chip integration. Generally, under cold conditions, batteries are exhausted sooner.

5.2.2 Field of view

The best field size and viewing direction depend on several parameters. The larger the field, the higher is the chance of catching meteors. In case of many bright meteors (low population index r, often near the activity peaks of meteor showers), this will indeed increase the number of photographed meteors. As we see from the above equation, a larger diameter d helps to reach fainter meteors. If we expect mainly fainter meteors, a faster lens (lower aperture number $A = f/d$) will do better. Another aspect is the angular velocity of the meteors which is lowest near the radiant or close to the horizon. A field low in the sky seems favourable because of the large atmospheric volume, but large distances to the trajectory and atmospheric extinction reduce the gain.

Further, the local circumstances have to be considered, such as artificial lights, moonlight, twilight sectors and the zodiacal light cones.

A compromise which works well in most cases is the use of a wide angle lens and a camera field centre which is about 20–30° from the radiant and about 40° above the horizon.

During the observation you should note the following information for each exposure:

- time for the beginning and end of the exposure (use UT to avoid confusion);
- if possible, time of appearance for all bright meteors;
- notes about other moving objects crossing the camera field;
- sky conditions, specifically about clouds near the start or end of the exposure.

5.3 Fireball patrols

5.3.1 Introduction

Fireballs are rare phenomena. Analysis of more than 5000 hours of visual observations suggests a mean annual rate of one sporadic meteor brighter than magnitude 0 every 2.7 hours and one meteor brighter than −3 mag in about 300 hours (Rendtel, 1990). Of course, there are significantly more bright meteors concentrated within or near the core regions of major meteor showers such as the Perseids or Geminids, but it is known that most meteoroids of cometary origin completely disintegrate before reaching about 50 km altitude. In contrast, the most interesting and dynamic events are the meteorite-dropping fireballs. These are all meteoroids entering the Earth's atmosphere at a velocity of less than about 25 km/s and reaching luminous end heights less than 25 km altitude. The probability of such events occurring in the evening hours is about four times greater than in the morning (Halliday, Blackwell & Griffin, 1984).

While a higher entry velocity does imply a higher amount of kinetic energy and thus also a brighter meteor, the luminous trail starts at a higher altitude and as a result the meteoroid fully ablates at a higher altitude. Therefore we expect more bright meteors in the morning hours, but more meteorite-producing fireballs in the evening sector.

The major goals of fireball photography are

- the recovery of fallen meteorites;
- the calculation of a fireball's atmospheric trajectory;
- the determination of the meteoroid's heliocentric orbit;
- securing photometric information that can reveal information concerning energy transformation along the trajectory.

5.3.2 Equipment

Bearing in mind the rarity of these events and the data we wish to record, the photography of fireballs, particularly of possible meteorite-producing events, requires two principal things:

- coverage of a very large field of view, ideally the whole sky (see Figure 5.3);
- imaging the event at a scale sufficient for accurate astrometric measurements.

To permit the entire sky to be imaged, the 'classical all-sky camera' was invented (Figure 5.4). It uses a convex mirror with a normal camera mounted above the mirror such that the camera can photograph the whole sky. This has some disadvantages, for instance,

- the camera body blocks the zenith area (see Figure 5.3);
- reflection from the mirror surface reduces the amount of light available for forming an image on the film in the camera and thus decreases the speed of the whole system. (A mirror that is used regularly reflects less than 80% of the incident light. The effective equivalent 'speed' of such a camera system is about $A = 11$.);
- it requires construction of large and cumbersome apparatus to hold the camera body (Figure 5.4);
- the mirror surface has to be recoated every 2–3 years to maintain acceptable reflectivity, a procedure that can be expensive.

For these reasons and because of the existing video camera networks (see Chapter 4, Section 4.4, page 97) the operation of the SLR-based network as described here will probably be terminated by mid 2022.

A better alternative is to use fish-eye lenses. Such lenses are available for large format cameras as well as for 35 mm-cameras and digital SLR cameras. The Zeiss-Distagon or the Russian Zodiak (or MC Arsat), both $f/3.5$; $f = 30$ mm, are of excellent quality and permit astrometric measurements to be made down to the horizon. Ceplecha, Bocek & Jezkova (1979) and Ceplecha et al. (1987) have also found that the photometric accuracy of these lenses is satisfactory over most of the visible field. Similar lenses can be found for almost all camera types. In general, cameras capture only the central part of the field that is optically available from the lens.

If you do not have a mirror camera or a fish-eye lens, you may still meaningfully contribute to our knowledge of fireballs. Here it may be most profitable to arrange a cooperative venture with other photographers at distances of about 50 km from your site. In this arrangement a certain area of sky will be covered from all the stations to improve the odds of photographing multi-station meteors. (For details see Section 5.4 on double-station work. See also the remark on casual fireball images on page 112.)

5.3.3 Film and exposure

The choice of film for fireball patrols involves requirements which are very different from the case of faint meteor photography already covered in Section 5.2. As an example, the all-sky cameras of the German fireball network (part of the larger European Network, EN, Figure 5.2) make a single all-night exposure per night. An example is shown in Figure 5.3. Usually, fish-eye lenses allow exposures of up to 7 hours duration in areas that are only slightly disturbed by city lights before fogging becomes a problem. Exposures of the order of several hours length are typical for fireball patrols. Bear in mind that the primary goal is not 'beautiful pictures' but images that permit astrometric measurements and photometry—hence black and white film is preferred.

Using digital cameras for patrol is difficult because of the limited battery life, but a power supply for a stationary camera setting could solve the problem. With a remote control, a shorter cadence of images could also be useful. As compared with the larger films, the spatial resolution will be lower, but still much better than the resolution of video systems (see Chapter 4).

An overview of the parameters of some photographic networks which have been in operation during the past 15 years is given in Koten et al. (2019) of which we briefly summarise a few parameters in Table 5.1.

Table 5.1: Photographic fireball networks (data from Koten et al. (2019), Table 4.3.)
EN – European Network, DN – Desert Network, TN – Tajikistan Network.

Project name	Exposure time	meteor lim. mag	Scale	Ref.
Analog EN	hours	−4	2°/mm	[1]
Digital EN	35 s	−2	3′ /px	[2]
Analog DN	hours	−4	2°/mm	[3]
Digital DN	29 s	+0.5	2′ /px	[4]
Analog TN	hours	−4	2°/mm	[5]

References: [1] Ceplecha and Rajchl (1965); Oberst et al. (1998); [2] Spurný et al. (2017); [3] Bland (2004); Bland et al. (2012); [4] Howie et al. (2017a,b); [5] Kokhirova et al. (2015)

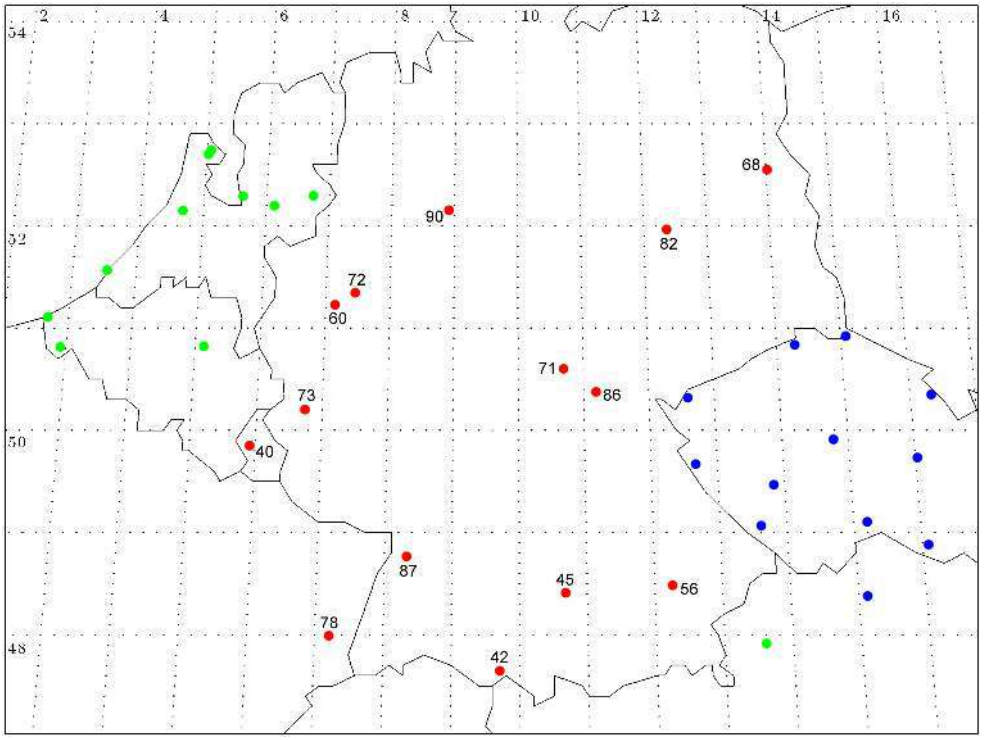


Figure 5.2: Map showing the locations of the permanent photographic stations of the European Network, EN (December 2021) in Germany, the Czech Republic and the Netherlands. Images from further all sky cameras (not all operated continuously) are included in the analysis of fireball events if available (map provided by Dieter Heinlein.)

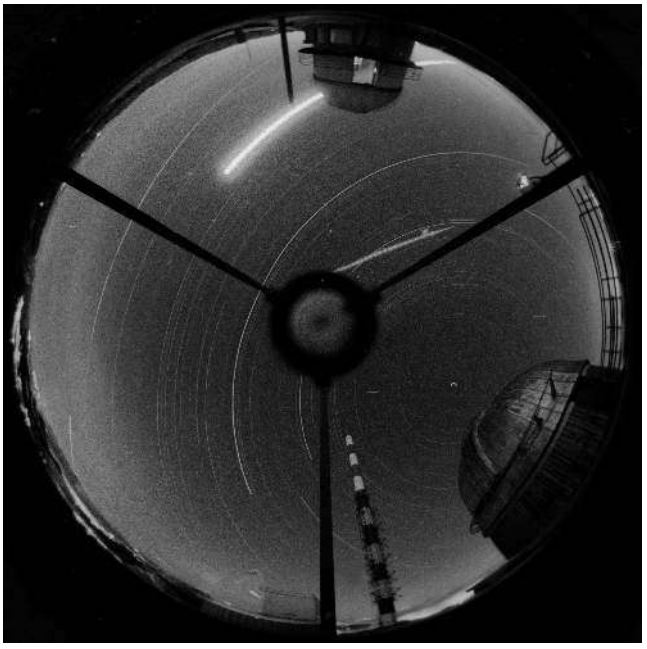


Figure 5.3: Image of an all sky mirror camera. The fireball occurred on 2008 January 13, $21^{h}32^{m}33.0^{s}$UT, the exposure lasted from $17^{h}00^{m}$until $5^{h}30^{m}$UT, and was taken at the station Wendelstein. Image courtesy of the DLR Institut für Planetenforschung, Berlin.



Figure 5.4: Mirror camera at the Wendelstein top. This camera caught the fireball shown in Figure 5.3.

5.3.4 Cleaning of the optics

After many of hours of operation, the front lens has to be cleaned *carefully*. Camera optics are covered by thin protective layers to reduce reflections (which is why they appear metallic-brown in reflected light). These layers are very sensitive to scratches. Some small grains that have collected on the lens could be silicates, and thus of comparable hardness to the glass itself and certainly far harder than the protective layer. Besides damage to the reflection-reducing layer, each scratch increases the amount of stray light entering the camera. As a rule, a small amount of dust on the front lens has less effect than any scratches. However, from time to time, you must clean the optics. You should do this immediately after your lens has been in the rain, since you will find the task much more difficult after drying has hardened the wet dust coating onto the lens.

After having removed the larger grains, you wipe very gently with cotton-wool and pure alcohol. Use each cotton-wool swab only once to lift away the particles from the lens. After doing this until no particle deposit is visible, you will see a surface that looks smeared and inhomogeneous. As the alcohol vaporises, the lens will cool slightly. Next, take another fresh, dry swab, breathe onto the lens and wipe the moisture away applying gentle pressure. This has to be repeated until, once again, the whole lens looks clear and homogeneous. As already pointed out, this should be done only with care and only when absolutely necessary (after about half a year of operations or following rain). If in any doubt, consult a specialist in this field. A good camera shop can provide advice on lens care. In principle these hints are also valid for cleaning the large surfaces of the mirrors used in the all-sky camera. If no protective layer has been placed on the mirror, however, you may remove portions of the reflecting layer and thus seriously damage the mirror. This may require a new aluminisation, which requires a special vacuum device and is expensive. Again, if you are unsure how to proceed, contact an optical specialist. Astronomical telescope makers may be helpful for this mirror problem.

5.3.5 Time of fireball appearance

Unfortunately, the photograph is unable to record the time at which the fireball appeared, but the knowledge of this precise moment is necessary for the computation of the initial heliocentric orbit. The time of appearance of a fireball is needed only for the determination of the right ascension of the radiant, not for the measurement of the trail or the reduction of the atmospheric trajectory. The radiant position is essential in determining the meteoroid's origin and is one of the most valuable aspects of fireball photography. In the evening hours, there is a chance that eyewitnesses may report a bright fireball, though, as the night proceeds, this probability progressively decreases as does the chance that meteor observers may be outside under good sky conditions nearby. The chance that an automated video system is operational in your vicinity is—in general—also low. Some cameras of fireball networks are equipped with photomultipliers to record the time of bright flashes.

Another possible source for the time of a bright fireball is through amateurs who have an automated radio forward scatter system. A long-duration reflection may be related to a fireball. For more details, see Chapter 6.

If you are observing while the camera is in operation, you should set your watch to a radio time signal, the most precise of which are time signals from special stations. In most parts of Europe you may use the DCF 77 station in connection with a radio-controlled clock, while in North America the short-wave signal from the WWV time station may be employed. For other regions, contact astronomical observatories in the vicinity for information or consult an almanac that annually publishes lists of suitable time signals and details of their broadcasting schedule and frequencies.

If no precise time of appearance is known for a fireball, the position in right ascension is uncertain by half the angle corresponding to the duration of the exposure (as we can estimate it relative to the trail's midpoint). For the case of all-sky or fish-eye photographs, you may use features on the horizon to figure out the horizontal coordinates that will then permit the calculation of the atmospheric trajectory. In such cases, however, it is impossible to find the orbit of the meteoroid and thus we cannot obtain any information concerning the origin of the particle.

5.4 Double-station photography

5.4.1 Computation of the direction of the optical axis

Different methods exist for computing where to direct a camera for double-station photography. The following section describes one possible way to get some results, but you may download the program QRICHT to calculate the optimal field of view for multi-station observations from `https://www.imo.net/photo/software`.

We assume meteors produce their maximum luminosity at about 90 km above the Earth's surface. This means we have to observe the same area at 90 km height in the atmosphere from two or more geographic locations. Mostly, we take a fixed point at 90 km altitude above a set location on the Earth which is at about an equal distance away from both observing stations. (e.g., at about 50 km distance). This point, called the projection point, can be determined with the help of an atlas or with a topographic map. First of all, the geographic latitude and longitude of this projection point $(\varphi_\mathrm{p}, \lambda_\mathrm{p})$ have to be determined.

For each observing station, we determine the elevation h and the azimuth Az at which the camera has to be aimed, to be sure to photograph the area at 90 km above this projection point. A few formulae using trigonometry allow us to solve this problem. An example will clarify the working procedure:

Step 1: Calculation of the angular distance from observing station to projection point. Since the computations are analogous for each observing station we need work with only one station here.

$$X = \arccos[\sin\varphi_\mathrm{p}\sin\varphi_0 + \cos\varphi_\mathrm{p}\cos\varphi_0\cos(\lambda_\mathrm{p}-\lambda_0)]; \quad (5.1)$$

$$Y = 60\cdot 1852\mathrm{m}\cdot X. \quad (5.2)$$

X is the angular distance on the spherical Earth's surface between the two places (in °). As one arc minute corresponds to 1852 meters, we find Y in meters.

Step 2: Computation of the elevation angle of the camera. Once we know the distance Y, it is very easy to determine the elevation h at which we have to aim the camera:

$$\tan h = \frac{90\ \mathrm{km}}{Y}, \qquad h = \arctan\frac{90\ \mathrm{km}}{Y}. \quad (5.3)$$

Step 3: Computation of the azimuth Az of the camera direction. The azimuth, where 0° = south and 90° = west, is found by introducing quantities A'', B'' as follows:

$$\sin(270^\circ-\mathrm{Az}) = \frac{B''}{Y} = \frac{60\cdot 1852(\varphi_\mathrm{p}-\varphi_0)}{Y} \quad (5.4)$$

$$\cos(270^\circ-\mathrm{Az}) = \frac{A''}{Y} \quad (5.5)$$

$$= \frac{\cos(\varphi_\mathrm{p}-\varphi_0)\cdot 60\cdot 1852(\lambda_\mathrm{p}-\lambda_0)}{2Y}$$

where $\tan(270^\circ-\mathrm{Az}) = B''/A''$ and thus $\mathrm{Az} = 270^\circ - \arctan(B''/A'')$. The values of $\sin(270^\circ-\mathrm{Az})$ and $\cos(270^\circ-\mathrm{Az})$ allow the determination of the correct quadrant where the azimuth is to be found. We remind readers who left school some time ago of the following rules:

$$\begin{aligned}
\sin+ \text{ and } \cos+ &\rightarrow 0^\circ < (270^\circ-\mathrm{Az}) < 90^\circ;\\
\sin+ \text{ and } \cos- &\rightarrow 90^\circ < (270^\circ-\mathrm{Az}) < 180^\circ;\\
\sin- \text{ and } \cos- &\rightarrow 180^\circ < (270^\circ-\mathrm{Az}) < 270^\circ;\\
\sin- \text{ and } \cos+ &\rightarrow 270^\circ < (270^\circ-\mathrm{Az}) < 360^\circ;
\end{aligned}$$

Figure 5.5 illustrates these rules.

Step 4: Computation of the declination δ and right ascension α. To point the camera exactly, it is recommended to convert the h and Az to right ascension α and declination δ, in order to find the selected area to be photographed in a star atlas. We compute the declination from:

$$\sin\delta = \sin\varphi_0\sin h - \cos\varphi_0\cos h\cos\mathrm{Az} \quad (5.6)$$

Once we know δ, we can compute the hour angle $\tau = \theta - \alpha$ by

$$\sin\tau = \frac{\cos h\sin\mathrm{Az}}{\cos\delta} \quad (5.7)$$

$$\cos\tau = \frac{\cos\mathrm{Az}\cos h\sin\varphi + \cos\varphi_0\sin h}{\sin\varphi_0\cos\delta} \quad (5.8)$$

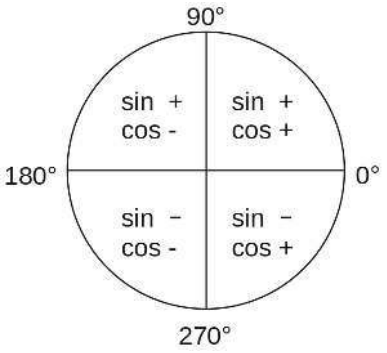


Figure 5.5: Sign of the trigonometric functions sin and cos.

Analogous to the computation of the azimuth, the values of $\sin(\theta-\alpha)$ and $\cos(\theta-\alpha)$ allow us to determine the right quadrant for $\tau = \theta - \alpha$. Once we have obtained $\tau = \theta - \alpha$, we can derive the right ascension of the camera direction when we know the local sidereal time θ. The local sidereal time can be obtained from any good astronomical yearbook or by a simple computational procedure.

5.4.2 Intersection of camera fields at a given height and determination of the camera directions

To determine the direction at which a camera has to be aimed for simultaneous photography, most people consider only the intersection of the optical axes at a height H, typically 90 km for most meteor photography. This method does not guarantee the cameras will not be pointed close to the horizon. The following numerical-graphical method prevents this. We assume that cameras with stereographic projection of the image (such as SLR cameras), with a focal length f (mm) and rectangular negatives $a \times b$ (in millimetres) are used. The semi-image angles are thus $\tan\alpha = a/2f$ and $\tan\beta = b/2f$ for the horizontal and vertical directions, respectively. For $f = 50$ mm and standard 35 mm-film we get $\alpha = 19.^\circ8$ and $\beta = 13.^\circ5$. Digital cameras with sensors smaller than the standard film format will image a smaller field (usually a factor of the field size or focal length is given to transform the data to the 35 mm-film format).

In Figure 5.6, the field of the camera is shaded. The camera is located at point W at the Earth's surface. R denotes the camera field centre in the sky, and WP is perpendicular to WR in the vertical plane. The surface at the height level H photographed in the atmosphere can be reconstructed when the dimensions b_1, b_2, d_1 and d_2 are known. Therefore, we need to compute these.

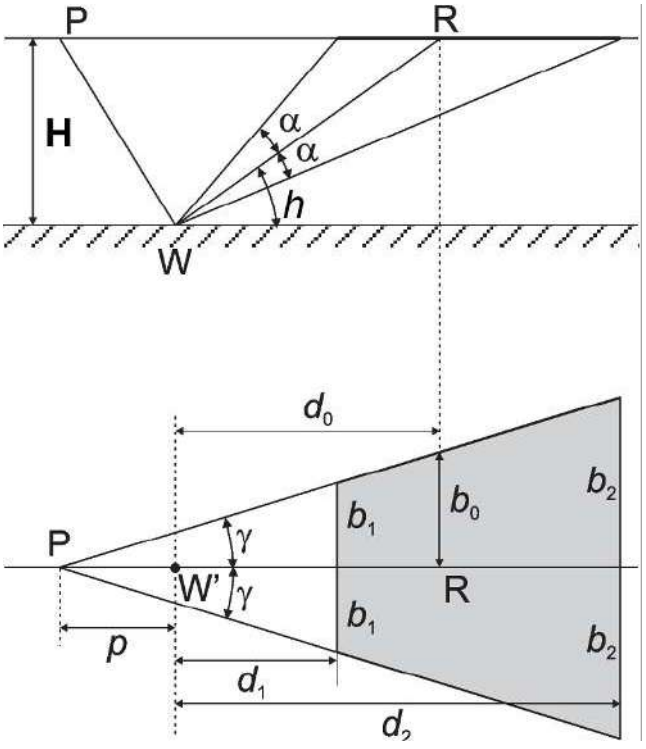


Figure 5.6: Camera field in the atmosphere at height level H. The lower part shows the situation projected onto the Earth's surface.

The formulae are

$$p = -H \tan h; \quad (5.9)$$

$$pd_0 = -H^2 \quad \text{whence} \quad d_0 = H/\tan h; \quad (5.10)$$

$$d_1 = \frac{H}{\tan(h+\alpha)}; \quad (5.11)$$

$$d_2 = \frac{H}{\tan(h-\alpha)}. \quad (5.12)$$

The computation of b_1 and b_2 is more complicated. First compute

$$b_0 = \frac{H \tan\beta}{\sin h}. \quad (5.13)$$

Next,

$$\tan\gamma = \frac{b_0}{d_0 - p} = \tan\beta \cos h; \quad (5.14)$$

$$b_1 = (d_1 - p)\tan\gamma; \quad (5.15)$$

$$b_2 = (d_2 - p)\tan\gamma; \quad (5.16)$$

$$b_1 = b_0\left(1 + \frac{d_1 - d_0}{d_0 - p}\right); \quad (5.17)$$

$$b_2 = b_0\left(1 + \frac{d_2 - d_0}{d_0 - p}\right). \quad (5.18)$$

The formulae (5.17) and (5.18) are better than (5.15) and (5.16) for numerical calculations when h is close to 90° (p very large). It is also interesting to know the surface area S (in km^2) of the camera field:

$$S = (d_2 - d_1)(b_1 + b_2) \quad (5.19)$$

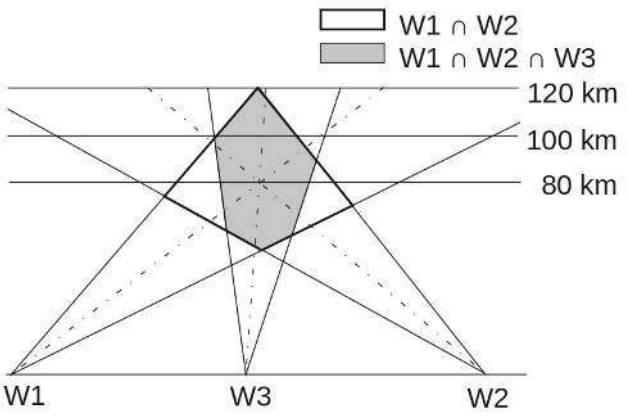


Figure 5.7: Intersection of camera fields in the meteor level between 80 and 120 km shown as a vertical cut.

5.4.3 Computation of the region of sky photographed

When a multiple station project is prepared, only one point is given to direct the camera; the point R at which the optical axis must be aimed. Where several cameras are used at one place, it is interesting to know whether some camera fields are overlapping, and, if so, by how much. Therefore the corners of each camera field are computed as projected onto the celestial sphere. In such a spherical projection, the camera field is of course no longer a rectangle.

Assuming that the camera is mounted horizontally, we can obtain the upper limit of the camera field by adding 27°/2 or to the elevation of the direction point R. Analogously, we can determine the lower limit by reducing the elevation of R by 13.°5.

Now, we determine the azimuth of the corners of the camera field. The angle on the azimuth scale becomes larger as we approach the zenith, in other words, the angle on the azimuth scale increases by a factor $1/\cos h$ where h is the height of the actual corner computed in the previous paragraph. If that was found to be 73.°5, the value being added to/subtracted from the azimuth value of point R equals $(39.°6/2)/\cos 73.°5 = 69°$.

5.4.4 Optimising the camera fields

As the basic principles of double station photography have now been explained, we can find out whether or not every meteor within the camera field will be caught at the two stations. Let us look once again at Figure 5.6. The bottom of our camera field photographs a region of the sky which is much closer to the horizon than the other parts of the image. Meteors that appear in the bottom region of the photo occur at a much larger distance away from the observer than the meteors caught in the centre. Due to this greater distance, these meteors appear fainter and the probability of photographing them decreases considerably. The loss in luminosity due to the distance relative to a standard distance of 100 km is given by

$$\Delta m = 2.5 \log(A^2/(100\text{ km})^2), \quad (5.20)$$

where A is the distance to the meteor in km. Atmospheric extinction will also reduce the meteor's luminosity. The absorption can be approximated by the following function (valid for a pure, terrestrial atmosphere):

$$\Delta m' = \frac{0.38}{\sin(\eta - 1)}, \tag{5.21}$$

where η is again the elevation for which the extinction is desired. For a polluted atmosphere $\Delta m'$ will be greater, as the value of 0.38 will no longer be valid. In populated areas, the ideal values of 0.38 will never occur, but will be at least 0.6 to 1.0. The absorption value varies strongly from one region to another and from one night to the next. The total loss in luminosity ΔM for a photographed meteor thus becomes $\Delta M = \Delta m + \Delta m'$.

The real loss in hourly rates is also determined by the mass distribution of the meteoroids, described by the population index r. For sporadic meteors, r varies mostly around 3.0. For shower meteors, r is generally smaller and is 2.0–3.0. The factor C which reduces the number of meteors recorded due to the loss of luminosity is written as: $C = r^{\Delta M}$. It is obvious that the lower the elevation of the camera, the fewer meteors we will photograph due to the loss in luminosity. There is, however, also a gain. The lower we aim the camera towards the horizon, the larger the intersection volume with the meteor layer in the atmosphere becomes. The photographed volume V at 100 km height increases by a factor C_V as a function of the camera elevation h roughly as

$$C_V = 1/\sin^2 h. \tag{5.22}$$

In order to find out whether or not we gain anything by selecting a given elevation of the camera, we compute

$$C_{\rm tot} = \frac{r^{-[0.38/\sin(h-1)-5\log\sin h]}}{\sin^2 h}. \tag{5.23}$$

For a perfectly transparent sky (absorption coefficient 0.38), it turns out we gain in terms of photographic hourly rates for most shower meteors ($r < 3.0$) by aiming the camera at a less than zenithal elevation (e.g., 30°). For meteor streams which are richer in faint meteors, it turns out the optimal elevation is around 50°. In the case of shower meteors we also have to consider systematic differences in angular velocity dependent on the direction and distance to the radiant (details are described in Chapter 3). In most cases, however, we will work where the sky is far from perfectly transparent, as most observers do their observational work close to their homes, often near towns or industrial areas. Because of the large absorption coefficients, it is not recommended to aim a camera at a low elevation in these cases. At most observing stations the photographic hourly rate will decrease as the zenith distance of the camera field increases. This explains why photographers can have very different degrees of success with the same kind of optics and film, but at different sites.

In double-station photography, it is important to try to photograph an area in such a way that the absolute limiting magnitude for meteors in both camera fields is, as far as possible, identical. Remember, however, that

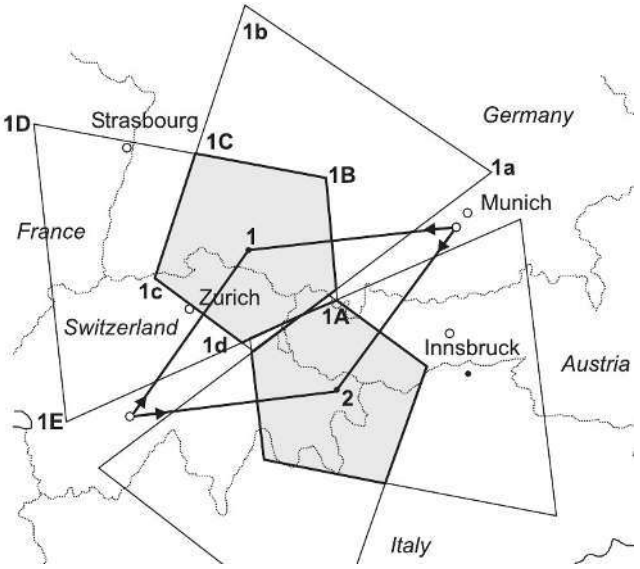


Figure 5.8: The camera fields for two stations, one in Switzerland, the other near Munich in Germany, as used during an actual observing campaign as projected onto a map. As can be seen, the camera fields cover large areas above France, Switzerland, Austria, Italy and Germany. Corners of two fields are marked (1A–E and 1a–d), which correspond to the positions indicated in Figure 5.9.

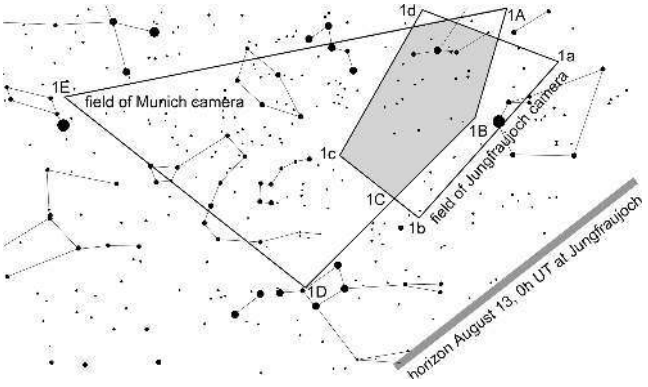


Figure 5.9: As seen from the Swiss station Jungfraujoch, the camera fields were projected at $0^{\rm h}$ UT onto a star map. This is helpful when positioning the cameras at night. Also the area photographed from Munich has been indicated (dashed field), which shows only a small part of this camera field is common with the corresponding one at Jungfraujoch.

- the camera fields must cover about the same volume in the atmosphere;
- the distance to the other stations of a network must be about equal.

At this stage, it becomes clear that the optimisation of a camera network becomes a complex organisational job. Even when the above criteria are fulfilled, there is still one important element to be considered. There is no guarantee that the photographed double station meteors will yield good results, as, for instance, the trail of the meteor and the two observing places may lie in

the same plane. The angle of convergence of the two photographed meteors will then be zero. Such a case is a most annoying problem, giving very poor computational results. In view of this problem, we need to take the geometric conditions of occurrence for shower meteors into account. The best way to improve our camera positions is to examine the entry angles of the shower meteors we intend to try to photograph by simulating the actual circumstances.

5.4.5 Simulating meteor trails for tests

We will not generate meteors at random, but will instead select where we will let the meteor appear (1), from which radiant it radiates (2), the time (3) and its absolute magnitude (4). With these four starting elements we can begin the simulation. The procedure, step by step is as follows:

We compute the azimuth a_R and elevation h_R of the radiant at the selected time and for the geographical position φ_b; λ_b above where the meteor starts at height h_b.

We compute the position of the ending point h_e of the meteor. From the length l (km), the azimuth and the elevation of the radiant: $h_\mathrm{e} = h_\mathrm{b} - l \sin h_\mathrm{R}$.

$$\lambda_\mathrm{e} = \lambda_\mathrm{b} \pm \frac{l \cos h_\mathrm{R} \sin a_\mathrm{R}}{1852 \cdot \cos \varphi_\mathrm{e} \cdot 60}; \qquad (5.24)$$

$$\varphi_\mathrm{e} = \varphi_\mathrm{b} \pm \frac{l \cos h_\mathrm{R} \cos a_\mathrm{R}}{1852 \cdot 60}. \qquad (5.25)$$

For some showers, the mean values for l and h_b can be found in research papers.

Finally, we calculate from h_e, φ_e, λ_e and h_b, φ_b, λ_b the azimuth and elevation for each observer W_1 and W_2 at locations φ_1, λ_1 and φ_2, λ_2.

5.4.6 Casual fireball images

A number of fireballs is recorded casually on video (security cameras or dashboard cameras) or on photographs. In some cases such images which are not taken as a part of a systematic survey can be of high scientific value. Positions can be measured even if the images were taken under rather poor circumstances if a calibration is possible. This is described in detail by Borovička (2014). For calibration purposes it is necessary to find the exact position of the camera when the fireball image was taken. Then, additional images in the same direction need to be taken to allow measurement of reference objects. Analysis of casual video recordings have been used to calculate orbits of the meteoroids causing seven recent meteorite falls (see the list in Borovička (2014)).

5.5 Meteor spectra

5.5.1 The camera and dispersing element

In principle, any camera can be converted into a spectrograph by placing a dispersing element (prism or grating) in front of the lens. Gratings have the advantage of linear dispersion, but they produce many spectra of different orders overlapping each other. Much of the light from the meteor ends up in the useless zeroth order (the 'normal' meteor image with no lines visible).

5.5.2 Prism spectrograph

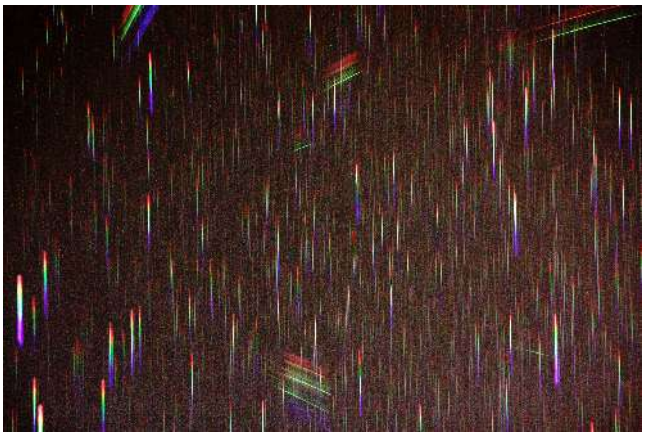


Figure 5.10: Example of Geminid spectra obtained with a DSLR camera and a prism in front of the lens (Cheng & Cheng, 2011).

Lenses with focal lengths of at least 50 mm are most useful for prism spectrographs. The reason for this is to ensure that a scale sufficient for analysis of the spectrum is achieved. An example is shown in Figure 5.10. If the dispersion (defined as the spread of the spectral wavelengths of light per unit length on the film/sensor) is too small, the lines are not well separated from each other. A large dispersion scale can be achieved using a prism with a large refracting angle, though this also means that the light must pass through a large quantity of glass, leading to light absorption. Alternatively, we may use a lens of longer focal length. A prism made of glass with a high refractive index n and a refracting angle $\alpha = 25°$–$30°$ combined with an $f = 100$ mm lens can produce useful results.

Because the camera field must be sufficiently large, small-frame cameras are less suitable. An old 6 cm × 9 cm bellows camera or a 9 cm × 12 cm plate camera are very well suited to meteor spectroscopy. Such cameras can often be found for very reasonable prices second-hand.

The prism employed should have a large deviation angle made of a glass with a high refractive index n. The position and orientation of the prism in front of the camera lens is very important. Care must be taken to ensure that no direct light falls on the lens, which

has to be completely covered by the prism. With a deviation angle α of the prism amounting to about 45°, the angle γ between the bottom of the prism and the camera lens should be about 25°. For a smaller angle α, the angle γ decreases.

It is convenient to fit the prism and camera into a box as this prevents light reflections on the prism from being projected through the camera lens. This box can also house some heating elements, as experience shows that large prisms are easily covered with dew.

5.5.3 Grating spectrograph

If a Rowland grating is in use, it is not necessary to use a lens with a long focal length. In this case, a small frame camera with a wide angle lens will suffice. The use of a diffraction grating has the advantage that a direct image of the meteor occurs on the film and that higher orders of the spectrum may also be recorded. The disadvantage is that the Rowland grating has to be large enough to cover the entire camera lens, a condition that increases the price of the grating considerably.

Inexpensive plastic transmission grating material is now available that can produce good results. This can be obtained from educational suppliers in 150 mm by 300 mm sheets with 500 and 1000 lines per mm (or 6 inch by 12 inch sheets with line counts of 12500 or 25000 lines per inch. Which line count and corresponding dispersion is a matter of choice related to the observer's goals. After cutting to the appropriate size it can be mounted in an empty rotating filter holder. This allows orientation to be varied as required. This technique is probably the least expensive and most flexible approach.

A singular advantage of using a transmission grating is almost linear dispersion. Suitable image processing and spectral analysis software is available on line and makes examination of spectra much more straightforward.

5.5.4 Spectrograph orientation

When the spectrograph is aimed at the sky, the orientation of the instrument requires special attention. The spectrograph must be oriented relative to the radiant in such a way that a bright meteor from that radiant will occur perpendicular to the dispersion direction of the spectrograph, in other words, parallel to the long-axis of the grating. Otherwise, the meteor will fill up its own spectral image. An example is presented by Russell (1990). Generally the magnitude threshold for a spectrograph is 2–3 magnitudes brighter than with the same lens used for direct imaging.

A list of 189 line identifications in a meteor spectrum can be found in Ceplecha (1966) and a list of 990 lines identified in a fireball spectrum is given by Ceplecha (1971). Analyses of meteor spectra are described in detail, e.g., by Borovička (2005) or Babadzhanov & Kokhirova (2007) and Jenniskens (2007). An overview of photographic meteor spectroscopy is given by Weber (2005). Cheng & Cheng (2011) report on some results of meteor spectra obtained with a DSLR camera equipped with a prism, including instructive examples and line identifications.

Suggestions for software (checked last 2021 Jan 10):
Image processing (for photometric and geometric corrections prior to spectrum extraction with particular attention to DSLR use) IRIS:
`http://www.astrosurf.com/buil/iris-software.html`
Spectrum processing software VSPEC:
`http://www.astrosurf.com/vdesnoux/`

5.6 Meteor trains

5.6.1 Regular trains



Figure 5.11: Detail of a 1-minute exposure showing a bright σ-Hydrid.



Figure 5.12: Detail of the 1-minute exposure immediately following the σ-Hydrid fireball shown in Figure 5.11. Another impressive train evolution is shown on the cover image of this Handbook.

Even regular meteor observers are surprised by bright meteors or fireballs. Normally, data about the brightness, time of occurrence, colours, and perhaps sound of a fireball are recorded in detail. Only for very bright and/or long-duration trains might someone think to take photographs of the train. General remarks on trains are given in section 2.9.3 on page 55.

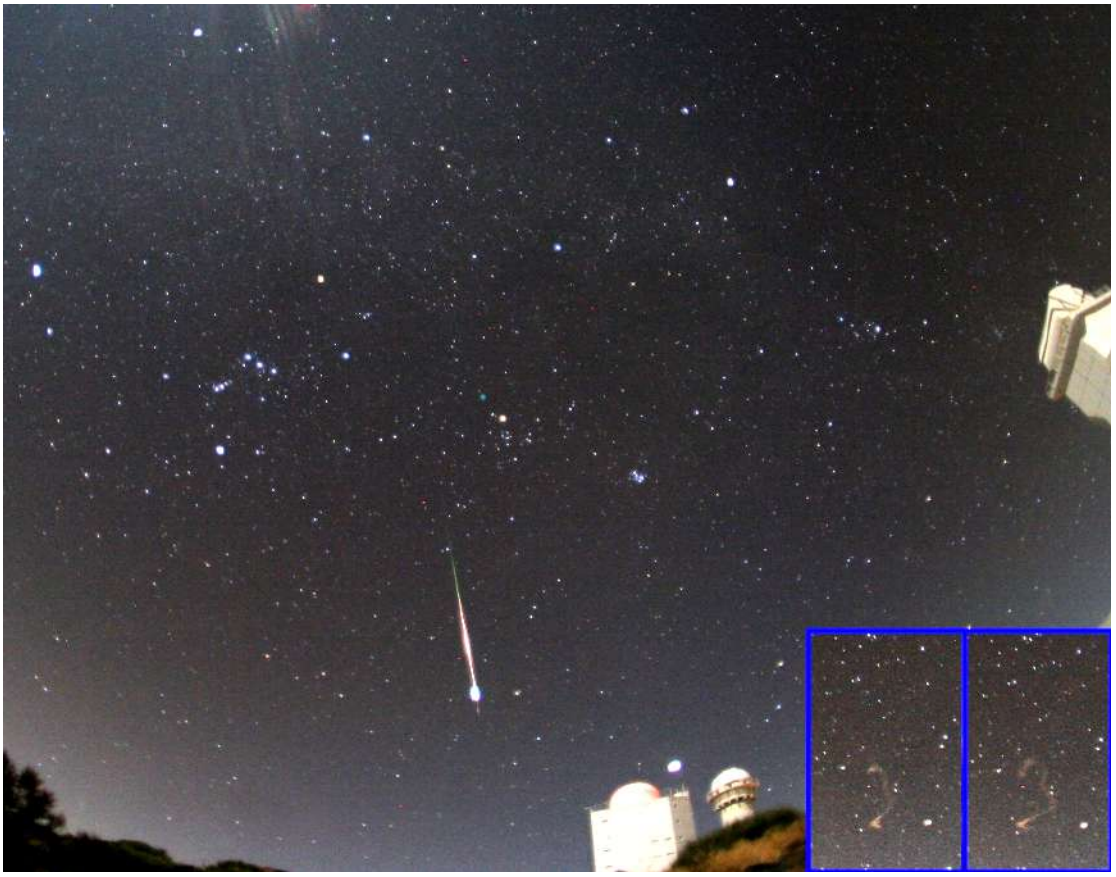


Figure 5.13: Leonid fireball on 2011 November 18, 0426 UT caught with a Canon EOS 20D and a $f = 8$ mm Peleng fish eye lens in a 1-min-exposure at the Observatorio del Teide, Tenerife, Spain (with the Moon high in the sky outside the shown field). The insets show the train 1 and 2 minutes after the fireball, respectively.

In this field, digital cameras have great advantages, particularly if equipped with timer remote controls. For example, one may start a continuous series of 1-minute exposures using a wide angle lens. Then, a bright meteor (see Figure 5.11) as well as the subsequent persistent train (Figure 5.12) are captured when occurring in the field. This is also perfectly visible on the photo of a bright Perseid fireball shown on the front cover of this Handbook.

In the case that the fireball occurs outside the field, one may immediately change the direction, thus missing only the first moment of the train. Another example is the Leonid fireball shown in Figure 5.13 which was visible for several minutes. The change of position and shape – a drift caused by upper atmosphere winds – can be easily traced if a series of images is made after the fireball appearance.

For very bright and long-duration trains, take a series of photographs to record the variations in brightness and shape. Each exposure should be between 10 and 30 seconds long. Guiding the photographs is not necessary. Generally, observers are not prepared in the manner we have just described, so chance plays a major role.

Due to the removal of reciprocity failure by electronic detectors the normal mode of operation, 20–30 second exposures, allows DSLR to capture trains more regularly than film based techniques. This has opened up the field to more detailed analysis.

5.6.2 Smoke trains

Since smoke trains (or dust trains) do not emit light, they appear dark, thus they are not visible in the night sky. They may be visible accompanying daylight fireballs as *smoke trains*, which then appear bright if lit by the Sun. A famous example is the impressive train left by the Chelyabinsk superbolide on 2013 February 15 (see discussion on page 22). In Figure 5.14 we show the dust train about half a minute after the fireball passage. The event happened shortly after sunrise so that the train was lit by the Sun with darker portions on the far side. It remained visible for more than an hour. Particles were found to form a closed band around the globe over the northern hemisphere (Gorkavyi et al., 2013).

Of course, it is not feasible to establish a regular survey for daylight events, but if you do accidentally see a bright fireball during the day, you should note if this kind of train is formed, and if so try to photograph it. In this circumstance, the rules of 'normal' (daylight) photography are valid, and no special instructions are necessary. To be sure that the structures in a daylight smoke train are measurable, take photos with different exposure times, both over- and underexposing the image, and with some reference points on the images to allow position measurements.



Figure 5.14: Sunlit smoke train left by the extremely bright superbolide (magnitude −28) which appeared on 2013 February 15 over the Chelyabinsk region in Russia. Photo by Marat Ahmetvaleev.

5.7 Unusual meteor trails

Meteoroids entering the Earth's atmosphere at 11–72 km/s appear as "straight" lines (moving on a great circle in the sky). Occasionally, visual observers claimed that they saw "wobbling" or curved meteors which was doubted. A comprehensive study of such reports was published by Beech (1988).

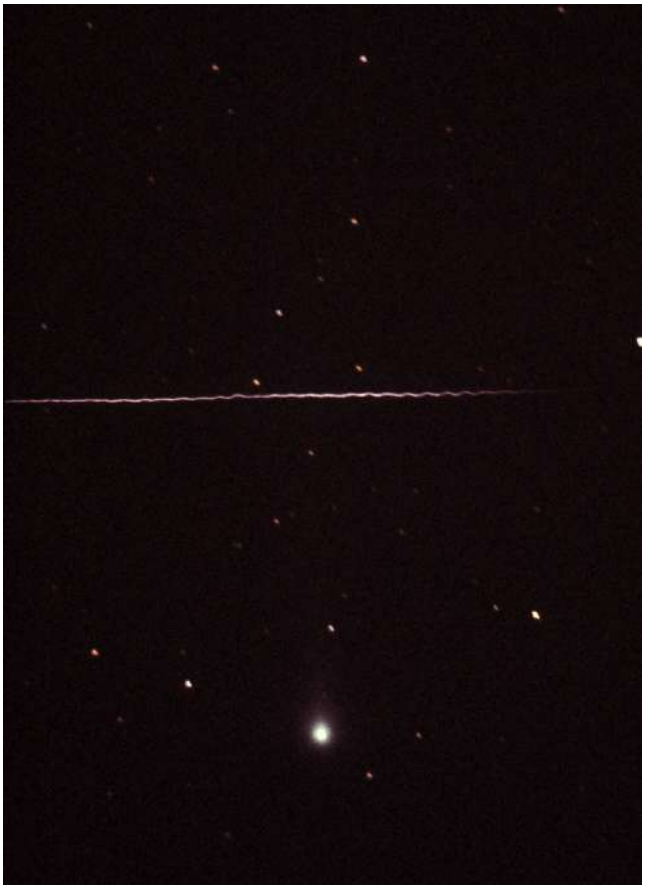


Figure 5.15: Non-linear trail of a meteor taken on 1986 January 1 through an 8-inch telescope, aiming for Comet 1P/Halley (courtesy of James R. Westlake, Colorado Mountain College).

Photographic meteor images and video meteors obviously prove a straight motion. However, there seem to be a few exceptions which have been widely discussed. Still, the reason(s) for a non-linear motion are not yet clear. In some examples, the meteors appeared close to the horizon, thus in about 300 km distance. An amplitude of the transverse shift of the order of 1′ corresponds to a linear motion of roughly 100 m.



Figure 5.16: A non-linear trail on an image taken on 2010 May 19 at 03:07 UT from the Teide Observatory at Tenerife with an $f = 8$ mm Peleng fish eye lens with a rather poor image quality close to the limb of the field (image: Jürgen Rendtel).

The image shown as Figure 5.15 was Astronomy Picture of the Day, 2005 February 2 (`https://apod.nasa.gov/apod/ap050202.html`; accessed on 2021 February 16). It was taken through an 8-inch telescope at prime focus. The target of photographer James R. Westlake of Colorado Mountain College was Halley's Comet on 1986 January 1. He saw the rather slow meteor drift through the field of view while guiding the image.

Another "twisting" meteor shown in Figure 5.16 was imaged on 2010 May 19 at 03:07 UT. As Astronomy Picture of the Day for 2010 June 2 (`https://apod.nasa.gov/apod/ap100602.html`) it caused a long discussion about possible explanations.

The meteor was not seen visually, hence its magnitude, its direction of motion and angular velocity are not known. The trail has an almost linear part (closer to the horizon) while the other section has an obvious wavy shape. In total, eight "periods" can be seen over the entire trail. It was suspected that the tripod was not stable enough and the meteor appeared right after the exposure start. Then, the wiggle might be an effect of the mechanical camera shutter (which is not likely as shown by several tests later). Shakes of the tripod by wind gusts kept over more than the duration of the



Figure 5.17: Two images showing non-linear trails taken during the Geminid observations in December 2017 from Tenerife (images: William Ward).



Figure 5.18: This image was taken on 2011 August 12, $00^{h}09^{m}$UT from Würzburg, Germany, with a $f = 10\,\mathrm{mm}$ lens ($d/f = 4.5$). The incoming clouds covered a large fraction of the sky when the two bright meteors (-2 and -4 mag) occurred about 10 seconds after each other. The trail of the first meteor is linear and while the second one closer to the horizon appears wavy. Since the exposure was terminated shortly after the second meteor (total exposure 21 seconds), a large effect of a bright winding train is unlikely (courtesy: Pierre Bader).

meteor are also unlikely since the tripod height was just about 20 cm (almost at the ground). The frequency can be estimated to be of the order of 8 Hz if the duration of the meteor was about a second.

Similar in their appearance are two meteor trails obtained by William Ward in December 2017 also from Tenerife during the Geminids (Figure 5.17). If there are 5 or 6 wobbles in an image over say 0.5 s, then the frequency of vibration would be 10–12 Hz but it must be very small in amplitude. A mirror slap was suggested as a reason because there were several cameras linked to the same controller. Given the weight of three cameras on a single tripod would be slightly top heavy any slight oscillations caused by the mirror slap and possibly combined with wind may set up a mechanical resonance, akin to a pendulum. With variations in wind it may explain why some images show the effect and others do not. Prior and subsequent images have been checked but the effect does not occur in any other images taken with the same set up.

Assuming that the meteors we found with non-linear trails lasted about 0.5 s to 1 s, the periodicity is of the order of 6–12 ms. It seems not physically realistic to assume that a meteoroid of a few millimetres size follows a zig-zag or spiral trajectory several hundred meters across. The forces the meteoroid would experience

are greater than the material strength and would cause fragmentation which cannot be found in the images.

The image with two bright meteor trails (Figure 5.18) is interesting as it has both a "normal" linear and a non-linear trail. The meteors were just 10 seconds apart, so vibrations of the camera can be excluded as a reason for the non-linearity. Occasionally, trails appear wavy on photographs due to the superposition of the actual meteor trail image and the subsequent persistent train with its winding structure. However, we may exclude this here as well, because the exposure was terminated only a few seconds after the bright meteor appeared.

At the moment we have no conclusive information whether a meteoroid is physically able to move in the way the images suggest. Video data of fragmenting meteors recorded by the Canadian Automated Meteor Observatory (CAMO) have been analysed (Stokan et al., 2014). During the fragmentation, transverse speed of the order of 100 m/s have been found which is much larger than expected. Several possible effects are discussed in this paper. The 6 ms to 12 ms estimated above are of a comparable order of magnitude to an analysis of a spiral *train* (Shigeno et al., 1988). Here the idea is that the meteoroid rotates (period 4.17 ms) and the emitted gas performs a spiral motion.

Several phenomena, such as quasi-periodic brightness variations (flickering), suggest that meteoroids rotate, probably already after ejection from a parent object (Čapek, 2021). High temporal resolution light curves shown by Spurný et al. (2007) hint at typical frequencies of the order of 10 Hz. Whether this is a chance coincidence or has implications for the understanding of the observed "oscillating trails" is not clear at this moment.

5.8 Artistic meteor imaging

It must not be forgotten that many observers enjoy the aesthetics of meteor photography. To those astro imagers the pursuit of an attractive picture is the very reason that they do it. Modern digital SLR cameras make the pursuit of artistic imaging easy and fun. One of the best things that you can do to improve your skills is to keep a notebook. This will prove invaluable as you gain experience, recording what works and what doesn't! A few things to consider are:

- note your location;
- record the date and time. Keep your camera clock accurate;
- record the camera details, especially the lens and ISO settings;
- note what you are imaging. What part of the sky or constellation are you concentrating on?, Are you out during a meteor shower?;
- record if you obtain the image you were seeking.

These things may not seem important, even for non scientific images, but they are. After a while exact dates/times etc. get forgotten. You may still have to trawl through, possibly hundreds, of images if you are looking for one in particular. A few notes and everything is much easier a few weeks/months later.

If you capture a pleasing imaging do not hesitate to send it to the WGN editor. Attractive pictures illustrating meteor astronomy are always needed.

Although you may be taking a picture for it's artistic qualities don't forget it just might be needed for analysis if it turns out to be an usual or extremely bright fireball, then those notes will be invaluable!

Acknowledgements

Dieter Heinlein provided us with recent information and figures concerning the status of the European Network. Thanks to James R. Westlake and Pierre Bader for sharing their images of non-linear meteor trails, and to Marat Ahmetvaleev for the permission to use his smoke train image.

References:

Babadzhanov P.B., Kokhirova G.I., 2007: Some results from the quantitative analysis of meteor spectra. *Advances in Space Research* **39,** 533–537.

Beech M., 1988: Non-linear meteor trails. *EMP* **42,** 185–199.

Bland P.A., 2004: Fireball cameras. The Desert Fireball Network. *Astron. Geophys.* **45,** 5.20–5.23.

Bland P.A., Spurný P., Bevan A.W.R., Howard K.T., Towner M.C., Benedix G.K., Greenwood R.C., Shrbený L., Franchi I.A., Deacon G., Borovička J., Ceplecha Z., Vaughan D., Hough R.M. 2012: The Australian Desert Fireball Network: a new era for planetary science. *Australian J. of Earth Sciences* **59,** 177–187.

Borovička J., 2005: Spectral Investigation of Two Asteroidal Fireballs. *EMP* **97,** 279–293.

Borovička J., 2014: The analysis of casual video records of fireballs, *in: M. Gyssens and P. Roggemans (eds.): Proceedings of the IMC, Poznan, 2013*, 101–105

Čapek D., 2021: Rotation of cometary meteoroids. *A&A* **,** submitted.

Carlson B.S., 2002: Comparison of modern CCD and CMOS image sensor technologies and systems for low resolution imaging. *Sensors, 2002. Proceedings of IEEE* **1,** 171–176.

Ceplecha Z., 1961: Determination of wavelengths in meteor spectra by using a diffraction grating. *BAC* **12,** 246–250.

Ceplecha Z., 1966: Complete data on iron meteoroid (Meteor 36221). *BAC* **17,** 195–206.

Ceplecha Z., 1967: Meteor spectra, *in: L. Kresák and P.M. Millman (eds.): Physics and Dynamics of Meteors.* IAU-Symp., 73–83.

Ceplecha Z., 1971: Spectral data on terminal flare and wake of double-station meteor no. 38421 (Ondřejov, Apr. 21, 1963). *BAC* **22,** 219–304.

Ceplecha Z., 1973: Evidence from spectra of bright fireballs, *in: C.L. Hemenway, P.M. Millman and A.F. Cook (eds.): Evolutionary and Physical Properties of Meteoroids.* Washington (NASA SP-319), 89–102.

Ceplecha Z., Bocek J., Jezkova M., 1979: Photographic data on the Brno fireball EN 140 977, SEP 14, 1977. *BAC* **30,** 220–225.

Ceplecha Z., Rajchl J., 1963: Meteor spectra with high dispersion. *Smithson. Contr. Astrophys.* **7,** 129–153.

Ceplecha Z., Rajchl J., 1965: Programme of fireball photography in Czechoslovakia. *BAC* **16,** 15–22.

Ceplecha Z., Spurny P., Bocek J., Novakova M., Polnitzky G., 1987: European Network fireballs photographed in 1978. *BAC* **38,** 211–222.

Cheng Sihao, Cheng Simiao, 2011: Meteor spectral observations with DSLR, normal lens and prism. *WGN* **39,** 39–46.

Gorkavyi N., Rault D.F., Newman P.A., Silva A.M., Dudorov A.E., 2013: New stratospheric dust belt due to the Chelyabinsk bolide. *Geophys. Res. Lett.* **40,** 4728–4733.

Halliday I., 1967: The influence of exposure duration and trail orientation on photographic meteor spectra, *in: L. Kresák and P.M. Millman (eds.): Physics and Dynamics of Meteors.* IAU-Symp., 91–104

Halliday I., Blackwell A.T., Griffin A.A., 1984: The frequency of meteorite falls on the earth. *Science* **223,** 1405–1407.

Howie R., Paxman J., Bland P.A., Towner M.C., Sansom E.K., Devillepoix H.A.R., 2017a: Submillisecond fireball timing using de Bruijn timecodes. *MAPS* **52,** 1669–1682.

Howie, R., Paxman J., Bland P.A., Towner M.C., Cupak M., Sansom E.K., Devillepoix H.A.R., 2017b: How to build a continental scale fireball camera network. *Experimental Astronomy* **43,** 237–266.

Jenniskens P., 2007: Quantitative meteor spectroscopy: elemental abundances. *Advances in Space Research* **39,** 491–512.

Kokhirova G.I., Babadzhanov P.B., Khamroev U.Kh., 2015: Tajikistan fireball network and results of photographic observations. *Solar System Research* **49,** 275–283.

Koten P., Rendtel J., Shrbený L., Gural P., Borovička J., Kozak P., 2019: Meteors and meteor showers as observed by optical techniques. In: *G.O. Ryabova, D.J. Asher, M.D. Campbell-Brown (eds.), Meteoroids. Sources of meteors on Earth and beyond.* Cambridge Univ. Press, 90–115.

Millman P.M., 1980: One hundred and fifteen years of meteor spectroscopy, *in: I. Halliday and B.A. McIntosh (eds.): Solid Particles in the Solar System.* IAU-Symp., 121–128.

Magnan P., 2003: Detection of visible photons in CCD and CMOS: A comparative view. *Nuclear Instruments and Methods in Physics Research* **A504,** 199–212.

Oberst J., Molau S., Heinlein D., Gritzner C., Schindler M., Spurny P., Ceplecha Z., Rendtel J., Betlem H., 1998: The "European Fireball Network": Current status and future prospects. *MAPS* **33,** 49–56.

Rendtel J., 1990: Fireball rates, *in: P. Spänyi, I. Tepliczky (eds.), Proceedings IMC Balatonföldvár, Hungary 1989.* IMO, 25–28

Russell J.A., 1990: Dissimilarities in Perseid meteoroids. *Meteoritics* **25,** 177–180.

Shigeno Y., Toda M., Kobayashi M., 1998: A spiral meteor train. *WGN* **26,** 220–225.

Spurný P., Borovička J., Mucke H., Svoreň J., 2017: Discovery of a new branch of the Taurid stream as a real source of potential hazardous bodies. *Astron. Astrophys.* **605,** A68.

Spurný P., Borovička J., Shrbený L., 2007: Automation of the Czech part of the European fireball network: equipment, methods and first results. In: *G.B. Valsecchi, D. Vokrouhlický, A. Milani (eds.), Near Earth Objects, our Celestial Neighbors: Opportunity and Risk, Proc. IAU Symposium 236.* Cambridge University Press, 121–130.

Weber M., 2005: Results of ten years of photographic meteor spectroscopy (1994–2003). *WGN* **33,** 21–22.

6 | Radio meteor observations

Cis Verbeeck, Jean-Louis Rault

6.1 Introduction

While radio observations are complementary to video and visual observations – allowing smaller particles to be observed with large statistics regardless of weather and time of day – they are a much less direct way of observing meteors. Hence, radio observations are more difficult to interpret. This chapter is intended to be a reference work for radio meteor workers, and should also provide a basic overview and understanding of radio meteor observations and their benefits to meteor workers that are not involved in radio observations or are relatively new to the field. The mathematical formulae given here are not essential for understanding the theory, and should in no case frighten the non-mathematical reader, who can simply ignore them. For improved readability of the text, all non-discussed symbols used in formulae are explained in Table 6.1 rather than in the text itself.

Section 6.2 describes the principle of specular reflection which governs radio meteor observations. Section 6.3 is a short introduction to forward scatter and radar systems aimed at the observation of meteors, while concrete examples of radio meteor observations are presented in section 6.4. Section 6.5 focuses on two important reflection mechanisms in radio meteor observations: underdense and overdense reflections. Distinguishing between underdense and overdense reflections is an important step in data reduction. Section 6.6 compares which meteor parameters can be recovered with a basic forward scatter setup, an interferometric setup, and a network of forward scatter stations. Section 6.7 addresses several approaches and examples to estimate the activity of the sporadic background and meteor showers. Finally, a few good places for further reading are recommended in section 6.8.

6.2 The principle of forward scatter and radar observations

6.2.1 Forward scattering and backscattering off a meteor trail

The general principle of meteor observation by forward scattering of radio waves off meteor trails is easy to understand. It is illustrated in Figure 6.1. A VHF radio receiver (about 30–100 MHz) is tuned to a radio transmitter located at a large distance (about 500–2000 km). Direct radio contact is impossible due to the curvature of the Earth. When a meteor enters the atmosphere, its plasma trail may reflect the radio waves from the transmitter to the receiver, via a point on the meteor called the *reflection point*. At the receiver, where the signal of the transmitter is normally not received, the broadcast can then be heard for a moment, as long as the meteor trail is present. Such reflections (also called "echoes") last from a tenth of a second to a few minutes.

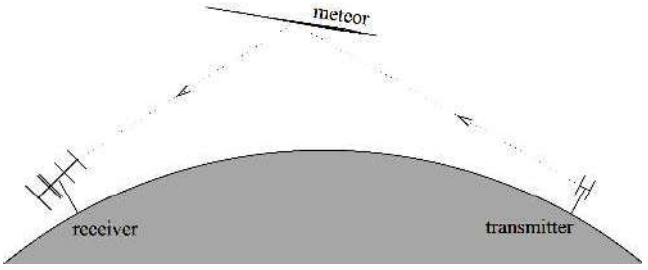


Figure 6.1: The principle of forward scatter observation of meteors. Signals from a radio transmitter are scattered to a receiver by a meteor trail, thus enabling the detection of the meteor.

This observation method became popular among amateur astronomers in the middle 1980s and is a variant of the radar observation method employed by professional astronomers since the end of World War II. Meteor scatter is also used to communicate in the VHF band over big distances (Schilling, 1993). In some forward scatter setups (e.g., in the BRAMS network, see section 6.3), the transmitter is so close to the receiver that the broadcasted signal is directly received. In this case, the meteor reflections are distinguished from the carrier wave using spectrograms (see section 6.4).

In a radar (also called backscatter system), transmitter and receiver coincide. Radars offer a much simpler reflection geometry than forward scatter, and in case discrete pulses are broadcast, the range (distance between radar and reflection point) can be obtained by measuring the travel time of the pulses. These systems, however, are much more expensive to build and maintain than their forward scatter counterparts. For this reason, professional meteor workers have focused almost exclusively on backscatter observations while amateurs

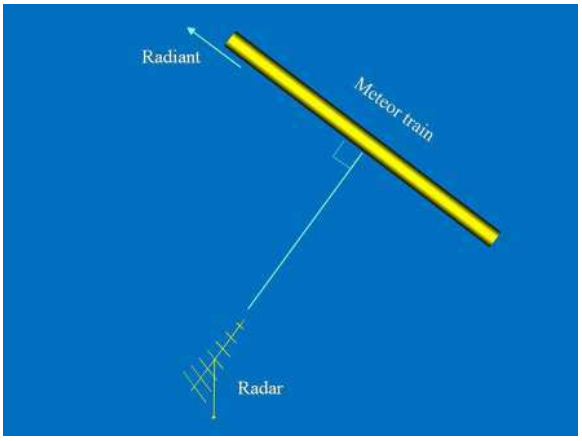


Figure 6.2: In a radar system, transmitter and receiver coincide.

typically employ a forward scatter setup. The radar geometry is illustrated in Figure 6.2.

6.2.2 The condition of specular reflection

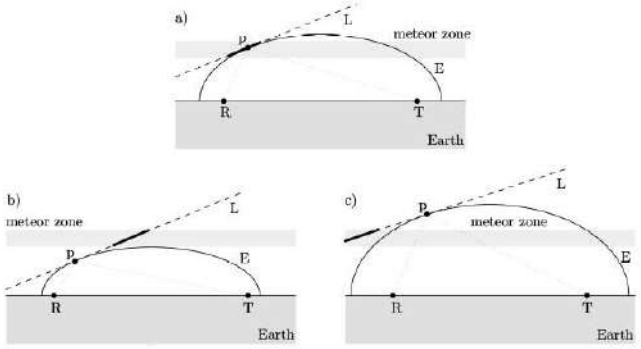


Figure 6.3: The reflection of radio waves off meteor trails is specular. It can therefore be compared to reflection of light off a mirror.

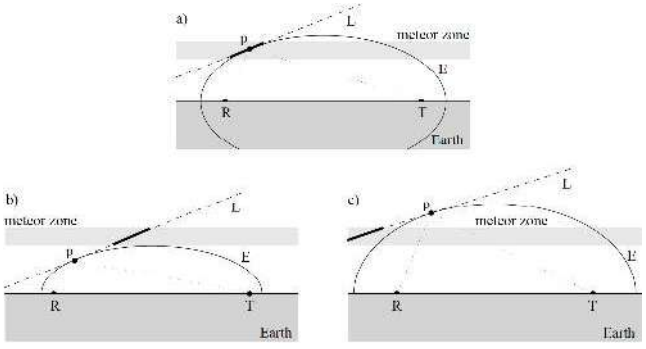


Figure 6.4: A meteor does not always reflect radio waves to the receiver. The signal is reflected in case *a*, but not in *b* or *c*. For simplicity, the Earth's surface was drawn flat.

An extremely important fact about the reflection of radio waves off meteor trails is that it is *specular* (except for HPLA radars, see section 6.3). In order to visualise the meaning of this statement, the transmitter can be thought of as a light bulb and the meteor as a long mirror, as shown in Figure 6.3. An observer sees the light bulb in only one point of the mirror. A direct and important consequence of the specularity of the reflection is that all the information derived from the radio observation of a meteor *only applies to the limited part of the trail that effectively reflects the radio waves*!

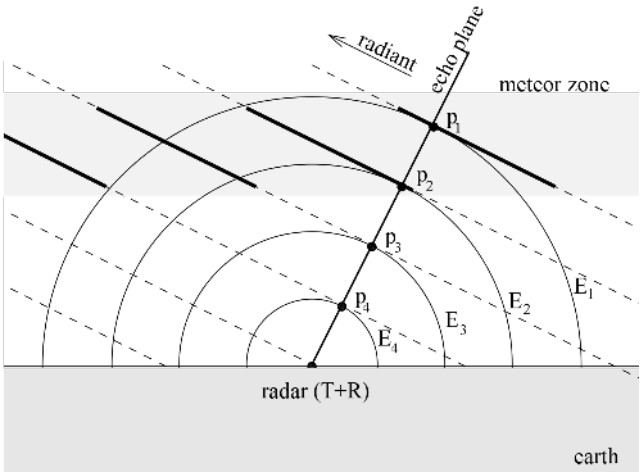


Figure 6.5: The formation of the echo plane for backscatter systems: all echoes ($\mathbf{p}_1$ and $\mathbf{p}_2$) from meteors of a particular stream are located in a plane.

The position of this specular area on the trail (which in this section will be referred to as a point (the reflection point) – see Wislez (2006) for more on this) depends only on the geometry of the reflection, i.e., the location of the transmitter, the receiver, and the meteor path. One way to find the reflection point $\mathbf{p}$ in a mathematical way (Figure 6.4*a*) is to take the line $\mathbf{L}$, defined by the meteor trajectory, and to look for an ellipsoid $\mathbf{E}$, with transmitter and receiver as foci, tangent to $\mathbf{L}$. This defines the point $\mathbf{p}$, and is an alternative formulation of the principle of Fermat (shortest optical path), governing all specular reflection phenomena. If $\mathbf{p}$ is a location on $\mathbf{L}$ where the ionisation produced by the meteoroid is small or nonexistent, no signal will be received by station $\mathbf{R}$ from this meteor (Figures 6.4*b* and 6.4*c*). If the ionisation in $\mathbf{p}$ is sufficient, like in Figure 6.4*a*, the signal is reflected to the receiver. Note that $\mathbf{p}$ is of course not required to be on the visual part of the trail. An echo can thus precede or follow a visual meteor with a few tenths of a second.

The specularity of the reflection has an important consequence for the observability of meteor showers. First consider transmitter and receiver at the same location, as for backscatter systems (Figure 6.2). In this case, the ellipsoid $\mathbf{E}$ becomes a sphere, which is much easier to visualise. Also consider a meteoroid stream. At a fixed moment in time, a meteoroid stream will produce a bunch of parallel meteors. These meteors will be tangent to spheres $\mathbf{E}_n$ in points $\mathbf{p}_n$ (Figure 6.5). These reflection points are all situated in the plane, passing through the transmitter/receiver point and perpendic-

ular to the radiant direction. This plane is called the *echo plane*. Seen from the transmitter/receiver point, all echo points are situated on a great circle in the sky, with the radiant as a pole.

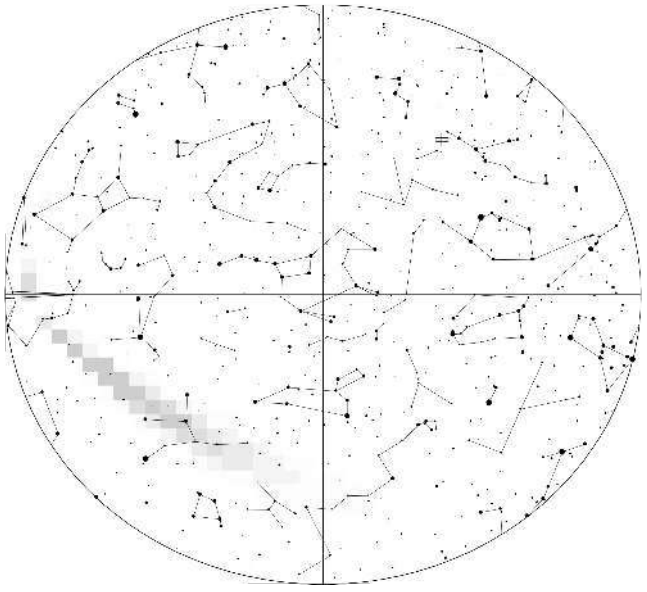


Figure 6.6: The echo surface of a stream as seen from the receiver, in the case of forward scatter. This figure was calculated by *Project Meteor*, a program by Paul Vauterin of the University of Ghent, Belgium.

For forward scatter systems, the echo plane changes into a curved *echo surface*. As seen from the receiver, the echoes do not appear on a great circle any more, but in a particular strip on the sky globe (Figure 6.6).

In some cases, winds at meteor altitudes can twist a trail that did not produce an echo into a reflecting position, yielding an echo only some time after the trail was formed. This phenomenon is called *non-specular reflection*, and is common for bright meteors. These meteors will thus not be observed in the echo surface corresponding to their shower.

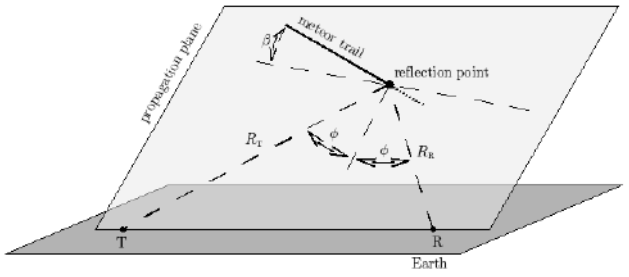


Figure 6.7: Basic forward scatter geometry. The various parameters are explained in the text.

The geometry of the reflection, which is governed by the specular criteria, is important to consider when performing calculations. Figure 6.7 defines the main geometrical parameters.

6.3 Forward scatter and radar setups

Forward scatter observations mostly employ frequencies between about 30 and 100 MHz. For many years, Band I TV transmitters (near 50 MHz) have been used to observe meteors by forward scattering. Nowadays, most of those analog transmitters are disappearing, moving to VHF or UHF digital TV transmissions. Still active Band I transmitters (mainly located in Eastern Europe) are listed in "TV offsets files" available on the Skywaves FM & TV DX forum (on Yahoogroups). In Belgium, dedicated transmitters are provided by the BRAMS radio meteor network (Lamy, 2012) and the astronomical association "Vereniging Voor Sterrenkunde" (VVS).

The main West-European transmitters currently used for forward scatter are:

- GRAVES radar (143.050 MHz), located near Dijon, France (`http://www.fas.org/spp/military/program/track/graves.pdf`)
- VVS beacon (49.990 MHz), located in Ieper, Belgium
- BRAMS beacon (49.970 MHz) located in Dourbes, Belgium (`http://brams.aeronomie.be/`)
- Radio France International (several frequencies on the 15, 17, and 21 MHz BC bands), located in Issoudun, France

In the USA and Canada, the SNOTEL transmitters working around 40 MHz can be used successfully for observing meteors. [1,2] Several radio amateur beacons around 50 MHz can be found at `www.keele.ac.uk/depts/por/50.htm`.



Figure 6.8: A typical receiving station in the BRAMS network.

Forward scatter receiving stations typically employ directional antennas (e.g., Yagi antennas) in combination with a commercial receiver, with a sound card to

[1] `http://en.wikipedia.org/wiki/SNOTEL`
[2] `http://wiki.radioreference.com/index.php/SNOTEL`

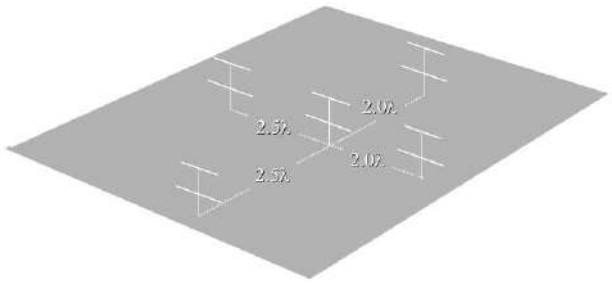


Figure 6.9: The antenna configuration of the CMOR radar at the University of Western Ontario near London, Ontario, Canada.

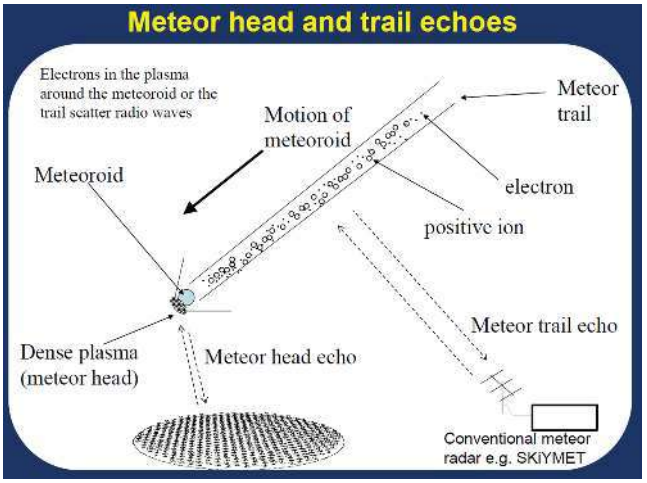


Figure 6.10: HPLA radars mainly observe head echoes, whereas meteor radars and forward scatter setups mainly observe specular echoes from the meteor trail.

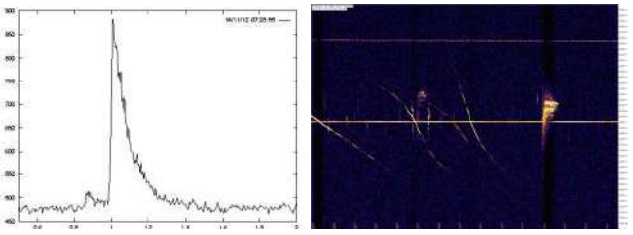


Figure 6.11: *Left:* Power profile of an underdense meteor. The time interval on the x-axis is 1.5 seconds. *Right:* Spectrogram featuring several underdense meteors (vertical lines on the left) and an overdense meteor (broad vertical line on the right). The curved shapes correspond to reflections off moving airplanes. The time interval on the x-axis is about 15 minutes.

convert the analog signal from the antenna to digital input for the computer. Forward scatter receiving stations are preferably fitted with a GPS receiver used for accurate time stamping of the recorded data. The BRAMS network currently includes over twenty receiving stations with identical three-element Yagi antennas and identical receivers. Figure 6.8 shows an example of a BRAMS receiving station. A dedicated BRAMS interferometer consisting of five such antennas in a well-defined geometrical pattern has been established in recent years (Lamy et al. 2018, Lamy et al. 2020).

It is important to make sure that the receiver's automatic gain control is switched off and that the sound card does not play similar tricks. In fact, for calculating parameters such as the mass index of a stream, the response curve of receiver and sound card are best measured, which allows to transform the values that come out of the sound card to the values that came out of the receiving antenna.

Meteor radars are a lot more expensive than forward scatter setups, and consequently are the domain of professional meteor researchers. Due to the use of radio pulses rather than continuous waves, radars are able to recover the distance between the radar and a meteor reflection point. Their symmetric geometry simplifies calculations, and most often they are organised as a series of interferometers, which allows the calculation of meteoroid orbits. The Canadian Meteor Orbit Radar (CMOR; Jones et al, 2005) near London, Ontario, Canada is a classical example of a meteor radar. It consists of three separate interferometric radars, synchronised in transmission and reception and operating from a single site. The antenna configuration of CMOR is presented in Figure 6.9.

High Power Large Aperture (HPLA) radars (Pellinen-Wannberg, 2004) are entirely different from meteor radars, though they can be used to observe meteors, too. Most of these, such as Arecibo, Millstone Hill, Sondrestrom, and EISCAT, have been designed to observe (at VHF and/or UHF) the very weak Thomson scattering from nominally free electrons through the ionosphere up to 2000 km altitude. The common feature for these instruments are the high power in megawatt class, the large signal collecting area of thousands of square meters and very high signal processing and data storage capabilities (and hence, the very high cost). HPLA radars operate from about 40 MHz to 1.3 GHz. For classical meteor radars, the opening angle is usually tens of degrees, whereas HPLA radars usually have very narrow beams (0.5 degree $\simeq$ 1 km at 100 km height).

Due to their high power, HPLA radars can observe much fainter plasma densities than meteor radars. Because of the narrow beam, specular reflection is very unlikely. As a result, HPLA radars observe mostly *head echoes*. A meteor head echo is a radio wave reflection from a plasma cloud directly around the moving meteoroid as it ploughs through the atmosphere (Dyrud et al., 2008; (see Figure 6.10). In the sequel, we limit ourselves to traditional forward scatter and radar systems, hence, to specular reflection.

6.4 What do radio observations look like?

In the 1980s and 1990s, most forward scatter setups recorded the power of the received signal as a function of time, which is called a *power profile*. Typical power

profiles show a relatively stable noise level, and meteors are visible as peaks that are significantly higher than the noise level. If a few hundreds of samples per second are available, detailed profiles of individual meteors can be obtained. These profiles provide interesting physical information about the reflection point, and allow among others to distinguish clearly between underdense and overdense reflections (see section 6.5).

In the last decade or so, most forward scatter setups calculate (power) spectrograms, which are obtained by taking a Fast Fourier Transform of the received signal. The result is a spectrum as a function of time (the x-axis represents time, the y-axis represents a spectral range of typically around 200 Hz, and the colour code provides the power at the corresponding time and frequency). If the carrier wave is observed directly, it shows on the spectrogram as a bright horizontal line. Meteor reflections are visible as bright narrow (underdense) or broad (overdense) vertical lines near the carrier wave, and reflections off airplanes show up as longer lived, bright curves. There are several software packets which allow the automatic calculation of spectrograms from the received signal. One of the most popular ones for radio meteor astronomy is the freeware SpectrumLab.[3] Note that a spectrogram can also have frequency on the x-axis and time on the y-axis; this depends on the settings of the recording software.

An example of a power profile and a spectrogram is provided in Figure 6.11. A spectrogram can be converted into a power profile, and if the sampling rate is high enough, then a power profile can be converted into a spectrogram as well. This is useful as power profile and spectrogram provide complementary information.

6.5 Underdense and overdense reflections

During the ablation of the meteoroid, meteoric and atmospheric atoms are ionised, creating a trail of ions and free electrons. The reflection of the radio waves is performed by these charged particles: the electric field vector of the incoming wave makes them vibrate, and oscillating charged particles emit electromagnetic waves. The absorbed energy from the radio wave is thus reemitted in all directions. Theoretically, both ions and electrons in the trail contribute to the scattered signal. However, the ions are too heavy to produce a significant contribution, so only the electrons have to be considered.

The reflection mechanism depends on the density of free electrons in the trail. Only the two extreme cases are considered in the classical meteor scatter theory: the *underdense* trails, where electron densities are low, and the *overdense* trails, where electron densities are high.

Underdense meteors of course correspond to faint meteors. Theory sets an upper limit on the line density for underdense reflection, approximately corresponding to 2×10^{14} electrons per meter. This is a line density generally associated with 5th magnitude meteors. Observations of underdense reflections cover a meteoroid mass range that is not observable with the naked eye.

Overdense meteors are less numerous and correspond to brighter meteors. The reflections can last for seconds.

Though the reflection mechanism depends on the volume density of electrons, it is useful to introduce the concept of the *electron line density* α, i.e., the total number of free electrons per unit of length of the trail. It is a constant for a given segment of the trail, if the attachment of free electrons to neutral atoms is neglected. The electron line density is related to the luminosity of the considered section of the meteor trail.

6.5.1 Scattering off underdense trails

In this approximation, the free electron volume density is so low that the radio waves can penetrate the trail without attenuation. Each free electron scatters the incoming wave individually, and the total signal received from the trail is the sum, taking into account the phase, of the signals from all individual electrons.

If all electrons are concentrated on a line (a cylinder with radius $r=0$), the received power $P_\mathrm{u}(r{=}0)$ is

$$P_\mathrm{u}(r{=}0) = \frac{P_\mathrm{T} G_\mathrm{T} G_\mathrm{R} \lambda^3 r_e^2 \alpha^2 \sin^2\gamma}{16\pi^2 R_\mathrm{T} R_\mathrm{R} (R_\mathrm{T} + R_\mathrm{R})(1 - \sin^2\phi\cos^2\beta)}, \tag{6.1}$$

if we consider a homogeneous electron line density and an infinitely long trail (approximations which are not always good!). The received power can be seen to increase strongly with longer wavelengths (lower frequencies). It is also dependent on the electron line density and the position and orientation of the trail.

Of course, in reality the electrons are not on a line, but show a circular Gaussian density distribution around the meteoroid path (if the effect of the Earth's magnetic field is neglected). The radius r of the meteor trail is defined as the radial distance at which the electron volume density is $1/e$ times ($\approx 37\%$) the central density. A Gaussian meteor trail of radius r gives rise to an echo power of

$$P_\mathrm{u}(r) = P_\mathrm{u}(r{=}0) \exp \frac{-8\pi^2 r^2}{\lambda^2 \sec^2\phi}. \tag{6.2}$$

This equation shows an attenuation of the signal, which is due to the loss of phase coherence between the scattered waves. Equation 6.2 will be used in section 6.5.6 to derive the evolution of the received power with time. Note that, in reality, the meteor column is cone-shaped rather than cylinder-shaped.

6.5.2 Scattering off overdense trails

When the electron volume density is high, the central part of the trail behaves like a plasma. Radio waves cannot penetrate the core of the trail anymore, and are scattered off the trail's core surface: in the classical theory, the meteor is approximated by a reflecting 'metallic' cylinder. The radio waves can reach the cylinder

[3] `http://www.qsl.net/dl4yhf/spectra1.html`

without attenuation, but are reflected on its surface. If the radio wavelength is small compared to the cylinder radius, the power scattered in the normal direction is directly proportional to the radius of the cylinder.

The main problem with this *metallic cylinder* approximation is that the effect of the lower density parts of the trail surrounding the high density core is not taken into account. Also, due to winds, an overdense trail loses its cylindrical aspect after some time. Last but not least, when the cylinder is thin, the reflected power is not proportional to the cylinder radius anymore. One should keep all these considerations in mind when using the metallic cylinder model.

This approximation gets even worse in the forward scatter case. The models are crude extensions of the backscatter theory. The main problem here is that the backscatter theory assumes a normal incidence on the trail, which is hardly ever true in forward scatter situations.

Now that the limitations of the model have been pointed out, we can take a look at the mathematical formulation, based on Hines & Forsyth (1957).

Total reflection takes place on the cylinder in the trail in which the electron volume density N is higher than the *critical volume density* N_c, given by

$$N_c = \frac{\pi}{\lambda^2 r_e}. \tag{6.3}$$

The corresponding *critical radius* r_c in a Gaussian distributed column with radius r is

$$r_c = \sqrt{r^2 \ln \frac{\alpha r_e \lambda^2 \sec^2 \phi}{\pi^2 r^2}}. \tag{6.4}$$

In the sequel, we will approximate the trail by a totally reflecting cylinder with radius r_c.

As already stated, when the radius of a metallic cylinder is big compared to the radio wavelength used ($r_c \gg \lambda$), the reflected power (in the normal direction) is proportional to the radius of the cylinder. This together with some considerations about the forward scatter geometry, yields an equation for the power received from a Gaussian trail with radius r:

$$P_o(r) = \frac{P_T G_T G_R \lambda^2 \cos\phi \sin^2\gamma}{32\pi^2 R_T R_R (R_T + R_R)(1 - \sin^2\phi\cos^2\beta)} r_c(r). \tag{6.5}$$

Here too, position and orientation play a major role in the received signal level, and longer wavelengths give stronger signals.

6.5.3 Scattering off transitional meteor trails

For low electron densities, the underdense model is a good approximation. The metallic cylinder approach for overdense meteors has its limitations, but can be used for high densities with some corrections. However, when the electron densities are moderate, the above approximations do not stand. This intermediate case is therefore not looked at in the classical theory. The traditional approach is to define a sharp

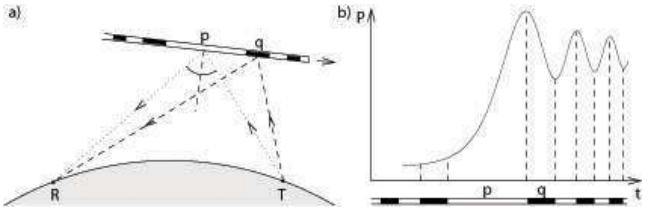


Figure 6.12: The origin of the Fresnel oscillations.

limit between overdense and underdense meteors at $\alpha = 2.4 \times 10^{14}\ e^-/\text{m}$, and to bear in mind that deviations from theory can occur when the electron line density is of the order of 10^{14} electrons per meter. The transition region can be described with the full wave theory (Jones, 1974).

6.5.4 Formation of the trail

Specular reflection can be explained by interference. Waves are in fact scattered in all directions from all parts of a mirror, but constructive interference only occurs in the direction predicted by geometrical optics. The closer a point of the mirror is to the geometrical reflection point, the more it influences the final signal. In radio meteor scatter, a few kilometres of the trail effectively contribute to the signal. It is thus more appropriate to talk of a reflecting section than of a reflection point, as was introduced in section 6.2.

Looking at Figure 6.12*a*, it is clear that a signal reflecting from point **q** travels a longer distance than a signal reflecting from point **p**. Therefore, there will be a difference in phase between both signals. One can define zones of constructive interference with the 'main signal' (the signal via **p**), and zones of destructive interference. They are coloured white and black, respectively, in Figure 6.12*a*. These zones are called the Fresnel zones.

During a meteoroid's flight, alternately 'white' and 'black' parts of the trail are formed, leading to signal strengthening and signal weakening by interference, thus resulting in a power profile (i.e., the evolution of received power in time) as shown in Figure 6.12*b*. The signal from a meteor typically takes less than a tenth of a second to rise to nominal power. When discussing diffusion in section 6.5.5, we will therefore consider the formation of the trail to be instantaneous.

Mathematically, the received power during the formation of the trail, considering an infinite trail length and homogeneous ionisation (again, this approximation does not always stand), is given by

$$P(r{=}0;t) =$$

$$P(r{=}0)\frac{1}{2}\left(\left[\int_{-\infty}^{x(t)} \cos\frac{\pi x^2}{2}\,dx\right]^2 + \left[\int_{-\infty}^{x(t)} \sin\frac{\pi x^2}{2}\,dx\right]^2\right).$$

$$= P(r{=}0)\frac{1}{2}(\mathbf{C}^2 + \mathbf{S}^2). \tag{6.6}$$

C and **S** are the Fresnel integrals, known from classical diffraction theory. The variable $x(t)$ relates to the

physical parameters according to

$$x(t) = vt\sqrt{\frac{2(R_\mathrm{T}+R_\mathrm{R})(1-\sin^2\phi\cos^2\beta)}{\lambda R_\mathrm{T}R_\mathrm{R}}}. \qquad (6.7)$$

Here, t was taken to be zero at the moment the meteoroid reaches the geometrical reflection point. The above equation was derived for a line trail ($r = 0$), and is adequate for underdense trails. Overdense reflections show a similar behaviour, but the mathematical derivation of that case is very difficult and has not been made yet for general geometries.

Note that when the size of the Fresnel zones is known, the velocity of the meteoroid can be found by measuring the frequency of the oscillations shown in Figure 6.12*b*.

The positions $s(n)$ of the n-th borders of the Fresnel zones depend on the geometry of the reflection and on the wavelength used. They are given by

$$s(n) = \sqrt{\frac{n\lambda R_\mathrm{T}R_\mathrm{R}}{(R_\mathrm{T}+R_\mathrm{R})(1-\sin^2\phi\cos^2\beta)}}. \qquad (6.8)$$

If Δt_{mn} is the time needed for the meteoroid to travel from point $s(m)$ to point $s(n)$, the velocity v of the meteoroid is given by

$$v = \frac{\sqrt{n}-\sqrt{m}}{\Delta t_{mn}}\sqrt{\frac{\lambda R_\mathrm{T}R_\mathrm{R}}{(R_\mathrm{T}+R_\mathrm{R})(1-\sin^2\phi\cos^2\beta)}}. \qquad (6.9)$$

Δt_{mn} can be derived from the recorded profile if the sample rate is high enough (about 1000 samples per second). Note that the full geometry of the reflection has to be known to derive the velocity.

The shape of the Fresnel oscillations can be altered by irregularities in the ionisation of the trail, the deceleration of the meteoroid and the diffusion of the trail.

6.5.5 Diffusion of the trail

Immediately after the trail is formed, the electrons and ions start diffusing in the surrounding atmosphere. At any time, the electron density distribution is considered to be Gaussian. The radius r of the Gaussian column changes with time t according to

$$r = \sqrt{r_0^2 + 4D_\mathrm{a}t}, \qquad (6.10)$$

where r_0 is the *initial radius* and D_a the *ambipolar diffusion coefficient*. We will first have a look at these parameters.

6.5.5.1 The initial radius r_0

During the ablation, meteoric atoms leave the meteoroid body with a velocity that is much higher than the thermal velocity of the atmospheric particles. These fast atoms are quickly slowed down by multiple collisions with the atmospheric atoms (thermalisation). The result of this process is that after a few milliseconds a trail with a finite radius is formed. This radius is called the initial radius and is dependent on the atmospheric density: the lower the density, the less atmospheric atoms there are to stop the fast meteoric ones from escaping from the meteoroid, so the larger the initial radius. Initial radii approximately range from ten centimetres to ten metres. Schilling (1993) gives an estimate of r_0, based on work of Bronshten:

$$r_0 = 2.58\times10^{12}\,\frac{\mu_\mathrm{a}v^{0.8}}{\rho_\mathrm{a}} \quad [\text{in m}]. \qquad (6.11)$$

There are many other approximative equations for the initial radius, but there is a very significant scatter in the theoretical and observational values.

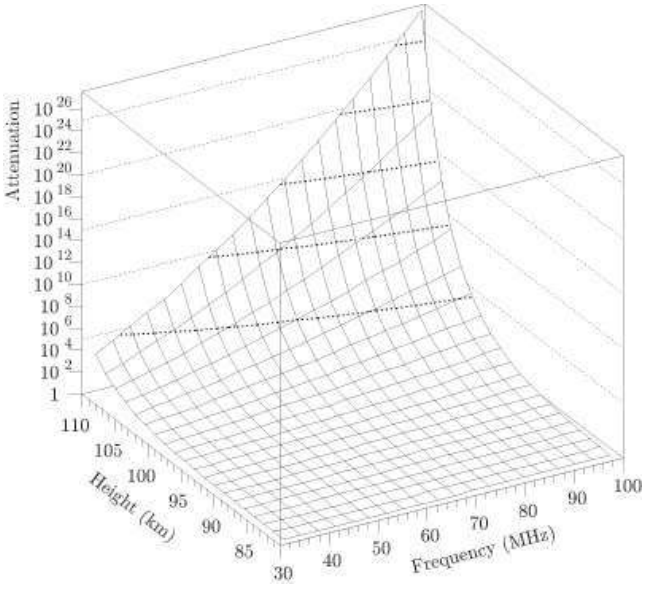


Figure 6.13: The attenuation of the power of underdense signals with height, leading to the echo ceiling. Note the power scale is logarithmic, so the rise in attenuation is very steep.

6.5.5.2 The selection effect of the initial radius

Consider an underdense trail. If the radius r of the trail is already important at the moment of creation, phase coherence between the scattered waves is lost from the beginning, and no significant power is reflected to the receiver. This is confirmed by equation 6.14, where the exponential part gets very small for big values of r. As the initial radius grows with height, the higher underdense meteors will be systematically cut out from the observations. The height at which the highest underdense meteors can be observed, is named the *echo ceiling*. Figure 6.13 depicts the attenuation of the power of underdense signals with height.

The ablation height of meteoroids rises with decreasing mass and increasing velocity. *Small* and *fast* meteoroids will thus always be discriminated against in radio observations.

The main advantage of forward scatter over backscatter lies in the $\sec^2\phi$ factor in equation 6.14. Its value can increase the denominator in the exponent, thus allowing greater values for r, bigger initial radii and thus greater heights. This can be seen as an increase of the wavelength to an effective wavelength $\lambda_\mathrm{eff} = \lambda\sec\phi$ in forward scatter geometries.

Note that overdense meteors do not have a theoretical echo ceiling, as the reflection takes place on their surface and not on the whole trail volume. However, as they correspond to heavier meteoroids, overdense meteors ablate lower in the atmosphere and an echo ceiling would have little effect.

6.5.5.3 The ambipolar diffusion coefficient D_a

The ambipolar diffusion coefficient D_a, as appearing in equation 6.12, specifies the speed of diffusion of the meteoric ions and the free electrons in the atmosphere, after the trail is thermalised. The difference with the regular diffusion coefficient is due to the ionic property of the diffusing matter. D_a is related to other physical quantities according to Greenhow & Neufeld (1955):

$$D_a = \frac{7\mu_a}{8\rho_a\sigma}\sqrt{\frac{kT}{\pi\mu_m}}. \qquad (6.12)$$

In practice, the main dependence is on the atmospheric density ρ_a.

Of course, a good atmospheric model is needed to get reliable values for the ambipolar diffusion coefficient. Very approximate values can be found by using the following empirical equation, suggested by Greenhow and Neufeld (1955):

$$\log D_a = 0.067h - 5.6, \qquad (6.13)$$

with the height h given in kilometres. The resulting value for D_a is expressed in square meters per second. Higher altitudes yield larger values for D_a.

6.5.5.4 The effect of diffusion on underdense reflections

Combining equations 6.2 and 6.10, we obtain the typical profile of an underdense meteor after formation:

$$P_u(t) = P_u(r{=}0)\exp\frac{-8\pi^2 r_0^2}{\lambda^2\sec^2\phi}\exp\frac{-32\pi^2 D_a t}{\lambda^2\sec^2\phi}. \qquad (6.14)$$

Hence, the received power decreases exponentially with time, with time constant

$$\tau_P = \frac{\lambda^2\sec^2\phi}{32\pi^2 D_a}. \qquad (6.15)$$

Usually, the decay time of an underdense echo is not defined by using the received power, but by using the amplitude of the received radio waves. This yields

$$\tau_A = \frac{\lambda^2\sec^2\phi}{16\pi^2 D_a} = 2\tau_P. \qquad (6.16)$$

This difference clearly points out that it is extremely important to have a set-up with an output that is in linear relation to the received *power* to use the equations as given. Consequently, recorded profiles should first be corrected for errors in the linearity of the system before processing.

It is interesting to take a quick look at the parameters governing the decay time of underdense meteors. Low frequencies (long wavelengths) yield longer echoes. The equation also shows that high meteors (big D_a) have a smaller decay time than low ones, and that forward scatter increases the duration of underdense meteor reflections with respect to radar observations at the same wavelength.

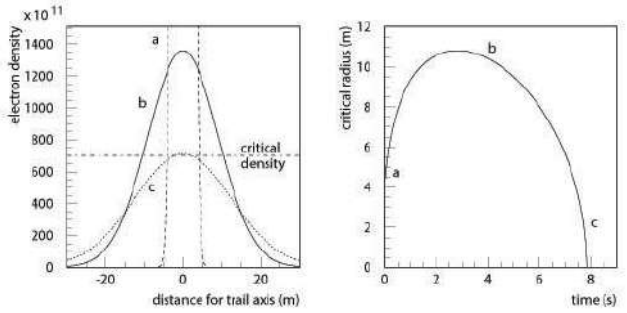


Figure 6.14: The diffusion of the trail is illustrated in the first figure, where the free electron density is shown for successive times a, b, and c. The second figure shows the evolution of the critical radius in time, which, according to the metallic cylinder approximation, is proportional to the received power from an overdense meteor.

6.5.5.5 The effect of diffusion on overdense reflections

Due to the diffusion of the trail, the radius of the overdense core of the trail increases with time. However, simultaneously, the central density of the trail decreases, which will eventually make the radius of the overdense cylinder shrink, until the overdense part totally disappears and only a big underdense trail is left (Figure 6.14*a*).

The evolution in time of the critical radius, and consequently the received power $P_o(t)$ in the metallic cylinder approximation, can easily be found by substituting equation 6.10 in equations 6.5 and 6.4, as we did in the underdense case. A plot of this function is given in Figure 6.14*b*. Remember that the used metallic cylinder approximation is not good for small radii, i.e., at the beginning and the end of the echo.

From this equation, the duration T_o of overdense reflections can be derived:

$$T_o = \frac{\alpha r_e\lambda^2\sec^2\phi}{4\pi^2 D_a} - \frac{r_0^2}{4D_a}. \qquad (6.17)$$

Note that this equation is highly unreliable for long-duration meteor reflections. Attachment of electrons to neutral atoms and molecules reduces the electron line density, limiting the duration of overdense reflections. It is difficult to quantify the rate of this attachment, as it is highly dependent on the surrounding atmosphere and on the degree of insolation of the trail. It has been shown that the recombination of electrons with ions can be mostly neglected.

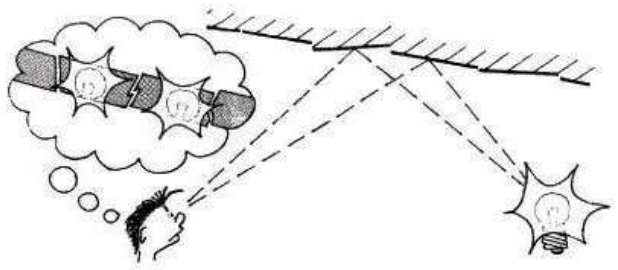


Figure 6.15: Appearance of secondary reflection points through the effect of wind shear.

6.5.6 Complete meteor power profiles

In the power profiles for underdense and overdense meteors derived in this section, the formative stage discussed in section 6.5.4 was not considered. A general combination of both formation and diffusion of a trail is very hard to do analytically. Therefore, the diffusion is generally only considered from $t = 0$ onwards (when the meteoroid passes through the reflection point), and the whole trail is supposed to have the same radius at a given moment (i.e., the trail is considered to be a cylinder rather than a cone). This yields:

$$P_{\mathrm{u/o}}(t) = \begin{cases} P_{\mathrm{u/o}}(0)\frac{1}{2}\left(\mathbf{C}^2(t) + \mathbf{S}^2(t)\right) & t \leq 0 \\ P_{\mathrm{u/o}}(t)\frac{1}{2}\left(\mathbf{C}^2(t) + \mathbf{S}^2(t)\right) & t \geq 0 \end{cases}. \tag{6.18}$$

$\mathbf{C}(t)$ and $\mathbf{S}(t)$ are the Fresnel-integrals, as introduced in equation 6.6. This approximation produces a bend in $t = 0$, which is however hardly noticeable when diffusion is not very strong.

6.5.7 Deep fading

In the upper atmosphere, strong winds distort the meteor trail. As a consequence, multiple reflection points can appear on the trail (think of a light bulb seen in a broken mirror, Figure 6.15). Radio waves from the different reflection points interfere. As the reflection points are not stationary due to the wind, interference conditions change continuously, and fast oscillations are observed in the received signal power, called *deep fading*. This feature can only be observed in meteors after several tenths of a second. Consequently, it does not affect typical underdense meteors, as these rarely last that long.

Another theory accounting for this deep fading is the blob theory, saying that an overdense trail tends to degenerate into a string of overdense clouds ('blobs'), each reflecting the radio waves to the receiver. Deep fading has been shown to be the result of both effects.

6.5.8 Examples of power profiles

The profiles shown below are (time, power)-registrations recorded by the RAMSES setup (Roelandts, 1994) at 200 samples per second. The time is expressed in seconds, the power is in an arbitrary unit.

The left panel of Figure 6.11 shows a typical power profile of an underdense meteor. The fast rise of the signal (about 25 ms) corresponds to the passage of the meteoroid through the first Fresnel zone, as discussed in section 6.5.4. The rise time carries information about the velocity of the meteoroid. The exponential fall of the received power (decay time τ_A of about 180 ms) is the result of the diffusion of the underdense trail in the atmosphere, as described in section 6.5.5.4. The decay time is related to the atmospheric density, and consequently to the altitude of the reflection point.

In the left panel of Figure 6.16, a "transition" meteor is shown. The meteor is initially overdense, and after the traditional fast rise of the signal, the received power slowly increases and decreases: the radius of the totally reflecting column first increases due to diffusion, but eventually decreases when the electron density gets too low (see Figure 6.14). When the overdense core of the trail has vanished, only an underdense trail remains. This accounts for the final exponential decay.

An enduring overdense meteor can be seen in the right panel of Figure 6.16. The features of an ideal overdense meteor can be seen initially (fast rise, followed by slower rise, as expected according to Figure 6.14), but after some tenths of a second wind shear creates multiple reflection points. Interference of the radio waves coming from the different reflection points produces strong oscillations in the signal power (as explained in section 6.5.7). Note the difference in time scale between the profiles shown in this section.

Of course, not all observed meteor profiles are as ideal as the ones shown. For instance, profiles can be altered by the superposition of the signals from different transmitters, if various transmitters at similar frequencies are scattering the signal. Also, an overdense trail may initially not be suitably oriented to reflect the radio waves to the receiver, but may start being visible after it has started to break up due to wind. A slowly rising signal will then be observed, with fluctuations due to deep fading.

Even if the observations were perfect, the theory, meteors, and atmosphere are not. The classical theory only considers the two extremes of purely underdense and purely overdense meteors. Furthermore, phenomena like irregular ionisation of the trail, loss of free electrons through attachment, turbulence, winds, the magnetic field of the Earth, etc., can seriously alter the obtained results. We also have neglected purely atmospheric effects like the absorption of the signal in the D-layer during daytime, etc. These, and many other effects, imply that interpretation of radio meteor observations always has to be done with extreme care.

Last but not least, signals from meteoric origin need to be distinguished from other sources of radio signals: man-made noise, lightning, atmospheric effects, etc.

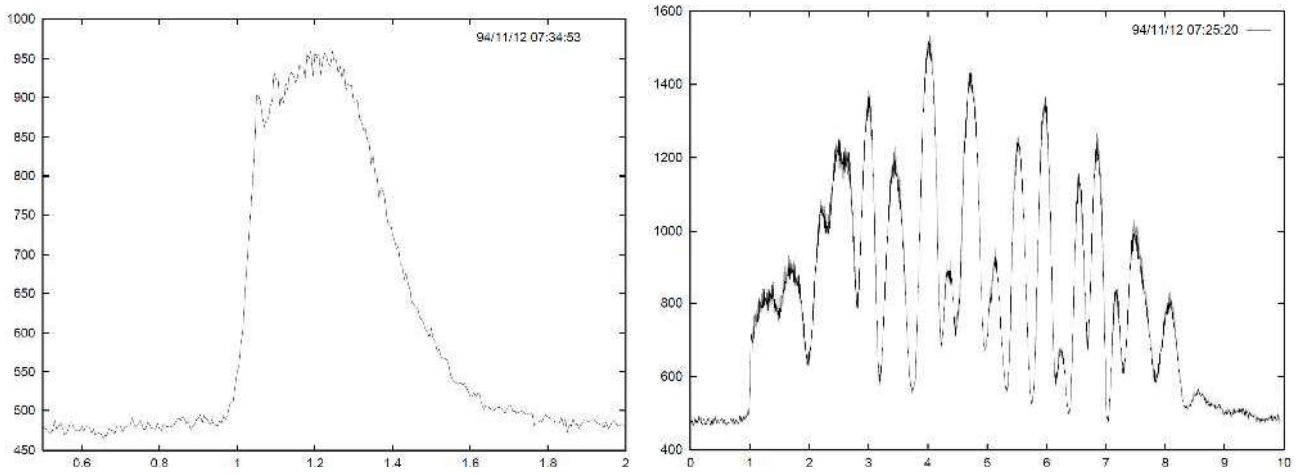


Figure 6.16: *Left:* Power profile of a typical overdense meteor. The time interval on the x-axis is 1.5 seconds. *Right:* Power profile of a long duration overdense meteor, showing interference patterns due to the appearance of secondary reflection points when the meteor trail is distorted by wind shear. The time interval on the x-axis is 10 seconds.

Table 6.1: Used symbols and their meaning.

c	Velocity of light ($2.997\,924 \times 10^8$ m/s in vacuum)
h	Height of the reflection point
k	Boltzmann constant ($1.380\,662 \times 10^{-23}$ J/K)
α	Line density of a section of the trail (cf. section 6.5)
r	Radius of a meteor trail (cf. section 6.5.1)
r_0	Initial radius of a meteor trail (cf. section 6.5.5.1)
r_c	Critical radius of an overdense meteor trail (cf. section 6.5.2)
r_e	Classical radius of the electron ($2.817\,938 \times 10^{-15}$ m)
$s(n)$	Position of the border of the n-th Fresnel zone (cf. section 6.5.4)
t	Time
D_a	Ambipolar diffusion coefficient (Schottky diffusion coefficient in neutral plasmas) (cf. section 6.5.5.3)
G_R, G_T	Gain of the receiver/transmitter antenna in the direction of the reflection point
N	Volume density of free electrons
N_c	Critical electron volume density (cf. section 6.5.2)
$P_\mathrm{o}(r)$, $P_\mathrm{u}(r)$	Received power from an overdense/underdense trail with radius r
P_T	Total emitted power of the transmitter
R_R	Distance between the receiver $\mathbf{R}$ and the reflection point $\mathbf{p}$ (cf. Figure 6.7)
R_T	Distance between the transmitter $\mathbf{T}$ and the reflection point $\mathbf{p}$ (cf. Figure 6.7)
T	Temperature
T_o	Duration of an overdense reflection
v	Velocity of the meteoroid
$\mathbf{C}(t)$, $\mathbf{S}(t)$	Cosine/Sine Fresnel-integral (cf. section 6.5.4)
β	Angle between the meteor path and the propagation plane (plane defined by $\mathbf{R}$, $\mathbf{T}$ and $\mathbf{p}$)
γ	Angle between the electric vector of the incoming wave and the direction of the receiver in $\mathbf{p}$
λ	Wavelength of the radio waves (relation to frequency ν: $\lambda\,\nu = c$)
λ_eff	Effective wavelength (cf. section 6.5.5.2)
μ_a, μ_m	Mean mass of atmospheric/meteoric atoms
ρ_a	Atmospheric density
σ	Collision cross section of meteoric atoms with atmospheric atoms ($\approx 7 \times 10^{-19}\mathrm{m}^2$)
τ_A	Decay time of the signal amplitude received from an underdense meteor
τ_P	Decay time of the power received from an underdense meteor
ϕ	Half forward scatter angle, i.e., the half of the angle $\widehat{\mathbf{RpT}}$ (cf. Figure 6.7)
Δt_{mn}	Time difference between the passage of the meteoroid in points $s(m)$ and $s(n)$ (cf. section 6.5.4)

6.6 Which information can we deduce from forward scatter observations?

In this section, a number of forward scatter setups for meteor astronomy are presented. The descriptions are inspired by existing systems. For each receiver setup described, it is explained which physical parameters can be determined, and how they can be obtained from the observations. The exact reduction techniques are however not addressed, only the concept is explained.

While the described systems are mostly derived from professional backscatter systems, there are some fundamental differences between backscatter and forward scatter systems that force a specific approach for forward scatter setups. Probably the most far-reaching difference is that in forward scatter setups the distance to the meteor trail cannot be measured. Another important difference is that the spherical symmetry that is present in backscatter setups, is broken with forward scatter geometries.

The reason why different setups are described below is that most amateur radio meteor observers will have serious restrictions on the budget available, so simple setups will be the most popular ones. Therefore it is important to discuss these systems' abilities too, and not only those of the ideal, full-featured system.

6.6.1 Which meteor parameters do we want to know?

The *flux density* and *mass index* of a meteoroid stream (or of the sporadic background) corresponding to the time of observation are important inputs for the study of meteoroid streams and their evolution, as well as for the estimation of the risk posed by meteoroids with respect to spaceflight. These parameters can be calculated from the statistics of the observed meteors, without requiring detailed information on individual meteors.

The meteoroid flux density $Q(m_0)$ of a given meteoroid stream is defined as the number of stream meteoroids with masses of at least m_0 that intersect the unit area, perpendicular to the meteoroid velocity vector, during one unit of time. Typically, a mass of 10^{-3} g is used for m_0. Typical values for $Q(m_0 = 10^{-3}\ \mathrm{g})$ are 10^{-12} to 10^{-11} m^{-2} s^{-1}.

The mass index s describes the meteoroid mass distribution within a meteoroid stream, which is governed by a power law (for a certain mass range). This means that the relation between the logarithm of the flux density $Q(m)$ and the logarithm of the mass m is a straight line with slope $1 - s$ (see Figure 6.17).

In order to model meteor streams and link them to parent bodies, the following details on individual meteoroids are of great value: radiant position, trajectory, orbit, velocity and deceleration in the atmosphere, and mass.

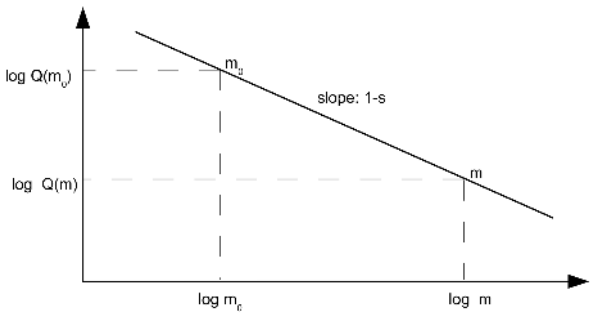


Figure 6.17: Linear relation between $\log Q(m)$ and $\log m$.

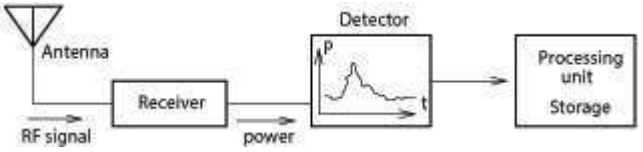


Figure 6.18: Scheme of a "basic system": an antenna, a receiver, and a detector that analyzes the evolution of the received power with time.

6.6.2 Meteor observations by a basic system

What we call a "basic system" here, is a single antenna system, a single receiver, and a detection system that simply plots or registers the evolution in time of the radio power received. The power profile may be translated into a spectrogram. A scheme is shown in Figure 6.18. In order to be able to fully analyse the power profiles, sample rates—or equivalent time resolutions—of 50 to 1000 samples per second are necessary.

Basic systems were used in the earlier days of meteor forward scatter experiments, and are currently very wide-spread in the amateur radio meteor world (see, e.g., Roelandts & Depoorter (1994) for the description of an amateur basic setup).

As will be discussed below, the parameters to be determined with such setups are the number of overdense and underdense meteors per time unit, the decay time of underdense meteors, and the duration and amplitude distribution of all meteors.

In order to obtain usable meteor reflection counts, a reliable detection algorithm is essential. Detection of meteor reflections in power profiles is typically performed by setting a detection threshold level. A detailed account on properly selecting the threshold level is given in (Belkovich et al. 2006). An overview of automatic detection algorithms of meteor reflections in spectrograms is presented in (Calders & Lamy 2014) and (Roelandts 2014).

Detection by the human eye – either in power profiles or in spectrograms – remains the most accurate way to detect meteor reflections, especially during major shower maxima, when a lot of complex-shaped overdense meteor reflections are present. However, this can be very labour-intensive. In order to obtain reliable detection of meteor reflections during major shower max-

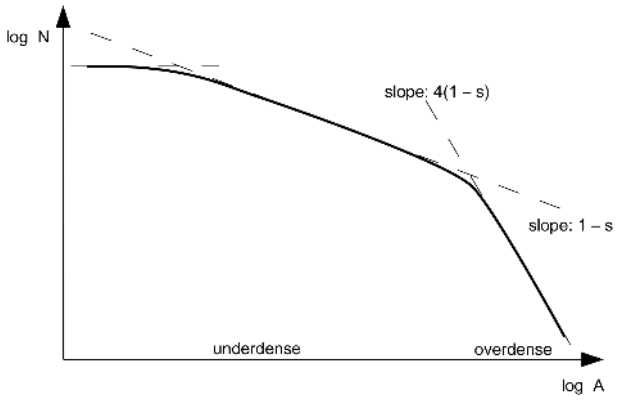


Figure 6.19: The structure of a logarithmic cumulative amplitude distribution graph ($\log A_0, \log N(A > A_0)$). It shows two quasi linear parts, whose slopes are related to the mass index of the observed meteors.

ima, the BRAMS meteor group has involved citizen scientists in the Radio Meteor Zoo project [4] (Calders et al. 2016, Calders et al. 2017), where manual detections by contributors are carefully translated into consolidated meteor reflection counts.

6.6.2.1 Meteor shower observations

The *number of overdense and underdense meteors* can be transformed into measures for the meteoroid flux density, which is itself connected to the meteoric particle density in space. For the determination of the flux density, a series of parameters should be known, like the observed radiant, the position of transmitter and receiver, the transmitter and receiver antenna gain pattern, etc. In most cases, the exact antenna gains are not known; in that case they can be approximated by using antenna simulation software such as EZNEC (Lowiessen, 2006) or 4NEC2.[5] Whereas EZNEC is free with some limitations, 4NEC2 is freeware.

Since calculation of the flux density is complicated (see Section 6.7.3.1), observers are encouraged to first calculate the Observability Function (see Section 6.7.3.2), which describes the sensitivity of the system for the meteors from a given radiant direction and provides a way to obtain a relative measure of the meteor activity, corrected for system sensitivity.

As stream membership of individual meteors cannot be determined with basic systems, sporadic meteors and meteors from other streams contaminate the flux densities derived for the analysed stream.

The *amplitude and duration distributions* of the meteors depend on the mass distribution of the observed meteors (note that the amplitude of the signal is proportional to the square root of its power). In logarithmic cumulative amplitude and logarithmic cumulative duration distribution graphs (see Figure 6.19), the direction coefficients (slopes) of the two linear parts in the graph are directly related to the mass index s. Here also, as stream membership determination is not possible with a basic setup, the mass index of streams is contaminated by meteors from other streams and sporadics. More details on how to compute the mass index of a stream can be found in Verbeeck & Wislez (2006).

[4] `https://www.zooniverse.org/projects/zooniverse/radio-meteor-zoo`

[5] `www.qsl.net/4nec2/`

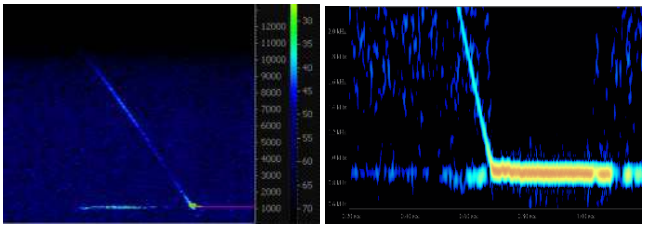


Figure 6.20: Two examples of a spectrogram featuring a meteor head echo. The head echo shows as an inclined line because of the Doppler shift corresponding to the meteoroid's speed with respect to the receiver. Right afterwards, the reflection on the trail shows as a horizontal line (since it does not move significantly with respect to the receiver). The horizontal line under the head echo is due to the turbulent plasma existing during the trail apparition.

6.6.2.2 Observations of individual meteors

The *decay time* of an underdense meteor yields a measure for the height of the reflection point, which, as we shall see in the next subsection, can be a useful parameter in the reduction of the data. Here also, the result is approximative, as the ambipolar diffusion coefficient – a quantity which rules the trail diffusion, and thus the decay time – does not depend directly on the height in the atmosphere, but rather on the atmospheric parameters: density, composition, and temperature. Equation (6.13) provides an empirical relationship between ambipolar diffusion coefficient and height. A good atmospheric model can increase the accuracy of the results somewhat.

Head echoes are not very frequently observed by forward scatter systems in the decametric or 50 MHz bands since they typically involve low radiated power and long wavelengths. In case a head echo is observed (see Figure 6.20), its speed with respect to the receiver can be calculated from the spectrogram. For optimal measurements of Doppler speeds, large bandwidths are preferred. Combined spectrogram observations from the same head echo meteor observed by many forward scatter setups may enable calculation of the meteoroid orbit (Steyaert, 2010).

6.6.3 Meteor observations by an interferometric station

In a basic station, most meteor parameters are unknown, mainly because the reflection geometry (position of the reflection point and orientation of the meteor) is unknown.

The setup considered in this subsection is a "basic setup" (see section 6.6.2), completed by a system that yields the azimuth and elevation (hereafter called the

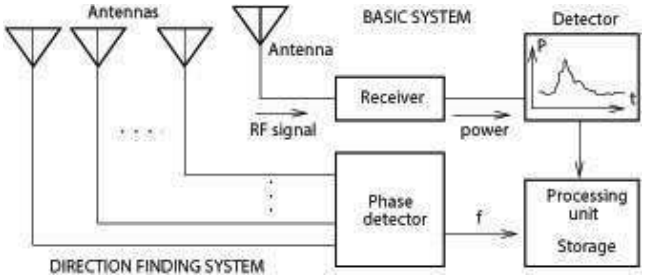


Figure 6.21: Scheme of a "direction finding system": next to the basic system, an interferometer is set up to determine the position of the reflection points in the sky.

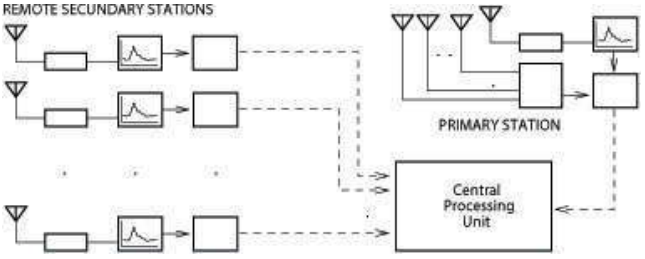


Figure 6.22: Scheme of a system with multiple receive stations: at sites located at a distance of several kilometers from a primary station, secondary stations are set up.

direction, while another term found in the literature is "angles of arrival") of the origin of each observed signal, i.e., the direction of the reflection point as seen from the receiver site. A scheme is given in Figure 6.21.

Many professional radar (backscatter) systems do have such a direction-finding or interferometric system. These professional systems have resolutions up to 1°. They are based on the comparison of the phase of the received signal at several antennas separated by distances up to a few wavelengths. The antenna configuration of the CMOR radar in Figure 6.9 will also be employed by the interferometric forward scatter system that is currently being built in the BRAMS network (Lamy, 2012).

6.6.3.1 Spatial position of the reflection point

Professional radars also measure the distance to the meteor by measuring the travelling time of a radar pulse. The spatial position of the reflection point can thus be derived, since the direction and distance are known. In forward scatter, distance determinations by radio wave travelling time measurements are not possible, since transmitter and receiver, which are separated by hundreds of kilometres, would have to be synchronised with microseconds precision. However, the direction, together with the estimated height of the reflection point (from the decay time of underdense reflections), can yield an approximate spatial position too. At the zenith, the accuracy of the range determined this way should be about 3 kilometres, while at the horizon it would reach 15 km.

6.6.3.2 Stream parameters

All meteors from a given stream have parallel paths. Due to the specularity of the reflection, all these meteors will have their reflection points located in one curved surface, that can be calculated (see section 6.2.2).

Now it can be checked whether a particular meteor reflection appears in the reflection surface associated with the stream of interest, and so stream membership can be determined. The parameters measured in the basic system (the flux and mass index) can now be calculated separately for each active stream, without contamination from other streams. To eliminate "false shower meteors," i.e., meteors that accidentally appear in the reflection surface of a stream but do not belong to the stream, the Fresnel oscillations of each meteor can be measured, to see if they are consistent with the velocity of the stream meteors (of which the directions are known).

The size of the Fresnel zones, as introduced in subsection 6.5.4 is highly dependent on the position of the reflection point (Verbeeck, 1996). It is thus only when both parameters are known that velocity measurements can be made. With a basic system, both are unknown, so velocity measurements are impossible. With a direction finding system, only the position is known. However, the direction of shower meteors is known, as they are known to originate from a given radiant. We can conclude that with a direction finding system, the velocity of identified shower meteors can be determined, but not that of sporadic meteors.

6.6.3.3 Ionisation in the reflection point

If the gain of the transmitter and receiver antennas are known and vary only slowly with direction in the direction of the reflection point, the received power can be derived fairly accurately, enabling an estimate of the electron line density at the reflection point through expressions like equations (6.2) and (6.5). This is a first indication of the minimal mass of the observed meteoroid.

6.6.4 Meteor observations by a network of observing stations

The real *direction of meteoroid flight* is unknown with a direction finding setup. Only the direction of the reflection point is measured there.

We now consider a "basic system," or a "direction finding system," with, at distances of a few kilometres, several similar "basic systems." These will be called "secondary stations," and their observations will be combined with those of the primary station. A scheme is shown in Figure 6.22.

As for each station the reflection geometry on a given meteor trail is slightly different, the different stations will receive signals from slightly different parts of the trail. Consequently, the moment of maximal signal rise (this is the moment at which the meteoroid passes through the reflection point) will be slightly different

for the different sites. When the recorders of the different receivers are synchronised, these time differences can be measured. Time differences go up to a few tenths of a second, for station separation distances of typically 5–10 kilometres. Larger distances reduce the chance for a meteor to be observable at all sites, while smaller distances reduce the accuracy of the observations.

Several professional backscatter meteor orbit systems are based on this principle.

6.6.4.1 Meteor path determination with a series of basic stations

Consider a setup with only "basic stations." In this case, only the time of appearance of the meteor signal and its power profile are measured at the different sites. For the path of the meteor to be determinable from these observations, at least six stations have to observe the meteor, since the position (three degrees of freedom) and the velocity vector (another three degrees of freedom) have to be found, and only the time of appearance is an accurate measurement.

The time observations of six stations result in a set of six non-linear equations with six variables. This set is very hard to solve analytically. Furthermore, this method does not take into account the deceleration of the meteoroid body, which can be significant. Though theoretically the deceleration can be introduced by using the velocity information in the Fresnel oscillations, a setup with only time-determining stations is probably not very feasible, and more than six stations per setup would be needed in practice, as it is possible that a given meteor is not observable at all station sites.

6.6.4.2 Meteor path determination when one of the stations is direction finding

If one of the stations is direction-finding, the problem gets much easier, since such a station can determine the direction of the reflection point, and a direction perpendicular to the meteor trail. Now three secondary stations are sufficient to complete the observations, since only the distance, path orientation, and velocity are still undetermined. The equation set also gets much easier to solve, especially when fitting methods are used.

Not all three secondary stations are mandatory, however. If one uses the information from the Fresnel oscillations in one station, one secondary station can be left out. By relying on the decay time of the underdense meteors for the determination of the range to the reflection point, a secondary station can be dropped too. Relying on those extra parameters however results in a loss of accuracy of the path determination.

One primary and one secondary station can thus in theory yield an approximate meteor path, and every extra station enhances the accuracy and the chance for the complete observation of individual meteors.

As individual meteoroid trajectories are now measured, unambiguous radiant determination is possible, even with very low meteor rates.

If the Fresnel oscillations from each station are examined, the velocity in the different reflection points can be measured, and thus also the deceleration of the meteoroid.

6.6.4.3 Meteoroid mass

As already stated, setups with secondary stations receive signals from different parts of the meteor trail. If the setups are power-calibrated, it is possible to deduce a value for the ionisation in the trail for each of the stations. This way, several points of the ionisation profile of the meteor trail can be found. By comparing with ablation models, this ionisation profile can yield the mass of the observed meteoroid. With the previously described techniques, only the mass *distribution* of a group of meteors could be estimated.

6.6.4.4 Conclusions on the capabilities of multiple receive stations

Combining a primary station with a series of secondary stations thus permits the collection of more detailed information on *individual* meteors. The trajectory, orbit, radiant, velocity, deceleration, and mass of individual meteoroids can now be determined. Information that was previously obtained statistically (like the mass index or radiant) can now be compared with the statistics on individually obtained data.

6.7 Sporadic and shower activity from forward scatter observations

Radio observations are a much less direct way of observing meteors than for instance visual or video observations, which makes it quite difficult to interpret raw meteor rates. In this section, various methods are presented to estimate sporadic and shower activity from forward scatter observations.

6.7.1 Estimating raw sporadic meteor rates

For observations performed by basic forward scatter stations, it is not possible to tell which individual meteor reflections are shower meteors. Hence, the only way to estimate shower activity is to estimate the sporadic background and subtract it from the total activity. We illustrate this process here in detail with the BRAMS observations of the Perseids 2016 (Verbeeck et al., 2018). The same method can be applied to estimate the sporadic background in any forward scatter observations.

Figure 6.23 shows an estimation of the sporadic background during the Perseids 2016 observations by BRAMS receiving station Humain. The top left plot shows the hourly number of meteor reflections observed for every UT hour of the day, on individual days some time away from the Perseid maximum (August 17 in blue; August 19 in green; their average with standard deviations as error bars in black). It is assumed that

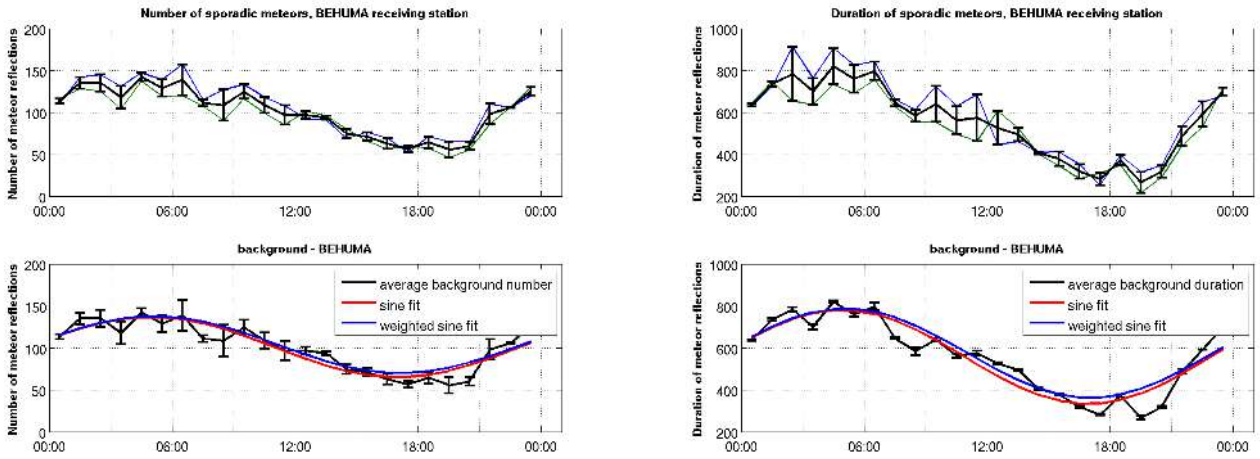


Figure 6.23: Estimation of the diurnal variation of the sporadic background during the BRAMS Perseids 2016 campaign (receiving station: Humain). *Top left:* Hourly number of meteor reflections observed on individual days, some time away from the Perseid maximum (August 17 in blue; August 19 in green; average in black). *Bottom left:* Average and sine fits of the hourly number of meteor reflections. *Top right:* Hourly total duration (s) of meteor reflections observed on August 17 and 19, and their average. *Bottom right:* Average and sine fits of the hourly total duration of meteor reflections. Times are in UT.

there is no significant shower activity on those days, so the observations represent the sporadic background at that time. The sporadic background during the Perseid maximum is assumed to be the same.

The bottom left plot shows the average hourly number of meteor reflections for every UT hour of the day (average over August 17 and 19), with the standard deviations as error bars (in black). Since a sinusoidal diurnal variation of the sporadic background is expected (Powell, 2017), a sine curve was fitted to these averages (both a weighted and unweighted fit). It is clear from Figure 6.23 that both fits are a good approximation of the average hourly number of meteor reflections. The sporadic background during the observations can be modelled as the weighted sine fit.

The plots on the right in Figure 6.23 apply the same ideas, but on the hourly total duration (in seconds) of meteor reflections. Meteor shower maxima typically feature a lot of long-duration (overdense) reflections, which often overlap with shorter (underdense) reflections. As a result, counting the number of reflections can be a rather inaccurate measure of meteor activity. The hourly total duration of meteor reflections provides a more robust measure of meteor activity. It is observed that the fitted sine curves shown in the bottom right plot of Figure 6.23 are a good representation of the average hourly total duration of meteor reflections. Hence, the hourly total duration of sporadic meteor reflections during the observations can be modelled as the weighted sine fit.

6.7.2 Estimating raw shower meteor rates

Once we have estimated the sporadic background, we can determine the estimated raw shower meteor activity by subtracting the sporadic background from the total observed activity. We illustrate this process here in detail with the BRAMS observations of the Perseids 2016 (Verbeeck et al., 2018). The same method can be applied to estimate the raw shower activity in any forward scatter observations.

Figure 6.24 shows an estimation of the Perseids 2016 activity as observed from the BRAMS station at Humain. The hourly total number of meteor reflections is shown in the top left plot (red curve). As a proxy for the diurnal variation of the sporadic background, the average hourly number of meteors observed away from the shower maximum is plotted (black circles for the average and black sine curve for is weighted sine fit), as explained in Section 6.7.1. An estimate of the number of Perseid reflections per hour (blue curve) is obtained by subtracting the modelled sporadic background (the black weighted sine fit) from the hourly total number of reflections. The Perseid radiant elevation is featured in the bottom left plot. The plots on the right in Figure 6.24 show the same curves, but for the hourly total duration of meteor reflections rather than the number of meteor reflections.

It is clear that the number of Perseid reflections is much smaller than the large number of underdense sporadic reflections (faint sporadic meteors) observed by Humain (top left plot in Figure 6.24). Hence, the scatter in the true sporadic rates (the difference between the real and modelled sporadic rates) hides the salient features in the Perseid rates. Since the proportion of Perseids to sporadics is a lot higher in the top right plot in Figure 6.24 (hourly total duration of meteor reflections), the Perseid maximum on August 12 stands out better in that plot.

This is even more the case in Figure 6.25, which shows the same plots as Figure 6.24, but only taking into account the larger particles (meteor reflections lasting at least 10 seconds). Both in the number of reflections

and the total duration of reflections, the Perseids clearly dominate the reflections lasting at least 10 seconds, and the Perseid maximum on August 12 stands out clearly.

A word of caution is in order. The shower meteor numbers shown above have not yet been corrected for the relative sensitivity of the forward scatter setup, which shows a large daily variation as the radiant crosses the sky. This daily variation is clearly seen in the plots (with a minimum near 18^{h} UT for the Perseids), meaning it is pointless at this stage to determine at which exact time the shower maximum occurred. Using an analogy with visual data, the raw forward scatter data presented here are similar to raw visual rates rather than ZHRs.

6.7.3 Correcting raw shower meteor rates for the sensitivity of the setup

So how important is it to correct the raw data for the sensitivity of the setup?

Figure 6.26 shows the estimated raw hourly number of Geminid reflections lasting at least 10 seconds in 2016–2019 from forward scatter observations at the BRAMS station of Humain, obtained by subtracting the estimated diurnal sporadic activity from the hourly total number of observed meteor reflections.

We would expect that large physical structures in the meteor stream would line up in the solar longitude plots of shower returns in different years. The peaks in estimated raw shower activity in different years do not correspond at all to the same interval in solar longitude, however (see the left panel in Figure 6.26). The right panel in Figure 6.26 clearly shows that the peaks in estimated shower activity do nicely align as diurnal patterns. Since the number of observed shower meteors is the product of the real number of shower meteors and the sensitivity of the system, these results strongly suggest that the sensitivity of the system is the dominant factor. Due to its dependence on the radiant position in the sky, the system sensitivity has a diurnal pattern, called the Observability Function (OF) (Verbeeck, 1997).

Different avenues to correct the raw shower meteor rates for the sensitivity of the setup are discussed in the next sections.

6.7.3.1 Estimating the flux density of a meteor shower

The flux density is the most useful measure of meteor activity and provides the number of meteoroids intersecting 1000 km^2 during one hour. However, calculation of the flux density is complicated and only possible when a lot of details about the forward scatter setup are well-known. Observers are encouraged to first calculate the Observability Function (Verbeeck, 1997), which describes the sensitivity of the system for the meteors from a given radiant direction (see Section 6.7.3.2).

For the calculation of flux densities, we refer to Verbeeck (2011), Ryabova (2008, 2009) and Verbeeck & Wislez (2006), and Suleymanova et al. (2007).

6.7.3.2 Correcting raw shower meteor rates by the Observability Function

Since calculation of the flux density is complicated, observers are encouraged to first calculate the Observability Function (OF) (Verbeeck, 1997), which describes the sensitivity of a forward scatter setup for the meteors from a given radiant direction. A relative measure of the shower meteor activity can be obtained by dividing the estimated raw number of shower meteors by the OF. However, only real flux densities provide absolute numbers.

6.7.3.3 Correcting raw shower meteor rates: inverse method

Steyaert et al. (2006) introduced an empirical way to estimate the Observability Function, the sporadic background, and a relative measure of meteor shower activity, provided only one meteor shower is active.

The method starts from the equation

$$O(t) = S(T) + Z(t) \cdot \mathrm{OF}(T), \tag{6.19}$$

where

$$T = \frac{t - t_0}{D}, \tag{6.20}$$

t is the time of observation, t_0 is the start time of the observation, D is the length of the day (so basically, T is a diurnal time variable between 0^{h} and 24^{h} UT), $O(t)$ is the observed number of meteor reflections at time t, $S(T)$ is the modelled diurnal variation of the number of sporadic reflections, $\mathrm{OF}(T)$ is the modelled diurnal variation of the Observability Function, and $Z(t)$ is the modelled level of shower activity.

$O(t)$ is known for every hour t in the observation period, and a double exponential model

$$Z(t) = \begin{cases} e^{-(t-t_{\mathrm{M}})/a} & t < t_{\mathrm{M}} \\ e^{-(t-t_{\mathrm{M}})/b} & t > t_{\mathrm{M}} \end{cases} \tag{6.21}$$

is assumed for $Z(t)$, where t_{M}, a, and b are formal parameters which have to be determined.

The continuous model of equation (6.19) is then replaced by its discrete counterpart

$$O_m = S_j + Z_m \mathrm{OF}_j, \tag{6.22}$$

where j takes values between 1 and 24 and m takes values between 1 and the number of hourly observation intervals n.

A least squares approach is employed to minimise

$$J = \frac{1}{2} \sum_m \sum_j (O_m - S_j - Z_m \mathrm{OF}_j)^2, \tag{6.23}$$

which allows the authors to express S_j and OF_j as a function of O_m and Z_m. Using equation (6.21), we can express J as a function of O_m, t_{M}, a, and b. A downhill

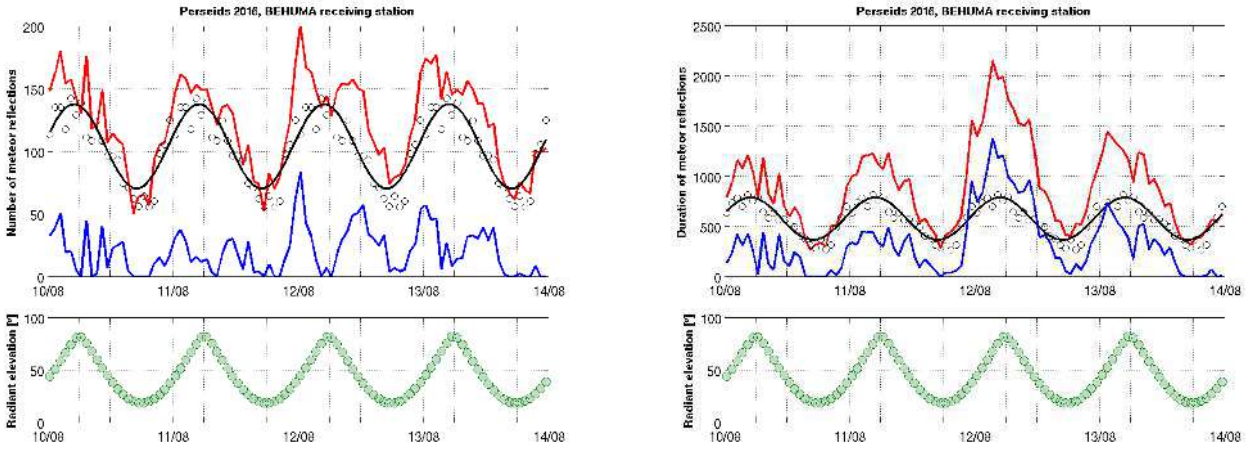


Figure 6.24: Estimation of Perseids 2016 activity (BRAMS receiving station: Humain). *Top left:* Hourly number of meteor reflections (upper red curve: total observed; black circles and curve: estimation of diurnal variation of sporadic background and its weighted sine fit; lower blue curve: estimated hourly number of Perseid reflections). *Bottom left:* Radiant elevation. *Top right:* Hourly total duration (s) of meteor reflections (upper red curve: total observed; black circles and curve: estimation of diurnal variation of sporadic background and its weighted sine fit; lower blue curve: estimated hourly total duration of Perseid reflections). *Bottom right:* Radiant elevation. Times are in UT.

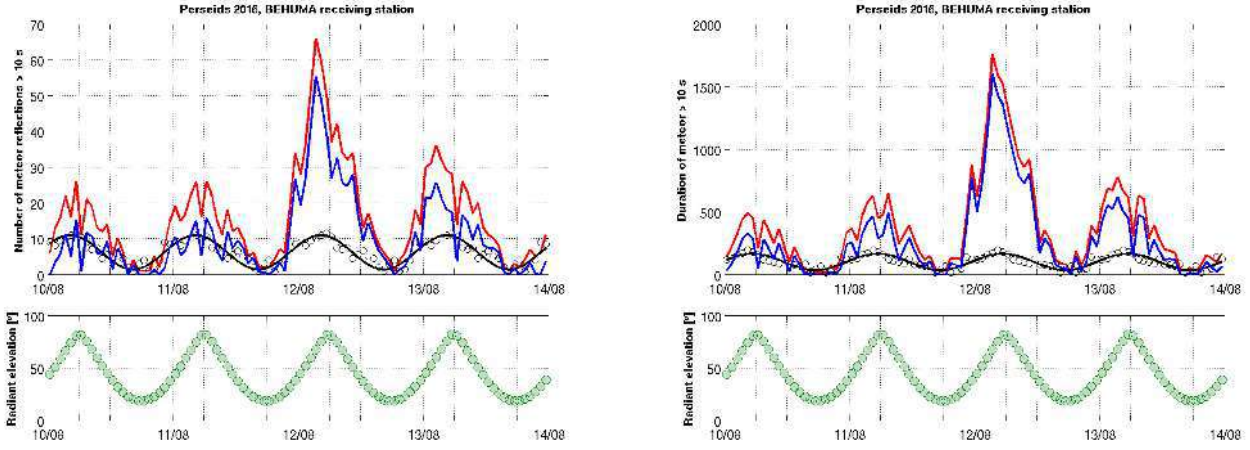


Figure 6.25: Estimation of Perseids 2016 activity (BRAMS receiving station: Humain). *Top left:* Hourly number of meteor reflections lasting at least 10 seconds (upper red curve: total observed; black circles and curve: estimation of diurnal variation of sporadic background and its weighted sine fit; lower blue curve: estimated hourly number of Perseid reflections). *Bottom left:* Radiant elevation. *Top right:* Hourly total duration (s) of meteor reflections lasting at least 10 seconds (upper red curve: total observed; black circles and curve: estimation of diurnal variation of sporadic background and its weighted sine fit; lower blue curve: estimated hourly total duration of Perseid reflections). *Bottom right:* Radiant elevation. Times are in UT.

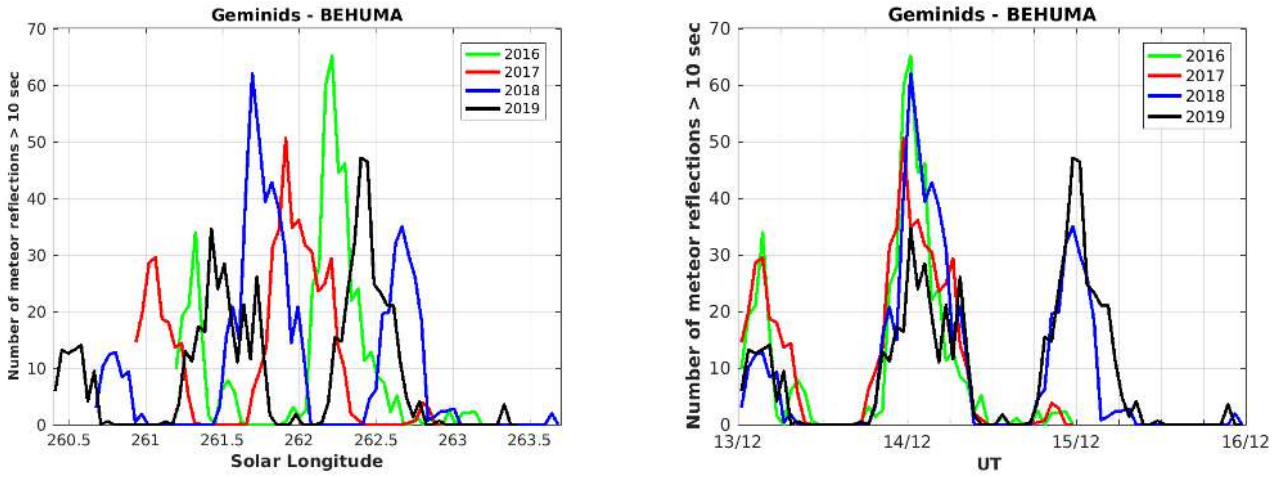


Figure 6.26: *Left:* the estimated hourly number of Geminid reflections observed by the BRAMS station at Humain, lasting at least 10 seconds in 2016–2019, expressed as a function of solar longitude (J2000). *Right:* the estimated hourly number of Geminid reflections observed by the BRAMS station at Humain, lasting at least 10 seconds in 2016–2019, expressed as a function of day and time (UT).

simplex numerical method (Vetterling et al., 1992) is then employed to find the parameters t_{M}, a and b that minimise J.

Filling in these values in (6.21), we obtain the (normalised) corrected shower activity Z_m, with the Observability Function OF_j and the sporadic activity S_j as a bonus.

Judging from the examples in (Steyaert et al., 2006) and (Steyaert, 2014), this method provides a good fit to the original data O_m. One limitation of the method is that an assumption is made on the shape of the shower activity profile $Z(t)$.

6.7.3.4 Correcting raw shower meteor rates: Activity Level and $\mathrm{ZHR_r}$

Another approach for correcting raw shower meteor rates is presented by Ogawa et al. (2002). Instead of trying to calculate or estimate the diurnal variation of the Observability Function as the radiant crosses the sky, the observations by a lot of different stations are corrected for other factors and then averaged. The "Activity Level" $A(t)$ at time t is defined as the difference of the observed hourly number of meteor reflections and the estimated hourly sporadic background, corrected for the average sensitivity of the setup and for the height of the radiant, and averaged over all forward scatter stations i, according to the formula

$$A(t) = \frac{1}{N} \cdot \sum_{i=1}^{N} A_i(t), \tag{6.24}$$

where N is the number of observing stations,

$$A_i(t) = \frac{H_{\mathrm{obs},i}(t) - H_{\mathrm{spo},i}(T)}{D_i \sin h_i(t)}, \tag{6.25}$$

and

$$T = \frac{t - t_0}{D}. \tag{6.26}$$

t is the time of observation, t_0 is the start time of the observation, and D is the length of the day (so basically, T is a diurnal time variable between 0^{h} and 24^{h} UT). Further, $H_{\mathrm{obs},i}(t)$ is the observed hourly number of meteor reflections at time t in station i, $H_{\mathrm{spo},i}(T)$ is the estimated hourly number of sporadic reflections at time of the day T in station i (this is a diurnal curve, defined for every UT hour of the day), D_i is the hourly average of this diurnal curve (i.e., $D_i = \frac{1}{24} \cdot \sum_{T=0}^{23} H_{\mathrm{spo},i}(T)$), and $h_i(t)$ is the altitude of the shower radiant at time t in station i.

The estimated hourly number of sporadic reflections $H_{\mathrm{spo},i}(T)$ is defined here as the hourly number of meteor reflections observed in station i at time of the day T, averaged over the last 10 days before start of the shower observations.

Though the Activity Level (AL) does not incorporate the (strong) diurnal changes in the Observability Function, it does take into account the average sensitivity of the setup through the parameter D_i, which allows to consistently average results of different stations. It seems that the diurnal variations in the Observability Functions of a lot of different stations cancel out to some extent when averaging $A_i(t)$ over many stations i.

For published shower results using the AL, see (Ogawa et al., 2002), (Rendtel et al., 2017), and (Ogawa and Steyaert, 2017). More information and results can be found at `https://www.iprmo.org/`.

Sugimoto[6] defines the "radio ZHR" $\mathrm{ZHR_r}$, which intends to compare shower meteor activity observed by forward scatter to visual ZHRs, and which is very similar to the AL.

To rescale the radio data to numbers comparable with visual observations, he defines the "Corrected Hourly Rate" at time t in forward scatter station i as

$$\mathrm{CHR}_i(t) = \frac{H_{\mathrm{obs},i}(t) - H_{\mathrm{spo},i}(T)}{D_i} \cdot S_{\mathrm{bas}}, \tag{6.27}$$

[6] `http://www5f.biglobe.ne.jp/~hro/ZHR/index.htm`

where $S_{\rm bas}$ is the average visual sporadic hourly rate corresponding to limiting magnitude +6.5 during the time of year covered by the sporadic background observations (i.e., during the 10 days prior to the start of the meteor shower observations). $S_{\rm bas}$ is a fixed function of the day of the year, and was derived empirically based on radio and visual data from several years.

The radio ZHR at time t in station i is then defined as

$$\mathrm{ZHR}_{\mathrm{r},i}(t) = \frac{\mathrm{CHR}_i(t)}{\sin h_i(t)}. \tag{6.28}$$

As in visual observations, the ZHR values of the individual stations are averaged to obtain the average radio ZHR at time t:

$$\mathrm{ZHR}_r(t) = \frac{1}{N} \cdot \sum_{i=1}^{N} \mathrm{ZHR}_{\mathrm{r},i}(t). \tag{6.29}$$

Similar to the AL, the radio ZHR does not take into account the diurnal variations in the Observability Function, but it seems these variations cancel out to some extent when averaging the radio ZHR over a lot of stations.

The radio ZHR rescales the sporadic radio counts to the sporadic visual counts, and applies the same rescaling to the shower radio counts. Because meteor showers and the sporadic background have different mass index, this rescaling will be less accurate for sensitive radio stations which can observe a significant amount of fainter meteors than those corresponding to visual magnitude +6.5.

ZHR_r results of major showers are regularly posted on Sugimoto's website[7].

6.8 Further reading

A comprehensive introduction to radio meteor astronomy plus in-depth theory about calculating meteor flux density and many other topics is provided in the *Proceedings of the Radio Meteor School 2005* (Verbeeck & Wislez, 2006), which is highly recommended to those who want to embark seriously on radio meteor science. Many further references are provided there as well.

Some information on radio meteor observations can be found on the radio pages of the IMO website[8], and questions to experts can be asked via e-mail to `radio@imo.net`. The CMOR website[9] provides a good introduction to radar observations. The RMOB website[10] collects radio meteor observations (without further data analysis) and provides several useful tools for radio meteor observers.

[7] `http://www5f.biglobe.ne.jp/~hro/Flash/index-e.htm`
[8] `www.imo.net/radio`
[9] `http://meteor.uwo.ca/research/radar/radarobserv.html`
[10] `http://www.rmob.org/livedata/main.php`

Acknowledgements

We are much indebted to Jean-Marc Wislez, who wrote the first version of the text and figures about the principle of specular reflection, the nature of underdense and overdense reflections, and the information we can deduce from forward scatter observations. This chapter has benefited from input by Hervé Lamy, Antonio Martínez Picar, Hiroshi Ogawa, and Chris Steyaert.

References

Belkovich O.I., Semegone J.M., Zigo P., Verbeeck C., 2006: Processing of radar observations 1: Sporadic background, detection threshold, radar sensitivity, in: C. Verbeeck, J.-M. Wislez (eds), Proceedings of the Radio Meteor School, Oostmalle 2005, 34–37.

Calders S., Lamy H., 2014: Automatic detection of meteors in the BRAMS data, in: J.-L. Rault, P. Roggemans (eds.): Proceedings of the IMC Giron 2014, IMO, 194–196.

Calders S., Verbeeck C., Lamy H., Martínez Picar A., 2016: The Radio Meteor Zoo: a citizen science project, in: A. Roggemans, P. Roggemans (eds.): Proceedings of the IMC Egmond 2016, IMO, 46–49.

Calders S., Lamy H., Martínez Picar A., Tétard C., Verbeeck C., Gamby E., 2017: The Radio Meteor Zoo: involving citizen scientists in radio meteor research, in: M. Gyssens, D. Pavlović, J.-L. Rault (eds.): Proceedings of the IMC Petnica 2017, IMO, 13–15.

Dyrud L., Wilson D., Boerve S., Trulsen J., Pecseli H., Close S., Chen C., Lee Y, 2008: Plasma and electromagnetic simulations of meteor head echo radar reflections, in: J.M. Trigo-Rodriguez, F.J.M. Rietmeijer, J. Llorca, D. Janches (eds.): Advances in Meteoroid and Meteor Science, 383–394, doi: 10.1007/978-0-387-78419-9_54.

Hines C.O., Forsyth P.A., 1957: The forward-scattering of radio waves from overdense meteor trails. *Can. J. Phys.* **35,** 1033–1041.

Jones J., Brown P., Ellis K.J., Webster A.R., Campbell-Brown M.D., Krzemenski Z., Weryk R.J., 2005: he Canadian Meteor Orbit Radar (CMOR): System overview and preliminary results. *Planet. Space Sci.* **53,** 413–421.

Jones J., Collins J.G., 1974: The mass distribution of radio meteors and the full-wave scattering theory. *MNRAS* **166,** 529–542.

Lamy H., 2012: `http://brams.aeronomy.be`

Lamy H., Tétard C., Anciaux M., Ranvier S., Martínez Picar A., Calders S., Verbeeck C., 2018: First observations with the BRAMS radio interferometer, in: M. Gyssens, J.-L. Rault (eds.): Proceedings of the IMC Petnica 2017, IMO, 132–137.

Lamy H., Anciaux M., Ranvier S., Martínez Picar A., Calders S., Calegaro A., Verbeeck C., 2020: Calibration of the BRAMS interferometer, in: U. Pajer, J. Rendtel, M. Gyssens, C. Verbeeck (eds.): Proceedings of the IMC Bollmansruh 2019, IMO, 33–38.

Lowiessen F., 2006: Using EZNEC for calculating antenna characteristics, in: C. Verbeeck, J.-M. Wislez

(eds), Proceedings of the Radio Meteor School, Oostmalle 2005, 82–84.

Ogawa H., Toyomasu S., Ohnishi K., Amikura S., Maegawa K., Jenniskens P., 2002: The 2002 Leonids as monitored by the International Project for Radio Meteor Observations. *WGN* **30,** 225–231.

Ogawa H., Steyaert C., 2017: Major and daytime meteor showers using global radio meteor observations covering the period 2001–2016. *WGN* **45,** 98-106.

Pellinen-Wannberg A., 2004: The EISCAT meteor-head method – a review and recent observations. *Atmos. Chem. Phys.* **4,** 649–655.

Powell C., 2017: Modelling & analysis of diurnal variation in meteor flux. *WGN* **45,** 32–37.

Rendtel J., Ogawa H., Sugimoto H., 2017: Meteor showers 2016: review of predictions and observations. *WGN* **45,** 49–55.

Roelandts T., Depoorter W., 1994: Description of the RAMSES automated forward scatter system, in: P. Roggemans (ed.), Proceedings IMC Puimichel 1993, 44–46.

Roelandts T., 2014: Meteor detection for BRAMS using only the time signal, in: J.-L. Rault, P. Roggemans (eds.): Proceedings of the IMC Giron 2014, IMO, 197–200.

Ryabova G.O., 2008: Calculation of the incident flux density of meteors by numerical integration I. *WGN* **36,** 120–123.

Ryabova G.O., 2009: Calculation of the incident flux density of meteors by numerical integration II. *WGN* **37,** 63–67.

Schilling D., 1993: Meteor burst communications. Theory and practice, Wiley Series in Telecommunications.

Steyaert C., Brower J., Verbelen F., 2006: A numerical method to aid in the combined determination of stream activity and observability function. *WGN* **34,** 87–93.

Steyaert C., Verbelen F., VVS Beacon Observers, 2010: Meteor trajectory from multiple station head echo Doppler observations. *WGN* **38,** 123–129.

Steyaert C., 2014: The global radio η-Aquariids 2013, in: M. Gyssens, P. Roggemans, P. Zoladek (eds.), Proc. IMC Poznan 2013, IMO, 73–77.

Suleymanova S., Verbeeck C., Wislez, J.-M., 2007: Calculating the meteoroid flux density of a meteor shower from radio forward scatter observations, in: F. Bettonvil, J. Kac (eds.), Proc. IMC Roden 2006, IMO, 162–174.

Verbeeck C., 1996: The first Fresnel zone and the power profile throughout the forward scatter reflection surface, in: P. Roggemans, A. Knöfel (eds.), Proc. IMC Brandenburg 1995, IMO, 83–98.

Verbeeck C., 1997: Calculating the sensitivity of a forward scatter setup for underdense shower meteors, in: A. Knöfel, P. Roggemans (eds.), Proc. IMC Apeldoorn 1996, IMO, 122-132.

Verbeeck, C. and Wislez, J.-M. (eds.), 2006: Proceedings of the Radio Meteor School, Oostmalle, Belgium, 2005. IMO, ISBN 2-87355-017-1.

Verbeeck C., Ryabova G.O., 2011: Calculation of the incident flux density of meteors by numerical integration: Improved geometrical approach. *Journal of Atmospheric and Solar-Terrestrial Physics* **73,** doi:10.1016/j.jastp.2010.10.005, 901–903..

Verbeeck C., Lamy H., Calders S., Tétard C., Martínez Picar A., 2018: Overview of major shower observations 2016–2017 by the BRAMS network, in: *M. Gyssens, J.-L. Rault (eds.): Proceedings of the IMC Petnica 2017,* IMO, 138–144.

Vetterling W., Teukolsky S., Press W., Flannery B., 1992: Numerical Recipes in C: The Art of Scientific Computing, chapter 10.4 Downhill Simplex Method in Multidimensions. Cambridge University Press, second edition.

Wislez J.M., 2006: Meteor astronomy using a forward scatter set-up, in: Proceedings of the Radio Meteor School, Oostmalle, Belgium, 2005. IMO, 85–107.

7 | Analyses and Calculations

Ralf Koschack, Jürgen Rendtel, Janko Richter

7.1 Introduction

Any observation of meteors from the Earth's surface is the attempt to obtain information about the meteoroids released from a parent object. The "detector area" is small, compared to the dimension of the structures within a meteoroid stream. Ideally, we might "install" a defined area, count the particles and determine their masses over a given time. To some extent, this has been achieved with the Long Duration Exposure Facility (LDEF) with an exposed surface area of about $130\,\mathrm{m}^2$ which was in a low-Earth orbit between April 1984 and January 1990 (See et al., 1990; McBride et al., 1995). Observing from the ground lacks the defined collecting area. Hence our data (numbers, brightnesses) are a statistical sample from which we calculate the masses per mass (brightness) interval and the flux density (as a total number of meteoroids in a certain mass range associated with a source (stream).

7.2 ZHR and population index

The visible number of meteors does not give a representative quantity for the activity of their meteor shower. Two observers watching from two locations at the same time will see different numbers of meteors. The observer facing a radiant at a low elevation will see fewer meteors than a colleague having the radiant higher in the sky. Also, bad sky conditions may decrease the number of meteors detected. An observer with very sensitive eyes will have an advantage over the less perceptive companion at the same location.

The standard quantity measuring meteor shower activity is the Zenithal Hourly Rate (ZHR). It involves corrections for radiant altitude and stellar limiting magnitude which on its own incorporates sky quality and observer's eye sensitivity at the same time.

Another important quantity to describe the characteristics of a meteor shower is the population index r. It describes how much the true number of meteors N increases from one magnitude class m to the next fainter one $m+1$:

$$r = \frac{N(m+1)}{N(m)}. \tag{7.1}$$

Details are discussed on page 143 and 148.

Observers have the impression though, that they *see* few meteors at very faint magnitudes. This is an effect of the limited perception quality of the eye-brain system. The *true number of meteors increases towards fainter magnitudes* in nearly all cases. The perception of meteors in visual observations is described by Koschack & Rendtel (1990) and for video meteor data by Molau, Barentsen and Crivello (2015).

Strictly speaking, we have to specify the magnitude range for which the derived value of r is valid. We usually do not mention this interval as we use visual data which cover the magnitude range $[-4;+6]$ where significant variations in r are rare. This does not hold for the fireball range and there are also indications that for meteors fainter than +5 mag the numbers change, too.

Let N be the number of shower meteors observed in a time period of effective length T_{eff}, that is after subtraction of possible breaks and dead time due to all types of notes taken. Then the observed ZHR is obtained by the formula

$$\mathrm{ZHR} = \frac{N}{T_{\mathrm{eff}}} \, \frac{r^{(6.5-\mathrm{lm}+\Delta\mathrm{lm})} \, F}{\sin h_{\mathrm{R}}} \tag{7.2}$$

where lm is the stellar limiting magnitude, F is a correction for possible obstructions of the field of view (see page 49), and h_{R} is the radiant elevation. The corrections are explained later in this section. The formula can be applied for radiant elevations $h_R \geq 10°$ as shown in section 7.3.3.

One of the problems that may occur in deriving a ZHR for an observer is a difference in his limiting magnitude for stars and that for meteors. Such individual perception effects are approximately accounted for by Δlm.

Another effect has been described for moonlit skies. Observers often report that relatively faint starts can still be seen but the corresponding meteors seem to be missing. This results in ZHR values which are undercorrected and needs further investigation. Hence the general advise to watch under a dark sky.

If there are outbursts happening or a major shower peaks, the interest of obtaining data is large enough to observe also under unfavourable circumstances. This

requires careful calibration and analysis later on. The same holds for difficult cases like daytime showers which may be attempted to observe in twilight conditions.

The ZHR and the population index are observational quantities; they describe standard measures for the *appearance* of a meteor shower. In a next step we describe physical quantities of meteoroid streams in space. The population index will be related to a measure of the distribution of particle masses instead of magnitudes. This leads naturally to the mass index s. The ZHR needs a conversion to actual numbers of particles in space. We call this quantity the particle number density ND. Note that this is not the density of the material of which the particles are made, but a number of meteoroids per unit volume. This value can also be converted into an average distance between meteoroids in space, and by applying the relative velocity of the meteoroids to the Earth, also to a flux density Q.

7.3 Analysis of visual observations

7.3.1 General remarks

Although we know how the characteristics of a meteoroid stream are measured, we need to describe the mathematical procedures applied to obtain the actual values. We know that meteors do not occur at constant time steps. Especially during periods of low numbers, the observations and the analysis needs to be described in terms of stochastic methods. As soon as the number of meteors is large, the differences become small and we may apply the known formulae for analyses. Here we start with the general stochastic approach.

7.3.2 The observable count of meteors

The count of observable meteors within an observation period depends only on three different factors. The first factor is the activity A of the meteor shower (number of meteors per time). The second factor C are the conditions under which an observation takes place (all correction factors). Both, A and C correspond to the two fractions in equation 7.2. Additionally, the count of observable meteors depends on randomness. Therefore, we can express these influencing factors in the following basic equation:

$$\mathrm{E}[n] = A \cdot C \ . \tag{7.3}$$

The expression $\mathrm{E}[n]$ is the mean expected count of observable meteors expressing their randomness. The difference between A and C is that we cannot control the activity A of the meteor shower, unlike the observational conditions. Various factors influence the observation conditions. One of the most important quantities is the time period of effective length T_{eff}, that is after subtraction of possible breaks and dead time due to all types of notes taken. Obviously, the longer one waits for meteors, the greater will be the number of meteors to be observed. Bad sky conditions may decrease the number of meteors detected. Also, an observer with very sensitive eyes will have an advantage over the less perceptive companion at the same location. Simplified, these observational conditions are summarized in the limiting brightness lm and are included in the observational conditions as a function $g(\mathrm{lm})$. Also an observer facing a radiant at a low elevation will see fewer meteors than a colleague having the radiant higher in the sky. This effect on the observation conditions is expressed with a function $z(h_{\mathrm{R}})$, where h_{R} is the height of the radiant above the horizon. The value of $z(h_{\mathrm{R}})$ is 1.0 if the radiant is at the zenith, otherwise it is greater than 1.0. In summary, we can thus express the observational conditions C as follows:

$$C = T_c = \frac{T_{\mathrm{eff}}}{F} \cdot \frac{g(\mathrm{lm})}{z(h_{\mathrm{R}})} \ , \tag{7.4}$$

where F is a correction for possible obstructions of the field of view (see page 49) and is always greater than or equal to 1.0. Since all factors except T_{eff} are without unit, we can describe the observing conditions C with a virtual waiting time T_c for meteors. Because T_{eff} is measured in hours, it follows that the activity of a meteor shower is measured in terms of the total number of meteors per hour. It follows from Equation (7.3) thus:

$$a = \frac{n}{T_c} \ , \tag{7.5}$$

where a is the *measured* activity A of the meteor shower. However, the activity of the meteor shower may change within a larger observation period. The measured value a is then an average statement about the activity of the meteor shower. Due to the randomness of the appearance of meteors, this is not measurable at smaller observation periods because of the resulting smaller number of meteors. For such periods, it can be assumed that the observed activity represents the current activity of the meteor shower.

7.3.3 The zenith correction factor

An observer with a radiant in the zenith will see more meteors from the same shower than another observer with the radiant just above the horizon. Here we will investigate this phenomenon in more detail and, similarly to the previous section, answer the question: 'How many meteors of the shower, n_{90}, would I have seen if the radiant had been at my zenith instead at the elevation h?' We say: 'z times more':

$$n_{90} = n_h \times z$$

or:

$$z = \frac{n_{90}}{n_h}. \tag{7.6}$$

We can consider the Earth to be stationary while the particles of the meteoroid stream move towards the Earth on parallel paths at geocentric velocity v_g. Since *geocentric velocity* means *velocity with respect to Earth's centre*, this is quite correct. The number of particles n contained in a given volume will be constant on average, which is determined by the *spatial number density* ND.

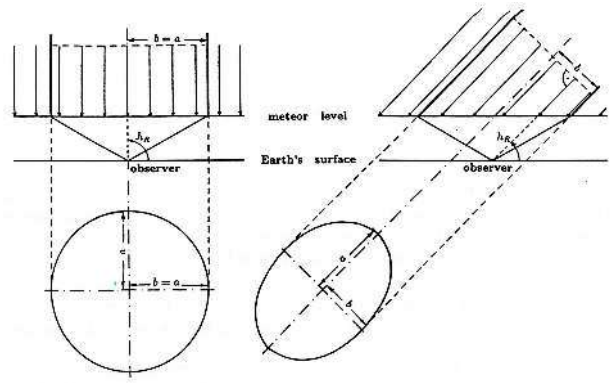


Figure 7.1: Determination of the zenith correction factor z. For detailed explanation please refer to the text.

The unit of the ND is 'particles per billion cubic kilometres' (10^{-9} km^{-3}) which corresponds to the number of particles within a cube of 1000 km edge length.

If the radiant of the shower is in the zenith, the particles are moving perpendicular to the horizon (left hand side of Figure 7.1). Assuming the horizon to be stationary, during one hour all the particles within a circular cross-section cylinder of radius a and altitude $l = v_g \times 3600$ s (v_g in km/s; 3600 s = 1 h) will occur as meteors in the field of view of the observer. The volume V of this cylinder is

$$V = \pi \times a^2 \times l \tag{7.7}$$

and the number of meteors per hour n is then

$$n = V \times \mathrm{ND}. \tag{7.8}$$

Thus we can write

$$n = \pi \times a^2 \times v_g \times 3600\mathrm{s} \times \mathrm{ND}. \tag{7.9}$$

If the radiant is **not** in the zenith but at a certain elevation h, the cylinder becomes an elliptical cross-section one (right hand side of Figure 7.1). While the area of the circle is calculated by $A = \pi \times a^2$ (where a is the radius), the area of the ellipse results from $A = \pi \times a \times b$ (where a is the semi-major and b the semi-minor axis). For a circle (i.e. at $h_\mathrm{R} = 90°$) $a = b$. The general form of the last equation is then

$$n = \pi \times a \times b \times v_\mathrm{g} \times 3600\mathrm{s} \times S. \tag{7.10}$$

In this equation only b depends on the radiant elevation h_R. b varies from $b = 0$ at $h_\mathrm{R} = 0°$ to $b = a$ at $h_\mathrm{R} = 90°$. The meteor number n is thus proportional to b. For the zenith correction factor z we can write:

$$z = \frac{n_{90}}{n_h} = \frac{\pi \times a^2 \times v_\mathrm{g} \times 3600 \text{ s} \times \mathrm{ND}}{\pi \times a \times b \times v_\mathrm{g} \times 3600 \text{ s} \times \mathrm{ND}} = \frac{a}{b}. \tag{7.11}$$

Looking at Figure 7.1, we find:

$$\sin h_\mathrm{R} = \frac{b}{a} \tag{7.12}$$

and thus:

$$z = \frac{1}{\sin h_\mathrm{R}} \tag{7.13}$$

valid for $10° \leq h_\mathrm{R} \leq 90°$

This is the most basic form for the zenith correction factor z. If the radiant elevation is less than 10° the formula becomes more complicated. It is even possible to see meteors from a shower if the radiant is slightly **below** the horizon. At −10° radiant elevation, however no meteors from the shower can be seen. In this sub-horizon case the number of meteors will be extremely small, and any result will be very unreliable.

As a good approximation, the radiant elevation for the middle of the observing interval can be used for the calculation of z. It can be calculated using a formula from spherical trigonometry:

$$\sin h = \sin\varphi \times \sin\delta + \cos\varphi \times \cos\delta \times \cos(\Theta - \alpha)$$

where:
φ is the geographical latitude of the observing site,
δ is the declination of the radiant,
α is the right ascension of the radiant (in °), and
Θ is the local sidereal time (in °) at the middle of the observing interval; $(\Theta - \alpha)$ is also known as the local hour angle.

Moving through the gravitational field of the Earth, the meteoric particles are **accelerated and deflected**. The deviation acts such that the radiant is shifted towards the zenith (Figure 7.2). This phenomenon is called **zenith attraction**. The increase in the meteors' velocity depends on their geocentric velocities, and it is stronger for slow particles. The amount of the zenith attraction depends on the geocentric velocity in the same way, and additionally on the radiant elevation; a radiant in the zenith cannot be attracted closer towards the zenith, while the effect is most noticeable for a radiant near the horizon. The angle za of the change in radiant elevation can be calculated by

$$\mathrm{za} = 2 \arctan\left(\frac{v_\infty - v_g}{v_\infty + v_g} \tan\left(\frac{z_0}{2}\right)\right) \tag{7.14}$$

where z_0 is the (undisturbed) zenith distance of the radiant (for the full details of radiant corrections see Gural, 2001). Table 7.1 shows the zenith attraction for different geocentric velocities and radiant elevations.

The zenith attraction causes the observed radiant we have to consider for the calculation of z to have a higher elevation than the geocentric radiant, whose elevation we have calculated. For $h_\mathrm{R} > 15°$ this effect is taken into account by the formulae:

$$v_\infty = \sqrt{123.06\,(\mathrm{km/s})^2 + v_\mathrm{g}^2} \quad (\text{see } [1]) \tag{7.15}$$

[1] The value of 125 (km/s)^2 is valid for a trajectory at the Earth's surface, while 123.06 (km/s)^2 holds for an altitude of 100 km (see Gural, 2001).

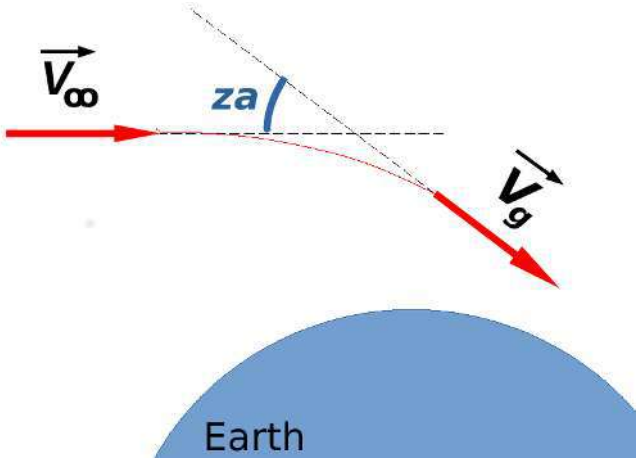


Figure 7.2: Zenith attraction (angle za) of the radiant of a meteor approaching the Earth at velocity $\vec{v}_\infty$; the velocity vector is changed to $\vec{v}_g$ in direction and magnitude.

Table 7.1: Zenith attraction (za, in degrees) dependent on the geocentric velocity v_g (in km/s) and the elevation h of the geocentric radiant (in degrees).

$v_g =$	11.2	20	30	40	60	71
			[km/s]			
$h = 20°$	13.°6	5.°6	2.°5	1.°6	0.°7	0.°5
30°	11.°2	4.°6	2.°1	1.°3	0.°6	0.°4
40°	9.°1	3.°7	1.°7	1.°0	0.°4	0.°3
60°	5.°2	2.°1	1.°0	0.°6	0.°3	0.°2

$$z = \frac{v_\infty}{v_\infty + v_g \times \sin h_R - v_g} \qquad (7.16)$$

valid for $15° \leq h_R \leq 90°$.

where:
– v_∞ is the pre-atmospheric velocity,
i.e. after acceleration by the Earth's gravitation,
– v_g is the geocentric velocity of the shower, and
– h_R is the elevation of the geocentric radiant.
These formulae are not the exact ones but sufficient approximations for visual meteors and radiant elevations in the range of interest, i.e., $h_R > 15°$. Considering the general accuracy of visual counts, we conclude that for most cases (radiant not close to the horizon, say $h_R \geq 20°$, and $v_\infty > \approx 30$ km/s), the basic correction given in Equation 7.13 is sufficient; especially for low velocity showers the Equation 7.16 is recommended.

Now we have obtained the correction factor for the geometrical conditions. But there is another effect affecting the number of meteors observable at different radiant elevations, and thus the zenith correction factor z. The maximum brightness of a meteor caused by a particle of a certain mass and velocity depends on its entry angle into the atmosphere. If the particle enters the atmosphere perpendicularly (i.e., $h_R = 90°$) the meteor becomes brighter with a shorter trajectory than if the atmosphere is entered at a smaller angle; due to the higher gradient of the air density along the trajectory the transformation of the kinetic energy of the particle into radiation happens in a shorter time span. In practical terms, this results in a reduction of the limiting magnitude for meteors, and at the same time in longer meteor paths, if the radiant elevation is less than 90°. If the difference between the maximum magnitudes of two meteors Δm caused by the same particle but at different entry angles (radiant elevations) is known, we can formally take into account this effect according to our knowledge of the correction factor for the limiting magnitude:

$$\Delta m = m_h - m_{90°} \qquad (7.17)$$

$$z_m = z \times r^{\Delta m} \qquad (7.18)$$

where:
– $m_{90°}$ is the maximum magnitude if $h_R = 90°$,
– m_h is the maximum magnitude at radiant elevation h_R
– z is the geometrical zenith correction factor,
– z_m is the zenith correction factor taking into account geometrical conditions and the decrease of the maximum magnitude.
On the other hand, a meteor with a longer path is more likely to be witnessed by an observer than a meteor with a shorter path (if the magnitudes are equal). To a certain extent this equalises the effect of the reduced magnitude.

Several authors (e.g., Zvolánková, 1983) tried to consider these effects using the simple formula:

$$z_m = z^\gamma \qquad (7.19)$$

with $\gamma \approx 1.2 - 1.5$. This is an approximation, however, since dependence on the population index r is neglected.

Δm with dependence on h is very difficult to determine. Most probably the geocentric velocity, the composition of the material, and the state of the high atmosphere (in the meteor region) have an additional influence on Δm. Thus the function $\Delta m(h_R)$ may differ from one shower to the next. The same is valid for the dependence of the trajectory length on h_R.

Recent investigations resulted in $\gamma \approx 1$ for visual observations, i.e. for witnessing a meteor, the reduction of its brightness predicted by the theory and finally found in visual data is approximately equalised by the increase of the path length (Bellot Rubio, 1995; Koschack, 1994). Therefore it is sensible to use the zenith correction factor only accounting for the geometrical conditions for computation of the ZHR.

The situation with the systematic errors caused by uncertainties in the zenith correction factor is similar to that for the limiting magnitude correction. Systematic errors rapidly increase under adverse conditions, here at low radiant elevations. While for a radiant near the zenith the application of a correction factor considering magnitude effect and increased path length is superfluous, this problem may become a more serious matter for a radiant at 10° elevation. This is the reason for suggesting that a shower radiant should have at least

20° elevation if the observation is to be treated for serious analyses. As pointed out in Chapter 2, this general rule does not apply in case of unusual activity.

7.3.4 The correction factor for the limiting magnitude

Under a very dark and transparent sky you will see more meteors than under hazy conditions. The limiting magnitude characterises the quality of the sky. When calculating the ZHR, the question 'How many meteors would we have observed under a sky of limiting magnitude +6.5?' has to be answered. We say 'c times more', i.e.,

$$n_{6.5} = c \times n_{\mathrm{lm}}. \tag{7.20}$$

Hence, the correction becomes the quotient between the numbers seen under standard conditions ($n_{6.5}$) and the number seen under the actual conditions n_{lm}

$$c = \frac{n_{6.5}}{n_{\mathrm{lm}}}. \tag{7.21}$$

Now we will determine the factor c. For this purpose, we need to know the population index r. It is given for the true meteor numbers N:

$$r(m) = \frac{N(m+1)}{N(m)} \tag{7.22}$$

The case of $r(m) =$ constant corresponds to an exponential distribution of the numbers N. For an exponential distribution with $r > 1$, the *true cumulative numbers* Φ can be used. $\Phi(m)$ is the true number of meteors of magnitude class m and brighter. $\Phi(+4^{\mathrm{m}}) = 20$ means that there were 20 meteors of magnitude +4.5 or brighter, for instance. The relationship mentioned above is

$$r = \frac{N(m+1)}{N(m)} = \frac{\Phi(m+1)}{\Phi(m)}. \tag{7.23}$$

Hence, can write

$$\Phi(m_0 + 1) = \Phi(m_0) \times r. \tag{7.24}$$

Setting $m_0 = 0^{\mathrm{m}}$, we find

$$\Phi(+1^{\mathrm{m}}) = \Phi(0^{\mathrm{m}}) \times r^1 \tag{7.25}$$

$$\Phi(+2^{\mathrm{m}}) = \Phi(1^{\mathrm{m}}) \times r = \Phi(0^{\mathrm{m}}) \times r^2 \tag{7.26}$$

$$\Phi(+3^{\mathrm{m}}) = \Phi(2^{\mathrm{m}}) \times r = \Phi(0^{\mathrm{m}}) \times r^3 \tag{7.27}$$

and so on, or generally

$$\Phi(m) = \Phi(0) \times r^m. \tag{7.28}$$

Applying this equation it is possible to calculate any cumulative true meteor numbers such as the meteor numbers two perfect observers (perception probability $p = 1$ for any magnitudes brighter than their limiting magnitude) would have observed, the first one at limiting magnitude lm and the second one at limiting magnitude +6.5

$$\Phi(\mathrm{lm}{-}0.5) = \Phi(0) \times r^{\mathrm{lm}-0.5}$$

$$\Phi(6) = \Phi(0) \times r^6 \tag{7.29}$$

Consider that the definition of the magnitude class $\Phi(6)$ means the true number of meteors brighter than +6.5 and $\Phi(\mathrm{lm}{-}0.5)$ those brighter than the limiting magnitude.

This way we can find

$$\frac{\Phi(6)}{\Phi(\mathrm{lm}-0.5)} = r^{6-(\mathrm{lm}-0.5)} = r^{6.5-\mathrm{lm}} \tag{7.30}$$

It is obvious that the left-hand side of this equation resembles the right hand side of the equation for c that we derived above, but instead of the true cumulative numbers, it refers to the observed (also cumulative) numbers. So, what is the difference between the real and the observed numbers? The observed numbers amount to a certain percentage of the true numbers. This percentage k is defined by the population index r and the probabilities of perception p. Since p depends on the difference between the meteor magnitude and the limiting magnitude, k is not affected by the limiting magnitude, i.e., each observer sees the same percentage k of the real number of meteors brighter than the individual's limiting magnitude $\Phi(\mathrm{lm}{-}0.5)$—given that the population index r is constant. This is illustrated by an example shown in Table 7.2.

In our example described by the values in Tables 7.2 and 7.3, observer 1 recorded 148 meteors ($\Phi(6) = 3280$), observer 2 only 49 meteors ($\Phi(5) = 1093$) during the same time. We find

$$k_1 = \frac{n_{6.5}}{\Phi(6)} = \frac{148}{3280} = 0.045 \tag{7.31}$$

$$k_2 = \frac{n_{5.5}}{\Phi(5)} = \frac{49}{1093} = 0.045. \tag{7.32}$$

This means that $k = k_1 = k_2$ as stated above. Now we can write

$$\frac{\Phi(6)}{\Phi(\mathrm{lm}-0.5)} = \frac{\frac{n_{6.5}}{k}}{\frac{n_{\mathrm{lm}}}{k}} = \frac{n_{6.5}}{n_{\mathrm{lm}}} = c = r^{6.5-\mathrm{lm}}. \tag{7.33}$$

This leads us to the final equation

$$c = r^{6.5-\mathrm{lm}}. \tag{7.34}$$

This is an exact correction factor if

- the population index r is precisely known and constant over the magnitude range;
- the reduction of the limiting magnitude for stars is equal to the reduction of the limiting magnitude for meteors.

The first condition cannot be fulfilled exactly and there will remain an uncertainty in r which may easily exceed ±0.2. If we imagine the situation where a population index $r = 3.0$ was assumed for the calculation of the correction c, while the true value was $r = 2.7$, we find the resulting errors of the ZHR for different limiting magnitudes as listed in Table 7.3.

Table 7.2: For a population index $r = 3.0$, we compare the counts of observer 1 with lm = 6.5 and observer 2 noting lm = 5.5.

Magn.	True number	Observer 1			Observer 2		
m	N	p	n	Φ	p	n	Φ
−1	1	1.0	1	1	0.90	1	1
0	3	0.90	3	4	0.80	3	4
+1	9	0.80	7	13	0.65	6	13
+2	27	0.65	18	40	0.38	10	40
+3	81	0.38	31	121	0.14	11	121
+4	243	0.14	34	364	0.044	11	364
+5	729	0.044	32	1093	0.010	7	1093
+6	2187	0.010	22	3280	0	0	1093
Σ			148			49	

Table 7.3: Errors in the correction factor c resulting from uncertainties of the population index r. In this example, we compare the correction c obtained from the assumed value $r = 3.0$ and the true value $r = 2.7$.

Lim. magn.	Corrections		Error
lm	$c(r = 3.0)$	$c(r = 2.7)$	(in %)
7.0	0.58	0.61	−5
6.5	1.00	1.00	0
6.0	1.73	1.64	5.5
5.5	3.00	2.70	11
5.0	5.20	4.44	17
4.5	9.00	7.29	23

It is obvious, that for a given, unavoidable, uncertainty in the population index r, the resulting uncertainty of the corresponding correction c and finally the error in the ZHR increases rapidly.

The second condition listed above is fulfilled if the reduction in the limiting magnitude is due to pure extinction (dust, haze). If it is mainly due to any illumination of the sky (artificial lights, the Moon, twilight), then this condition is not completely fulfilled, i.e., the limiting magnitude for meteors decreases more strongly than that for stars, which are used to determine lm and are then used for the calculation.

Both error sources are of systematic character, i.e., they act in a specific direction. Thus they cannot be reduced by the application of statistical procedures such as averaging many data.

Imagine we are analysing the ZHR of a shower. Due to unavoidable uncertainties the population index has been determined as $r = 3.0$ while its real value was $r = 2.7$. For this analysis we are using a large number of meteor observations, say 100, carried out at the same time under poor conditions, say lm = 4.5. We calculate the individual ZHRs using $r = 3.0$. Due to random errors the individual ZHRs scatter. Next we average the ZHRs to find the real (most probable) value. But since **all** the individual ZHRs are too high by 23% (as shown in Table 7.3), the average ZHR also has a systematic error of +23%. Since we do not know the value and the sign of the error in r we do not know that our result (the average ZHR) is affected by a systematic error of +23%.

For this reason, observations carried out under a sky of limiting magnitude less than about 5.0 impose large uncertainties. Therefore, a dark observing site is essential for good observations. In the case of exceptional events, of course, observations are made under poorer conditions than usual. A chance to obtain reliable data on the stream is given when a large number of reports is available. Therefore, ZHR profiles of shower peaks and outbursts can be calculated if observed by numerous observers and based on the population index profile obtained from the relevant magnitude data. An example for the Geminid 2018 data analysis (Rendtel, 2019) shows that a large sample including (almost) all reported data can help to cover as much as possible of the profile while a selection will immediately cause gaps.

7.3.5 The randomness of meteors

The waiting time for a randomly observed meteor is stochastically independent and memoryless. This means that the waiting time for a certain meteor does not depend on how much time has already passed or how long we have waited for the previous meteor. This also applies if the activity of the meteor shower is precisely known. From this follows the Poisson distribution, that expresses the probability P of a given number of meteors n occurring in a fixed interval of time t with a known constant mean rate A and independently of the time since the last event. It is:

$$P(n \text{ meteors in interval } t) = \frac{(A\ t)^n e^{-A\ t}}{n!}\ , \quad (7.35)$$

where e is Euler's number ($e = 2.71828...$) and $n!$ is the factorial of n. From it follows how many meteors we would observe on average $\mathrm{E}[n]$ as well as the variance $\mathrm{Var}[n]$ of the meteors to be observed:

$$A \cdot t = \mathrm{E}[n] = \mathrm{Var}[n]. \quad (7.36)$$

This corresponds to the statement made in Equation (7.3). An illustrative representation of the Poisson distribution is shown in Figure 7.3.

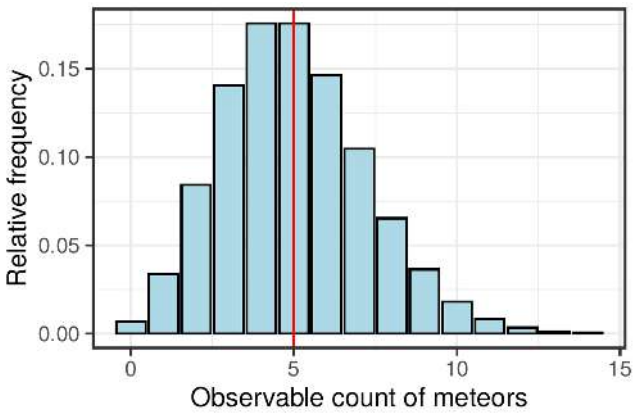


Figure 7.3: The relative frequency distribution of the number of meteors for an observation of one hour and an activity of 5 meteors per hour. As expected, about 5 meteors are observed on average (red line). The frequency of observing less than 2 meteors is 4%, observing more than 9 meteors at 3%.

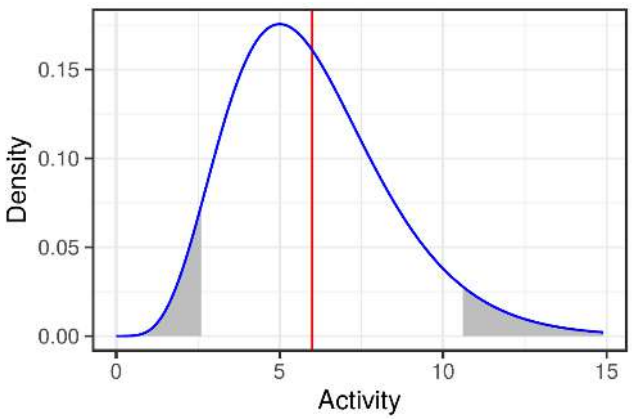


Figure 7.4: The probability density of the activity of a meteor shower for an observation of 5 meteors within one hour. No prior knowledge about the activity is used ($\alpha_0 = 1, \beta_0 = 0$). The maximum value of the density (mode) is 5.0, the mean value is 6.0 (red line). Gray areas mark the extreme quantiles. I.e., we should not accept these values for the activity with a probability of 10%.

We can also apply the Poisson distribution on observable magnitude classes. For this purpose, we imagine that each magnitude class is a subshower of the meteor shower. Also, each observation of a magnitude class is stochastically independent and memoryless. This means that the magnitude of a meteor does not depend on the magnitude of a previously observed meteor. Simplified, meteors do not know each other and do not communicate with each other.

In the analysis of observed meteors, the number of observed meteors is known, in contrast to the activity of the meteor shower. The Poisson distribution is an a priori distribution, since in it we assume a known activity of the meteor shower. Therefore, the Poisson distribution cannot be used directly to estimate the activity. To determine the activity, the Bayes estimator is used. It is an estimator or decision rule that minimises the expected value of the activity. This allows us to make statements about the activity of the meteor shower based on the observed number of meteors. The conjugate prior to the Poisson distribution is a gamma distribution. Thus, the density of the probability of activity is:

$$p(A; \alpha, \beta) = \frac{1}{\Gamma(\alpha)} \, \beta^{\alpha} A^{\alpha-1} e^{-\beta A} \tag{7.37}$$

for $A \geq 0$ and $\alpha, \beta > 0$, where $\Gamma(\alpha)$ is the gamma function. From it follows the expected value of the activity $\mathrm{E}(A)$, its expected variance $\mathrm{Var}[A]$ and the mode:

$$\mathrm{E}[A] = \frac{\alpha}{\beta} \, , \tag{7.38}$$

$$\mathrm{Mode}[A] = \frac{\alpha - 1}{\beta} \text{ for } \alpha \geq 1 \, , \tag{7.39}$$

$$\mathrm{Var}[A] = \frac{\alpha}{\beta^2} \, , \tag{7.40}$$

$$\mathrm{E}[\ln(A)] = \psi(\alpha) - \ln(\beta) \, , \tag{7.41}$$

where ψ is the digamma function. Likewise,

$$\mathrm{Var}[\ln(A)] = \psi^{(1)}(\alpha) \, , \tag{7.42}$$

where $\psi^{(1)}$ is the trigamma function. The mode $\mathrm{Mode}[A]$ is the value at which the probability density takes its maximum value. In other words, it is the value that is most likely to be accepted based on the observation result. The difference between mode and mean is shown in Figure 7.4. Sufficient approximations for the digamma and trigamma function are for $\alpha \geq 2.0$:

$$\psi(\alpha) \approx \ln(\alpha - 0.5) \, , \tag{7.43}$$

$$\psi^{(1)}(\alpha) \approx \frac{1}{\alpha - 0.5} \, . \tag{7.44}$$

From the Poisson distribution, for k of independent observations, where n_i meteors were each observed in a time interval t_i, it follows that

$$\alpha = \alpha_0 + \sum_{i=1}^{k} n_i \tag{7.45}$$

$$\beta = \beta_0 + \sum_{i=1}^{k} t_i \, , \tag{7.46}$$

where α_0 and β_0 are called hyperparameters.

It is often useful to think of the hyperparameters as corresponding to the observation of a certain number of meteors in a *pseudo-observation* with the properties specified by the parameters. The α_0 and β_0 values can be thought of as corresponding to α_0 observed meteors in a fixed time interval of length β_0 when the posterior mode is used to choose an optimal parameter setting. The mode specifies which activity is most probable. For $\alpha_0 + 1$ the posterior mean is used to choose an optimal parameter setting. This value indicates what activity we should expect. If there is no knowledge about the expected activity of the meteor shower before the observations, then $\alpha_0 = 0, \beta_0 = 0$ should be chosen to obtain the mode of the activity. This result also corresponds to that of the maximum likelihood estimator. Respectively, the posterior mean results from $\alpha_0 = 1, \beta_0 = 0$.

To get a better understanding of these hyperparameters, let us assume that one hour was observed but no meteor appeared. Additionally, there is no prior knowledge of meteor shower activity. With $\alpha_0 = 0, \beta_0 = 0$ we obtain an activity of 0.0 ± 0.0. On the one hand, this corresponds to our perception that the shower shows no activity. On the other hand, the variance indicates that we are very sure that the shower has no activity. This is a contradiction to the assumption that we have no prior knowledge about the activity, because any other activity including 0.0 would also be possible to obtain the same result. With the posterior mean ($\alpha_0 = 1, \beta_0 = 0$) we get a different result. We obtain for the activity 1.0 ± 1.0 respectively that the activity is between 0.0 and 2.0. This is more in accordance with our ideas about the activity of the meteor shower. We can approximately say with this values that the activity is not much greater than 2.0.

Other values for the hyperparameters α_0 and β_0 can be used, especially if prior knowledge of the meteor shower activity is available. These can be causal or, e.g., come from previous observations of past years. One can thus obtain more accurate estimates of the activity of the shower. Conversely, this can make the estimate for the activity overly predetermined. Therefore, other hyperparameters should be used with caution.

7.3.6 The ZHR estimation

The standard quantity measuring meteor shower activity is the Zenithal Hourly Rate (ZHR). The ZHR is defined as the activity of the meteor shower at a limiting magnitude of 6.5:

$$\mathrm{ZHR} := A(\mathrm{lm} = 6.5) \tag{7.47}$$

We apply the simple linear regression model to estimate the ZHR. This is possible because the logarithm of the waiting time for a single meteor is homoscedastic. This means that the variance does not depend on its value. For the estimation of the ZHR, we assume that k observations are available in a time period. In addition, we assume that the ZHR is constant during this period and that the meteors are Poisson distributed in all observations.

First we determine the average limiting magnitude $\overline{\mathrm{lm}}$

$$N = \sum_{i=1}^{k} n_i \ , \tag{7.48}$$

$$\overline{\mathrm{lm}} = \frac{1}{N} \sum_{i=1}^{k} n_i \cdot \mathrm{lm}_i \ . \tag{7.49}$$

Here n_i is the total number of recorded meteors of the i-th observation and lm_i is the limiting magnitude at that observation. Then, all known correction coefficients must be applied. This results in a corrected observation time t_i for the i-th observation and its total sum:

$$t_i = r^{(\mathrm{lm}_i - \overline{\mathrm{lm}})} \cdot \frac{T_{\mathrm{eff},i}}{F_i \cdot z(h_{\mathrm{R},i})} \ , \tag{7.50}$$

$$T = \sum_{i=1}^{k} t_i \ . \tag{7.51}$$

As an preliminary result, we obtain an estimate of the activity of the meteor shower at a limiting magnitude of $\overline{\mathrm{lm}}$:

$$\widehat{A}_{\mathrm{lm}=\overline{\mathrm{lm}}} = \frac{N+1}{T}. \tag{7.52}$$

The symbol $\widehat{A}$ is used to indicate that it is an estimate of the activity. As described in 7.3.5, we assume here that there is no prior knowledge of shower activity. Therefore, we use the term $N + 1$.

Usually, on average, observations do not take place at a limiting magnitude of $\mathrm{lm} = 6.5$. Therefore, we perform a statistical prediction for this limiting magnitude. Since the linear regression is based on the logarithm of the waiting time for a meteor, we need the logarithm of the activity of the meteor shower according to Equation (7.41):

$$\widehat{\mathrm{la}} := \widehat{\ln(A)}_{\mathrm{lm}=\overline{\mathrm{lm}}} \ , \tag{7.53}$$

$$= \psi(N+1) - \ln(T) \ , \tag{7.54}$$

$$\approx \ln(N+0.5) - \ln(T), \text{ for } N \geq 1 \ . \tag{7.55}$$

The variance of the estimated value $\widehat{\mathrm{la}}$ is as specified by Equation (7.42):

$$\widehat{\sigma_{\mathrm{la}}}^2 = \psi^{(1)}(N+1) \ , \tag{7.56}$$

$$\approx \frac{1}{N+0.5}, \text{ for } N \geq 1 \ . \tag{7.57}$$

Also, the r-value is needed for the prediction of the ZHR. We have to suppose that this value is not known exactly. Because of the linear model, the variance $\sigma^2_{\ln(r)}$ of this value is needed. Here, it is a reasonable assumption for the linear model that $\ln(r)$ is normally distributed. Therefore, using the log-normal distribution, we can derive the variance $\sigma^2_{\ln(r)}$ for the r-value from the assumed variance σ_r^2 :

$$\sigma^2_{\ln(r)} \approx \ln\left(1 + \frac{\sigma_r^2}{r^2}\right). \tag{7.58}$$

We can now predict the ZHR with:

$$\mathrm{logZHR} := \widehat{\ln(A)}_{\mathrm{lm}=6.5} \ , \tag{7.59}$$

$$= \ln(r) \cdot (6.5 - \overline{\mathrm{lm}}) + \widehat{\mathrm{la}} \ , \tag{7.60}$$

where logZHR is the logarithm of ZHR. The estimated variance of the log ZHR follows from:

$$\sigma^2_{\mathrm{logZHR}} = \widehat{\sigma_{\mathrm{la}}}^2 + \sigma^2_{\ln(r)} \cdot (6.5 - \overline{m})^2 \ . \tag{7.61}$$

In this equation, it is well seen that the larger the distance of the mean limiting magnitude $\overline{\mathrm{lm}}$ from 6.5, the larger the error of the ZHR prediction. This is not the case if we would assume that the r-value is known exactly ($\sigma_{\ln(r)} = 0$). However, this would not make sense

because then the measured variance of the activity at a limiting magnitude of $\overline{\text{lm}}$ could also be assumed for unusual limiting magnitudes. It would not be consistent with our beliefs that we could predict relatively accurately the activity of the meteor shower for e.g. a limiting magnitude of lm = 9.0. On the other hand, it is well seen in Equation (7.60) and Equation (7.61) that for $\overline{\text{lm}} \approx 6.5$ neither the r-value nor its variance are relevant for estimating the ZHR.

To obtain the ZHR and its variance we again use the gamma distribution and determine its parameters with:

$$\alpha = \frac{1}{\sigma^2_{\text{logZHR}}} + 0.5 \,, \tag{7.62}$$

$$\beta = \frac{e^{-\text{logZHR}}}{\sigma^2_{\text{logZHR}}} \,. \tag{7.63}$$

Finally, if $\alpha \geq 2.0$, then we obtain the ZHR and its standard deviation with:

$$\widehat{\text{ZHR}} = \frac{\alpha}{\beta} \,, \tag{7.64}$$

$$\widehat{\sigma_{\text{ZHR}}} = \frac{\sqrt{\alpha}}{\beta} \,. \tag{7.65}$$

If $\alpha < 2.0$, then this would correspond to an observed pseudo total count of $N < 1$ meteors at a limiting magnitude of 6.5. It would then not only be mathematically more complex to calculate α and β. $\alpha < 2.0$ also corresponds as if no meteor had been observed. Therefore, it is also generally not reasonable to accept such ZHR estimates.

As an example, let's evaluate a single observation. Suppose $n = 5$ meteors of a meteor shower were observed within $T_{\text{eff}} = 0.5$ hours. There were no interferences e.g. by clouds, therefore is $F = 1.0$. The determined limiting magnitude of this observation is lm = 6.0. The radiant was 30 degrees above the horizon, accordingly $z = 1/\sin(30 \text{ degrees}) = 2.0$. Since this is a single observation, the total number of observed meteors is $N = n = 5$, and the mean limiting magnitude is $\overline{\text{lm}} = \text{lm} = 6.0$. According to Equation (7.50) we obtain the corrected observation time with:

$$\begin{aligned} T = t &= r^{(6.0-6.0)} \cdot \frac{0.5}{1.0 \cdot 2.0} \,, \\ &= 1.0 \cdot \frac{0.5}{1.0 \cdot 2.0} \;=\; 0.25 \,. \end{aligned}$$

Following Equation (7.5), the *observed activity* of the shower is $a = 5/0.25 = 20.0$ meteors per hour.

Let us now discuss the result of our observation. The appearance of a meteor depends on randomness. For this observation, this could mean that the meteor shower activity was higher than observed, but unfortunately only 5 meteors were seen. But it could also be that the activity was lower and by random more meteors were observed. What meteor shower activity should we assume based on the observational result? Assuming we have no prior knowledge of meteor shower activity, we therefore choose $\alpha_0 = 1, \beta_0 = 0$ and obtain:

$$\begin{aligned} \alpha &= \alpha_0 + n \;=\; 1 + n \;=\; 1 + 5 \;=\; 6 \,, \\ \beta &= \beta_0 + t \;=\; 0 + t \;=\; 0 + 0.25 \;=\; 0.25 \,, \\ \text{E}[A] &= \frac{\alpha}{\beta} \;=\; \frac{6}{0.25} \;=\; 24.0 \,, \\ \text{Var}[A] &= \frac{\alpha}{\beta^2} \;=\; \frac{6}{0.25^2} \;=\; 96.0 \,. \end{aligned}$$

Since the standard deviation is $\sigma_A = \sqrt{\text{Var}[A]}$, we obtain as an estimate for the meteor shower activity:

$$\begin{aligned} \widehat{A}_{\text{lm}=6.0} &= \text{E}[A] \;=\; 24.0 \,, \\ \sigma_A &= \sqrt{\text{Var}[A]} \,, \\ &= \sqrt{96.0} \;\approx\; 9.8 \end{aligned}$$

and therefore

$$\begin{aligned} \widehat{A}_{\text{lm}=6.0} &\approx 24.0 \pm 9.8 \,, \\ &\approx 14.2 \text{ to } 33.8 \,. \end{aligned}$$

We must note that the standard deviation $\sigma_A \approx 9.8$ is not an absolute limit, but the deviation from the activity to be expected on average.

We now want to estimate what the activity of the meteor shower would be if the observation had been made at a limiting magnitude of lm = 6.5. This is the estimation of the ZHR. For this prediction, the r-value $r = 2.0 \pm 0.2$ is assumed. First, we need the estimate of the logarithm of the previously determined values of the activity and its variance:

$$\begin{aligned} \widehat{\text{la}} &:= \widehat{\ln(A)}_{\text{lm}=6.0} \,, \\ &= \psi(N+1) - \ln(T) \,, \\ &\approx \ln(N+0.5) - \ln(T) \,, \\ &= \ln(5+0.5) - \ln(0.25) \;\approx 3.09 \,, \\ \widehat{\sigma_{\text{la}}}^2 &= \psi^{(1)}(N+1) \,, \\ &\approx \frac{1}{N+0.5} \,, \\ &= \frac{1}{5+0.5} \;\approx 0.18 \,. \end{aligned}$$

The variance of the logarithm of the r value is:

$$\begin{aligned} \sigma^2_{\ln(r)} &\approx \ln\left(1 + \frac{\sigma_r^2}{r^2}\right) \,, \\ &= \ln\left(1 + \frac{0.2^2}{2.0^2}\right) \;\approx 0.01 \,. \end{aligned}$$

As an intermediate result we get the logarithm of the ZHR as well as its variance:

$$\begin{aligned} \text{logZHR} &= \ln(r) \cdot (6.5 - \overline{\text{lm}}) + \widehat{\text{la}} \,, \\ &= \ln(2.0) \cdot (6.5 - 6.0) + 3.09 \;\approx 3.44 \,, \\ \sigma^2_{\text{logZHR}} &= \widehat{\sigma_{\text{la}}}^2 + \sigma^2_{\ln(r)} \cdot (6.5 - \overline{m})^2 \,, \\ &= 0.18 + 0.01 \cdot (6.5 - 6.0)^2 \;= 0.1825 \,. \end{aligned}$$

We can now calculate the estimated logarithm of the ZHR into the ZHR. For this purpose, we determine the

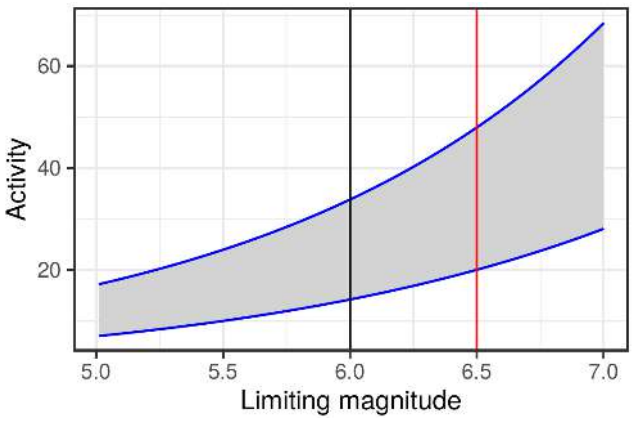


Figure 7.5: Prediction of activity in a limiting magnitude range of 5.0 to 7.0. The example from Section 7.3.6 is used for the prediction. The black line marks the limiting magnitude at which the observation was made, the red line the limiting magnitude of 6.5.

parameters of the gamma distribution with:

$$\begin{aligned}\alpha &= \frac{1}{\sigma^2_{\log\mathrm{ZHR}}} + 0.5 \,, \\ &= \frac{1}{0.1825} + 0.5 \approx 6.0 \,, \\ \beta &= \frac{e^{-\log\mathrm{ZHR}}}{\sigma^2_{\log\mathrm{ZHR}}} \,, \\ &= \frac{e^{-3.44}}{0.1825} \approx 0.175 \,.\end{aligned}$$

Since $\alpha = 6.0 \geq 2.0$, the quality of our observation is sufficient to obtain the prediction of the ZHR:

$$\begin{aligned}\widehat{\mathrm{ZHR}} &= \frac{\alpha}{\beta} \\ &= \frac{6.0}{0.175} \approx 34.3 \\ \widehat{\sigma_{\mathrm{ZHR}}} &= \frac{\sqrt{\alpha}}{\beta} \,, \\ &= \frac{\sqrt{6.0}}{0.175} \approx 14.0 \,.\end{aligned}$$

In summary, the assumed ZHR of the observation is thus:

$$\begin{aligned}\widehat{\mathrm{ZHR}} &\approx 34.3 \pm 14.0 \,, \\ &\approx 20.3 \text{ to } 48.3 \,.\end{aligned}$$

The prediction interval of activity for various limiting magnitudes for this observation is shown in Figure 7.5. As we can see from the values, the quality of the observation is low. In rare cases due to chance, meteor shower activity may have been even lower or higher. Other influences can also tend to worsen the data quality.

7.4 Determination of the population index

7.4.1 Basics and methods

The population index r is a very basic property of a meteoroid stream. It quantifies the magnitude distribution of meteors and, after a converting procedure, the mass distribution of the meteoroids. Further, the computation of the ZHR requires the knowledge oft he population index.

The population index r was introduced in Section 7.3.4 and is defined by equations 7.22 and 7.23 on page 143. For the complete description of the method, we repeat these here. The population index r is given for the true meteor numbers N by

$$r(m) = \frac{N(m+1)}{N(m)} \tag{7.66}$$

The case of $r(m) =$ constant corresponds to an exponential distribution of the numbers N. For an exponential distribution with $r > 1$, the *true cumulative numbers* Φ can be used. $\Phi(m)$ is the true number of meteors of magnitude class m and brighter. $\Phi(+4\,\mathrm{mag}) = 20$ means that there were 20 meteors of magnitude +4.5 or brighter, for instance. The relationship mentioned above is

$$r = \frac{N(m+1)}{N(m)} = \frac{\Phi(m+1)}{\Phi(m)}. \tag{7.67}$$

By definition, the population index r refers to a magnitude. Analyses have shown that in most cases r is constant over wide range of magnitudes, say from -2 to $+5$ mag ([2]). For most meteoroid streams and for sporadic meteors we can assume r to be constant for typical magnitudes of visual meteors. As a visual observer can see only a fraction of meteors actually appearing, we need to know perception probabilities for determination of the population index. Perception probabilities have been determined for a group of experienced observers under dark transparent skies (Koschack & Rendtel 1990a, 1990b; see also Section 7.6). Table 7.4 and Figure 7.6 show the perception probabilities $p(\Delta m)$ as a function of the magnitude difference to the limiting magnitude for an observing field of 52°5 radius. Note that magnitude class +6 contains all meteors $+6.5 > m > 5.5$, i.e. at lm = 5.8 a few meteors of +6 (Δm) = −0.2) can be seen.

[2] This is also observed in video meteor data. Here the low light level limit is determined by the sensor and the lens. An example is found in Margonis et al. (2019) for a series of Perseid observations 2010–2016.

Table 7.4: Perception probabilities $p(\Delta m)$ for an experienced observer under dark sky conditions, averaged over a field of view with a radius of 52°.5. Δm is the difference between the limiting magnitude and the meteor magnitude $\Delta m = \mathrm{lm} - m$

Δm	$p(\Delta m)$	Δm	$p(\Delta m)$	Δm	$p(\Delta m)$
−0.4	0.00046	2.4	0.13000	5.2	0.77000
−0.2	0.00110	2.6	0.16000	5.4	0.79000
0.0	0.00230	2.8	0.20000	5.6	0.81000
0.2	0.00460	3.0	0.24000	5.8	0.83000
0.4	0.00810	3.2	0.29000	6.0	0.85000
0.6	0.01220	3.4	0.34674	6.2	0.87000
0.8	0.01820	3.6	0.40000	6.4	0.89000
1.0	0.02570	3.8	0.46000	6.6	0.91000
1.2	0.03444	4.0	0.52000	6.8	0.93000
1.4	0.04365	4.2	0.57544	7.0	0.94000
1.6	0.05495	4.4	0.63096	7.2	0.96000
1.8	0.06918	4.6	0.67764	7.4	0.98000
2.0	0.08511	4.8	0.71000	7.6	1.00000
2.2	0.10351	5.0	0.74000	7.8	1.00000

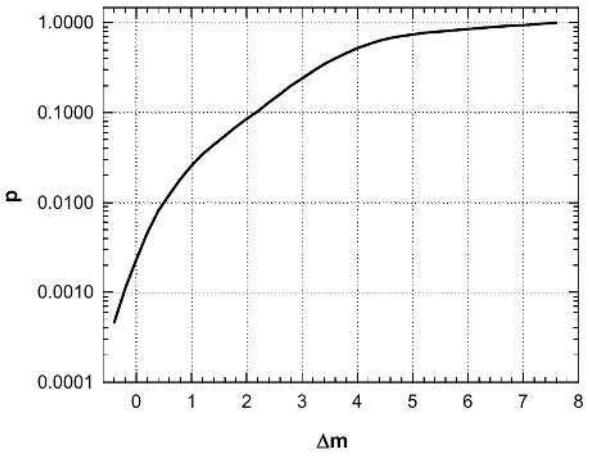


Figure 7.6: Perception probabilities $p(\Delta m)$ for an experienced observer under a dark sky, averaged over a field of view with a radius of 52°.5. Δm is the difference between the limiting magnitude and the meteor magnitude $\Delta m = \mathrm{lm} - m$. (Numerical values are given in Table 7.4.)

For a numerical approximation the following computer code can be used:

```
p(x) = 10^((a+cx+ex^2+gx^3)/(1+bx+dx^2+fx^3))
for -0.4 <= x <= 7.6
p(x) = 1.00 for x >= 7.6
with
x = Δ m = lm - m
a = -2.6114012   b = 0.026855133   c = 1.4267014
d = -0.15984339  e = -0.2717859   f = 0.031934995
g = 0.017006668
```

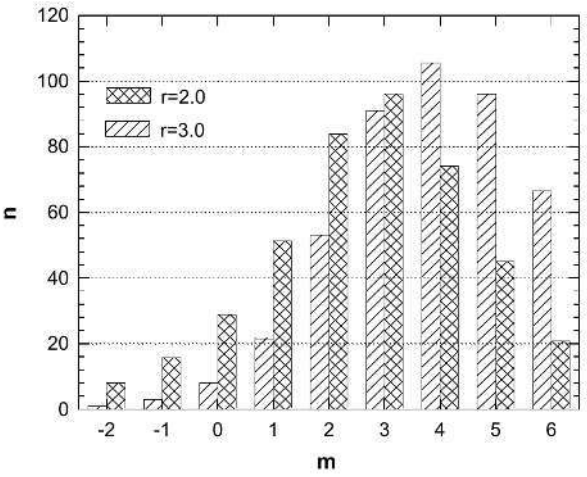


Figure 7.7: Meteor numbers n per magnitude class m visible at population indices $r = 2.0$ and $r = 3.0$ as simulated and listed in Table 7.5

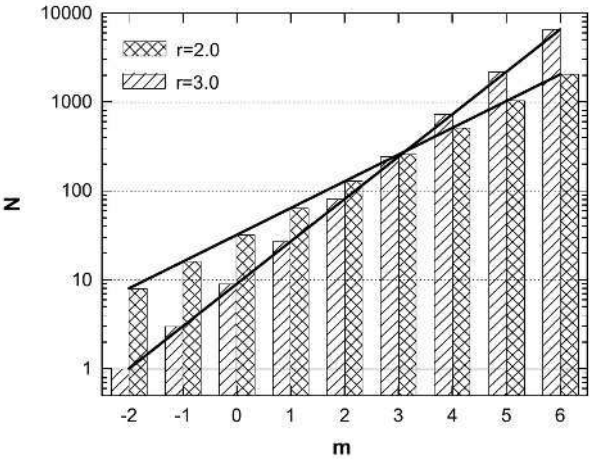


Figure 7.8: True meteor numbers N per magnitude class m at population indexes $r = 2.0$ and $r = 3.0$ as simulated and listed in Table 7.5. In a logarithmic scale there is linear slope of N versus m.

To illustrate the impact of the population index on a visual meteor observation, we show results of a simulation of visual observations at $\mathrm{lm} = 6.5$ and different population indices in Table 7.5. A visual observer witnesses $n = p \times N$ of the true number of meteors N. Note that this is a simulation, in a real observation you cannot see $n = 28.8$ meteors. In Figures 7.7 and 7.8, the true numbers N and the visible numbers n are plotted. At $r = 2.0$ a visual observer will see most meteors in magnitude class +3, at $r = 3.0$ in magnitude class +4 (Figure 7.7). In the logarithmic scale of Figure 7.8, the true numbers show a linear slope versus the magnitude class.

In Table 7.5 the average magnitude of the visible meteors is calculated. For $r = 2.0$ we find an average magnitude $m_{\mathrm{avg}} = 2.65$, for $r = 3.0$ we find $m_{\mathrm{avg}} = 3.81$. The difference between lm and m_{avg} directly depends on the population index r, i.e. r can easily be determined from average magnitude of visible meteors. This

Table 7.5: Simulation of visual observations (lm=6.5) for population indexes $r = 2.0$ and $r = 3.0$. p – perception probability, N – true meteor number, n – visible meteor number.

m	lm-m	p	$N(r = 3.0)$	$n(r = 3.0)$	$N(r = 2.0)$	$n(r = 2.0)$
−2	8.5	1.00000	1	1.0	8	8.0
−1	7.5	0.99000	3	3.0	1	15.8
0	6.5	0.90000	9	8.1	3	28.8
1	5.5	0.80000	27	21.6	64	51.2
2	4.5	0.65500	81	53.1	128	83.8
3	3.5	0.37500	243	91.1	256	96.0
4	2.5	0.14500	729	105.7	512	74.2
5	1.5	0.04400	2187	96.2	1024	45.1
6	0.5	0.01015	6561	66.6	2048	20.8
total			9841	446.4	4088	423.8
m_{avg}				3.81		2.65
$\text{lm} - m_{\text{avg}}$				2.69		3.85

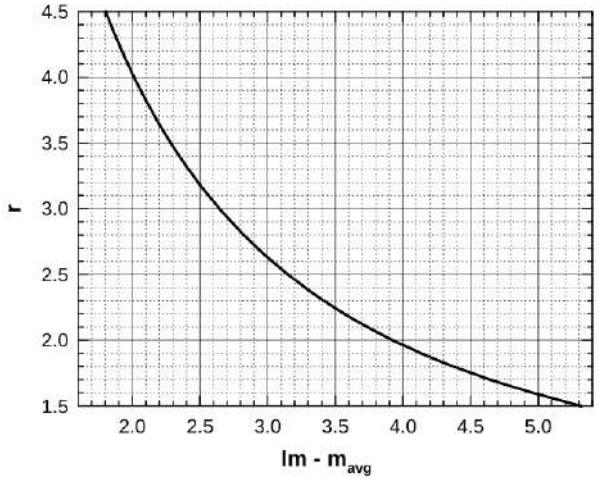


Figure 7.9: Conversion function for the population index r and the difference Δm between lm and average magnitude of meteors seen m_{avg}. $\Delta m = \text{lm} - m_{\text{avg}}$.

relation is listed in Table 7.6 and shown in Figure 7.9. This method is very simple but has some disadvantages:

1. The conversion function bases on the assumption of a constant population index over the entire range of visual magnitudes. Within this method there is no chance to check whether this assumption meets reality. For any magnitude distribution, even if it is not based on a constant r, we can compute an average magnitude and from this we derive a value of r.

2. The conversion function bases on perception probabilities determined for experienced observers under dark sky. If the real perception probabilities differ from this – due to illuminated sky background or less experience of observers – the value of r will be affected by systematic errors which cannot be minimised by averaging many observations.

Table 7.6: Conversion table for the population index r and the difference Δm between lm and the average magnitude of meteors seen m_{avg}.

Δm $= \text{lm} - m_{\text{avg}}$	r	Δm $= \text{lm} - m_{\text{avg}}$	r
1.5	5.317		
1.6	4.954	3.1	2.563
1.7	4.642	3.2	2.487
1.8	4.370	3.3	2.416
1.9	4.133	3.4	2.348
2.0	3.923	3.5	2.284
2.1	3.736	3.6	2.224
2.2	3.568	3.7	2.167
2.3	3.415	3.8	2.113
2.4	3.277	3.9	2.062
2.5	3.150	4.0	2.014
2.6	3.033	4.1	1.967
2.7	2.925	4.2	1.923
2.8	2.825	4.3	1.8 81
2.9	2.732	4.4	1.841
3.0	2.645	4.5	1.803

For a computer code this numerical approximation can be used:

```
y = a + bx^c
for 1.8 <= x <= 5.4
with y = r; x = Δm = lm - m_avg
a = 0.26204182 b = 8.3279447 c = -1.144563
```

There is an *alternative method* for the determination of the population index, based on a logarithmic plot of true meteor numbers in Figure 7.8. Instead of true numbers per magnitude class $N(m)$, true *cumulative* numbers $\Phi(m)$ are used. $\Phi(m = +6)$ for instance, is the true number of meteors with magnitudes brighter than +6.5 mag. The true cumulative numbers $\Phi(m)$

are less affected than the true numbers $N(m)$ by scatter due to the randomness of meteors and by inaccurate meteor magnitude estimates. Log[$\Phi(m)$] is plotted versus m and a linear regression is applied to the dataset: $\log[\Phi(m)] = a + b * m$ with

$$b = \frac{n \sum_{i=1}^{n} x \cdot y - \left(\sum_{i=1}^{n} x\right) \cdot \left(\sum_{i=1}^{n} y\right)}{n \sum_{i=1}^{n} x \cdot x - \left(\sum_{i=1}^{n} x\right)^2}$$

$$a = \frac{\left(\sum_{i=1}^{n} x \cdot x\right) \cdot \left(\sum_{i=1}^{n} y\right) - \left(\sum_{i=1}^{n} x \cdot y\right) \cdot \left(\sum_{i=1}^{n} x\right)}{n \sum_{i=1}^{n} x \cdot x - \left(\sum_{i=1}^{n} x\right)^2}$$

$x = \mathrm{m}$,
$y = \log(\Phi\mathrm{m})$,
n – number of data points
and finally: $r = 10^b$

7.4.2 Comparison of both methods

Both methods are based on probabilities of perception. The values given in Figure 7.6 and Table 7.4 were determined for a group of experienced observers under dark and transparent sky. For unexperienced observers or skies with light pollution (scattered light and thus reduced contrast) there may be differences. The variation of perception probabilities for light polluted skies is subject of ongoing investigations. Unexperienced observers probably see fewer faint meteors than experienced observers while for brighter meteors the perception probabilities will be approximately the same. In Figure 7.10 an arbitrary example is shown: for the faintest meteors the perception probability of an unexperienced observer is just 50% of that of an experienced observer. Both curves approach each other and from $\Delta m = 4.0$ onwards they are identical.

The resulting conversion functions $r = f(\mathrm{lm} - m_{\mathrm{avg}})$ are shown in Figure 7.11. If the true population index is $r = 3.0$ the (arbitrarily) unexperienced observer will get $\mathrm{lm} - \mathrm{lm}_{\mathrm{avg}} = 2.95$. Applying the conversion function for experienced observers, the value $\mathrm{lm} - \mathrm{lm}_{\mathrm{avg}} = 2.95$ results in $r = 2.67$. If the conversion function for experienced observers is used for results of less or unexperienced observers, the population index is systematically underestimated. This bias cannot be eliminated by averaging lots of observations. The effect reduces if the population index is small.

Table 7.7 shows the simulation of the (arbitrarily) unexperienced observer for the case $\mathrm{lm} = 6.0$ and $r = 3.0$. The true meteor numbers "N true" are multiplied with the effective perception probabilities of the (arbitrarily) unexperienced observer "p effective" to compute the meteor numbers "n visible" seen by this observer. This simulated observation is analysed by the two different methods to determine the population index.

The method applying the conversion function $r = f(\mathrm{lm} - m_{\mathrm{avg}})$:
we obtain $m_{\mathrm{avg}} = 3.02$ (i.e. $\mathrm{lm} - m_{\mathrm{avg}} = 2.98$). Within

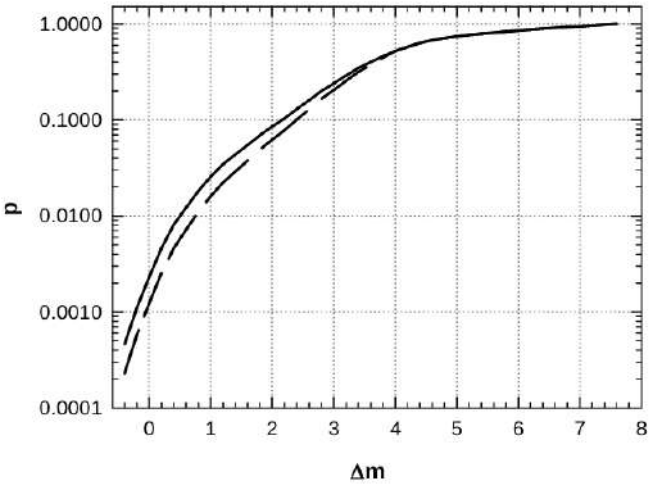


Figure 7.10: Perception probabilities $p(\Delta m)$ averaged over a field of view with a radius of 52 °5. Δm is the difference between the limiting magnitude and the meteor magnitude $\Delta m = \mathrm{lm} - m$. Solid line – for an experienced observer under dark sky; dashed line – unexperienced observer (arbitrary example).

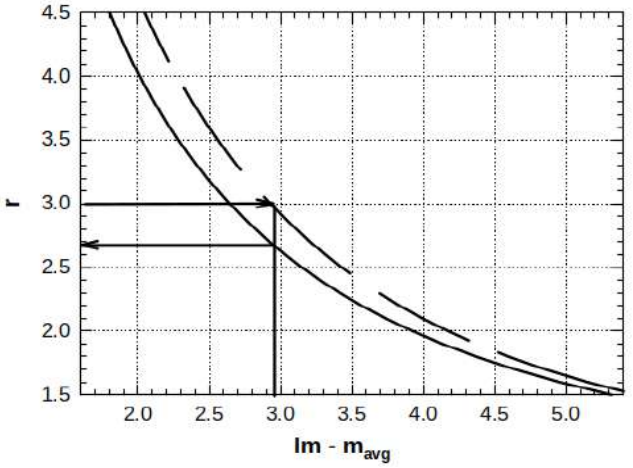


Figure 7.11: Conversion function for the population index r and the difference Δm between lm and the average magnitude of meteors seen m_{avg} – $\Delta m = \mathrm{lm} - m_{\mathrm{avg}}$. Solid line: for an experienced observer under dark sky. Dashed line: unexperienced observer (arbitrary example from Figure 7.10). Further explanations are given in the text.

graphic accuracy, this corresponds to the result from Figure 7.12. Using the standard conversion function, a value of $r = 2.65$ is determined. The difference to the true population index ($r = 3.0$) is -0.35.

Linear regression method:
true meteor numbers "N standard" and true cumulative numbers "Φ standard" were calculated using standard perception probabilities "p standard". For reasons of numerical accuracy, this simulation worked using many meteors (total of 16,630 meteors seen). Real observation samples which are available for analyses are usually smaller. In consequence, for the method with a linear regression, magnitude classes of about -1 and fainter

Table 7.7: Simulation of a meteor observation at $r = 3.0$ and $\mathrm{lm} = 6.0$. Perception probabilities "p effective" for an (arbitrarily) unexperienced observer according to Figure 7.10. The observer sees "n visible" meteors. This observation is analysed based on standard perception probabilities "p standard" (Figure 7.6). True meteor numbers "N standard" and true cumulative numbers "Φ standard" were calculated.

m	$\mathrm{lm}-m$	p effective	N true	n visible	p standard	N standard	Φ standard
−6	12	1.00000	1	1	1	1	1
−5	11	1.00000	3	3	1	3	4
−4	10	1.00000	9	9	1	9	13
−3	9.0	1.00000	27	27	1	27	40
−2	8.0	1.00000	81	81	1.00000	81	121
−1	7.0	0.94000	243	228	0.94000	243	364
0	6.0	0.85000	729	620	0.85000	729	1093
1	5.0	0.74000	2187	1618	0.74000	2187	3280
2	4.0	0.52000	6561	3412	0.52000	6561	9841
3	3.0	0.20502	19683	4035	0.24000	16814	26655
4	2.0	0.05765	59049	3404	0.08511	39996	66652
5	1.0	0.01434	177147	2540	0.02570	98818	165469
6	0.0	0.00122	531441	651	0.00230	283021	448491
total			797161	16630		448491	
m_{avg}				3.02			
$6.0-m_{\mathrm{avg}}$				2.98			

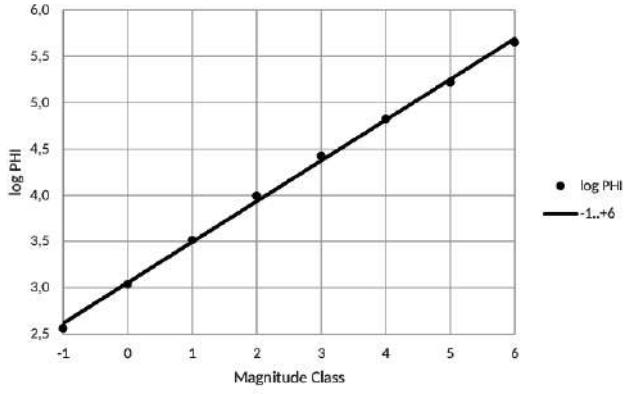


Figure 7.12: Linear regression of log "Φ standard" from Table 7.7. From the slope we obtain $r = 2.75$.

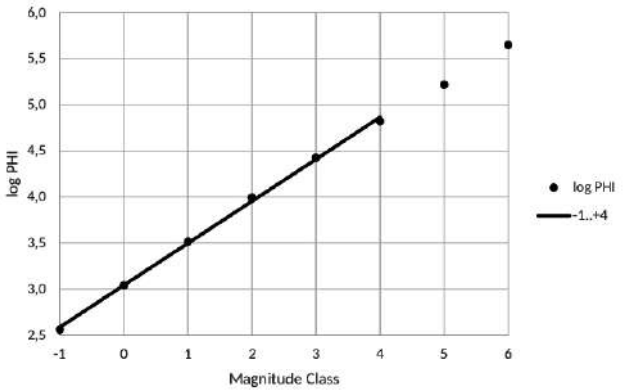


Figure 7.13: Linear regression of "$\log \Phi$ standard" from Table 7.7 excluding the two faintest magnitude classes. From the slope we obtain $r = 2.86$.

will be available. The plot of the linear regression of $\log \Phi(m)$ in the interval $-1 \leq m \leq +6$ is shown in Figure 7.12. From the slope of regression line we get $r = 2.75$. Positions of data points to the regression line indicate that there is a systematic anomaly. In most cases, an anomaly is due to perception probabilities of faint meteors.

The regression method allows us to restrict the magnitude interval such that faint meteors are excluded. Figure 7.13 shows the linear regression for the interval $-1 \leq m \leq 4$ which gives $r = 2.86$. Restricting further to the interval $-1 \leq m \leq 3$, the regression yields $r = 2.94$ (Figure 7.14) which is very close to true value of $r = 3.0$.

For real analyses, a restriction to magnitudes brighter than $\mathrm{lm} - m = 2.0$ will be practicable; a further restriction to e.g. $\mathrm{lm} - m > 3.0$ will suffer from scatter of meteor numbers which is absent in this simulation.

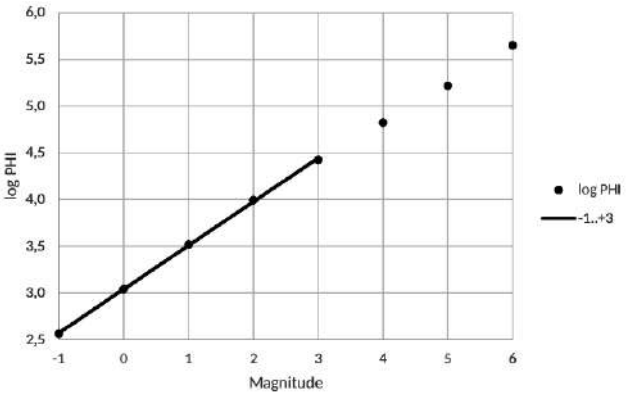


Figure 7.14: Linear regression of "$\log \Phi$ standard" from Table 7.7 excluding the three faintest magnitude classes. From the slope we now obtain $r = 2.94$.

Summary:

The true (defined) population index of our simulation was $r = 3.0$. The conversion function $r = f(\mathrm{lm} - m_{\mathrm{avg}})$ yields $r = 2.65$ for the unexperienced observer. There is no possibility to detect the bias. The plot of the regression line and the data points $\log \Phi(m)$ shows that there must be a bias. With this information we may search for possible sources of the bias. In our example, the bias was greatly reduced by excluding faint meteors from the regression. Perception probabilities of experienced observers obtained under dark skies probably present the upper limit of perception probabilities of "typical" observers (not considering unknown personal effects). Hence the method using the conversion function $r = f(\mathrm{lm} - m_{\mathrm{avg}})$ will always be biased. Averaging lots of observations cannot remove this bias since the average perception probabilities of contributing observers are expected to be below the perception probabilities of experienced observers under dark skies.

The bias of this method with the conversion function is smaller for low population indices. For this reason the method of using the conversion function $r = f(\mathrm{lm} - m_{\mathrm{avg}})$ may provide reliable results as long as the population index is below about 2.3 to 2.5 (see Figure 7.11).

7.4.3 A "real world" example

This section should not be read like a school book. We illustrate the steps of the determination of the population index and discuss upcoming problems to help you to compile your own "tool box" for the determination of the population index. For our example we analyse magnitude distributions of two observers observing at the same site during the Leonid outburst on 1999 November 18 under dark and transparent skies. Both observers had lot of experience over decades of regular visual observations and were members of the group of observers from which the perception probabilities described in the beginning of this section have been determined.

We will focus on systematic effects. For this reason we analyse just two main intervals: the outburst on 1999 November 18, 01:35–02:35 UT and a post-outburst period on 1999 November 18, 02:35–05:00 UT. Magnitude distributions and further data for both observers and for both intervals are given in Table 7.8.

For didactic reasons, we will start with the analysis of the post-outburst interval. Figure 7.15 shows a bar diagram of the magnitude distributions for both observers. There is nothing special. As the effective observing times differ only little, the numbers of bright meteors are comparable for both observers. Due to the better lm, observer B saw more faint meteors.

Applying the method with the conversion function $r = f(\mathrm{lm} - m_{\mathrm{avg}})$ we find $r = 2.03$ for observer A and $r = 2.01$ for observer B.

The linear regression plot in the magnitude interval $[-1; +6]$ is largely fine for both observers (Figure 7.16).

Table 7.8: Magnitude distributions of Leonids observed on 1999 November 18 by two observers at the same location. The radiant elevation h_R refers to the middle of the interval.

Interval [UT]	0134 – 0236	0135 – 0235	0236 – 0500	0235 – 0512
Observer	A	B	A	B
Teff [min]	61	60	134	116
lm	6.30	7.25	6.30	7.25
h_R [deg]	29	29	50	51
Magn. class	Number of meteors			
−6	0	0	1	0
−5	0	0	0	0
−4	0	0	0	1
−3	0	0	1	0.5
−2	1.5	0	7.5	8.5
−1	11	5	13.5	18
0	29	8	21	22.5
1	95	25	41	37
2	152.5	82.5	59	48
3	214.5	259	57.5	76
4	220	480.5	64	130.5
5	110.5	528	31	147.5
6	8	116	5.5	24.5
7	0	1	0	0
Tot	842	1505	302	514
m_{avg}	2.98	4.14	2.44	3.36
$\mathrm{lm} - m_{\mathrm{avg}}$	3.32	3.11	3.86	3.89
Meteors / hr	828	1505	135	266

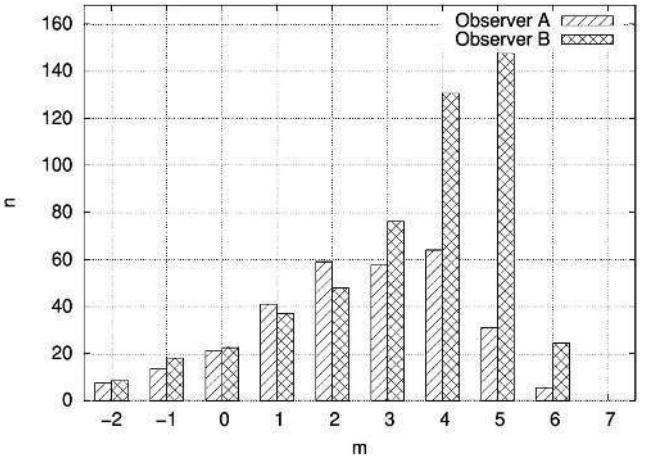


Figure 7.15: Magnitude distributions of the Leonid post-outburst interval 1999 November 18, 02:35–05:12 UT for observer A (lm = 6.30) and observer B (lm = 7.25) as listed in Table 7.8.

There is a small deviation from the linear regression line with a little lack of +3 mag meteors and a small excess of +5 mag meteors which is more prominent for observer B. The population indices obtained from the regression are:

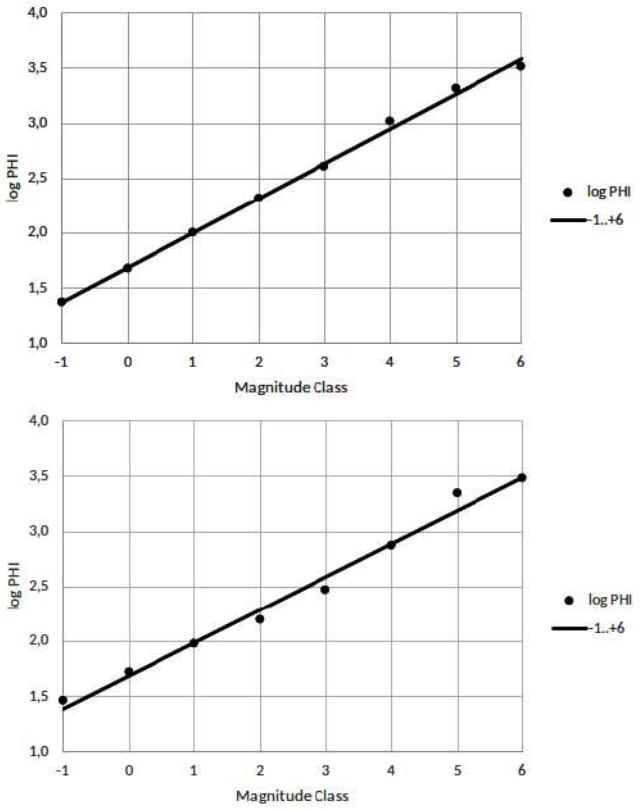


Figure 7.16: Linear regression for the magnitude distributions of the post-outburst Leonid interval 1999 November 18, 02:35–05:12 UT.
Top: observer A (lm = 6.30),
bottom: observer B (lm = 7.25).

observer A $[-1;+6]$, $r = 2.07$,
observer B $[-1;+6]$, $r = 2.00$.
If faint meteors are excluded from the analysis, we find:
observer A $[-1;+4]$, $r = 2.11$,
observer B $[-1;+5]$, $r = 2.00$.

For the post-maximum interval both methods provide $r = 2.0 \ldots 2.1$ for both observers. We can consider this result to be almost free of bias.

Figure 7.17 shows magnitude distributions for the outburst interval. As the effective observing time is almost identical for both observers, observing at the same site, the number of bright meteors ($m \leq +2$) should be comparable, but there are differences. If we add 1 mag to the magnitudes of observer A or if we subtract 1 mag from the magnitudes of observer B, the numbers become comparable. For one or for both observers there seems to be some systematic shift in magnitude estimates of bright meteors. Magnitude estimates especially for bright meteors require comparison of the meteor with stars. During the outburst with (on average) 25 meteors per minute for observer B and 14 meteors per minute for observer A, this comparison could have been done less carefully. Magnitude estimates of fainter meteors should be more accurate under these circumstances as visual impression without comparison to stars gives more accurate magnitude estimates than for bright meteors.

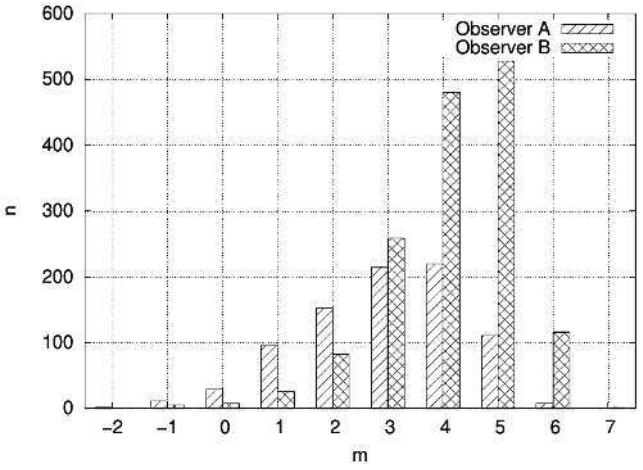


Figure 7.17: Magnitude distributions during the Leonid outburst period on 1999 November 18, 01:35-02:35 UT for observer A (lm = 6.30) and observer B (lm = 7.25), listed in Table 7.8.

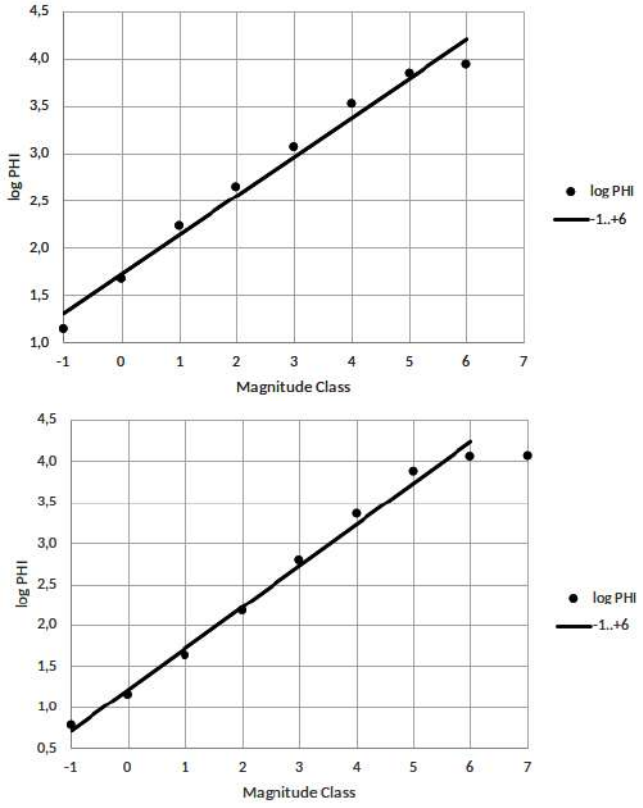


Figure 7.18: Linear regression for the magnitude distributions of the outburst Leonid interval on 1999 November 18, 01:35–02:35 UT.
Top: observer A (lm = 6.30),
bottom: observer B (lm = 7.25).

The method using the conversion function $r = f(\mathrm{lm} - m_{\mathrm{avg}})$ yields $r = 2.37$ for observer A and $r = 2.53$ for observer B.

The linear regression plot in the magnitude interval $[-1;+6]$ shows a drop of the slope for magnitudes $+5 \ldots +7$ (Figure 7.18). The population index we derive

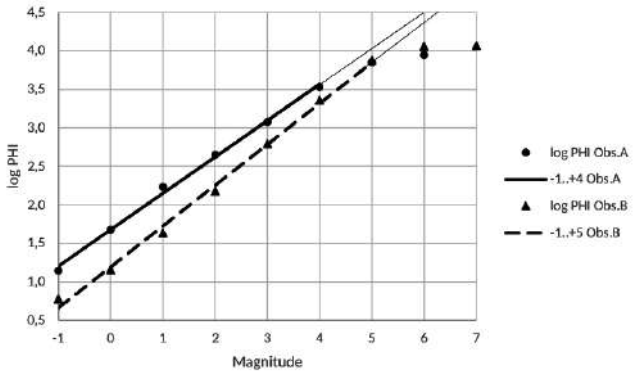


Figure 7.19: Linear regression for the magnitude distributions of the outburst Leonid interval on 1999 November 18, 01:35–02:35 UT, omitting the faint magnitude classes. Observer A (lm = 6.30), observer B (lm = 7.25).

from the regression is:
magnitude interval $[-1; +6]$:
observer A $r = 2.60$,
observer B $r = 3.19$.

If faint meteors are excluded, we find (Figure 7.19):
observer A, $[-1; +4]$, $r = 2.97$
observer B, $[-1; +5]$, $r = 3.39$
Let us analyse the information of Figure 7.19 in more detail:
observing at the same site for same effective observing time, the true cumulative numbers $\Phi(m)$ should be identical. For bright meteors there is large difference: for observer A $\Phi(0\,\mathrm{mag})$ is about 3 times larger than for observer B, which cannot be caused by different perception probabilities. As already discussed in the beginning, there must have been some bias in estimation of magnitude of bright meteors. If data points of observer A for magnitudes $-1 \ldots +2$ are horizontally shifted by 1 mag to the right, they correspond to results of observer B. Vice versa if data points of observer B for magnitudes $0 \ldots +3$ are horizontally shifted by 1 mag to the left, they correspond to results of observer A. The difference decreases for fainter meteors and, most interesting, for magnitudes +5 and +6 true cumulative numbers are almost identical for both observers.

As it cannot be decided which observer was affected by a bias of magnitude estimation of bright meteors, we assume the average regression line to be the best estimate and obtain $r = 3.18$.

Note: bias of magnitude estimates affects the result of the determination of the population index for both methods. When analysing results of many observers, this is a random error which can be eliminated by averaging.

Next we discuss the true cumulative number at magnitude +6. Numbers of both observers differ by about 20% only. Considering that magnitude class +6 is very close to limiting magnitude of observer A, this is quite good match. The average number $\Phi(+6)$ of both observers just amounts to some 35% of the number to be expected from the average regression line. There is a clear lack of meteors of magnitude class +6. Let us consider the possibility that this virtual lack of +6 meteors is caused by the reduction of perception probabilities during the Leonid outburst. Observer B (lm = 7.25) noted during the observation that there was a virtual lack of faint meteors. At a visible rate of 1500 meteors per hour, a few 60 second counts yielded to some 40 meteors at maximum.

Observer B: “Saturation occurred just during 3 or 4 short moments when some 10 meteors appeared within two seconds. These meteors have not been recorded. During 99% of the observing time, there was enough capacity to watch for fainter meteors. But only very few actually appeared.” At lm = 7.25, meteors of +6 can be detected reliably. Perhaps there was some minor reduction of perception probability due to high rate but this cannot explain the major lack of magnitude +6 meteors. With very high probability there was a lack of faint meteors during outburst. $\Phi(+5)$ amounts to some 80% of what was to be expected for $r = 3.18$, $\Phi(+6)$ to some 35%,and $\Phi(+7)$ to some 15%. The result for $\Phi(+7)$ is rather uncertain (close to lm = 7.25, one observer only). This means that the population of Leonid outburst differed from an exponential magnitude distribution for magnitudes of about +5 to fainter magnitudes. With this finding, it becomes impossible to determine a population index from the conversion function $r = f(\mathrm{lm} - m_{\mathrm{avg}})$ as this function bases on an exponential magnitude distribution. An average $r = 2.45$ determined by the conversion function is far away from $r = 3.18$ determined by the regression method for magnitudes brighter than +5.

Furthermore it becomes impossible to determine ZHR using correction factor for limiting magnitude described in Section 7.3.4. as this bases on an exponential magnitude distribution.

For illustration we find using data given in Table 7.8:
outburst interval: $r = 3.18$, observer A ZHR = 2153, observer B ZHR = 1303
post outburst interval: $r = 2.05$, observer A ZHR = 204, observer B ZHR = 200
For the post outburst interval – when the magnitude distribution was exponential – there is practically no difference between the ZHR of both observers. As soon as the magnitude distribution is not exponential, the correction factor for the limiting magnitude does not work properly resulting in very large bias of the ZHR if the limiting magnitude differs from +6.5 mag. Note that $\Phi(+6)$ is the true number of meteors brighter +6.5 in an observing field of $52\overset{\circ}{.}5$ radius. There is a good agreement of the values $\Phi(+6)$ of both observers for the outburst period (nearly identical effective observing time).

The ZHR is no appropriate measure for meteor activity in case of a non-exponential magnitude distribution. In Section 7.6.2 (page 160) this will be discussed in more detail. Analysis of magnitude distributions by the method of a linear regression is the only way to show whether the magnitude distribution is exponential or not, or, in other words: if the population index

r is constant within the magnitude range covered by observing method.

If the magnitude distribution is exponential, there is a method to compute the population index based on meteor counts done at different lm:
From

$$\mathrm{ZHR}_1 = \mathrm{ZHR}_2$$

$$\frac{n_1 \times r^{(6.5-\mathrm{lm}_1)} \times \mathrm{zm}_1}{T_{\mathrm{eff}1}} = \frac{n_2 \times r^{(6.5-\mathrm{lm}_2)} \times \mathrm{zm}_2}{T_{\mathrm{eff}2}}$$

we find

$$r = \exp\left(\frac{\ln\left[(n_1 * \mathrm{zm}_1/T_{\mathrm{eff}_1})/(n_2 * \mathrm{zm}_2/T_{\mathrm{eff}2})\right]}{(\mathrm{lm}_1 - \mathrm{lm}_2)}\right)$$

n – meteor numbers
zm – zenith correction factors
Teff – effective observing times

For the data of Table 7.8 we find from meteor counts at different limiting magnitude lm:
outburst interval: $r = 1.84$
post outburst interval: $r = 2.01$
The result of the post outburst interval corresponds perfectly to results of both other methods, while result of the outburst interval is completely off.

7.4.4 Conclusions for population index calculation

Detailed analysis of the magnitude distribution should be the first step of analysing data of a meteor shower.

The method with a linear regression is the only way to show:

- whether a magnitude distribution is exponential or not, or, in other words, whether the population index r is constant within the magnitude range covered by the observing method, and
- whether there is any bias, such as lower perception for faint meteors, caused by unexperienced observers.

Do not focus on good time resolution at this step, choose intervals long enough to include many observations to reduce scatter. Only if an exponential magnitude distribution has been proven by the regression method, you can think about using the method with the conversion function $r = f(\mathrm{lm} - m_{\mathrm{avg}})$.

The method applying the conversion function enables a higher temporal resolution (shorter intervals) as with small meteor numbers scatter of regression method becomes large. If the population index is small (below about $r = 2.3$), the bias of the conversion function method due to lower perception for faint meteors is reasonably small. In other cases or if you want to get very accurate results, both methods can be combined. First both methods are simultaneously applied to longer (identical) intervals with sufficient data to apply the regression method. There may be an offset between the more accurate regression method excluding the faintest meteors from the analysis and the conversion function method. In the next step, shorter intervals are analysed, using the conversion function method. The offset determined before is applied to results of the conversion function. This way you can obtain an accurate r-profile with high temporal resolution.

Until now visual observing is the only method providing numerous and reliable magnitude data for detailed analysis of the population index r. This should be strong motivation to continue visual observing with careful magnitude estimates.

7.5 Accuracy of the ZHR

7.5.1 General remarks

In analyses of meteor shower activity, an average ZHR – shown as a data point – is determined from a number of individual ZHRs. The average ZHR is affected by noise and by bias.

Noise results from:

1. randomness of meteors
2. different perception probabilities of observers

Noise can be reduced by averaging many observations in global analyses. From the standard deviation σ of the average ZHR the width of the 68.1% confidence interval can be estimated. The 68.1% confidence interval means that "with a probability of 68.1% the true ZHR, $\mathrm{ZHR}_{\mathrm{true}}$, is within the interval $\mathrm{ZHR}_{\mathrm{avg}} \pm d\,\mathrm{ZHR}_{\mathrm{noise}}$" with $d\mathrm{ZHR}_{\mathrm{noise}} = \sigma/\sqrt{(n)}$;
σ – standard deviation of the average ZHR, and
n – number of individual ZHRs used for computation of the average ZHR.

Bias results from:

1. an error due to zenith correction factor,
2. an error due to limiting magnitude correction factor.

Bias acts into a specific direction. If, for instance, the true zenith exponent is $\gamma = 1.3$ while ZHR was computed with $\gamma = 1.0$, the average of ZHR from global analysis will be systematically too small (negative bias). Bias cannot be eliminated by averaging many observations in a global analysis.

For any average ZHR, the total error $d\mathrm{ZHR}_{\mathrm{tot}}$ (again, 68.1% confidence interval) considering noise and bias should be given in the form

$$d\mathrm{ZHR}_{\mathrm{tot}} = \sqrt{(d\mathrm{ZHR}^2_{\mathrm{noise}} + d\mathrm{ZHR}^2_{\mathrm{biasZC}} + d\mathrm{ZHR}^2_{\mathrm{biaslmC}})}$$

where the indices biasZC and biaslmC refer to the bias caused by zenith correction factor and limiting magnitude correction factor, respectively.

While $d\mathrm{ZHR}_{\mathrm{noise}}$ can be easily determined, biases due to correction factors for radiant elevation and limiting

magnitude need to be estimated based on the average radiant elevation (for the included ZHRs) and the average limiting magnitude.

7.5.2 Bias due to the zenith correction factor

In Section 7.3.3, the zenith exponent $\gamma = 1.0$ is suggested for the determination of the ZHR from visual observations. Some authors find $\gamma = 1.2 - 1.5$ while for video meteors $\gamma = 1.75$ has been determined (Molau, 2012).

To estimate the bias due to the zenith correction factor $d\mathrm{ZHR}_{\mathrm{biasZC}}$ we need to estimate how much zenith exponent used for our analysis ($\gamma_{\mathrm{an}} = 1.0$) may differ from the true zenith exponent referring to the 68.1% confidence interval. With this estimate and the average radiant elevation $h_{R,\mathrm{av}}$ of the included intervals we find:

$$\frac{d\mathrm{ZHR}_{\mathrm{biasZC}}}{\mathrm{ZHR}_{\mathrm{av}}} = \frac{\sin^{\gamma_{\mathrm{min,max}}}(h_{R,\mathrm{av}})}{\sin^{\gamma_{\mathrm{an}}}(h_{R,\mathrm{av}})} - 1$$

Table 7.9 shows the relative bias of the average ZHR depending on the average radiant elevation $h_{R,\mathrm{av}}$ and the estimate of the maximum true zenith exponent γ_{max} if the ZHR computation was done with $\gamma = 1.0$.

If, for instance, $\gamma_{\mathrm{max}} = 1.2$ is considered to be a reasonable estimate for the upper limit of the zenith exponent, we find 9% bias of the ZHR due to the zenith correction factor for $h_R = 40°$.

In Section 7.3.3 there is a discussion about the compensation of effects at low radiant elevation

- longer paths of meteors increase the visual perception probability
- fainter maximum magnitude of meteors reduce their visual perception probability

which should result in a zenith exponent for visual observations of about $\gamma = 1.0$. For individual showers (composition of meteoroids, atmospheric entry velocity) this compensation effect may be less strong or stronger. Consequently, the true zenith exponents are expected to differ from $\gamma = 1.0$. For the determination of the bias due to the zenith correction, an estimation of the 68.1% confidence interval of the zenith exponent with $\gamma_{\mathrm{an}} \pm 0.2$ seems to be reasonable. With this we find

$$d\mathrm{ZHR}_{\mathrm{biasZC}} = \mathrm{ZHR}_{\mathrm{avg}} \times (\sin^{-0.2}(h_{R,\mathrm{av}}) - 1).$$

The effect on the ZHR due to this bias is shown in Figure 7.20.

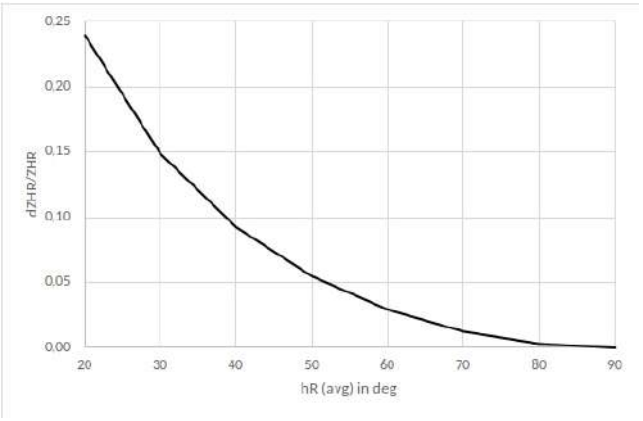


Figure 7.20: Half width of the 68.1% confidence interval given in fractions of the average ZHR, $d\mathrm{ZHR}_{\mathrm{biasZC}}/\mathrm{ZHR}_{\mathrm{av}}$, versus the average radiant elevation. The 68.1% confidence interval of the zenith exponent is estimated to be $\gamma_{\mathrm{an}} \pm 0.2$.

7.5.3 Bias of the limiting magnitude correction factor

As shown in Section 7.4.3, the correction factor for the limiting magnitude can be determined only if the population index is constant for the range of visual magnitudes. Otherwise the ZHR must not be computed from data with the limiting magnitude differing from +6.5 mag. In this case, flux densities are to be calculated according to the procedure described in Section 7.6.2.4. The considerations below presume a constant population index for the range of visual magnitudes.

Note: the correction factor for the limiting magnitude (Section 7.3.4, equation 7.30) bases on the assumption that the meteor limiting magnitude in the centre and at the border of the field of view changes exactly like the stellar limiting magnitude in the field centre.

If the limiting magnitude changes due to light pollution or moonlight (scattered light), this assumption is no longer true. This results in a bias of the limiting magnitude correction factor.

Using statistical methods, Richter (2021) analysed global Perseid data with limiting magnitudes between 4.0 mag and 7.0 mag (average 5.9 mag). The best fit was obtained applying a population index $r = 1.4$ used in Equation 7.30 for the correction factor of the limiting magnitude. The true population index for Perseids is about $r = 2.2$. The problems discussed above resulted in huge difference between true population index and the population index determined by the best fit in Equation 7.30.

For an average limiting magnitude of $lm = 5.9$, the correction factor according to Equation 7.30 amounts to 1.60 for $r = 2.2$ and 1.22 for $r = 1.4$. The correction factor determined by the statistical method is considered to be more accurate than the one based on the true population index and Equation 7.30. In this example with an average $lm = 5.9$, the application of the true population index in Equation 7.30 resulted in too high ZHR. The bias is +31%! This topic requires more detailed analyses, but this example alone shows the order of the ZHR bias to be expected from an inaccurate correction factor for the limiting magnitude. Table 7.10 demonstrates the bias depending on the limiting magnitude.

Table 7.9: Zenith correction factors z for different zenith exponents γ. Half widths of the 68.1% confidence intervals given in fractions of the average ZHR, $d\mathrm{ZHR}_{\mathrm{biasZC}}/\mathrm{ZHR}_{\mathrm{av}}$ depending on the average radiant elevation $h_{R,\mathrm{av}}$ and estimate of the maximum true zenith exponent $\gamma_{\max}$ if the ZHR computation was done with $\gamma_{\mathrm{an}} = 1.0$.

h_R	$\gamma = 1.0$	$\gamma_{\max} = 1.1$		$\gamma_{\max} = 1.2$		$\gamma_{\max} = 1.3$		$\gamma_{\max} = 1.4$		$\gamma_{\max} = 1.5$	
[°]	z	z	$\frac{\mathrm{dZHR}}{\mathrm{ZHR}}$	z	$\frac{\mathrm{dZHR}}{\mathrm{ZHR}}$	z	$\frac{\mathrm{dZHR}}{\mathrm{ZHR}}$	z	$\frac{\mathrm{dZHR}}{\mathrm{ZHR}}$	z	$\frac{\mathrm{dZHR}}{\mathrm{ZHR}}$
15	3.86	4.42	0.14	5.06	0.31	5.80	0.50	6.64	0.72	7.60	0.97
20	2.92	3.26	0.11	3.62	0.24	4.03	0.38	4.49	0.54	5.00	0.71
25	2.37	2.58	0.09	2.81	0.19	3.06	0.29	3.34	0.41	3.64	0.54
30	2.00	2.14	0.07	2.30	0.15	2.46	0.23	2.64	0.32	2.83	0.41
35	1.74	1.84	0.06	1.95	0.12	2.06	0.18	2.18	0.25	2.30	0.32
40	1.56	1.63	0.05	1.70	0.09	1.78	0.14	1.86	0.19	1.94	0.25
50	1.31	1.34	0.03	1.38	0.05	1.41	0.08	1.45	0.11	1.49	0.14
60	1.15	1.17	0.01	1.19	0.03	1.21	0.04	1.22	0.06	1.24	0.07
70	1.06	1.07	0.01	1.08	0.01	1.08	0.02	1.09	0.03	1.10	0.03
80	1.02	1.02	0.00	1.02	0.00	1.02	0.00	1.02	0.01	1.02	0.01
90	1.00	1.00	0.00	1.00	0.00	1.00	0.00	1.00	0.00	1.00	0.00

Table 7.10: Limiting magnitude correction factors c for different population indices r(best fit) determined from the best fit of Equation 7.30 (a detailed explanation is given in the text) for different limiting magnitudes lm. Relative errors dZHR/ZHR of the ZHR if the true population index $r_{\mathrm{true}} = 2.2$ (top) and $r_{\mathrm{true}} = 3.2$ (bottom) was used in Equation 7.30 instead of r(best fit).

$r_{\mathrm{true}} = 2.2$

	lm = 5.0		lm = 5.5		lm = 6.0	
r_{bestfit}	c	$\frac{\mathrm{dZHR}}{\mathrm{ZHR}}$	c	$\frac{\mathrm{dZHR}}{\mathrm{ZHR}}$	c	$\frac{\mathrm{dZHR}}{\mathrm{ZHR}}$
2.2	3.26	0.00	2.20	0.00	1.48	0.00
2.0	2.83	0.15	2.00	0.10	1.41	**0.05**
1.8	2.41	0.35	1.80	**0.22**	1.34	0.11
1.6	2.02	**0.61**	1.60	0.38	1.26	0.17
1.4	1.66	0.97	1.40	0.57	1.18	0.25

$r_{\mathrm{true}} = 3.2$

	lm = 5.0		lm = 5.5		lm = 6.0	
r_{bestfit}	c	$\frac{\mathrm{dZHR}}{\mathrm{ZHR}}$	c	$\frac{\mathrm{dZHR}}{\mathrm{ZHR}}$	c	$\frac{\mathrm{dZHR}}{\mathrm{ZHR}}$
3.2	5.72	0.00	3.20	0.00	1.79	0.00
3.0	5.20	0.10	3.00	0.07	1.73	**0.03**
2.8	4.69	0.22	2.80	**0.14**	1.67	0.07
2.6	4.19	**0.37**	2.60	0.23	1.61	0.11
2.4	3.72	0.54	2.40	0.33	1.55	0.15

The bias strongly increases towards poor limiting magnitudes. This effect by poor limiting magnitudes due to bright sky background is double:

1. the average limiting magnitude will be worse and increases the bias (columns from right to left in Table 7.10).

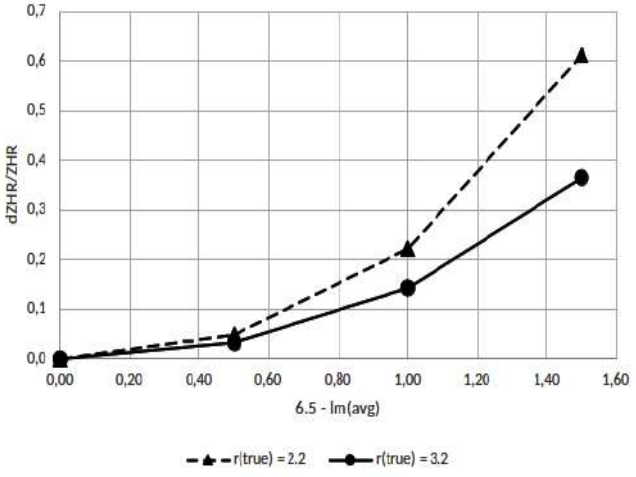


Figure 7.21: Half width of the 68.1% confidence interval given in fractions of average ZHR $d\mathrm{ZHR}_{\mathrm{biaslmC}}/\mathrm{ZHR}_{\mathrm{av}}$ versus the average limiting magnitude based on the values marked bold in Table 7.10.

2. the difference between the true population index r(true) and the population index determined from the best fit of Equation 7.30 will be larger because the assumption that the limiting magnitude for meteors in the centre and at the border of the field of view changes exactly like the limiting magnitude for stars in the centre of the field will be fulfilled worse with brightening sky. This increases the bias again (lines from top to bottom in Table 7.10).

For the estimation of the 68.1% confidence interval of the limiting magnitude correction factor, it seems reasonable to take into account this double effect by using the relative ZHR errors marked in bold in Table 7.10. Figure 7.21 shows relative ZHR errors dZHR/ZHRavg versus the limiting magnitude based on the marked values in Table 7.10.

For a computer code the following approximation is to be used:

```
  dZHRbiaslmC = ZHRav * exp( a + b*r + c *
exp(lmav-6.5))
```

with

```
r   true population index
lmav   average limiting magnitude
a= 2.1252476
b= -0.50632575
c= -6.7506121
```

7.5.4 Conclusions

For any average ZHR, the 68.1% confidence interval should be given:

$$\mathbf{ZHR_{avg} \pm dZHR_{tot}}$$

$$d\mathrm{ZHR}_{\mathrm{tot}} = \sqrt{(d\mathrm{ZHR}^2_{\mathrm{noise}} + d\mathrm{ZHR}^2_{\mathrm{biasZC}} + d\mathrm{ZHR}^2_{\mathrm{biaslmC}})}$$

with

$$\boldsymbol{dZHR_{noise} = \sigma/\sqrt{(n)}}$$

σ – standard deviation of the average ZHR

n – number of individual ZHR used for the computation of the average ZHR

$$\boldsymbol{dZHR_{biasZC} = ZHR_{av} \times (\sin^{-0.2}(h_{R,av}) - 1)}$$

$h_{R\mathrm{av}}$ – average radiant elevation

$$\boldsymbol{dZHR_{biaslmC} =}$$

$$\mathbf{ZHR_{av} \times \exp\left(a + b * r + c \times \exp\left(lm_{av} - 6.5\right)\right)}$$

r – true population index

lm_{av} – average limiting magnitude

$a = 2.1252476$

$b = -0.50632575$

$c = -6.7506121$

Table 7.11: Half widths of 68.1% confidence intervals of the average ZHR, $d\mathrm{ZHR}_{\mathrm{tot}}$, for different sets of observation data. $d\mathrm{ZHR}_{\mathrm{noise}}$ was arbitrarily choosen. Further explanations in the text.

$r = 2.2$ $\mathrm{ZHR}_{\mathrm{av}} = 100$	Example 1	Example 2	Example 3
$d\mathrm{ZHR}_{\mathrm{noise}}$	3.0	5.0	8.0
$h_{R,\mathrm{av}}$ [°]	35	40	45
lm_{av} [mag]	5.50	5.80	6.00
$d\mathrm{ZHR}_{\mathrm{biasZC}}$	11.8	9.2	7.2
$d\mathrm{ZHR}_{\mathrm{biaslmC}}$	23.0	9.6	4.6
$d\mathrm{ZHR}_{\mathrm{tot}}$	26.0	14.3	11.7

Often the 68.1% confidence interval of the average ZHR based on the noise only, $d\mathrm{ZHR}_{\mathrm{noise}}$, is given. For maximum periods of major showers, this interval often is just ± 3 to 5% of the $\mathrm{ZHR}_{\mathrm{av}}$. If we add reasonable estimates of the bias from Sections 7.5.2 and 7.5.3, the 68.1% confidence interval becomes much broader. Table 7.11 shows three examples for arbitrary chosen 68.1% confidence intervals based on noise only, $d\mathrm{ZHR}_{\mathrm{noise}}$. In example 1, all observations are included in the analysis. Due to the large number of observations we get a small $d\mathrm{ZHR}_{\mathrm{noise}}$. In examples 2 and 3, the observations with poor limiting magnitude or low radiant elevation have been excluded from the analysis. Average limiting magnitude and radiant elevation increase compared to example 1, but also $d\mathrm{ZHR}_{\mathrm{noise}}$ increases due to the smaller number of observations. The total width of 68.1% confidence interval $d\mathrm{ZHR}_{\mathrm{tot}}$ decreases from example 1 towards example 3 as the components of the bias are reduced by better circumstances $(lm_{\mathrm{av}}, h_{R,\mathrm{av}})$.

Note: in analyses of shower activity, limits for lm and h_R should be chosen in an iterative procedure. The combination of limits for lm and h_R yielding the smallest width of the 68.1% confidence interval is to be considered the best trade-off between low noise and low bias.

7.6 Flux density and spatial number density from visual observations

7.6.1 Introduction

The standardisation of meteor observations (not only in the visual branch) allows globally-obtained results for annual shower returns (e.g. Velkovic et al., 2019, for the Perseids 2018; Rendtel, 2020, for the Geminids 2018) as well as combination of data from several years (e.g. Rendtel, 2005, for the Geminids; Rendtel, 2008, for the Orionids; Egal et al., 2020, for the Eta Aquariids and Orionids).

As a kind of standard, we determine the ZHR in combination with the population index r. In order to have a large sample and to obtain "around the clock" profiles of the ZHR and the population index, the International Meteor Organization needs a lot of results from around the globe. We can never have too many data. These "around the clock" ZHR and population index profiles are the basis for the computation of a profile of the meteoroid stream's spatial number density (i.e. the number of particles per volume unit) or flux density (i.e. the number of particles crossing a certain normal area of the atmosphere per unit of time). The spatial number density usually is given as "meteoroids per billion km^3", the flux density unit is "meteoroids per million km^2 per hour". It is necessary to use the appropriate terms when discussing meteor-related items and add the mass or magnitude ranges for which the given numbers are valid.

Each analysis of a meteoroid stream is carried out at different steps.

- First, we observe a certain rate from a given meteor shower, depending on a number of influences. We can calibrate this rate to standard conditions, and call it the ZHR. This allows us to combine results obtained under different observing circumstances and to describe the appearance of a given shower during a return or over long periods.

- Next, we may calculate a flux or spatial number density of meteoroids causing meteors brighter than +6.5 absolute magnitude for each of the meteoroid streams, thus getting information about the actual meteoroid stream causing the meteor event we observed.

- By reducing the data of different streams to the same scale and mass range of meteoroids, we get a number density profile for the meteoroid streams, and can compare them, or draw conclusions about processes related to the creation and evolution of the streams.

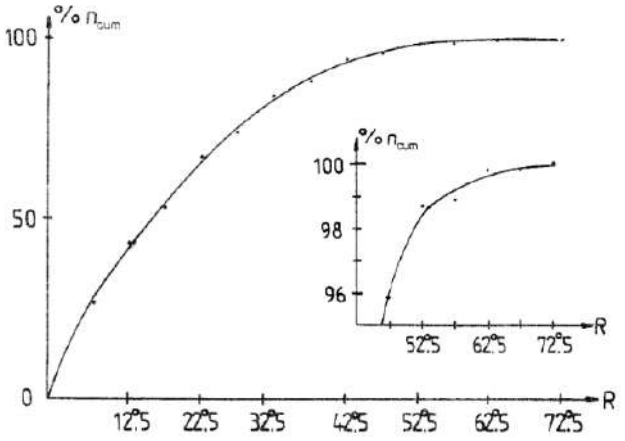


Figure 7.22: Cumulative numbers of meteors versus distance to the centre of the field of view R for a group of experienced visual observers under dark sky. 98.7% of all meteors were recorded within distance of maximum 52 °5 from the centre of the field of view.

7.6.2 Determination of the flux density and the spatial number density of meteoroids causing meteors brighter than +6.5mag absolute magnitude

The procedure summarised here was published in Koschack & Rendtel (1990a, 1990b). For more details please refer to the original publications. Here we add some examples to demonstrate the meaningfulness and effect of some parameters.

7.6.2.1 The observed field

In order to calculate the flux density from the visual ZHR, it is necessary to know the area surveyed by an observer at the meteor level. For a large sample of meteors, the distance to the centre of field of view was recorded. The field of view was divided into radial distance classes R of 5° width. (The distance class $R = 5°$ includes meteors seen at distances 0° – 7 °5. The other distance classes cover 5° rings, i.e. $R = 30°$ includes meteors detected between 27 °5 and 32 °5.) Figure 7.22 shows the cumulative numbers of meteors seen in the distance classes. About 98.7% of all meteors were recorded within 52 °5 distance from centre of the field of view. The remaining 1.3% were spread between distances of 52 °5 and 72 °5. With this result, the effective radius of the field of view was defined to be 52 °5.

Figure 7.23 shows the projections of the field with $R = 52\,°5$ onto the meteor level (height $H = 100$km) for fields centred at the zenith ($h_f = 90°$) and at $h_f = 50°$, respectively. The field centred at $h_f = 50°$ covers a larger area at the meteor level, but its major part is located close to the horizon with a large distance to the observer. Meteors at large distances appear fainter. As an example, a meteor passing near the zenith of one observer (100km distance) appears to a second observer at another place in about 10° elevation (500km distance). At the second location, this meteor appears 3.5 mag

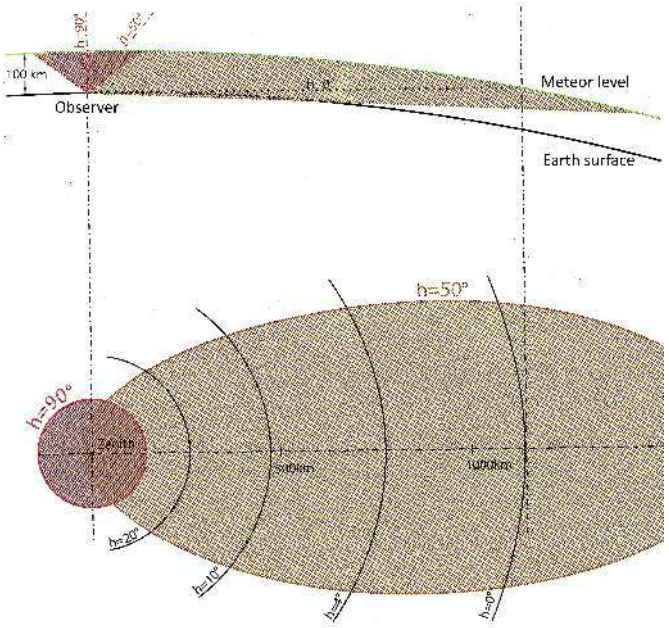


Figure 7.23: Projection of a zenith centred field of view ($h_f = 90°$) and a field of view centred at $h_f = 50°$ onto the meteor level ($H = 100$km) at the right scale.

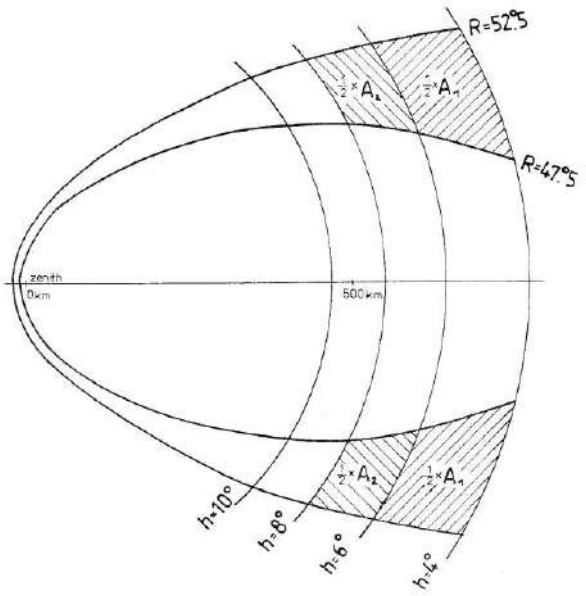


Figure 7.24: Principle of the determination of the standard areas for each distance class. As an example, the outer parts of a field at $h_f = 50°$ are shown (hatched areas).

fainter than for at the first observer's site with the trajectory near the zenith.

In order to derive the particle flux through an area, it is necessary to refer to a standard area $A_{\rm red}$ (distance to the observer 100km, no atmospheric extinction ε). The areas A_i are calculated for small elevation zones centred at h_i and summarized:

$$A_{\rm red} = \sum_i A_i r^{5 \log \frac{100\text{km}}{d} - \varepsilon_i} \qquad (7.68)$$

The procedure is visualised in Figure 7.24. The total area $A_{\rm red}$ is calculated. For the determination of the probabilities of perception it is necessary to know the portion of the total area $A_{\rm red}$ for each distance class of 5° width.

The situation was analysed for the range of $r = 1.5 - 4.5$, $h_f = 40° - 90°$, and $H = 90 - 110$ km. It was found that the effect of H is negligible. Figure 7.25 shows the standard area $A_{\rm red}$ versus the population index r for different elevations of the field centre. For high values of the population index, $A_{\rm red}$ is largest for a zenith centred field, while for a small population index the reduced field $A_{\rm red}$ is largest for $h_f = 50°$. For the "usual" range of the population index $r = 2.2 - 3.5$, $A_{\rm red}$ depends only very little on h_f. For this reason, further considerations are based on $h_f = 50°$. Numerical values can be seen from Table 7.12. For a computer code, the following numerical approximation is to be used:

$$A_{\rm red} = 37200\text{km}^2 \times (r - 1.3)^{-0.748} \qquad (7.69)$$

where $A_{\rm red}$ is in km^2.

Note the strong dependence of $A_{\rm red}$ on the population index. For the determination of the flux, an accurate population index is required.

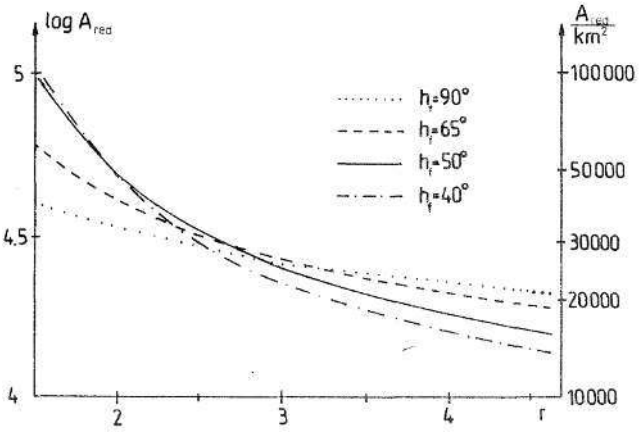


Figure 7.25: Dependence of standard area $A_{\rm red}$ for a visual observer on the population index r for different elevations of the centre of the field of view h_f.

Table 7.12: Standard area $A_{\rm red}$ of a visual observer for different values of the population index r.

r	$A_{\rm red}$ [km^2]	r	$A_{\rm red}$ [km^2]
1.8	62120	2.8	27330
1.9	54750	2.9	26050
2.0	48940	3.0	24920
2.1	44260	3.1	23910
2.2	40450	3.2	23000
2.3	37290	3.3	22190
2.4	34630	3.4	21450
2.5	32390	3.5	20770
2.6	30460		
2.7	28790		

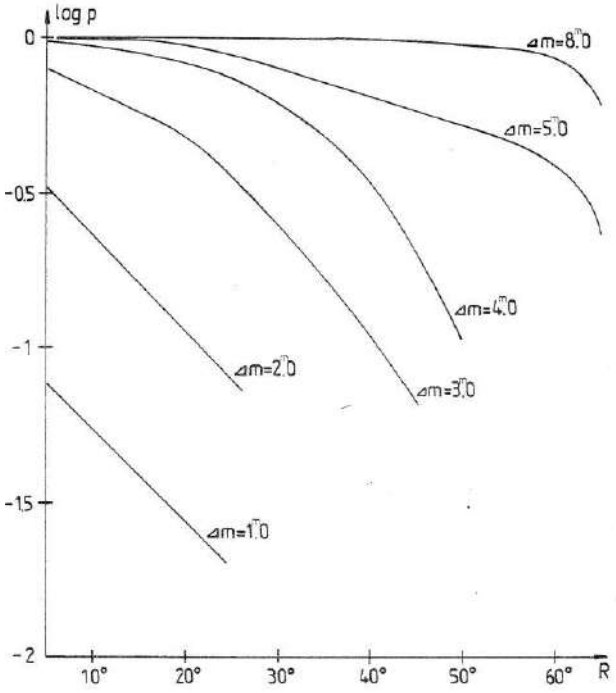


Figure 7.26: Perception probabilities p for a group of experienced observers under dark sky determined by modified double count observations. Variables are the distance to the centre of field of view R (in degrees) and difference of meteor magnitude to stellar limiting magnitude $\Delta m = \mathrm{lm} - m$.

7.6.2.2 Probabilities of perception for visual observers

Probabilities of perception have been determined for a group of experienced observers under dark sky, applying a modified double count method versus distance to centre of the field of view and versus magnitude (written as difference to star limiting magnitude). Figure 7.26 gives an overview of the results.

Average perception probabilities for a field of view of $R = 52\overset{\circ}{.}5$ radius were computed, using fractions of the standard area of each distance class A_{red}, R of total standard area A_{red}.

$$p(\Delta m) = \sum_{R=5^\circ}^{50^\circ} p(\Delta m, R) \frac{A_{\mathrm{red,R}}}{A_{\mathrm{red}}} \qquad (7.70)$$

The fractions $(A_{\mathrm{red,R}})/(A_{\mathrm{red}})$ depend only little on the population index r and the elevation of the centre of the field of view and were calculated for average conditions $h_f = 50°$, $r = 2.7$ (Figure 7.27).

Perception probabilities for faint meteors ($\Delta m < 2$) determined from double count observations are biased (too large). For this reason, they were determined from magnitude distributions of the sporadic meteors. First, the population index r was calculated for each observer per night, applying the method described in Section 7.4 for the magnitude interval $\Delta m > 2$ using perception probabilities determined by the procedure described above.

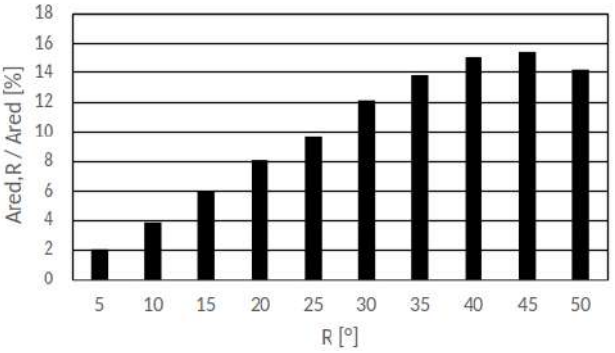


Figure 7.27: Fractions of the standard area of each distance class A_{red}/R of the total standard area A_{red} of the field of $R = 52\overset{\circ}{.}5$ radius.

For the magnitudes $\Delta m > 2$ we get a linear equation ([3])

$$\log \Phi(m) = a \times m + b$$

with $r = 10^a$.
From this we find the true number of meteors φ in the magnitude class m:

$$\log \varphi(m) = a \times m + b + \log(1 - 10 - a)$$

.

Since the population index of sporadic meteors can be considered to be constant over the visual magnitude range, the regression line may be extrapolated towards fainter magnitude classes $\Delta m < 2$. The probability of perception $p(m)$ is computed from the observed number n of meteors of magnitude class $m, n(m)$ and the true number $\varphi(m)$:

$$p(m) = \frac{n(m)}{\varphi(m)}$$

.

Both sets of perception probabilities (for bright meteors determined by the modified double count and for faint meteors determined from magnitude distribution of sporadic meteors) fit well in the transition range around $\Delta m = 2$.

The final result is shown in Figure 7.28. Note that the magnitude class +6 contains meteors $+6.5 > m > 5.5$, i.e. at $\mathrm{lm} = 5.8$ a few meteors of +6 ($\Delta m = -0.2$) can be seen.

For a numerical approximation the following computer code can be used:

```
p(x) = 10^((a+cx+ex^2+gx^3)/(1+bx+dx^2+fx^3))
for -0.4 <= x <= 7.6
p(x) = 1.00 for x >= 7.6
with
x = Δ m = lm - m
a = -2.6114012   b = 0.026855133   c = 1.4267014
d = -0.15984339 e = -0.2717859   f = 0.031934995
g = 0.017006668
```

[3] As in the previous sections, we use $\varphi(m)$ for the true numbers, $\Phi(m)$ for the cumulative true numbers.

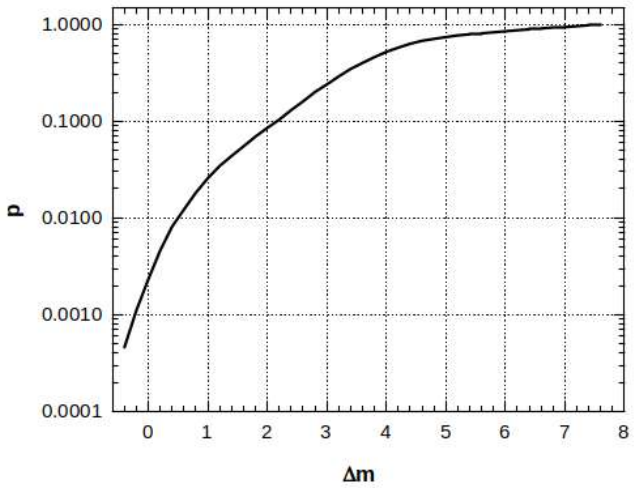


Figure 7.28: Perception probabilities $p(\Delta m)$ for an experienced observer under dark sky, averaged over a field of view with a radius of $R = 52\,^{\circ}5$. Δm is the difference between the limiting magnitude and the meteor magnitude $\Delta m = lm - m$.

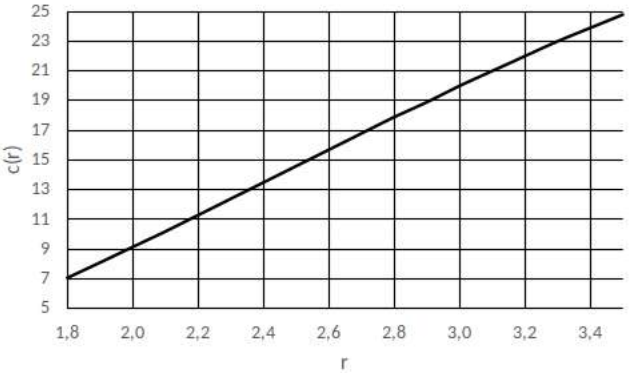


Figure 7.29: Factors $c(r)$ to transform the observed ZHR into the true ZHR within a field of $52\,^{\circ}5$ radius.

7.6.2.3 Flux and spatial number density for meteors of absolute magnitude brighter than +6.5

First, the true zenithal hourly rate $\mathrm{ZHR}_{\mathrm{true}}$ for a field of $R = 52\,^{\circ}5$ radius has to be computed from the observed ZHR:

$$\mathrm{ZHR}_{\mathrm{true}} = \mathrm{ZHR} \times c(r) \tag{7.71}$$

with

$$c(r) = \frac{\sum_{m=-\infty}^{+6} r^m}{\sum_{m=-\infty}^{+6} r^m p(6.5-m)} \tag{7.72}$$

Since the ZHR refers to lm = 6.5, the perception probabilities $p(6.5-m)$ are used. As very bright meteors do not contribute significantly to the total, $c(r)$ was computed for magnitude interval $-6 <= m <= +6$ with a step width of 1 mag – confer with Table 7.13 and Figure 7.29.

Table 7.13: Factors $c(r)$ to transform the observed ZHR into the true ZHR within a field of $52\,^{\circ}5$ radius.

r	$c(r)$	r	$c(r)$
1.8	7.08	2.8	17.9
1.9	8.11	2.9	18.9
2.0	9.16	3.0	20.0
2.1	10.2	3.1	21.0
2.2	11.3	3.2	22.0
2.3	12.4	3.3	23.0
2.4	13.5	3.4	23.9
2.5	14.6	3.5	24.8
2.6	15.7		
2.7	16.8		

For a computer code, this numerical approximation can be used

$$c(r) = 10.65 \times r - 12.15 \tag{7.73}$$

In (Koschack & Rendtel, 1990b) slightly different values were found from averaging individual $c(r)$ of five experienced observers. Here we prefer the $c(r)$ based on a straightforward procedure described here and in (Koschack & Rendtel, 1990a).

7.6.2.4 Summary: Computation of flux and spatial number density based on the visual ZHR

From Sections 7.6.2.1 and 7.6.2.2 we find

$$Q(m < 6.5) = \mathrm{ZHR} \times c(r)/A_{\mathrm{red}}(r) \tag{7.74}$$

$$Q(m < 6.5) = \mathrm{ZHR} \times (10.65 \times r - 12.15) \times (r - 1.3)^{0.748}/37200\mathrm{km}^2 \tag{7.75}$$

$Q(m < 6.5)$is the flux of meteoroids causing meteors brighter than +6.5 absolute magnitude, given in meteoroids per km^2 per hour ($\mathrm{km}^{-2}\ \mathrm{h}^{-1}$).

$$\mathrm{ND}(m < 6.5) = Q(m < 6.5)/(3600\mathrm{s/h} \times v_g) \tag{7.76}$$

$ND(m < 6.5)$ is the spatial number density of meteoroids causing meteors brighter than +6.5 absolute magnitude in meteoroids per km^3 (km^{-3}), with v_g, the geocentric velocity of shower meteoroids in km/s.

Note: this procedure can be applied only as long as the population index r is constant over the visual magnitude range (cf. Section 7.4).

Figure 7.30 demonstrates the strong dependence of the conversion factor of the ZHR into flux density on the population index. If the ZHR is constant and the population index increases from 2.0 to 3.0, then the flux density increases by a factor of 4! In other words: during periods characterised by a high population index, a visual observer can only see a considerably smaller fraction of meteors encountering Earth's atmosphere (flux). This is dicussed in some more detail in Section 7.6.6.

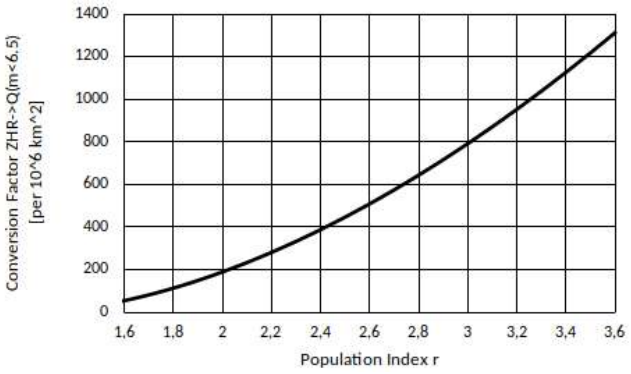


Figure 7.30: Conversion factor of ZHR (unit meteors per hour) into flux $Q(m < 6.5)$ expressed as "meteoroids per hour per 10^6 km^2").

7.6.2.5 Determination of flux and spatial number density if the population index r is not constant

We return to our example of the Leonid outburst on 1999 November 18 from Section 7.4.3. For the post-outburst interval 1999 November 18, 02:36–05:12 UT, the population index was found to be constant over the visual magnitude range $-1 \leq m \leq +6$ ($r = 2.05$). During the outburst interval 1999 November 18, 01:34–02:36 UT, there was a lack of Leonids fainter than magnitude class +5. For the magnitude range $-1 \leq m \leq +5$, the population index was $r = 3.18$. Table 7.14 shows the magnitude distributions and the ZHR for both observers. While the ZHR for the post-outburst interval with a constant population index for the visual magnitude range was almost the same for both observers, there is a major difference for the outburst interval, where a lack of faint meteors was found. The limiting magnitude correction from Section 7.3.4 does not work if there is a real lack of faint meteors.

Note: if the population index is not constant for the visual magnitude range, especially if there is a real lack or excess of faint meteors, the ZHR cannot be computed if the limiting magnitude is different from lm = 6.5.

With the probabilities of perception (Figure 7.28), there is a possibility to determine the flux directly without the intermediate step of a ZHR computation. In Table 7.15, the magnitude distributions from Table 7.14 are shown (n is the observed number of Leonids). The zenith corrected true hourly rate per magnitude class m, $n_{\mathrm{true,corr}}(m)$, is computed from the observed number n, the effective time, the zenith correction factor z, and the perception probability $p(\mathrm{lm} - m)$:

$$n_{\mathrm{true,corr}}(m) = n(m) \times z/\big(p(\mathrm{lm} - m) \times T_{\mathrm{eff}}\big). \quad (7.77)$$

The true zenithal hourly rate for a field with a radius of 52 °.5 of meteors of absolute magnitude class $m < m_{\mathrm{lim}}$, $\mathrm{ZHR}_{\mathrm{true}}(m < m_{\mathrm{lim}} + 0.5)$, is

Table 7.14: Magnitude distributions and ZHR for two experienced observers for the Leonid maximum 1999 November 18. Outburst interval 01:34–02:36 UT, post-outburst interval 02:36–05:12 UT.

Observer	A	B	A	B
Interval [UT]	0134 – 0236	0135 – 0235	0236 – 0500	0235 – 0512
Teff [h]	1.02	1.00	2.23	1.93
lm	6.30	7.25	6.30	7.25
c	1.26	0.42	1.15	0.58
h_R [deg]	29	29	50	51
z	2.06	2.06	1.31	1.29
Magn. class	Number of Leonids			
−6	0	0	1	0
−5	0	0	0	0
−4	0	0	0	1
−3	0	0	1	0.5
−2	1.5	0	7.5	8.5
−1	11	5	13.5	18
0	29	8	21	22.5
1	95	25	41	37
2	152.5	82.5	59	48
3	214.5	259	57.5	76
4	220	480.5	64	130.5
5	110.5	528	31	147.5
6	8	116	5.5	24.5
7	0	1	0	0
Tot	842	1505	302	514
ZHR	2146	1304	204	200

$$\mathrm{ZHR}_{\mathrm{true}}(m < m_{\mathrm{lim}} + 0.5) = \sum_{m=-\infty}^{m_{\mathrm{lim}}} n_{\mathrm{true,\,corr}}(m). \quad (7.78)$$

Note that the magnitude class +6, for instance, contains meteors of magnitude range $+5.5 < m < 6.5$. In column $m = +6$ we find $\mathrm{ZHR}_{\mathrm{true}}(m < 6.5)$, in column $m = +5$ we find $\mathrm{ZHR}_{\mathrm{true}}(m < 5.5)$, and so on.

The flux of meteoroids causing meteors brighter than magnitude limit $m_{\mathrm{lim}} + 0.5$ absolute magnitude is

$$Q(m < m_{\mathrm{lim}} + 0.5) = \mathrm{ZHR}_{\mathrm{true}}(m < m_{\mathrm{lim}} + 0.5)/A_{\mathrm{red}}(r) \quad (7.79)$$

$Q(m < m_{\mathrm{lim}} + 0.5)$ is the flux of meteoroids causing meteors brighter than $m_{\mathrm{lim}} + 0.5$ absolute magnitude, given in meteoroids per km^2 per hour (unit km^{-2} h^{-1}).

At this point, the dependence of A_{red} on the population index r needs to be considered – the value of A_{red} was determined assuming on constant population index for the visual magnitude range.

Strictly spoken, the flux density can be computed only for a magnitude range of a constant population index. In our example, this is possible for the outburst interval by giving $Q(m < 5.5)$. In order to compare the flux density for different regions of the stream, we wish

Table 7.15: Example data set from the Leonid maximum 1999 November 18 as given in Table 7.14. m – magnitude class, $p(\mathrm{lm}-m)$ – perception probability (shown in Figure 7.28), n – observed number of Leonids per magnitude class, $n_{\mathrm{true,corr}}$ – zenith corrected true hourly rate (field of radius 52.°5) per magnitude class, $\mathrm{ZHR_{true}}$ – true zenithal hourly rate for a field of 52.°5 radius for meteors of magnitude $m < m_{\mathrm{lim}} + 0.5$.

	m	–6	–5	−4	−3	−2	−1	0	1	2	3	4	5	6	7
Obs. A	$p(lm-m)$	1	1	1	1	1	0.96	0.87	0.77	0.55	0.29	0.10	0.03	0.0046	0
0134–0236	n	0.0	0.0	0.0	0.0	1.5	11.0	29.0	95.0	152.5	214.5	220.0	110.5	8.0	0.0
Outburst	$n_{\mathrm{true,corr}}$	0.0	0.0	0.0	0.0	3.0	23.1	67.3	249.2	560.0	1493.8	4443.1	7438.9	3512.4	0.0
	$\mathrm{ZHR_{true}}$	0.0	0.0	0.0	0.0	3.0	26.2	93.5	342.7	902.6	2396.5	6839.6	14278.5	17790.8	17790.8
Obs. B	$p(lm-m)$	1	1	1	1	1	1	0.96	0.87	0.77	0.55	0.29	0.10	0.03	0.0046
0135–0235	n	0.0	0.0	0.0	0.0	0.0	5.0	8.0	25.0	82.5	259.0	480.5	528.0	116.0	1.0
Outburst	$n_{\mathrm{true,corr}}$	0.0	0.0	0.0	0.0	0.0	10.3	17.2	59.2	220.7	970.1	3413.2	10876.8	7965.3	447.8
	$\mathrm{ZHR_{true}}$	0.0	0.0	0.0	0.0	0.0	10.3	27.5	86.7	307.4	1277.4	4690.7	15567.5	23532.8	23980.6
Obs. A	$p(lm-m)$	1	1	1	1	1	0.96	0.87	0.77	0.55	0.29	0.10	0.03	0.0046	0
0236–0500	n	1.0	0.0	0.0	1.0	7.5	13.5	21.0	41.0	59.0	57.5	64.0	31.0	5.5	0.0
Post-outb.	$n_{\mathrm{true,corr}}$	0.6	0.0	0.0	0.6	4.4	8.3	14.2	31.3	63.0	116.5	376.0	607.0	702.4	0.0
	$\mathrm{ZHR_{true}}$	0.6	0.6	0.6	1.2	5.6	13.9	28.0	59.3	122.3	238.8	614.8	1221.8	1924.2	1924.2
Obs. B	$p(lm-m)$	1	1	1	1	1	1	0.96	0.87	0.77	0.55	0.29	0.10	0.03	0.0046
0235–0512	n	0.0	0.0	1.0	0.5	8.5	18.0	22.5	37.0	48.0	76.0	130.5	147.5	24.5	0.0
Post-outb.	$n_{\mathrm{true,corr}}$	0.0	0.0	0.7	0.3	5.7	12.0	15.7	28.4	41.7	92.4	300.8	985.9	545.9	0.0
	$\mathrm{ZHR_{true}}$	0.0	0.0	0.7	1.0	6.7	18.7	34.4	62.8	104.5	196.8	497.6	1483.5	2029.3	2029.3

to refer to magnitude +6.5, i.e. we want to compute $Q(m < 6.5)$.

The dependence of A_{red} on the population index mainly results from brighter meteors appearing in larger angular distance from the centre of the field of view. Those meteors are closer to the horizon which implies a large distance to the observer (the apparent brightness of the meteor is fainter due to the large distance). The fraction of bright meteors depends on the population index. Faint meteors can be seen close to the centre of the field only. These have a constant distance to the observer.

If the population index is different for faint meteors, A_{red} is affected only little by the different population index for faint meteors. For this reason A_{red} computed for a population index of brighter meteors can be used for computation of flux including faint meteors. In our example of the 1999 Leonid outburst, $Q(m < 6.5)$ can be computed with A_{red} based on $r = 3.18$ determined for the magnitude range $-1 \leq m \leq +5$.

If the population index varies for bright meteors (say $m \leq +3$), then A_{red} needs to be determined by a numeric procedure based on the actual magnitude distribution.

In Table 7.16 we give the flux density values calculated for the Leonid data of our example. For the post outburst interval with a constant population index, the flux density values $Q(m < 6.5)$ computed from the observed ZHR and from the true $\mathrm{ZHR_{true}}$ are essentially the same. For the outburst interval with a lack of faint meteors, the flux density computed from the observed ZHR is too high. The conversion factor $c(r)$ (Table 7.13) converts the ZHR into $\mathrm{ZHR_{true}}$. It accounts for faint meteors which are not witnessed due to the low perception probability. For the outburst interval, $c(r)$ is too large because the fraction of faint meteors was in fact smaller than expected on the basis of a constant population index.

Note: if the population index varies over the visual magnitude range (approximately −2 ...+6 mag), the flux density cannot be computed from the ZHR even if limiting magnitude was exactly +6.5.

The difference is larger for observer A ($lm = 6.30$) than for observer B ($lm = 7.25$). Due to the lack of faint meteors, the limiting magnitude correction (see Section 7.3.4) results in too high values of the ZHR for $lm < 6.5$ and in a too small ZHR for $lm > 6.5$. For $lm > 6.5$ (observer B), both errors ($c(r)$ and the limiting magnitude correction factor) compensate partially; for $lm < 6.5$ (observer A) both errors add. At $lm = 6.3$, the error already is more than 100%, for lower limiting magnitudes it will become even larger.

The example of Leonid maximum 1999 November 18 illustrates the importance of a careful analysis of the population index r according to Section 7.4. Any anomaly (e.g. the lack of faint meteors – see [4]) must be considered in the determination of the flux density. Otherwise the flux density values are subject to very large biases of more than 100%.

7.6.3 Relation between the mass of a meteoroid and the brightness of the resulting meteor

If we (the Earth, a spacecraft, ...) pass a given meteoroid stream (described by its number density ND and mass index s) at different velocities, the appearance and effects are quite different. Assuming that the velocity $v_2 = 2 \times v_1$, the kinetic energy is $E_2 = 4 \times E_1$ as it increases with v^2. Meteoroids of the same mass will produce much brighter meteors (depending on the luminous efficiency briefly discussed in the Introduction

[4] In some streams, particles as large as 10^{-6} g are lost due to the combined effects of radiation pressure and ejection velocity (Moorhead, 2021). This is close to the 22×10^{-6} g (22 mg) of a +6.5 mag Leonid (last line in Table 7.17)

Table 7.16: Flux density Q (in meteoroids per km^2 per hour) determined by different methods for the example of the Leonid maximum 1999 November 18 (Table 7.14). The population index is taken from Section 7.4.3.

r A_{red} [km^2]	Outburst interval 3.18 ($m \leq +5$) 23199		Post outburst interval 2.05 ($m \leq +6$) 46131	
	Obs. A	Obs. B	Obs. A	Obs. B
ZHR	2146	1304	204	200
$Q(m < 6.5)$ from ZHR	2.01	1.22	0.043	0.042
$\mathrm{ZHR}_{\mathrm{true}}(m < 6.5)$	17791	23533	1924	2029
$Q(m < 6.5)$ from $\mathrm{ZHR}_{\mathrm{true}}$	0.77	1.01	0.042	0.044
$\mathrm{ZHR}_{\mathrm{true}}(m < 5.5)$	14278	15567	1222	1483
$Q(m < 5.5)$ from $\mathrm{ZHR}_{\mathrm{true}}$	0.62	0.67	0.026	0.032

Table 7.17: Absolute meteor magnitudes applying Verniani's (1973) equations for different meteoroid masses and meteor showers with different velocities V_g. The bottom lines give the meteoroid masses which are needed to produce a +6.5 mag meteor (reference limiting magnitude).

Mass [g]	Apparent magnitude DRA 20km/s	GEM 35km/s	QUA 41km/s	PER 59km/s	LEO 71km/s
10	−1.11	−3.48	−4.16	−5.70	−6.49
1	+1.19	−1.18	−1.86	−3.40	−4.19
0.1	+3.49	+1.12	+0.44	−1.10	−1.89
0.01	+5.79	+3.42	+2.74	+1.20	+0.41
0.001	+8.08	+5.72	+5.04	+3.50	+2.71
0.0001	+10.4	+8.02	+7.34	+5.80	+5.01
0.0048	+6.50				
0.00045		+6.50			
0.00023			+6.50		
0.000049				+6.50	
0.000022					+6.50

on page 8). This also means that meteoroids which are too small to produce visible meteors at v_1 may become visible at higher velocities.

Using the relation between meteoroid mass, geocentric velocity and apparent meteor magnitude given by Verniani (1973), we find the values shown in Table 7.17.

For completeness, we include the relation derived by Verniani (1973):
The number of electrons per metre (Verniani's q_m) was derived empirically from underdense radio meteors. This electron line density can be related to the absolute meteor magnitude m. Finally, the coefficients are transferred to allow using common units. The magnitude m of a meteor caused by a meteoroid with the mass M (in grams) at a velocity V_g (in km/s) is

$$m = 40 - 2.5 \log \left(2.73 \cdot 10^{10} \times M^{0.92} \times V_g^{3.91}\right). \quad (7.80)$$

Transforming this equation we find:

$$M = \left(3.6603 \times 10^5 \times 2.5119^{-m} \times v_g^{-3.91}\right)^{1.087}$$

$$v_g = \left(3.6603 \times 10^5 \times 2.5119^{-m} \times M^{-0.92}\right)^{0.25575}$$

Note that we cannot evaluate the accuracy of this relation derived by Verniani (1973).

An example: the Earth encounters the Geminid stream at 35 km/s and give a peak ZHR of about 150. To produce a +6.5 mag Geminid, we need a meteoroid of just 0.45 mg. If the same stream is passed at 70 km/s (approximately like the Leonids), the ZHR should then be about 300 for geometric reasons (twice the velocity). A meteoroid which caused a +6.5 mag (original) Geminid now appears as a +3.5 mag meteor. Depending on the population index, the ZHR is additionally increased since meteoroids of 0.45 mg produce a +3.5 mag meteor at 70 km/s. If the population index is constant, the ZHR increases by factor $r^{6.5-3.5}$. Considering $r = 2.2$, this factor is 10.6, and consequently the ZHR would be around 3000.

To produce a +6.5 mag meteor at 70 km/s, we only need 0.02 mg – but how many of such small meteoroids exist in the stream? If there would be a lower mass limit or number decrease, the population index would decrease towards fainter magnitudes. In this case the ZHR would be less than 3000 (there are less faint meteors).

These differences also emphasize the note concerning the population index r which is not necessarily constant over a large magnitude range. If we assume – as an illustrating example only – that meteoroid streams mainly consist of particles between 0.001 g and 1 g, this translates into a magnitude range [+8; +1] for the Draconids, but [−4; +3] for the Leonids. Vice versa, if we refer to the magnitude range [−2; +5] covering the usual range of observed for all showers, we implicitly compare meteoroids of masses in the range 20 g – 0.05 g (Draconids) with 0.1 g – 0.1 mg (Leonids).

The distribution of the amount of meteoroids over a large mass interval is complex and can be approximated

by an exponential correlation over a certain range only (see, e.g., Jenniskens (2006), p. 548–549). Therefore the population index describing the magnitude distribution in a given shower needs to be accompanied with a magnitude interval for which this value is valid. This also concerns the relation to the mass interval of the corresponding meteoroids characterized by the mass index s explained in the Glossary.

7.6.4 Determination of the flux density and spatial number density for meteoroids of masses of at least 1 mg based on visual observations

We start with a flux density for meteoroids causing meteors of at least +6.5 absolute magnitude $Q(m < 6.5)$ and find:

$$Q(M > 10^{-3}\mathrm{g}) = Q(m < 6.5) \times r^{(m_1 - 6.5)}$$

where m_1 is the absolute magnitude of meteor caused by meteoroid of 10^{-3}g at v_g of the stream

$$m_1 = 40 - 2.5 \log(4.748 \times 10^7 \times v_g^{3.91})$$

The velocity $v_{g,0}$ at which a meteoroid of 10^{-3} g produces a meteor of +6.5 is $v_{g,0} = 29.1$ km/s and we find

$$Q(M > 10^{-3}\mathrm{g}) = Q(m < 6.5) \times r^{(9.775 \times \log(29.1\mathrm{km/s}/v_g))} \quad (7.81)$$

Written for general limits of the magnitude m_{lim} and the mass M_{lim} this is

$$Q(M > M_{\mathrm{lim}}) = Q(m < m_{\mathrm{lim}}) \times r^{(40 - 2.5 \log(2.732 \times 10^{10} \times M_{\mathrm{lim}}^{0.92} \times v_g^{3.91}) - m_{\mathrm{lim}})} \quad (7.82)$$

According to Table 7.17, a Leonid meteoroid of 10^{-3} g causes meteor of +2.71 mag. If we base on $Q(m < 6.5)$, the conversion factor is $r^{(2.71-6.5)}$. Due to large difference of magnitudes, the conversion factor is heavily affected by any inaccuracy and/or slight variation of the population index over the magnitude range under consideration. At $r = 2.0$, an error of the population index of ±0.2 results in an error of the conversion factor of ±40%, at $r = 3.0$ the error is ±30%, respectively.

For this reason it is worth to think about:
(1) setting a mass limit of $M_{\mathrm{lim}} = 10^{-4}$g for streams with $v_g > 45 \ldots 50$ km/s
or
(2) application of the procedure described in Section 7.6.2.4 if the mass limit of 10^{-3} g is required.

Using the procedure described in Section 7.6.2.4, the flux density of meteoroids causing meteors brighter than absolute magnitude +3.5, $Q(m < 3.5)$, or absolute magnitude +2.5, $Q(m < 2.5)$, respectively, can be determined directly from magnitude distributions. This way the conversion factors get closer to 1.0 for "fast" streams and are less affected by any inaccuracy and/or slight variation of the population index over the magnitude range under consideration. On the other hand, the inaccuracy of visual magnitude estimates will affect single results. This can be seen in Table 7.15 and has been discussed in Section 7.4.3 for that specific example. But in global analysis with observational data of many observers, the inaccuracy of visual magnitude estimates is considered to be an error of noise-type. The resulting error of $Q(m < m_{\mathrm{lim}})$ can be substantially reduced or even eliminated by averaging many observations. Careful magnitude estimates according to instructions given in Chapter 2 are essential for later analyses.

The spatial number density ND (in meteoroids per km^3) is computed from the flux density

$$\mathrm{ND}(M > M_{\mathrm{lim}}) = Q(M > M_{\mathrm{lim}})/(3600\mathrm{s/h} \times v_g)$$

7.6.5 Comparison of major streams in terms of ZHR and spatial number density

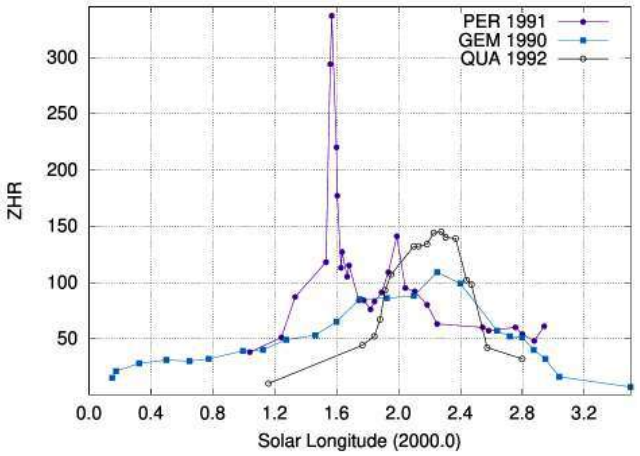


Figure 7.31: Comparison of three major showers (1990 Geminids, 1992 Quadrantids, and 1991 Perseids) in terms of their ZHRs. The solar longitude $\lambda_\odot$ (J2000.0) value 0.0 in this graph refers to 260 °.0 for the Geminids, to 280 °.9 for the Quadrantids and to 138 °.0 for the Perseids, respectively.

A comparison of different meteoroid streams or meteor showers requires comparable quantities. The ZHR was introduced as standard measure for the characterisation of visual meteor rates of meteor showers observed under different circumstances, such as radiant elevation and limiting magnitudes. The ZHR is the meteor rate an observer would see under specific (defined) circumstances. Comparing different showers in terms of their ZHRs, we are comparing the *impression* the observer gets of the meteor showers. In Figure 7.31, the ZHRs of three major northern hemisphere showers are compared: the 1990 Geminids (Roggemans & Koschack, 1991), the 1992 Quadrantids (Rendtel et al., 1993), and the 1991 Perseids (Koschack et al., 1993).

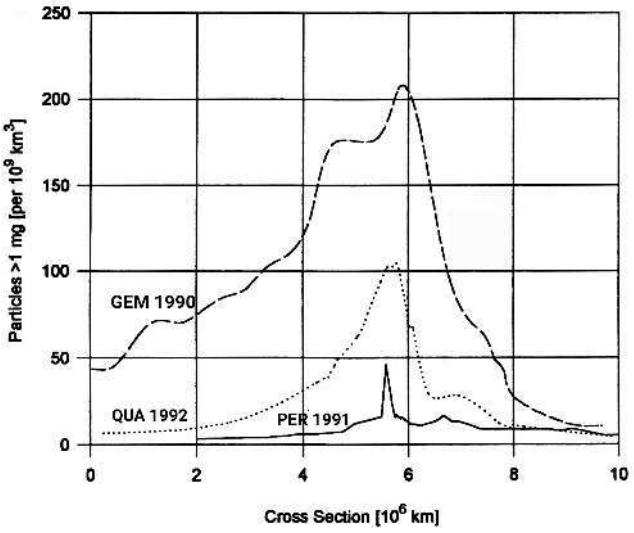


Figure 7.32: Spatial number density of meteoroids of at least 1 mg, ND($M > 10^{-3}$g), in meteoroids per 10^9km^3 (per cube of 1000 km edge length) plotted versus the distance (in 10^6 km) the Earth moved along the cross section through the stream. Spatial number densities were determined from the ZHRs plotted in Figure 7.31.

Of these three, the 1991 Perseids was the most impressive event followed by the excellent 1992 return of the Quadrantids and the "normal" Geminid display of 1990.

An imaginary observer in the interplanetary space would use the spatial number density of particles of a certain mass range to compare different meteoroid streams. For example, we could compare the number of particles per unit volume with masses exceeding 1 mg. On Earth, different circumstances, namely geocentric velocities v_g, result in different ZHRs caused by streams of the same spatial number density. If the same particle stream is passed at a higher velocity, the particles will arrive at a greater numerical rate and cause brighter meteors.

In Figure 7.32 the spatial number density of meteoroids of at least 1 mg, $ND(M > 1\text{mg})$, in meteoroids per 10^9km^3 (that is a cube of 1000 km edge length) is plotted versus the distance (in 10^6 km) the Earth moved along the cross section through the stream. Figure 7.32 illustrates the impact of the velocity a meteoroid stream encounters the Earth on the grandiosity of the meteor shower we can enjoy.

7.6.6 Impact of the encounter velocity and the mass index of a meteoroid stream on the visual ZHR

In this section we want to show the impact of mass distribution and encounter velocity of a meteoroid stream onto its display for visual observers in more detail.

We refer to the relation between mass of meteoroid, encounter velocity, and magnitude of resulting meteor

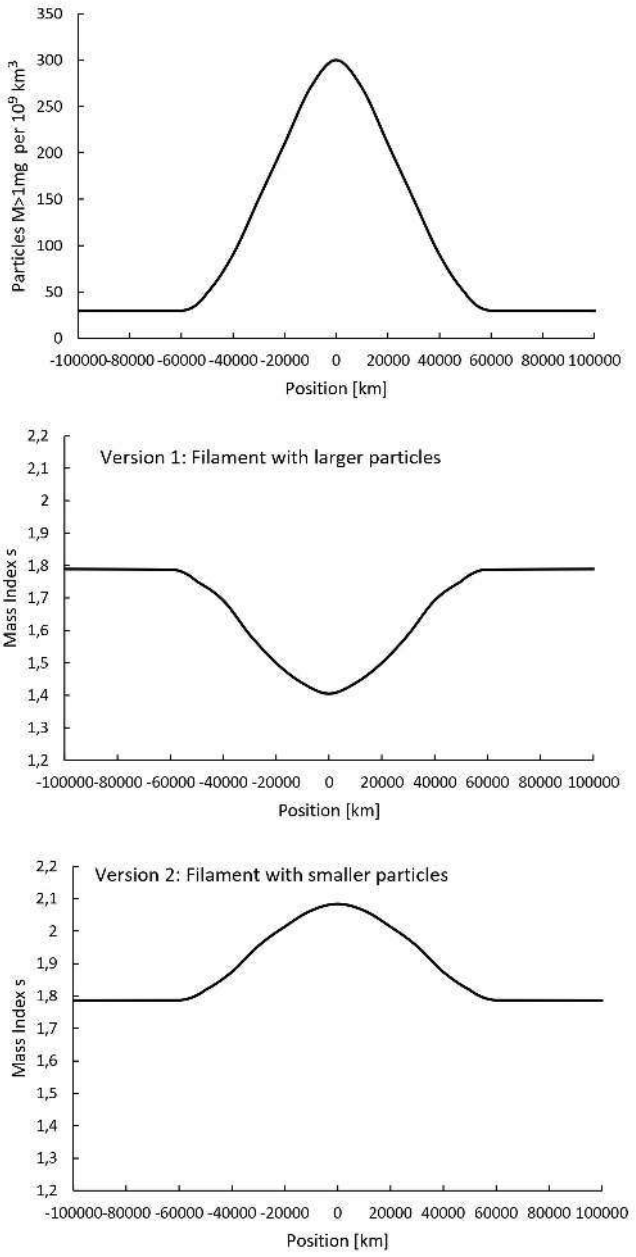


Figure 7.33: Profiles of number density and mass index along Earth's path through a hypothetic meteoroid stream.

determined by Verniani (1973) and described in Section 7.6.3.

In our example, the Earth encounters an arbitrary meteoroid stream with a number density of 30 particles of $M > 1$ mg per 10^9km^3 ("background stream") at different velocities. Within this stream there exists a dust filament with a peak number density of 300 particles of $M > 1$ mg per 10^9km^3 and a full width at half maximum (FWHM) of 60,000 km. The mass index s over the mass range [15 g; 0.02 mg] is assumed to be constant – which is of course hypothetic. Within the dust filament the mass index s is assumed to change according to two different versions:

1. the filament consists of larger particles than the

Table 7.18: Magnitude of a meteoroid of 1 mg and mass range corresponding to the visual magnitude range for different encounter velocities v_g according to Verniani (1973); cf. Section 7.6.3.

v_g [km/s]	Magnitude of a 1 mg meteoroid [mag]	Mass range corresponding to the vis. mag range [−1.5;+6.5]
20	+8.10	[14.8 g; 4.9 mg]
30	+6.37	[2.6 g; 0.88 mg]
40	+5.15	[0.78 g; 0.26 mg]
50	+4.21	[300 mg; 0.10 mg]
60	+3.43	[139 mg; 0.046 mg]
70	+2.78	[72 mg; 0.024 mg]

"background stream" (minimum of the mass index s at the centre/peak time);

2. the filament consists of smaller particles than the "background stream" (maximum of the mass s index at the centre/peak time).

The profiles of the number density ND and the mass index s along the Earth's path through the hypothetic stream are shown in Figure 7.33. Table 7.18 shows the mass ranges corresponding to the visual magnitude range and the magnitude of a 1 mg meteoroid for different encountering velocities according to Verniani (1973).

The different profiles in Figure 7.34 show how a visual observers witnesses the hypothetic meteor shower in terms of the population index and the ZHR:

1. With increasing encounter velocity, the peak caused by the filament becomes shorter – a geometric effect due to the increasing velocity.

2. The population index is not affected by the encounter velocity.

3. The ZHR of the background activity increases from just 2.2 at $v_g = 20\,\mathrm{km/s}$ to an impressive 500 at $v_g = 70\,\mathrm{km/s}$ ($r = 2.20$). This is due to the increase of the meteor magnitude with increasing velocity and the geometric effect caused by the velocity.

4. The ZHR of a peak strongly depends on the mass index s of the filament causing the peak. If the filament consists of larger particles (lower mass index), the peak ZHR is higher because visual observers can see a larger fraction of brighter meteors, confer Figure 7.29 in Section 7.6.2.3 (page 163).

From these findings two main conclusions can be drawn:

1. The detection limit of slow meteoroid streams is much higher than for fast streams. The famous Perseids could hardly be detected if the Earth would encounter this stream at 20 km/s instead of the real 59 km/s. In this case, a maximum ZHR of just about 1(!) could be "detected" instead of about 100 at $v_g = 59\,\mathrm{km/s}$. This implies a strong selection effect. Some slow meteoroid streams with a number density comparable to that one of the Perseids are likely to exist but they remain undetectable. Streams we cross at low velocities, such as the Draconids or κ-Cygnids, have a higher number density than impressive fast streams. For this reason, detectable slow meteoroid streams, and especially small and not very impressive peaks should get at least the same attention as impressive fast streams.

2. The profile of the population index r is as important as the ZHR profile. For each meteor shower analysis an accurate profile of the population index with high temporal resolution should be determined if the data sample is sufficient.

At this point we close this chapter with the levels of analysis already described in Section 7.6.1:

First, we observe a certain rate from a given meteor shower, which is dependent on a number of influences. With the population index we can calibrate this rate to standard conditions, and call it the ZHR. This allows us to combine results obtained under different observing circumstances and to describe the appearance of a given shower during a return or over long periods.

Next, we may calculate a flux or spatial number density of meteoroids causing meteors brighter than +6.5 absolute magnitude for each of the meteoroid streams, thus getting information about the actual meteoroid stream causing the meteor event we observed.

By reducing the data of different streams to the same scale and mass range of meteoroids, we get a number density profile for the meteoroid streams, and can compare them, or draw conclusions about processes related to the creation and evolution of the streams.

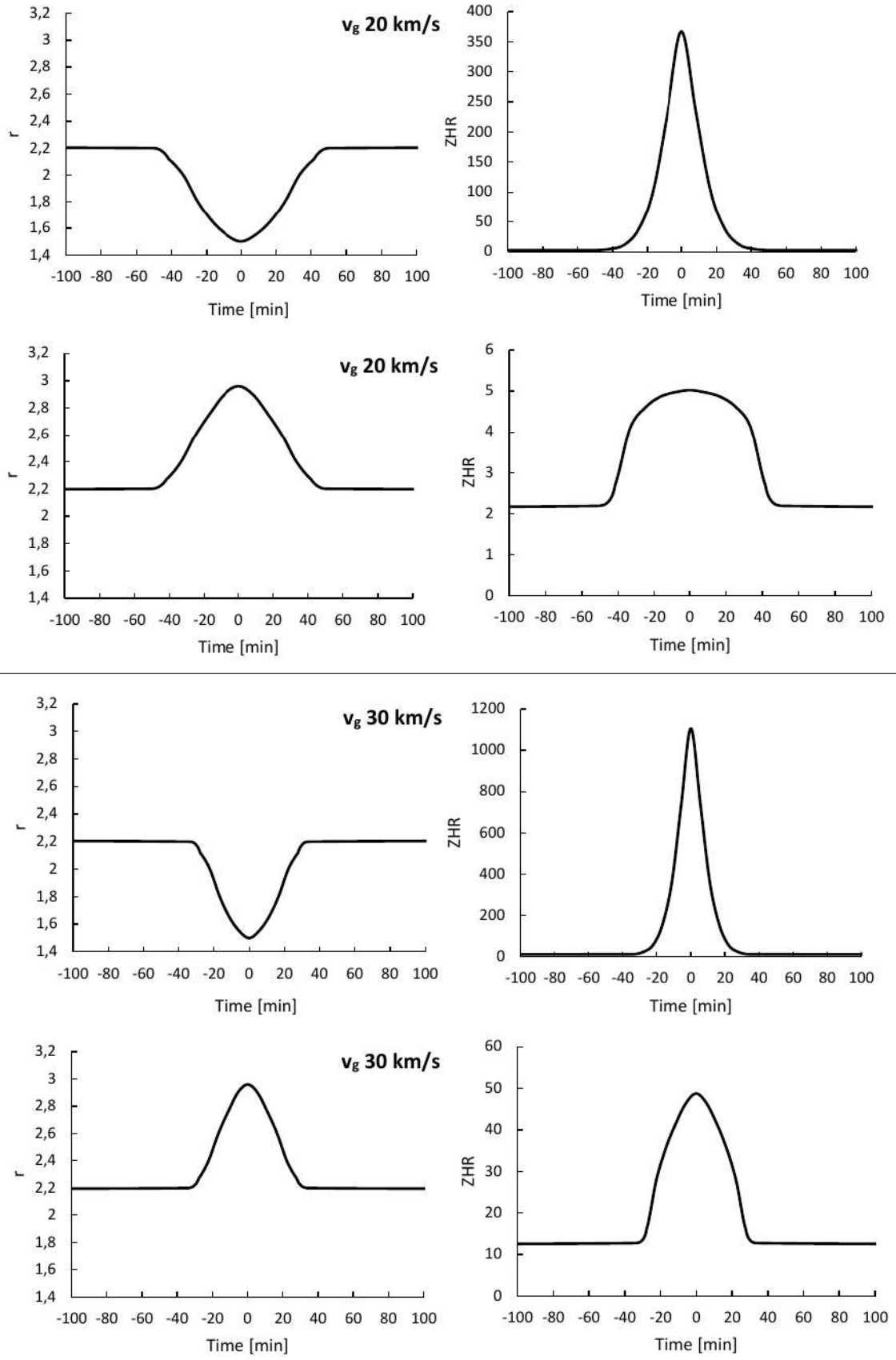


Figure 7.34: Profiles of population index and ZHR resulting from the two hypothetic meteoroid streams shown in Figure 7.33. For each velocity, the top panel shows the parameters and effects for the filament with the **minimum** of the mass index at the peak time and the bottom panel illustrates the filament with the **maximum** of the mass index at peak time. (Graphs for higher velocities on the following pages.)

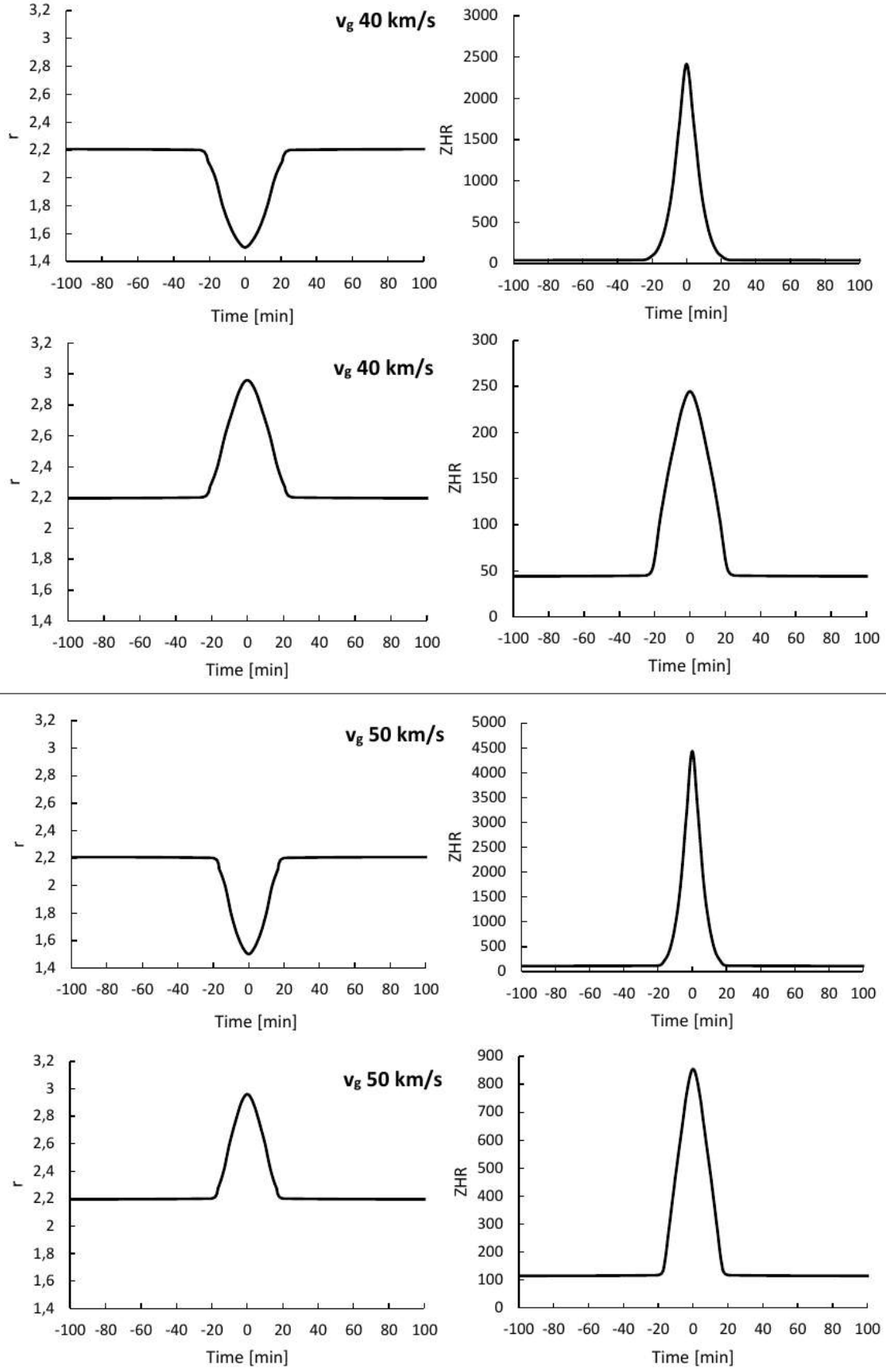


Figure 7.34, continued.

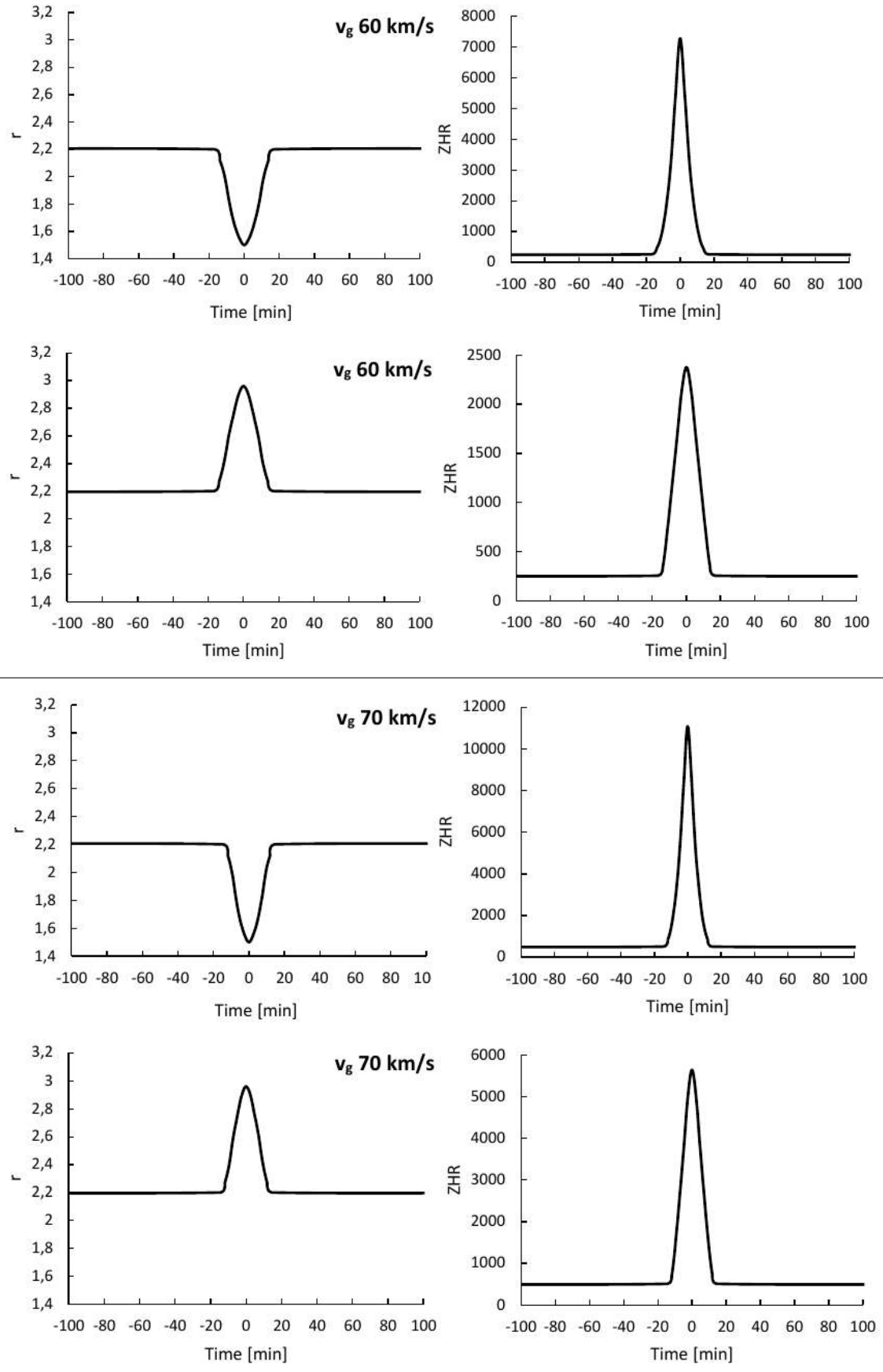


Figure 7.34, continued.

References

Bellot Rubio L.R., 1995: Effects of a dependence of meteor brightness on the entry angle. *A & A* **301,** 602–608.

Ceplecha Z., 1992: Influx of interplanetary bodies onto Earth. *A & A* **263,** 361–366.

Egal A., Brown P.G., Rendtel J., Campbell-Brown M., Wiegert P., 2020: Activity of the Eta-Aquariid and Orionid meteor showers. *A&A* **640,** A58.

Gural P., 2001: Fully correcting for the spread in meteor radiant positions due to gravitational attraction. *WGN* **29,** 134–138.

Jenniskens P., 2006: Meteor showers and their parent comets. Cambridge Univ. Press.

Koschack R., 1988: On the determination of the probability of perception for visual meteors. *WGN* **16,** 77–84, 157.

Koschack R., 1994: Single body theory and zenith correction factor, in *A.Knöfel, P.Roggemans (eds.): Proc. IMC 1994*, IMO, Mechelen. 31–43

Koschack R., Arlt R., Rendtel J., 1993: Global analysis of the 1991 and 1992 Perseids.. *WGN* **21,** 152–167.

Koschack R., Rendtel J., 1990a: Determination of spatial number density and mass index from visual meteor observations (I). *WGN* **18,** 44–58.

Koschack R., Rendtel J., 1990b: Determination of spatial number density and mass indexfrom visual meteor observations (II). *WGN* **18,** 119–140.

Kresáková M., 1966: The magnitude distribution of meteors in meteor streams. *Contr. Skalnaté Pleso Obs.* **3,** 75–109.

Margonis A., Christou A., Oberst J., 2019: Characterization of the Perseid meteoroid stream through SPOSH observations between 2010–2016. *A&A* **626,** A25, 9pp..

McBride N., Taylor A.D., Green S.F., McDonnell J.A.M., 1995: Asymmetries in the natural meteoroid population as sampled by LDEF. *Planetary and Space Science* **43,** 757–764.

Molau S., Barentsen G., 2012: Meteor shower flux densities and the zenith exponent. Proceedings of IMC 2012

Molau S., Barentsen G., Crivello S., 2015: Obtaining population indices from video observations of meteors. In: J.-L. Rault, P. Roggemans (eds.): Proceedings of the IMC, Giron, France, 2014, pp. 74–80.

Moorhead A.V., 2021: Forbidden mass ranges for shower meteoroids. *Icarus* **354,** 113949; https://doi.org/10.1016/j.icarus.2020.113949.

Öpik E., 1955: The distribution of meteor stream intensity over the celestial sphere. *Contr. Armagh Obs.* **15,** 147–173.

Rendtel J., 2005: Evolution of the Geminids observed over 60 years. *EMP* **95,** 27–32.

Rendtel J., 2008: The Orionid meteor shower observed over 70 years. *EMP* **102,** 103–110.

Rendtel J., 2019: On a possible recurring feature in the Geminid stream. *WGN* **47,** 180–183.

Rendtel J., 2020: Geminids 2018. In: *U. Pajer, J. Rendtel, M. Gyssens, C. Verbeeck (eds.): Proceedings of the International Meteor Conference Bollmannsruh, Germany, 2019*, pp. 183–188.

Rendtel J., Koschack R., Arlt R., 1993: The 1992 Quadrantid meteor stream.. *WGN* **21,** 97–109.

Rendtel J., Velkovic K., Weiland T., Verbeeck C., Knöfel A., 2019: Perseids 2018 – Analysis of global visual data. *WGN* **47,** 18–25..

Richardson J., 1999: A detailed analysis of the geometric shower radiant altitude correction factor. *WGN* **27,** 308–317.

Richter J., 2021: Simultaneous estimation of ZHR and the limiting magnitude correction factor. *WGN* **49,** 35–41.

Roggemans P., Koschack R., 1991: The 1990 Geminids.. *WGN* **19,** 184–193.

See T., Allbrooks M., Atkinson D., Simon C., Zolensky M., 1990: Meteoroid and debris impact features documented by the Long Duration Exposure Faciliy: a preliminary report. Space & Life Sciences Directorate, Solar System Exploration Division, Planetary Materials Branch Publication # 84, JSC # 24608, 599 pp.

Velkovic K., Rendtel J., Verbeeck C., Weiland T., Knöfel A., 2019: Tricks of the trade: global analysis of visual meteor observations using VMDB and MetFns – an example. In: *R. Rudawska, J. Rendtel, C. Powell, R. Lunsford, C. Verbeeck, A. Knöfel (eds.): Proceedings of the International Meteor Conference Pezinok-Modra, Slovakia, 2018*, pp. 57–63.

Verniani F., 1973: An analysis of the physical parameters of 5759 faint radio meteors. *J. Geophys. Res.* **78,** 8429–8462.

Zvolánková J., 1983: Dependence of the observed rate of meteors on the zenith distance of the radiant. *BAC* **34,** 372–375.

8 | Appendix

Glossary

***a*:** → semimajor axis of an orbit.

ablation: removal of material by attrition, e.g., by passage through the atmosphere.

absolute magnitude: the stellar magnitude any meteor would have if placed in the observer's zenith at a height of 100 km.

altiude: the angular distance of a celestial body above or below the horizon, measured along the great circle passing through the body and the zenith. Altitude is 90° minus zenith distance.

Amor asteroids: asteroids having perihelion distance 1.017au $< q \leq$ 1.3au.

aphelion distance: Q, distance of greatest heliocentric separation for a body in an eccentric orbit; $Q = a(1 + e)$.

Apollo asteroids: asteroids having semimajor axis $a \geq$ 1.0au, and perihelion distance $q \leq$ 1.017au.

ascending node: → nodes.

asteroid: one of a number of objects ranging in size from sub-km to about 1000 km, most of which lie between the orbits of Mars and Jupiter; also called 'minor planet'. Their designations are supplied by the IAU's Minor Planet Center.

The preliminary designations consist of the year of discovery, an upper case letter to indicate the half-month in that year (A = Jan. 1–15, B = Jan. 16–31, ... Y = Dec. 16–31, I being omitted), a second upper case letter in sequence, and when this sequence of 25 (I again being omitted) has been completed it is repeated and followed by a sequential number (written as a subscript, if possible). Before 1925 the system consisted simply of a sequential pair of letters (and initially only a single letter), and the subsequent interpolation of additional objects was troublesome. The modern system is therefore now also used for unnumbered pre-1925 objects, except that the initial 1 in the year is replaced by A.

The permanent designation consists of numbers and names, beginning with 1 Ceres, given to asteroids for which orbits are accurately determined. Asteroid 5000 was numbered in 1991 November and asteroid 500 000 in 2017 October. The numbers are supplied by the Minor Planet Center after orbits have been fitted to observations at several different oppositions. Names are proposed by discoverers to the Working Group for Small Body Nomenclature of IAU Division F and cannot be adopted until the least two months after an asteroid is numbered. Most numbered asteroids have not yet been named, although there are already more than 20 000 names.

Aten asteroids: asteroids having semimajor axis $a <$ 1.0 au, and aphelion distance $Q >$ 0.983 au.

au: astronomical unit. The mean distance of the Earth from the Sun, equal to 1.496×10^{11} m.

azimuth: the angular distance measured clockwise along the horizon from a specified reference point (usually north) to the intersection with the great circle drawn from the zenith through a body on the celestial sphere.

bolide: → fireball.

Brownlee particles: interplanetary dust particle (IDP), also has sometimes been known as a micrometeoroid or, after entry into the Earth's atmosphere, a → micrometeorite.

comet: an object composed of solid particles and volatile ices (such as H_2O, CO, CO_2, NH_3). When a comet moves close enough to the Sun, the higher temperature causes ices near the surface to sublimate. As the gases expand, they drag → meteoroids with them, away from the comet's solid nucleus. Meteoroids escaping the nucleus move on to orbits independent of (though initially similar to) the comet. Gas molecules liberated from the nucleus are subsequently photodissociated (producing OH, CN, C_2 etc.) or ionised by solar radiation.

Icy bodies too far from the Sun to show activity (escaping gas and dust) are classified observationally and in databases with → asteroids. An active comet shows a coma (expanding cloud of escaping matter), and sometimes a dust tail and an ion tail, around perihelion. Comets become extinct if enough volatiles are lost. Active lifetimes are typically hundreds of perihelion passages.

Most active comets have highly elliptical orbits (or even parabolic to within observed accuracy), nearly always dynamically unstable. Orbits can reach a few times 10^4 au from the Sun. Long-period (> 200 year) orbits comprise a substantial majority of the

discovered population. Known, active comets tend to have a nuclear diameter between a kilometer and a few tens of km.

comets, nomenclature (old): when a newly discovered comet was confirmed, the IAU Central Bureau for Astronomical Telegrams assigned a provisional designation consisting of the year of discovery followed by a lowercase letter in order of discovery for that year. The discoverer's name is attached to the designation. If a reliable orbit is later established, the comet was given a permanent designation consisting of the year of perihelion passage followed by a Roman numeral in order of perihelion passage. Comets with orbital periods $>$ 200 years were called 'long-period'; those with periods $<$ 200 years are indicated by P/ preceding the name of the comet and are called 'short period' comets.

comets, nomenclature (modern): the principal designations used for comets consist of the year and an upper-case letter to indicate the halfmonth of discovery in that year (A = Jan. 1–15, B = Jan. 16–31, C = Feb. 1–15, ..., Y = Dec. 16–31, I being omitted), followed by a numeral showing the order of announcement of discovery in that halfmonth. The halfmonths are as used for discoveries of minor planets, the difference being that minor-planet designations have a second letter (in addition to possible numerals) to indicate the order of discovery announcement. 'Discovery' refers to the time when the discovery observation is actually made. The new cometary designations are prefixed, generally by P/ or C/, according as to whether the orbit is periodic (short-period, or observed at multiple perihelion returns) or not. The symbol D/ is used for 'defunct' comets, or periodic comets which either are known no longer to exist, or for which the (current) orbit is poorly known. The prefix A/ would be used to denote an object given a cometary designation but deemed to be a minor planet. X/ is used for comets for which it is not possible to compute orbits – and that in some cases may never in fact have existed. I/ for interstellar objects was added in 2017. Permanent numbers are given to periodic comets when they are confirmed as returning to perihelion more than once; the permanent number is written before the P, e.g. 1P/Halley.

declination: angular distance north or south of the celestial equator; symbol δ or abbreviation De.

descending node: → nodes.

direct motion: → prograde motion.

dust (interplanetary): particles originating or existing in interplanetary space with sizes smaller than than meteoroids (the dividing line may be taken at around 30μm.

dust trail: particle ensemble ejected around one perihelion passage of a meteoroid stream's parent object.

***e*:** eccentricity of an elliptical orbit. The amount by which the orbit deviates from circularity: $e = c/a$, where c is the distance from the centre to a → focus and a is the → semimajor axis.

ecliptic: plane of the Earth's orbit.

epoch: an arbitrary fixed instant of time or date used as a chronological reference datum for calendars, celestial reference systems, star catalogs, or orbital motions.

escape velocity: the velocity required to escape entirely from the gravitational field of an astronomical body; equlas the minimum impact velocity for any body arriving from a very great distance.

fall: a meteorite that was seen to fall. Such meteorites are usually recovered soon after the fall and are relatively free of terrestrial contamination and weathering effects.

find: a meteorite that was not seen to fall but was found and recognised subsequently.

fireball: a bright meteor, also called bolide. Several definitions have been used by various authors. In the IMO all meteors of at least -3^{m} are regarded as fireballs. Extremely bright events (magnitude -17 or brighter) are designated as "superbolides".

focus: in an astronomical context, the focus of a heliocentric elliptical orbit is the point where the sun is located. In geometry, an ellipse has two foci; astronomers call the focus without the sun the empty focus.

geocentric: Earth-centred.

heliocentric: Sun-centred.

horizon: a plane perpendicular to the line from an observer to the zenith. The great circle formed by the intersection of the celestial sphere with a plane perpendicular to the line from an observer to the zenith is called the astronomical horizon.

***i*:** inclination of an orbit. The angle between an asteroid's orbit and the plane of the → ecliptic (or between a satellite's orbit and the planet's equatorial plane).

IAU: International Astronomical Union.

$\lambda_\odot$: → solar longitude.

long-period comet: a comet with an almost parabolic orbit and a period of revolution round the Sun exceeding 200 years. Some have orbital periods of millions of years.

magnitude: an arbitrary number, measured on a logarithmic scale, used to indicate the brightness of an object. If I_i is the brightness of star i amd m_i its magnitude, then $m_1 - m_2 = -2.5 \log(I_1/I_2)$. Two stars differing by 5 magnitudes differ in luminosity by a factor of 100. One magnitude difference is the fifth root of 100, or a factor of about 2.512. The brighter the star, the lower the numerical value of the magnitude and very bright objects have negative magnitudes.

mass index: s – the number N of meteoroids having individual masses between m and $m + dm$ is $dN = \text{constant} \times m^{-s} dm$. The cumulative number of particles with masses greater than m is proportional to m^{1-s}. The → population index r can be converted into the mass index s. Assuming that the shape of the meteor light curve does not change over the magnitude range and based on a mass–luminosity relation published by Verniani, $s = 1 + 2.3 \log r$.

meteor: the light phenomenon produced by a → meteoroid experiencing frictional heating when entering a planetary atmosphere; also used for the glowing meteoroid itself. If particularly large, it is described as a → fireball.

meteoric: the adjectival form pertaining to meteor and meteoroid.

meteorite: a natural object of extraterrestrial origin (→ meteoroid) that survives passage through the atmosphere.

meteoroid: a natural small (generally sub-km; IAU definition: 30μm to 10 m) solid object in an independent orbit in the Solar System.

meteoroid stream: stream of solid particles released from a → parent body (→ comet or → asteroid), generally through the influence of Solar radiation. The various ejection directions and ejection speeds of individual → meteoroids determine the width of a stream and the particles' distribution around the overall average orbit.

meteor shower: many → meteors appearing to radiate from a common point in the sky caused by the collision of the Earth with a stream of meteoric particles.

micrometeorite: a small extraterrestrial particle that has survived entry into the Earth's atmosphere. The actual size is not rigorously constrained but is operationally defined by the collection procedure because small particles are more abundant than large ones. In practice, the micrometeorites being studied in the laboratory after collection in the stratosphere are rarely as large as 50μm.

minor planet: → asteroid.

nodes: the points at which the orbit of a planet, asteroid, comet or meteoroid crosses the plane of the → ecliptic. The object moves from south to north of the ecliptic at the ascending node, and from north to south at the descending node. The longitude of the ascending node is one of the six orbital elements and measures the angle between the ascending node and → vernal equinox, measured in the plane of the ecliptic.

ω: argument of perihelion (or, more generally, argument of periapse for a body orbiting an object other than the Sun). Angular distance (measured in the plane of a body's orbit in the direction of motion) from the ascending → node to the → perihelion point.

Ω: longitude of ascending → node. The angle between some line in the reference plane (usually the direction to the → vernal equinox) and the point where the body crosses the reference plane moving south to north.

orbital elements: six quantities that fully describe an orbit; along with the time, they specify the position of an orbiting body along its path. A typical set of orbital elements are: (1) → semimajor axis a; (2) → eccentricity e; (3) → inclination i; (4) longitude of the ascending → node Ω; (5) argument of periapse ω; and (6) the time of passage through periapse T.

parent body: a → comet or → asteroid which released → meteoroids, dust, and gas when approaching the inner Solar System for a potential → meteoroid stream.

Also used for the body on or in which a given meteorite or class of meteorites was located prior to ejection as ≈ meter-sized objects.

perihelion distance: q, distance of the least heliocentric separation for a body in an eccentric orbit; $q = a(1 - e)$.

persistent train: → train.

perturbation: an additional force on an orbiting object that is small compared to the gravitational force exerted by the central mass around which it is orbiting. Perturbations on meteoroids orbiting the Sun arise from the gravity of planets and from radiative effects such as → Poynting-Robertson and → Yarkovsky. They cause changes in → orbital elements.

population index r: increase of the true number of meteors of magnitude class $N(m + 1)$ relative to the magnitude class $N(m)$: $r = N(m + 1)/N(m)$; see page 139

Poynting-Robertson effect: a dissipative force due to the anisotropic loss of momentum by a particle

through re-radiation of solar energy. This causes aphelion collapse, reducing the orbit's → a and → e such that a circular orbit is eventually attained and the particle spirals slowly toward the Sun. Small particles (below 1 cm) are most severely affected because the force (relative to solar gravity) varies as the reciprocal of its size.

prograde motion: motion in the same direction as the prevailing direction of motion. As viewed from the north, prograde motion is counter-clockwise, or west to east.

q: → perihelion distance.

Q: → aphelion distance.

radiant: the point where the backward projection of the meteor trajectory intersects the celestial sphere, or the backwards prolongation of the apparent trails of a given meteor as seen by observers at different locations.

radiant drift: change of a radiant position in the sky that results from the Earth's changing position as it moves along its orbit (i.e., the changing radiant of a single shower as a function of date)

radiant shift: differences in the position of a radiant in the sky due to effects like → zenithal attraction, or referring to radiant positions from different → dust trails.

retrograde motion: motion in the opposite direction as the prevailing direction of motion. As viewed from the north, retrograde motion is clockwise, or east to west.

right ascension: angular distance east of the → vernal equinox, as measured on the celestial equator; symbol α, abbreviation RA. Can be given in degrees or hours and minutes, with $1^{\mathrm{h}} = 15°$, or $1° = 4^{\mathrm{m}}$.

semimajor axis: half the length of the major axis (long axis) of an ellipse; a standard element used to describe an elliptical orbit.

short-period comet: a → comet with an orbital period of < 200 years.

solar longitude: $\lambda_\odot$, angular distance along the Earth's orbit, measured from the → vernal equinox. It gives the position of the Earth at its orbit and hence is more appropriate information on a meteor shower's maximum than the date.

standard epoch: a date and time that specifies the reference system to which celestial coordinates are referred. Prior to 1984 coordinates of star catalogs were commonly referred to the mean equator and equinox of the beginning of a Besselian year. Beginning with 1984 the Julian year has been used, as denoted by the prefix J, e.g., J2000.0.

sunrise, sunset: the times at which the apparent upper limb of the Sun is on the astronomical horizon; i.e., when the true zenith distance, referred to the centre of the Earth, of the central point of the disk is $90°50'$, based on adopted values of $34'$ for horizontal refraction and $16'$ for the Sun's semidiameter.

superbolide: → fireball.

train: light/material behind a meteoroid; see page 55.
- *wake* – luminosity just behind the meteor head.
- *green train* – short-duration trains exclusively formed by the green oxygen line at 557.7 nm.
- *persistent train* – self-luminous, visible for tens of minutes after the meteor.
- *reflection/dust train* – not self-luminous; visible in twilight/daylight.

trajectory: path of a meteor in the Earth's atmosphere.

twilight: the interval of time preceding sunrise and following sunset during which the sky is partially illuminated. Civil twilight comprises the interval when the zenith distance, referred to the centre of the Earth, of the central point of the Sun's disk is between $90°50'$ and $96°$, nautical twilight comprises the interval from $96°$ to $102°$, astronomical twilight comprises the interval from $102°$ to $108°$.

Universal Time (UT): the local mean time of the prime meridian. It is the same as Greenwich mean time, counted from 0 hour beginning at Greenwich (observatory) mean midnight. It is based on the average motion of the Sun as seen from the Earth (Greenwich meridian) and provides a single timescale to which observations can be referred.

vernal equinox: the intersection of ecliptic and celestial equator where the Sun is moving from south to north.

wake: → train.

Yarkovsky effect: the effect of rotation on the trajectory of a small particle orbiting the Sun (compare → Poynting-Robertson effect). If the orbiting body is rotating, there is a temperature variation over its surface, and it will reradiate the incident radiation anisotropically, causing a → perturbation to its orbit.

zenith distance: the angular distance of a celestial body (or point in the sky) from the zenith (overhead point).

zenithal attraction: the effect of the Earth's gravity on a meteoric body increasing the velocity and moving the radiant towards the zenith.

ZHR: Zenithal Hourly Rate – number of shower meteors corrected to standard conditions; see page 139.

Reference

Definitions of altitude, azimuth, epoch, horizon, standard epoch, sunrise and twilight are all taken from the Explanatory Supplement to the Astronomical Almanac, edited by S.E. Urban and P.K. Seidelmann (University Science Books; 3rd ed. 2012).

Journal abbreviations

A&A – Astronomy and Astrophysics

BAC – Bulletin of the Astronomical Institutes of Czechoslovakia

EMP – Earth, Moon, and Planets

JBAA – Journal of the British Astronomical Association

JATP – Journal of Atmospheric and Solar-Terrestrial Physics

MAPS – Meteoritics and Planetary Science

MNRAS – Monthly Notices of the Royal Astronomical Society

WGN – WGN, Journal of the International Meteor Organization

Authors

Rainer Arlt, Leibniz-Institut f. Astrophysik, 14482 Potsdam, Germany;
rarlt@aip.de

Peter G. Brown, Department of Physics and Astronomy, University of Western Ontario, 1151 Richmond Street, London, Ontario, Canada N6A 3K7;
pbrown@uwo.ca

Pete Gural, Gural Software and Analysis LLC, 12241 Eliza Court, Lovettsville, Virginia, USA 20180;
pgural@gmail.com

Ralf Koschack, International Meteor Organization, Hauptstraße 35, 18469 Velgast, Germany;
ralf.koschack@gmx.de

Sirko Molau, International Meteor Organization, Abenstalstraße 13b, 84072 Seysdorf, Germany;
sirko@molau.de

Jean-Louis Rault, Société Astronomique de France, 16, rue de la Vallée, 91360 Epinay sur Orge, France;
f6agr@orange.fr

Jürgen Rendtel, International Meteor Organization, Eschenweg 16, 14476 Potsdam, Germany;
jrendtel@web.de

Cis Verbeeck, International Meteor Organization, Bogaertsheide 5, 2560 Kessel, Belgium;
cis.verbeeck@scarlet.be

William Ward, International Meteor Organization, 84 Woodwynd, Kilwinning, KA13 7DJ, Scotland, UK;
bill_meteor@yahoo.com

The International Meteor Organization

http://www.imo.net

The International Meteor Organization

The International Meteor Organization (IMO) was founded in 1988 and has more than 350 members now. The IMO was created in response to an ever growing need for international cooperation of meteor amateur work. The collection of meteor observations by several methods from all around the world ensures the comprehensive study of meteor showers and their relation to comets and interplanetary dust. Membership includes a subscription to WGN, the Journal of the IMO.

IMO Council

President: Cis Verbeeck, Belgium. E-mail: cis.verbeeck@gmail.com

Vice-President: Juraj Tóth, Slovakia. E-mail: toth@fmph.uniba.sk

Secretary-General: Robert Lunsford, U.S.A. E-mail: lunro.imo.usa@cox.net

Treasurer: Marc Gyssens, Belgium. E-mail: marc.gyssens@uhasselt.be

Other Council members:
Karl Antier, France. E-mail: karl.antier@gmx.fr
Javor Kac, Slovenia. E-mail: javor.kac@gmail.com
Detlef Koschny, the Netherlands. E-mail: detlef.koschny@esa.int
Sirko Molau, Germany. E-mail: sirko@molau.de
Vincent Perlerin, France. E-Mail: vperlerin@gmail.com
Jürgen Rendtel, Germany. E-mail: jrendtel@web.de

Commission Directors

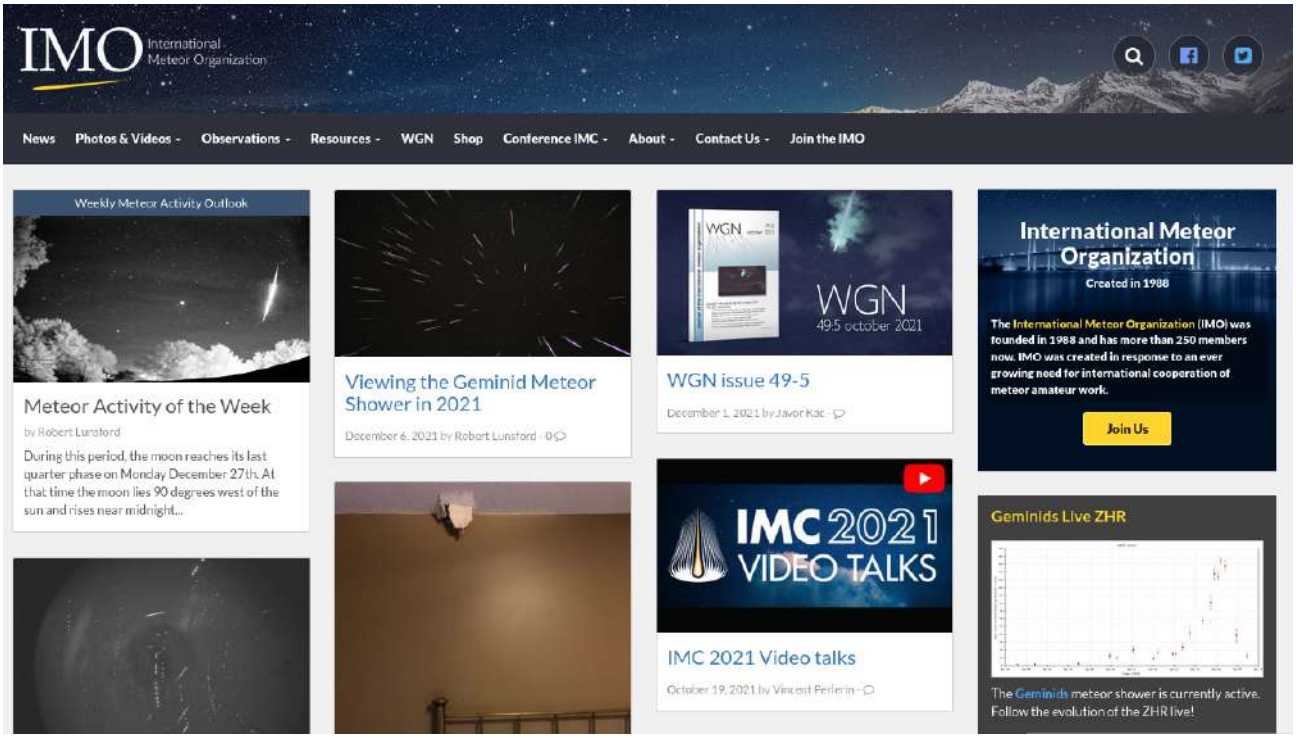
Photographic Commission: William Ward, 84 Woodwynd, Kilwinning, KA13 7DJ, Scotland, U.K.; E-mail: photo@imo.net

Radio Commission: Christian Steyaert, Kruisven 66, B-2400 Mol, Belgium; E-mail: radio@imo.net

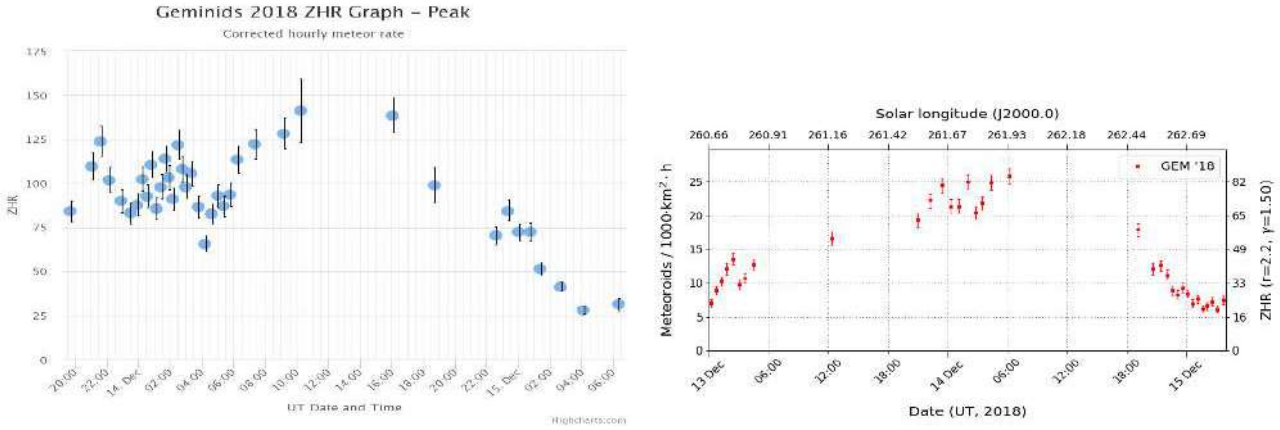
Video Commission: Sirko Molau, Abenstalstraße 13b, D-84072 Seysdorf, Germany; E-mail: video@imo.net

Visual Commission: Jürgen Rendtel, Eschenweg 16, D-14476 Potsdam, Germany; E-mail: visual@imo.net

Fireballs: please use the online fireball report form https://fireballs.imo.net/members/imo/report_intro to report your fireball observations (available in 30 languages!). You can integrate the fireball form into your own website, creating a fireball form in your own language without any reference to IMO!



The web page of the *International Meteor Organization*



Geminids 2018 – an example live graph as derived from the incoming visual data and the corresponding fluxviewer graph from video data.

ISBN 978-2-87355-034-9